

Dissertation

Phase behavior of simple liquids

ausgeführt zum Zwecke der Erlangung des akademischen
Grades eines Doktors der technischen Wissenschaften unter der Leitung
von

Univ.Doz. Ass.Prof. Dipl.-Ing. Dr.techn. Gerhard Kahl
Institut für Theoretische Physik

eingereicht an der Technischen Universität Wien
Fakultät für Technische Naturwissenschaften und Informatik

von

Dipl.-Ing. Andreas Lang
9225664
Bendlgasse 24/3, 1120 Wien

Wien, am 12. April 2001

Zusammenfassung

Einfache Flüssigkeiten können ein enorm reiches Phasenverhalten zeigen. Das Hauptaugenmerk dieser Dissertation ist die Beschreibung einiger Methoden, welche die Berechnung der strukturellen Eigenschaften und der Phasendiagramme einer breiten Palette von Systemen ermöglichen. Die Potentiale einiger dieser System (wie das 'square-well' Potential) sind von rein akademischer Bedeutung; andere wie das Asakura-Oosawa Potential beschreiben (zumindest qualitativ) das Verhalten einer Kolloid-Polymer Mischung.

Die Methoden welche zur Berechnung des flüssigen Zustandes eingesetzt wurden, sind die 'optimized random phase approximation', die 'mean spherical approximation' die Rogers-Young Näherung und die 'zero separation' Theorie. Für den festen Zustand haben wir Dichtefunktionalmethoden benutzt; diese basierten entweder auf der 'weighted density functional' Näherung ('modified weighted density approximation' und 'correlation modified weighted density approximation') oder auf fundamentalen Maßtheorien (fundamental measure theory), wie das Rosenfeld Funktional für harte Kugeln oder der 'soft fundamental measure theory' für andere Potentiale.

In den Phasendiagrammen, die mittels der oben aufgelisteten Theorien berechnet wurden, fanden wir einige interessante Phänomene (zum Beispiel isostrukturelle fest-fest Übergänge und trikritische Punkte); unsere Resultate bestätigten dabei die Ergebnisse von Computersimulationen.

Abstract

Simple liquids can show an enormously rich phase behavior. The focus of this thesis is to describe some methods to determine the structural properties and phase diagrams of a wide range of systems. The potentials of some of these systems are purely academic like the square-well potential; others like the Asakura-Oosawa potential capture (at least qualitatively) the behavior of a colloid-polymer mixture.

The methods we used for the liquids state are the optimized random phase approximation, the mean spherical approximation, the Rogers-Young approximation and the zero separation theory. For the solid state, we have used density functional methods; they are based on the weighted density functional approach (modified weighted density approximation and correlation modified weight density approximation) or the fundamental measure theory (Rosenfeld functional for hard spheres and soft fundamental measure theory for other potentials).

In the phase diagrams calculated using the methods listed above, we found some interesting phenomena (for instance isostructural solid-solid transitions and tricritical points); our results are able to confirm simulation data.

For my parents
Stefanie and Hermann

This thesis is based on the following original papers:

Section 6.1:

A. Lang, C.N. Likos, M. Watzlawek, and H. Löwen
Fluid and solid phases of the Gaussian core model
J. Phys.: Condens. Matter **12**, 5087 (2000)

Section 6.2:

C.N. Likos, A. Lang, M. Watzlawek, and H. Löwen
Criterion for determining clustering versus reentrant melting behavior of bounded interaction potentials
Phys. Rev. E **63**, 31206 (2001)

Section 6.4:

A. Lang, G. Kahl, C.N. Likos, H. Löwen, and M. Watzlawek
Structure and thermodynamics of square-well and square-shoulder fluids
J. Phys.: Condens. Matter **11**, 10143 (1999)

Contents

Introduction	1
2 The systems	5
2.1 System parameters	5
2.1.1 One-component systems	5
2.1.2 Binary Systems	6
2.2 Interatomic potentials	6
2.2.1 Hard-sphere potential	7
2.2.2 Square-well/square-shoulder potential	8
2.2.3 Hard-sphere Yukawa potential	9
2.2.4 Asakura-Oosawa potential	10
2.2.5 Gaussian core potential	13
2.2.6 Fermi distribution potential	14
2.2.7 Penetrable spheres model	14
2.2.8 Error function potential	14
3 Basics of liquid state theory	17
3.1 Ornstein-Zernike equation	17
3.2 Thermodynamic properties	19
3.2.1 Internal energy U	19
3.2.2 Pressure p	20
3.2.3 Helmholtz free energy A	21
3.2.4 Chemical potential μ	23
3.2.5 Isothermal compressibility χ_T	23
3.3 Thermodynamic inconsistency	24
4 Theoretical concepts	27
4.1 Perturbation theory	27
4.1.1 Basic ideas of the ORPA	29
4.1.2 Structure for the one component system	29
4.1.3 Structure for the binary system	31
4.1.4 Thermodynamic properties	32
4.1.5 Mean spherical approximation	38
4.1.6 Reference system (one component case)	39
4.1.7 Reference system (binary case)	40

4.1.8	Free volume approximation for A	42
4.2	Integral equations	43
4.2.1	Percus-Yevick approximation	44
4.2.2	Hypernetted chain approximation	44
4.2.3	Rogers-Young approximation	44
4.2.4	Zero separation closure	45
4.2.5	Numerical algorithms	47
4.2.6	Thermodynamic properties	51
4.3	Classical density-functional theory	51
4.3.1	WDA and MWDA	53
4.3.2	cMWDA	56
4.3.3	Fundamental measure theory	58
4.3.4	Evaluation of Φ	61
4.3.5	Roth's approach	66
4.3.6	Soft fundamental measure theory	67
4.3.7	Test particle limit	78
4.4	Simple perturbation theory for A in the solid state	81
4.5	Einstein model for the solid	82
5	Phase equilibria	85
5.1	One Component systems	85
5.1.1	Binodals	85
5.1.2	Spinodals	86
5.2	Binary systems	88
5.3	Entropy and freezing	90
6	Results	93
6.1	Gaussian core model	93
6.1.1	Structure	93
6.1.2	Phase diagram	100
6.2	Phase behavior of bounded potentials	104
6.2.1	Clustering versus reentrant melting behavior	104
6.2.2	The model and the mean-field limit	105
6.2.3	Spinodal instability and freezing	106
6.2.4	Comparison with simulations	108
6.3	One component hard sphere system	120
6.3.1	Fluid structure	120
6.3.2	Thermodynamic properties of the fluid	122
6.3.3	Fluid-solid phase transition for the HS system	126
6.3.4	Solid structure	131
6.4	Square well and square shoulder systems	139
6.4.1	Fluid structure	139
6.4.2	Thermodynamic properties	143
6.4.3	Phase diagrams	147
6.5	Asakura-Oosawa potential	166

6.6	One-component Yukawa potential	175
6.6.1	Vapor-liquid coexistence	175
6.6.2	Fluid-solid coexistence	178
6.7	Double square-well/square-shoulder potential	183
6.8	Binary phase diagrams	188
6.8.1	Truncated hard sphere-Yukawa potentials	188
Conclusion		197
A Abbreviations		199
A.1	List of abbreviations	199
B Mathematical definitions		201
B.1	Fourier transformation	201
B.1.1	Fourier transformation of a scalar function	201
B.1.2	Fourier transformation of a vector function	202
B.1.3	Fourier transformation of a tensor function	203
B.1.4	Fast Fourier transformation	205
B.1.5	Numerical problems	207
B.2	Convolutions	210
B.2.1	Scalar-Scalar	210
B.2.2	Scalar-Vector	210
B.2.3	Scalar-Tensor	211
B.3	Parseval theorem	211
C Ordered solid state		213
C.1	Lattice parameters	213
C.2	One-particle density for the ordered solid state	213
C.3	Pair distribution function in the solid	215
D Numerical methods		217
D.1	Steepest descent algorithm	217
D.2	Newton-Raphson method	217
Bibliography		221
Acknowledgment		227
Curriculum Vitae		229

Introduction

Investigations of phase transitions in condensed matter systems belong to the most challenging and most fascinating problems in physics. The complexity of phase transitions, the large variety of phases, and the discovery of new phases (such as quasicrystals) guarantee that scientists will be kept busy in the near future and will not lose interest in investigating these fascinating phenomena. During the past years, significant contributions in the descriptions of phase transitions in condensed matter physics have been proposed in theoretical or computational physics [1]. Therefore, theoretical concepts in combination with computational tools can be considered nowadays as complements to experimental techniques: on the one side they are able to reproduce experimental results with high accuracy and contribute in this way to a deeper insight into these phenomena; on the other side they can sometimes even predict (at least in a qualitative way) results which - due to extreme conditions (such as high pressure or low temperature) - are barely accessible in experiment.

Phase transitions in condensed matter phases are every-day phenomena and consequently very familiar (e.g., freezing or vaporization); therefore a deeper understanding of these phenomena is of a more widespread interest and not only a pure academic problem. Phase transitions are practically ubiquitous in our everyday lives, ranging from very simple, commonplace events to rather complicated and sophisticated production processes in industry where special knowledge of the phase-diagrams of substances is required and used. Therefore, the technological aspect of investigations in phase diagrams is of utmost importance and industrial developments and processes often rely on accurate and reliable phase diagrams. In particular in this field, theoretical investigations of phase diagrams might be helpful in replacing (at least partly) ‘real’ experiments: so, for example, computer experiments might be more economical than real experiments or theoretical investigations might indicate whether it is worthwhile to push experiments in a direction where difficult experimental conditions are to be expected.

With this thesis we intend to contribute to a deeper understanding of phase transitions. Among the various theoretical methods which were proposed over the last decades to describe these phenomena, we have chosen an access that - during the past years - has proven to be very successful (see, for instance, [2]): this approach focuses on the molecular aspect of these phenomena by trying to understand them from the microscopic point of view. The method we have chosen is based on statistical mechanics and it is liquid-based, i.e., it views a phase transition such as freezing as a condensation of liquid density modes. Classical density functional theory (DFT) is based on the reformulation of statistical mechanics in the language of functionals and direct correlation functions; its essence is

that the grand potential of a given system is a unique functional of the (inhomogeneous) one-particle density and that this functional is minimized by the equilibrium one-particle density. Liquid state theories provide us with information about the structure and the thermodynamics of the *homogeneous* liquid; these data are required for the liquid phase itself and for the solid phase when the ordered phase (the crystal, for instance) is viewed as a spatially modulated liquid. In principle, these two ingredients are sufficient to describe ‘standard’ phase transitions in simple systems (liquid-vapor, liquid-liquid, liquid-solid and solid-solid transitions).

It should also be mentioned that this combination of classical DFT plus liquid state theory for the homogeneous liquid phase can be successfully applied for several other classes of problems in liquid state (or condensed matter) physics, i.e., to describe strongly inhomogeneous systems [3]: phenomena such as nucleation [4], structure and thermodynamics of interfaces and surfaces, or wetting problems [5] can be described very conveniently within this framework.

The contributions of this thesis to classical liquid state theory and classical DFT are the following:

- **liquid state theory:** We have implemented some of the ‘standard’ liquid state theories [6] [optimized random phase approximation [7] (ORPA), exponential approximation [7, 8] (EXP), hypernetted chain approximation [9] (HNC), Percus-Yevick approximation [10] (PY) and Rogers-Young approximation [11] (RY)] in order to evaluate and compare the thermodynamic properties and structure functions for systems with a wide variety of interparticle potentials [bounded ones such as the Gaussian core potential (subsection 2.2.5), the Fermi distribution potential (subsection 2.2.6), the penetrable spheres model (subsection 2.2.7) or the error function potential (subsection 2.2.8) and unbounded ones (containing a hard core) like the hard-sphere potential (subsection 2.2.1), the square-well/square-shoulder potential (subsection 2.2.2), the double square-well/double square-shoulder potential (subsection 2.2.2.1), the hard-sphere Yukawa potential (2.2.3) and the Asakura-Oosawa potential (subsection 2.2.4)]. The liquid state theories used in this thesis are perturbation theories or integral equations. Whenever possible, the obtained results were compared with the ones from computer simulations or other theories (which are not discussed in this work). Additionally, we have examined the problem of thermodynamic self consistency for some of the methods presented here.

Although most of the theories mentioned above were introduced decades ago, they are still able to give remarkably good results when compared to more advanced ‘modern’ theories [such as the soft fundamental measure theory (SFMT) coupled with the test particle limit (TPL), see below].

- **classical density functional theory:** In this thesis we have used different types of classical density functional theories. The well established class of weighted density approximation functionals [modified weighted density approximation [12] (MWDA) and correlation weighted density approximation [13] (cMWDA)] were, along with the results of the liquid-state theories as an input, used to discover the solid phase of the system. From the class of fundamental measure theories (FMT), we have used the Rosenfeld functional [14] to yield both the liquid and solid structure of a

hard sphere system. As a rather new approach, we have used the soft fundamental measure theory [15] (SFMT) (a generalized version of the Rosenfeld functional), to get the structure functions of the liquid and the thermodynamic properties of the solid for some systems. Additionally, the test particle limit [16, 17] (TPL) was used to correct the unphysical behavior the fundamental measure theory predicts for the structure functions of the examined systems.

Both of these two classes of theories (weighted density approximations and fundamental measure theories) were also the baseline for some simple first order perturbation theories, the free volume approximation (FVPA, see section 4.1.8) and the modified perturbation approximation (MPA, see section 6.6.1). Although the functionals based on the weighted density approach are rather dated, they give in most cases better results than the more sophisticated fundamental measure theory functionals.

Using those theories, we have calculated the liquid-liquid phase diagrams for both one-component [Gaussian core potential (subsection 6.1.2), hard-sphere potential (subsection 6.3.3), square-well and square-shoulder potential (subsection 6.4.3), Asakura-Oosawa potential (subsection 6.5) and double square-well/double square-shoulder potential (subsection 6.7)] and binary systems [hard-sphere Yukawa potential]; for one-component systems we have, whenever possible, calculated also the liquid-solid (and solid-solid) phase transitions [where the crystal structure of the solid was either face centered cubic (fcc) or body centered cubic (bcc), see appendix C.1]. The model potentials we considered are not simple academic creations; in many cases they describe the effective interactions in colloidal suspension or solutions, such as charge-stabilized colloids (Yukawa), polymer chains (Gauss) or colloid-polymer mixtures (Asakura-Oosawa).

The thesis is organized as follows: In chapter 2 the different interparticle potentials of the one-component and binary systems used in this thesis are introduced. In chapter 3 the fundamental relations for the structure and the thermodynamic properties are developed. In chapter 4 the theoretical concepts (as mentioned above) used in this work to evaluate the structure and thermodynamic properties of the liquid and the solid state are introduced. In chapter 5 we summarize the methods used to obtain phase diagrams of one-component and binary systems. The results are presented and discussed in chapter 6. We summarize and conclude in chapter 7. The appendices A to D contain a list of abbreviations (appendix A), some mathematical definitions used in this work (appendix B), important relations and definitions for the solid state (appendix C) and a short summary of two numerical methods (appendix D).

Chapter 2

The systems

2.1 System parameters

2.1.1 One-component systems

In a one-component system there is only one species of particles that interact via pair-potentials $\phi(\vec{r})$; in this thesis all the potentials are radially symmetric [$\phi(\vec{r}) = \phi(r)$] and density independent. In the liquid and the gas phase we consider homogeneous and isotropic systems, i.e., at every space point the mean density is constant. The solid phases of the system are inhomogeneous (the particles are centered around the lattice points). The system of N particles is confined in a volume V ; we define the number density ρ as:

$$\rho = \frac{N}{V}. \quad (2.1)$$

The potentials used in this thesis are characterized by a scaling parameter σ in distance (such as the hard sphere diameter) and a scaling parameter ε in energy. It is convenient to define a reduced dimensionless number density ρ^* via

$$\rho^* = \frac{N}{V}\sigma^3 \quad (2.2)$$

and - for the temperature T - a reduced dimensionless temperature T^* via

$$\frac{1}{\beta\varepsilon} = \frac{k_B T}{\varepsilon} = T^*, \quad (2.3)$$

where β is the Boltzmann factor. Further, we define the packing fraction η via

$$\eta = \frac{V_p}{V} = \frac{\pi}{6}\rho\sigma^3 = \frac{\pi}{6}\rho^*, \quad (2.4)$$

which - for the case of hard spheres - corresponds to the ratio of volume occupied by the particles, V_p , to the volume V .

2.1.2 Binary Systems

In a binary system there are two species of particles labeled by indices 1 and 2, hence the system is characterized by a set of three interatomic potentials,

$$\phi_{11}(r) \quad ; \quad \phi_{12}(r) = \phi_{21}(r) \quad ; \quad \phi_{22}(r). \quad (2.5)$$

In this thesis we consider a special group of binary systems, the so called symmetric binary systems: here the like interactions are equal, only the unlike particles see a different interaction

$$\phi_{11}(r) = \phi_{22}(r) \neq \phi_{12}(r).$$

In the binary case a volume of V is occupied by N_1 particles of species 1 and N_2 particles of species 2, hence we can define two partial number densities

$$\rho_1 = \frac{N_1}{V} \quad ; \quad \rho_2 = \frac{N_2}{V}, \quad (2.6)$$

and the total number density

$$\rho = \rho_1 + \rho_2 = \frac{N_1 + N_2}{V}.$$

Further, it is convenient to define the concentrations of species i , c_i ,

$$c_1 = \frac{N_1}{N} = \frac{\rho_1}{\rho} \quad ; \quad c_2 = \frac{N_2}{N} = \frac{\rho_2}{\rho} \quad ; \quad c_1 + c_2 = 1.$$

The potentials are characterized by length scales σ_{ij} ($\sigma_{ii} = \sigma_i$) and energy scales ε_{ij} ($\varepsilon_{ii} = \varepsilon_i$).

Introducing a size-ratio q of the two length scales

$$q = \frac{\sigma_2}{\sigma_1}$$

we can again define reduced (partial or total) number densities

$$\begin{aligned} \rho_1^* &= \rho_1 \sigma_1^3 \quad ; \quad \rho_2^* = \rho_2 q^3 \sigma_1^3 \\ \rho^* &= \rho_1^* + \rho_2^* = \frac{N}{V} (c_1 + c_2 q^3) \sigma_1^3. \end{aligned}$$

The packing fraction is now defined as

$$\eta = \frac{\pi}{6} \sigma_1^3 (\rho_1 + \rho_2 q^3) = \frac{\pi}{6} \sigma_1^3 \rho (c_1 + c_2 q^3) = \frac{\pi}{6} \rho^*.$$

2.2 Interatomic potentials

In this chapter we give an overview over the various potentials used in this thesis. Besides the definition of each potential we will also show the corresponding Mayer function which is defined as

$$f(r) = e^{-\beta\phi(r)} - 1. \quad (2.7)$$

2.2.1 Hard-sphere potential

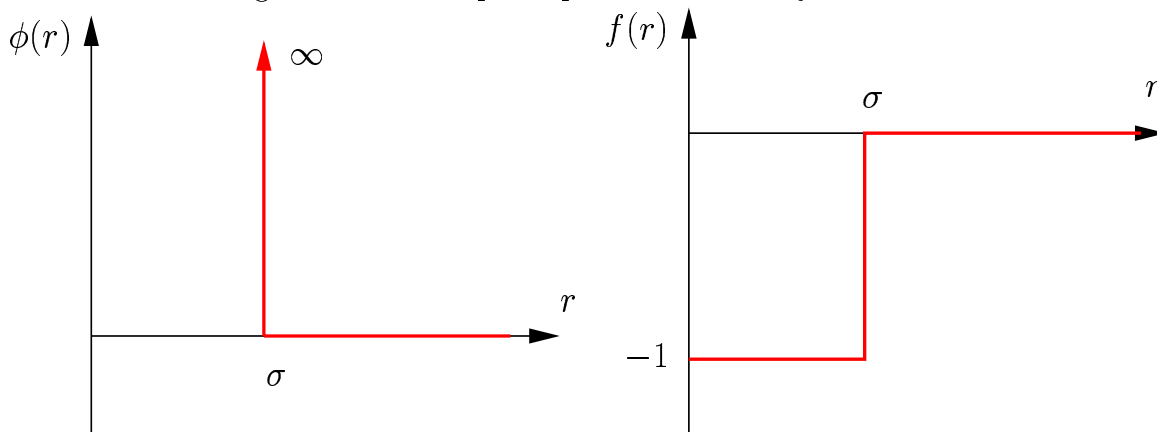
The hard-sphere (HS) potential is defined via

$$\phi(r) = \begin{cases} \infty & r < \sigma \\ 0 & r \geq \sigma \end{cases} . \quad (2.8)$$

with the Mayer function

$$f_{HS}(r) = \begin{cases} -1 & r < \sigma \\ 0 & r \geq \sigma \end{cases} .$$

Figure 2.1: Hard-sphere potential and Mayer function



For many years, the HS system was a very useful but purely theoretical construction. A purely hard potential does not materialize in atomic systems. However, with the advance of colloidal science, it became possible to prepare samples which are extremely close in their behavior to an ideal HS system. By index matching colloidal particles with the surrounding solvent, the van der Waals attraction can be drastically reduced (see [18]) and the interaction between the colloids is then dominated by the repulsive core [19, 20, 21]. The HS system is without doubt the best examined system in liquid state theory; its structural and thermodynamic properties have been studied thoroughly. For the HS potential the Percus-Yevick (PY) approximation is analytically solvable [10], however this solution has some problems to reproduce the results (pressure) from computer simulations for high packing fractions. For the thermodynamic properties the empirical Carnahan-Starling [22] equations leads to an excellent agreement with simulation results. To improve the agreement for the structure, Verlet and Weis [23] and also Henderson and Grundke [24] proposed a semiempirical parameterization of the correlation functions. Further, the HS potential plays an important role as a reference system in perturbation theories since it captures the main features of the repulsive part of a typical interatomic potential.

2.2.2 Square-well/square-shoulder potential

The square-well/square-shoulder (SW/SS) potential is given by a HS core and an adjacent constant perturbation. We use the following definition

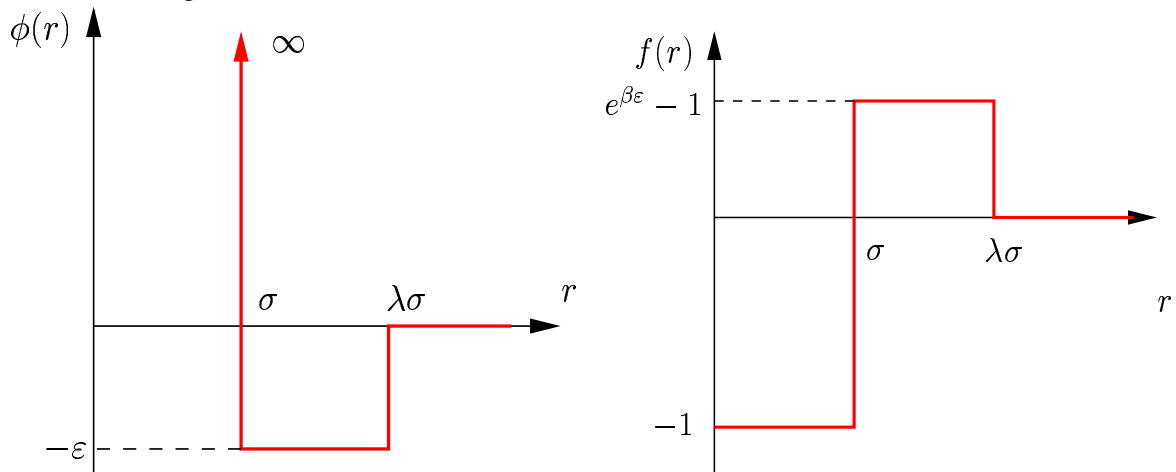
$$\phi(r) = \begin{cases} \infty & r < \sigma \\ -\varepsilon & \sigma \leq r \leq \sigma\lambda \\ 0 & r > \sigma\lambda \end{cases} ,$$

where λ is the perturbation width. For positive ε , the perturbation is attractive (square-well); if ε is negative the perturbation is repulsive (square-shoulder). The Mayer function for this potential is

$$f(r) = \begin{cases} -1 & r < \sigma \\ e^{\beta\varepsilon} - 1 & \sigma \leq r \leq \sigma\lambda \\ 0 & r > \sigma\lambda \end{cases} .$$

Although this potential seems rather academic, it captures (to a certain extent) the be-

Figure 2.2: Square-well potential with $\lambda = 2$ and Mayer function

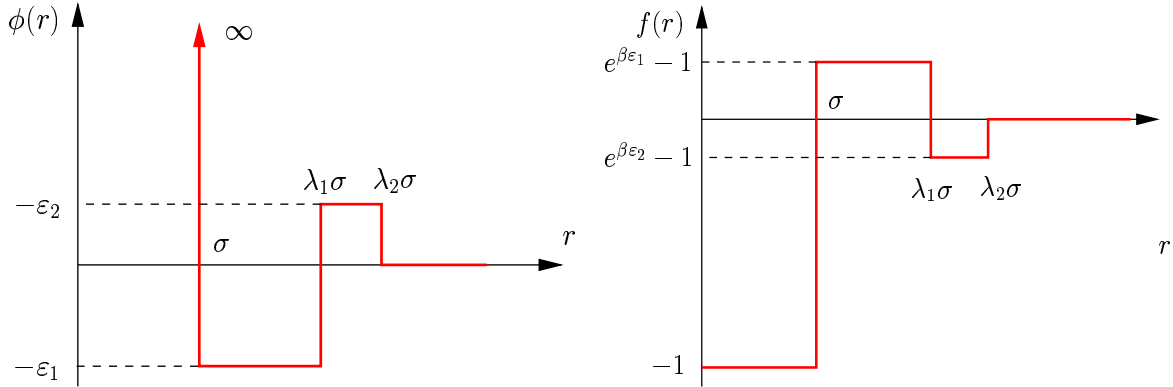


havior of mesoscopic spherical particles (interacting via a hard-sphere-like interaction) in a microscopic solvent (assuming that the mesoscopic particles and the particles of the solvent have no or only very weak interactions). The SS potential models the interaction potential of sterically stabilized colloids with short grafted chains, whereas the SW potential models the potential of colloid-polymer mixtures or atomic systems with van der Waals attractions.

For small perturbation widths there exists a semi-analytic solution of the Percus-Yevick approximation derived by Nezbeda [25].

2.2.2.1 Double square-well/double square-shoulder potential

The double square-well/double square-shoulder (DSW/DSS) potential is simply an extension of the SW/SS potential, introducing a second step:

Figure 2.3: Double-well potential with $\lambda_1 = 2$, $\lambda_2 = 2.5$, $\varepsilon_1/\varepsilon_2 = -\frac{5}{3}$ and Mayer function

$$\phi(r) = \begin{cases} \infty & r < \sigma \\ -\varepsilon_1 & \sigma \leq r \leq \sigma\lambda_1 \\ -\varepsilon_2 & \sigma\lambda_1 < r \leq \sigma\lambda_2 \\ 0 & r > \sigma\lambda_2 \end{cases},$$

with the Mayer function

$$f(r) = \begin{cases} -1 & r < \sigma \\ e^{\beta\varepsilon_1} - 1 & \sigma \leq r \leq \sigma\lambda_1 \\ e^{\beta\varepsilon_2} - 1 & \sigma\lambda_1 \leq r \leq \sigma\lambda_2 \\ 0 & r > \sigma\lambda_2 \end{cases}.$$

The reduced temperature will be defined via one of the parameters ε_i , the other one being related via a factor ε_r , i.e.,

$$\varepsilon_2 = \varepsilon_1\varepsilon_r$$

This potential type shows a very rich phase behavior in the fluid state, for instance one can encounter up to two critical points [see section 6.7].

2.2.3 Hard-sphere Yukawa potential

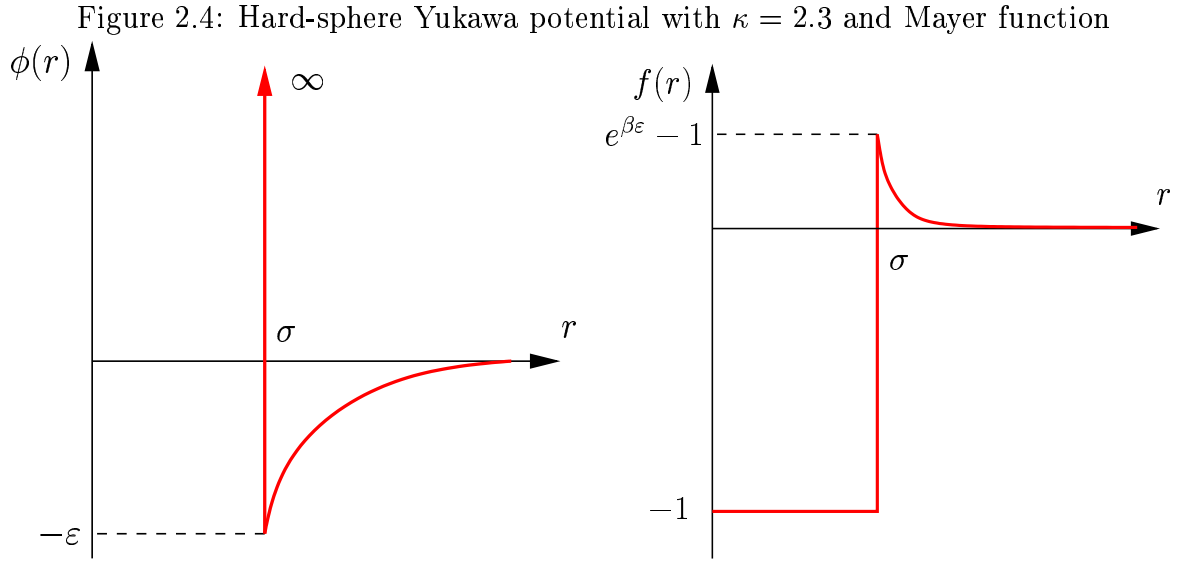
The hard-sphere Yukawa (HSY) potential is given by a hard-sphere core and an adjacent exponential perturbation. We use the following definition

$$\phi(r) = \begin{cases} \infty & r < \sigma \\ -\varepsilon\frac{\sigma}{r}e^{-\kappa(r-\sigma)} & r \geq \sigma \end{cases},$$

where κ is the so called inverse screening length. The Mayer function of this potential is

$$f(r) = \begin{cases} -1 & r < \sigma \\ \exp\left[\beta\varepsilon\frac{\sigma}{r}e^{-\kappa(r-\sigma)}\right] - 1 & r \geq \sigma \end{cases}.$$

The HSY potential is the effective potential of charge-stabilized colloidal suspensions



(approximated within the Derjaguin-Landau-Verwey-Overbeek (DLVO) theory, see [26, 27]) [2]: such suspensions are created by putting big particles with surface radicals into a polar solvent like water. Most of the charged surface groups dissociate into to solvent and form counterions carrying one or two elementary charges. Consequently, the colloidal particles become highly charged and may be called macroions (they carry typically 100-10000 elementary charges). Since the counterion distribution is diffuse due to their finite temperature, the screening of the macroions is imperfect and a screened Coulomb repulsion between the macroions is the result. The HSY potential now models the interaction potential between the macroions.

2.2.3.1 Truncated Hard-sphere Yukawa potential

The truncated HSY potential (tHSY) is a modification of the original HSY potential where one sets

$$\phi(r) = 0 \quad \text{for} \quad r > \lambda\sigma,$$

where $\lambda\sigma$ is the so called truncation radius. This potential was introduced because for computer simulations the potential is always truncated (due to the finite range of the simulation box).

2.2.4 Asakura-Oosawa potential

The Asakura-Oosawa (AO) potential was proposed by Asakura and Oosawa in 1954 [28] (and later developed independently by Vrij [29]) to model the interaction between colloidal particles and nonadsorbing (free) polymers in a solvent. This model is an extreme non-additive binary hard-sphere model, in which the colloids are treated as hard spheres (with diameter σ) and the interpenetrable, non-interacting polymers (polymer coils, diameter

σ_p) are treated as point particles but which are excluded from the colloids to a center-of-mass distance of $(\sigma_c + \sigma_p)/2$ [i.e., the polymers can approach the colloids up to a distance of $\sigma_p (= q\sigma)$].

The potential is given by

$$\phi(r) = \begin{cases} \infty & r < \sigma \\ -\frac{1}{\beta} \frac{\pi}{6} \sigma_p^3 z_p \frac{(1+q)^3}{q^3} \left[1 - \frac{3r}{2(1+q)\sigma} + \frac{r^3}{2(1+q)^3 \sigma^3} \right] & \sigma \leq r \leq \sigma + \sigma_p \\ 0 & r < \sigma + \sigma_p \end{cases},$$

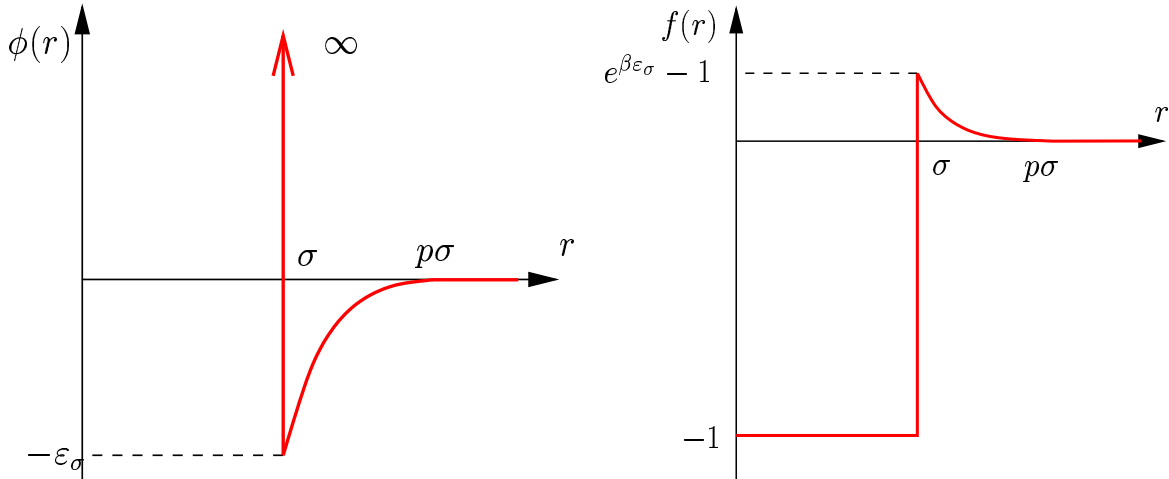
where μ_p is the chemical potential of the polymer coils and $z_p = e^{\beta\mu_p}/\Lambda^3$ is the fugacity of the polymer particles (Λ is the de Broglie thermal wavelength). In this model, $\frac{\pi}{6} z_p$ can be replaced with η_p^r , the packing fractions of the polymers in a reservoir (which is in thermal, mechanic and particle equilibrium with the polymers). The explicit form of the effective pair potential of the colloids is derived by integrating out the degrees of freedom of the polymer particles in the grand canonical partition function of the colloid-polymer mixture and neglecting contributions due to particle interactions of order three or higher (for nonadditive systems see [30], for additive systems we refer to [31]).

After introducing the parameter $p = 1 + q$ we can rewrite the potential as follows:

$$\phi(r) = \begin{cases} \infty & r < \sigma \\ -\frac{1}{\beta} \eta_p^r \left(\frac{p}{1-p} \right)^3 \left[1 - \frac{3}{2} \frac{r}{p\sigma} + \frac{1}{2} \left(\frac{r}{p\sigma} \right)^3 \right] & \sigma \leq r \leq p\sigma \\ 0 & r < p\sigma \end{cases},$$

where η_p^r is the packing fraction of the polymer coils as described above. The prefactor

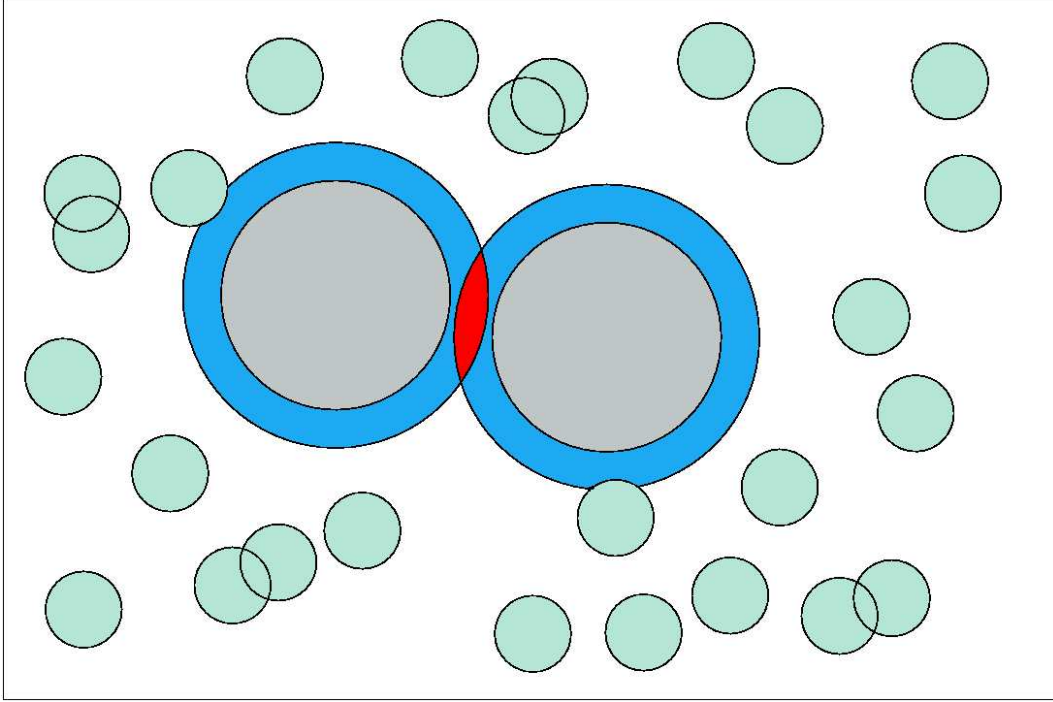
Figure 2.5: Asakura-Oosawa potential with $q = 0.8$ ($p = 1.8$) and Mayer function



η_p^r/β can be interpreted as the “strength” of the attractive tail. The value of the potential at $r = \sigma$ is equal to

$$-\varepsilon_\sigma = -\frac{\eta_p^r}{\beta} \left(\frac{p}{1-p} \right)^3 \left[1 - \frac{3}{2p} + \frac{1}{2p^3} \right].$$

Figure 2.6: The depletion mechanism. The two big spheres (diameter σ) are each surrounded by a depletion layer of thickness $\frac{\tau}{2}$, where τ is the diameter of the small spheres. The overlap area of the two depletion layers is depicted by the lens-shaped area between the two big spheres.



The Mayer function of this potential is equal to

$$f(r) = \begin{cases} -1 & r < \sigma \\ \exp \left\{ \eta_p^r \left(\frac{p}{1-p} \right)^3 \left[1 - \frac{3}{2} \frac{r}{p\sigma} + \frac{1}{2} \left(\frac{r}{p\sigma} \right)^3 \right] \right\} - 1 & \sigma \leq r \leq p\sigma \\ 0 & r > p\sigma \end{cases} .$$

The AO potential describes the effective potential of large (colloidal) particles which are immersed in a solvent including of smaller macromolecules (polymer coils). The attractive behavior of this potential can be explained in two different ways. Whenever two colloidal particles come close to each other, the number of polymer coils between these two particles becomes smaller; hence there is an unbalanced pressure on the two colloidal particles by the polymer coils from the ‘outside’ pushing them together. This is the so called *depletion mechanism*; another explanation can be seen in figure 2.6. The solvent particles (diameter τ) are interacting with the mesoscopic particles (with diameter σ) by means of the hard-sphere potential, thus the solvent particles are excluded from a sphere of diameter $\sigma + \tau$ surrounding each mesoscopic particle (denoted by the so called *depletion layer* in figure 2.6). Whenever the depletion layers of two mesoscopic particles overlap, the total available volume of the solvent particles increases by the overlap volume (denoted as the lens-shaped area in figure 2.6). As shown in [18], this leads to an (entropy

driven) attractive interaction between the two mesoscopic particles.

2.2.5 Gaussian core potential

The Gaussian core potential (or Gaussian core model, GCM) is a bounded potential and is defined by

$$\phi(r) = \varepsilon e^{-\left(\frac{r}{\sigma}\right)^2}. \quad (2.9)$$

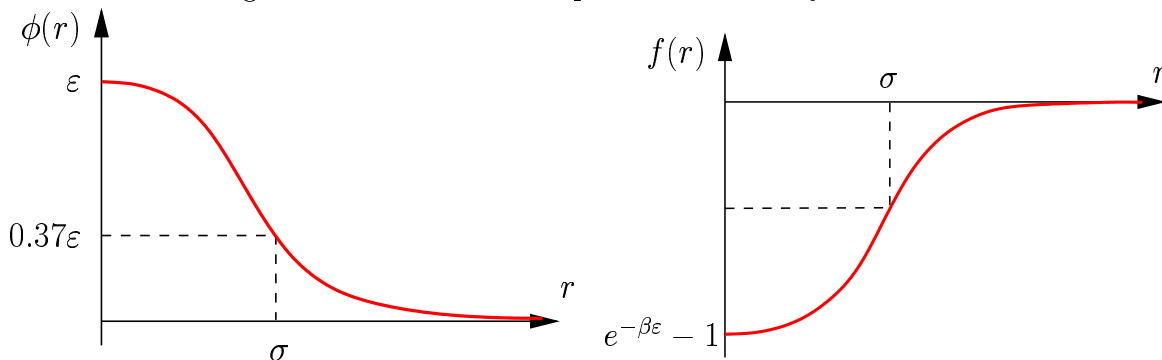
The Mayer function of this potential is given by

$$f(r) = \exp\left(-\beta\varepsilon e^{-\left(\frac{r}{\sigma}\right)^2}\right) - 1.$$

This potential allows, for instance, a partial or complete overlap of two particles. Such a phenomenon can be observed in polymers: in a solution of polymer coils the potential of mean force, acting between the center of masses of the coils, is given by a pair potential $\phi(r)$. For these ‘effective’ particles it is *not* forbidden that two center of masses are located at the same point.

A Gaussian pair potential was first proposed fifty years ago by Flory and Krigbaum [32] for the effective interaction between the centers of mass of two polymer chains. As a realistic model for a bounded potential, the Gaussian core model in the present form was introduced by Stillinger [33]. This work was complemented later by molecular dynamics simulations [34, 35], high-temperature expansions [36] and the discovery of exact duality relations in the crystalline state [37] (see section 6.1). The effective interaction between linear polymers has been extensively studied by computer simulations, both on-lattice [38, 39] and off-lattice [40, 41, 42, 43, 44, 45]. The structure and thermodynamic properties (including a quantitative phase diagrams, see section 6.1.2) of the GCM has been studied recently in [46] using integral equations. For a detailed study of the Gaussian core potential see section 6.1.

Figure 2.7: Gaussian core potential and Mayer function



2.2.6 Fermi distribution potential

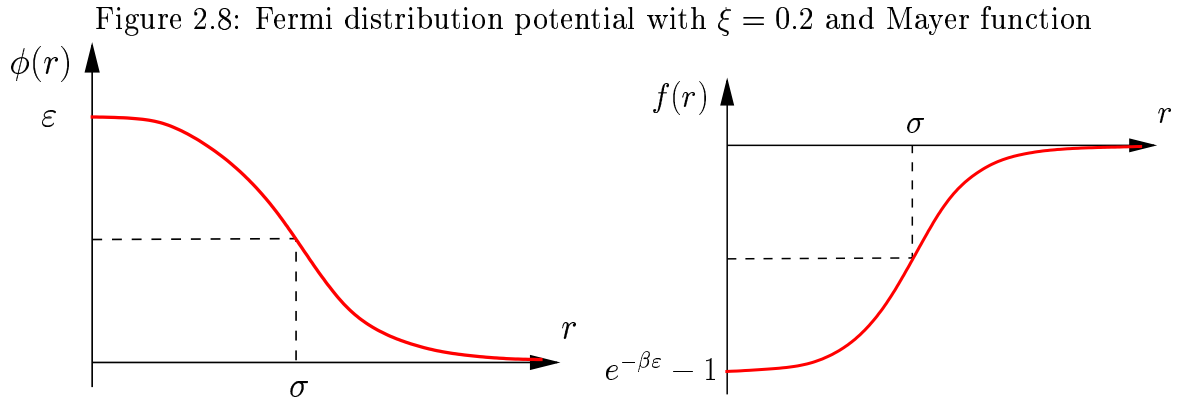
The Fermi distribution potential (or Fermi distribution model, FDM) is a bounded potential and is defined as

$$\phi(r) = \varepsilon \frac{1 + e^{-\sigma/\xi}}{1 + e^{(r-\sigma)/\xi}}, \quad (2.10)$$

with the Mayer function

$$f(r) = \exp\left(-\beta\varepsilon \frac{1 + e^{-\sigma/\xi}}{1 + e^{(r-\sigma)/\xi}}\right) - 1.$$

ξ is a “smoothing parameter”, having the dimension of length. With this parameter one can tune this potential from the penetrable sphere model (PSM, $\xi \rightarrow 0$, see below) to a constant potential [$\xi \rightarrow \infty$, $\phi(r) = \varepsilon$].



2.2.7 Penetrable spheres model

The penetrable spheres model (PSM) is the limiting case of the FDM ($\xi \rightarrow 0$) and is given by

$$\phi(r) = \begin{cases} \varepsilon & r < \sigma \\ 0 & r \geq \sigma \end{cases},$$

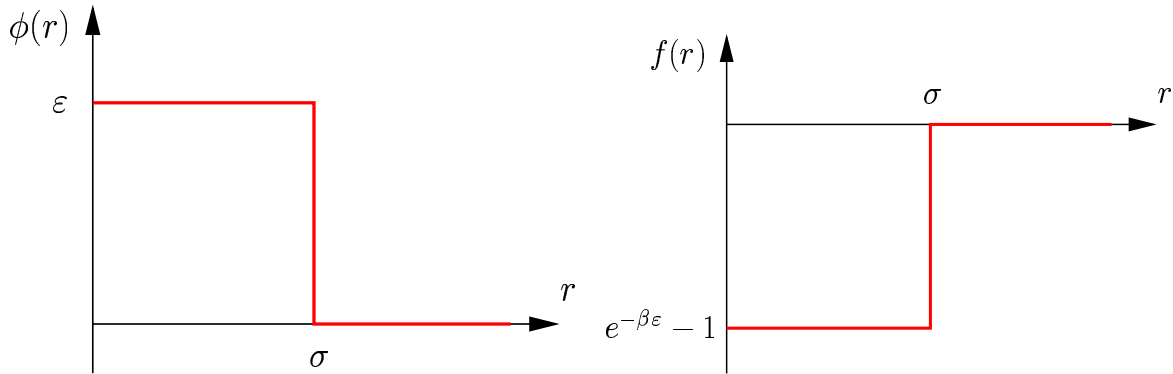
with the Mayer function

$$f(r) = \begin{cases} e^{-\beta\varepsilon} - 1 & r < \sigma \\ 0 & r \geq \sigma \end{cases}.$$

2.2.8 Error function potential

The error function (ERF) potential is a rather academic case. One reason to introduce this potential is the fact that its Mayer function can be de-convolved in the framework of

Figure 2.9: Penetrable sphere model and Mayer function



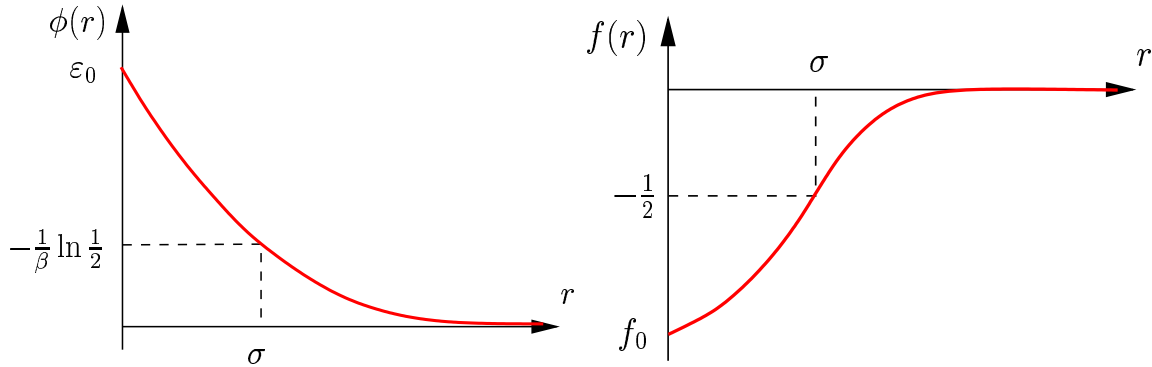
the Soft fundamental measure theory (as shown in section 4.3) analytically (under certain assumptions for the potential parameters). The definition of this potential is

$$\phi(r) = -\frac{1}{\beta} \ln \left[\frac{1 + \operatorname{erf} \left(\frac{r-\sigma}{a} \right)}{2} \right],$$

where $\operatorname{erf}(x)$ is the error function given by

$$\operatorname{erf}(x) = \frac{2}{\sqrt{\pi}} \int_0^x dt e^{-t^2}.$$

This definition leads to the Mayer function

Figure 2.10: Error function potential with $a = 1$ and Mayer function

$$f(r) = -\frac{1}{2} \left[1 - \operatorname{erf} \left(\frac{r-\sigma}{a} \right) \right].$$

For $r = 0$ the potential and the Mayer function have the values

$$\phi(r=0) = \varepsilon_0 = -\frac{1}{\beta} \ln \left[\frac{1 - \operatorname{erf} \left(\frac{\sigma}{a} \right)}{2} \right] \quad ; \quad f(r=0) = f_0 = -\frac{1}{2} \left[1 + \operatorname{erf} \left(\frac{\sigma}{a} \right) \right].$$

In the limit $a \rightarrow 0$ the Mayer function becomes

$$f(r) = \begin{cases} -1 & r < \sigma \\ 0 & r \geq \sigma \end{cases}$$

the HS model (which can also be interpreted as a special case of the penetrable sphere model). Another limit is that if a is small enough ($a < 0.3$), $f(r = 0)$ is approximately equal to -1 and the potential is very similar to having a hard core.

Chapter 3

Basics of liquid state theory

3.1 Ornstein-Zernike equation

The Ornstein-Zernike (OZ) [47] equation relates the total correlation function $h(r)$ and the direct correlation function $c(r)$ of a fluid. For the case of a uniform, one-component liquid this equation is given by [6]

$$h(r) = c(r) + \rho \int_{\mathbb{R}^3} d^3 r_1 c(|\vec{r} - \vec{r}_1|) h(r_1) = c(r) + \rho (c * h)(r), \quad (3.1)$$

where ρ is the number density (2.1) and the asterisk $*$ denotes a convolution. The interpretation of the OZ relation is as follows: the *total* correlation function $h(r)$ between two particles is given by the *direct* correlation function $c(r)$ plus the *indirect* correlation via all other particles in the system.

For convenience, we introduce the radial distribution function $g(r)$, defined as

$$g(r) = h(r) + 1.$$

Physically, the quantity $\rho g(r)$ is proportional to the conditional probability density of finding a particle at the distance r given that another particle is located at the origin.

For binary systems the OZ equations are now a set of three coupled integral equations (with $i, j = 1, 2$):

$$\begin{aligned} h_{ij}(r) &= c_{ij}(r) + \sum_{k=1}^2 \rho_k \int_{\mathbb{R}^3} d^3 r_1 c_{ik}(|\vec{r} - \vec{r}_1|) h_{kj}(r_1) \\ &= c_{ij}(r) + \sum_{k=1}^2 \rho_k (c_{ik} * h_{kj})(r), \end{aligned} \quad (3.2)$$

where the ρ_i are the partial number densities (2.6), the $c_{ij}(r)$ are the partial direct correlation functions and the $h_{ij}(r)$ are the partial total correlation functions. Due to the

symmetry of equation (3.2) with respect to the indices, the correlation functions $h_{ij}(r)$ and $c_{ij}(r)$ fulfill the following relations:

$$h_{12}(r) = h_{21}(r) \quad ; \quad c_{12}(r) = c_{21}(r).$$

We define partial pair distribution functions $g_{ij}(r)$ like in the one component case:

$$g_{ij}(r) = h_{ij}(r) + 1.$$

To solve the OZ-equation(s) one requires a further (functional) relation between the correlation functions and the pair potentials, known in the literature as closure relations (the closure relations used in this thesis are summarized in section 4.2). Such relations can be derived from exact diagrammatic expansions of statistical mechanics, introducing simplifying approximations.

It is convenient to introduce for subsequent calculations the following functions:

$$e(r) = e^{-\beta\phi(r)} \tag{3.3}$$

and the so called cavity function $y(r)$:

$$y(r) = \frac{h(r) + 1}{e(r)} = g(r)e^{\beta\phi(r)}. \tag{3.4}$$

In Fourier space, the OZ equation (3.1) reads (where Fourier transformed functions are denoted via a tilde)

$$\tilde{h}(k) = \tilde{c}(k) + \rho\tilde{h}(k)\tilde{c}(k). \tag{3.5}$$

From this equation we can express $\tilde{h}(k)$ and $\tilde{c}(k)$ as

$$\tilde{h}(k) = \frac{\tilde{c}(k)}{1 - \rho\tilde{c}(k)} \tag{3.6}$$

$$\tilde{c}(k) = \frac{\tilde{h}(k)}{1 + \rho\tilde{h}(k)}. \tag{3.7}$$

$\tilde{h}(k)$ is related to the static structure factor $S(k)$, which can be determined in scattering experiments, through:

$$S(k) = 1 + \rho \int_{\mathbb{R}^3} d^3r_1 e^{i\vec{k}\vec{r}_1} h(r) = 1 + \rho\tilde{h}(k) = \frac{1}{1 - \rho\tilde{c}(k)}. \tag{3.8}$$

In the binary case it is convenient to introduce matrices \mathcal{C} and \mathcal{H} , defined via

$$(\mathcal{C})_{ij}(k) = \tilde{C}_{ij}(k) = \sqrt{\rho_i\rho_j}\tilde{c}_{ij}(k) \quad ; \quad (\mathcal{H})_{ij}(k) = \tilde{H}_{ij}(k) = \sqrt{\rho_i\rho_j}\tilde{h}_{ij} \tag{3.9}$$

After a Fourier transformation of equation (3.2) we get

$$\tilde{H}_{ij}(k) = \tilde{C}_{ij}(k) + \sum_{l=1,2} \tilde{C}_{il}(k)\tilde{H}_{lj}(k). \tag{3.10}$$

In matrix notation, this equation reads

$$\mathcal{H} = \mathcal{C} + \mathcal{C} \cdot \mathcal{H}, \quad (3.11)$$

where the dot denotes a matrix multiplication. From this equation one can derive relations similar to (3.6), (3.7):

$$\mathcal{H} = (\mathbb{I} - \mathcal{C})^{-1} \cdot \mathcal{C} \quad ; \quad \mathcal{C} = \mathcal{H} \cdot (\mathbb{I} + \mathcal{H})^{-1},$$

where \mathbb{I} is the 2x2 unity matrix and $(\mathcal{A})^{-1}$ denotes the inverse of the matrix \mathcal{A} . The definition of the static structure factor for binary systems is:

$$\mathcal{S}(k) = \mathbb{I} + \mathcal{H} = (\mathbb{I} - \mathcal{C})^{-1}. \quad (3.12)$$

3.2 Thermodynamic properties

Once the OZ equation has been solved with the help of a closure relation, the thermodynamic properties of the system can be calculated. It is convenient to split thermodynamic quantities into two contributions:

- The ideal part ('id') describes the corresponding thermodynamic property for an ideal gas; here all these quantities can be calculated analytically.
- The contribution to a thermodynamic property arising from the (pair) interactions is the excess part ("ex") and has to be calculated - in general - numerically.

3.2.1 Internal energy U

The ideal part of the internal energy is given by

$$U_{id} = \frac{3}{2} N k_B T. \quad (3.13)$$

We have used the following reductions for U_{id}

$$U_{id}^* = \frac{2\beta}{3N} U_{id} = 1 \quad (3.14)$$

$$U_{id}^+ = \rho \frac{2\beta}{3N} U_{id} = \rho. \quad (3.15)$$

The first reduction (with respect to the number of the particles) leads to a dimensionless quantity, the dimension of the second reduction is equal to an inverse volume. To make the second reduction also dimensionless, one can multiply the result with σ^3 . In the following reductions of the first kind will be marked with an asterisk (*) as a mark, reductions of the second kind will be characterized by a plus (+).

For the excess part of the internal energy one finds [6]

$$U_{ex} = \rho \frac{N}{2} \int_{\mathbb{R}^3} d^3r g(r) \phi(r). \quad (3.16)$$

Hence we obtain for U

$$U = U_{id} + U_{ex} = Nk_B T \left[\frac{3}{2} + \frac{\rho}{2} \int_{\mathbb{R}^3} d^3 r g(r) \beta \phi(r) \right].$$

After introducing the reduced pair potential $\phi^*(r)$ defined as

$$\phi(r) = \varepsilon \phi^*(r) \quad ; \quad \beta \phi(r) = \frac{1}{T^*} \phi^*(r)$$

the reduced internal energy $U^* = \frac{2\beta}{3N} U$ reads

$$U^* = 1 + \frac{\rho}{3T^*} \int_{\mathbb{R}^3} d^3 r g(r) \phi^*(r). \quad (3.17)$$

For binary systems one finds

$$U = U_{id} + \rho \frac{N}{2} \sum_{i,j=1}^2 c_i c_j \int_{\mathbb{R}^3} d^3 r g_{ij}(r) \phi_{ij}(r),$$

where U_{id} is given by equation (3.13).

3.2.2 Pressure p

The pressure can be split into the ideal part

$$p_{id} = \frac{N}{V\beta}$$

and the excess part (valid only for density independent pair potentials)

$$p_{ex} = -\frac{1}{3} \frac{N}{V} \frac{\rho}{2} \int_{\mathbb{R}^3} d^3 r \left(\vec{r} \cdot \vec{\nabla} \right) \phi(r) g(r) = -\frac{2\pi}{3} \rho^2 \int_0^\infty dr r^3 \frac{d\phi(r)}{dr} g(r). \quad (3.18)$$

In this expression care has to be taken if the pair potential $\phi(r)$ [and hence the pair distribution function $g(r)$] have discontinuities. In this case we rewrite the integrand of the equation above using (3.3) and (3.4):

$$g(r) \frac{d\phi(r)}{dr} = y(r) e(r) \left(-\frac{1}{\beta e(r)} \frac{de(r)}{dr} \right) = -\frac{y(r)}{\beta} \frac{de(r)}{dr},$$

leading to

$$p = \frac{N}{V\beta} + \frac{2\pi}{3} \frac{N}{V\beta} \rho \int_0^\infty dr r^3 \frac{de(r)}{dr} y(r) = p^v. \quad (3.19)$$

The superscript v indicates that the pressure is calculated using the virial, hence the pressure obtained via this route is also called the virial pressure. It should be noted that this equation is in particular useful if $y(r)$ is a continuous function [see section 4.1.4 for the special case of the ORPA].

We define the reduced quantities

$$p^* = \frac{\beta}{\rho} p \quad \text{and} \quad p^+ = \beta p,$$

so that $p_{id}^* = 1$ and $p_{id}^+ = \rho$. For the binary case one finds

$$p = p_{id} - \frac{2\pi}{3} \rho^2 \sum_{i,j=1}^2 c_i c_j \int_0^\infty dr r^3 \frac{d\phi_{ij}(r)}{dr} g_{ij}(r). \quad (3.20)$$

3.2.3 Helmholtz free energy A

The ideal part of the Helmholtz free energy, A_{id} , is given by

$$\frac{\beta A_{id}}{N} = \ln(\rho \Lambda^3) - 1. \quad (3.21)$$

where β is equal to $\frac{1}{k_B T}$ with k_B being the Boltzmann's constant, ρ is the number density and Λ is the Broglie thermal wavelength

$$\Lambda = \sqrt{\frac{2\pi\beta\hbar^2}{m}},$$

where m is the mass of one particle and \hbar is Planck's constant. To justify a classical treatment of static properties of the system it is necessary that $\Lambda/a \ll 1$, where $a \simeq \rho^{-\frac{1}{3}}$. The term $\ln \Lambda$ can be split into

$$\ln \Lambda = \frac{1}{2} \ln \frac{2\pi\beta\hbar^2}{m} = -\frac{1}{2} \ln T + C,$$

where C contains system parameters which are not important for our purposes (evaluation of the structure functions, calculation of phase diagrams and so on). The free energy A is related both to the internal energy as well as to the pressure via the following relations

- energy route

$$U = A + TS = A - T \left(\frac{\partial A}{\partial T} \right)_{V,N} = \left(\frac{\partial A}{\partial \frac{1}{T}} \right)_{V,N}$$

- virial route

$$p^v = - \left(\frac{\partial A}{\partial V} \right)_{T,N}. \quad (3.22)$$

Hence A can be obtained p via thermodynamic integration along isotherms (virial route):

$$\begin{aligned} A_{ex}(V, T) &= A_{ex}(0, T) - \int_0^V dV' p_{ex}(V') \\ A_{ex}(\rho, T) &= A_{ex}(0, T) + N \int_0^\rho d\rho' \frac{p_{ex}(\rho')}{\rho'^2} \end{aligned} \quad (3.23)$$

or from U along isochores (energy route):

$$\frac{A_{ex}(V, T_1)}{T_1} = \frac{A_{ex}(V, T_0)}{T_0} + \int_{\frac{1}{T_0}}^{\frac{1}{T_1}} d\frac{1}{T} U_{ex}(T). \quad (3.24)$$

We use the following reduced quantities for the Helmholtz free energy A :

$$A^* = A \frac{\beta}{N} \quad ; \quad A^+ = A \frac{\beta}{V} = A^* \rho.$$

Using the two different integrations with the reductions defined above, leads to

$$A_{ex}^*(\rho, T) = A_{ex}^*(0, T) + \int_0^\rho d\rho' \frac{p_{ex}^*(\rho')}{\rho} \quad (3.25)$$

$$A_{ex}^*(\rho, T_1^*) = A_{ex}^*(\rho, T_0^*) + \frac{3}{2} \int_{\frac{1}{T_0^*}}^{\frac{1}{T_1^*}} d\frac{1}{T^*} T^* U_{ex}^*(T^*), \quad (3.26)$$

where the prefactor $\frac{3}{2}$ comes from the reduction of the internal energy. For binary systems the Helmholtz free energy for the ideal system is given by

$$\frac{\beta A_{id}}{N} = \sum_{i=1}^2 c_i \ln (\rho_i \Lambda_i^3) - 1, \quad (3.27)$$

where Λ_i is the Broglie thermal wavelength of particle species i :

$$\Lambda_i = \sqrt{\frac{2\pi\beta\hbar^2}{m_i}},$$

with m_i being the mass of the particles of species i .

3.2.4 Chemical potential μ

The chemical potential for a one-component and binary systems respectively, can be calculated from the free energy via

$$\mu = \left(\frac{\partial A}{\partial N} \right)_{T,V} \quad ; \quad \mu_i = \left(\frac{\partial A}{\partial N_i} \right)_{T,V,\{N_j\}} \quad , \quad i = 1, 2, \quad (3.28)$$

where in the last equation all particle numbers N_j with $j \neq i$ must also be held constant. The ideal part is given by

$$\mu_{id} = \frac{1}{\beta} \ln(\rho \Lambda^3) \quad ; \quad \mu_{id;i} = \frac{1}{\beta} \ln(\rho_i \Lambda_i^3) \quad ,$$

the reduced chemical potentials are defined as

$$\mu_{id}^* = \beta \mu_{id} \quad \text{and} \quad \mu_{id;i}^* = \beta \mu_{id;i} \quad .$$

By multiplying these equation by ρ one obtains the other set of reduced quantities, μ_{id}^+ and $\mu_{id;i}^+$. Equation (3.28) can be written for the one component case using reduced quantities as

$$\begin{aligned} \frac{\mu^*}{\beta} &= \frac{1}{\beta} \left(\frac{\partial(NA^*)}{\partial N} \right)_{T,V} = \frac{1}{\beta} \left[A^* + \rho \left(\frac{\partial A^*}{\partial \rho} \right)_{T,V} \right] = \frac{1}{\beta} \left(\frac{\partial A^+}{\partial \rho} \right)_{T,V} \\ \mu^* &= A^* + p^* . \end{aligned} \quad (3.29)$$

The last equation is one form of the Gibbs-Duhem relation.

3.2.5 Isothermal compressibility χ_T

The isothermal compressibility is defined as

$$\chi_T = -\frac{1}{V} \left(\frac{\partial V}{\partial p} \right)_T = \frac{1}{\rho} \left(\frac{\partial \rho}{\partial p} \right)_T \quad , \quad (3.30)$$

for the ideal gas one finds

$$\chi_{T,id} = \frac{\beta}{\rho} \quad .$$

One can show [6], that the isothermal compressibility can be calculated from the correlation functions (which are of course density-dependent) via

$$\begin{aligned} \frac{\rho}{\beta} \chi_T &= \frac{\chi_T}{\chi_{T,id}} = 1 + \rho \int_{\mathbb{R}^3} d^3r h(r) = S(k=0) \\ \beta \left(\frac{\partial p}{\partial \rho} \right)_T &= 1 - \rho \tilde{c}(k=0; \rho) . \end{aligned} \quad (3.31)$$

For binary systems the isothermal compressibility is found to be [6]:

$$\frac{\chi_T}{\chi_{T,id}} = \left[1 - \rho \sum_{i,j=1}^2 c_i c_j \tilde{c}_{ij}(k=0; \rho) \right]^{-1}.$$

The pressure can be calculated from (3.31) via thermodynamic integration:

$$p(\rho) = p(0) + \frac{1}{\beta} \int_0^\rho d\rho' \frac{1}{1 + \rho' \tilde{h}(k=0; \rho')} = p(0) + \frac{1}{\beta} \int_0^\rho d\rho' [1 - \rho' \tilde{c}(k=0; \rho')] = p^c. \quad (3.32)$$

The pressure obtained via this route will be denoted as the compressibility pressure, p^c . If we insert this pressure into equation (3.25) we get

$$A_{ex}(\rho) - A_{ex}(0) = -\frac{N}{\beta} \int_0^\rho d\rho' \frac{1}{\rho'^2} \int_0^{\rho'} d\rho'' \rho'' \tilde{c}(k=0; \rho'').$$

With $A_{ex}(0) = 0$ (ideal gas) and partial integration we get

$$\begin{aligned} A_{ex}(\rho) &= -\frac{N}{\beta} \left\{ - \left[\frac{1}{\rho'} \int_0^{\rho'} d\rho'' \rho'' \tilde{c}(k=0; \rho'') \right]_0^\rho + \int_0^\rho d\rho' \tilde{c}(k=0; \rho') \right\} \\ \frac{\beta}{V} A_{ex}(\rho) = A_{ex}^+(\rho) &= \int_0^\rho d\rho' (\rho' - \rho) \tilde{c}(k=0; \rho') = - \int_0^\rho d\rho' \int_0^{\rho'} d\rho'' \tilde{c}(k=0; \rho''). \end{aligned} \quad (3.33)$$

Using the last equation we can obtain $\tilde{c}(k=0; \rho)$ via the compressibility equation (compressibility sum rule)

$$\tilde{c}(k=0; \rho) = -\frac{d^2 A_{ex}^+(\rho)}{d\rho^2}. \quad (3.34)$$

3.3 Thermodynamic inconsistency

In the last subsections we have derived the formulae needed to calculate the thermodynamic properties of a system from its structure. Further, we have shown that one thermodynamic quantity (as, for example, the pressure p) can be calculated via different routes (corresponding to different thermodynamic relations). If the structure functions could be calculated exactly, then all these different routes would yield the same results for one thermodynamic quantity. However, due to the various simplifications and approximations made in the concepts (by introducing the so-called closure relations) and, to a lesser extend, in the numerical calculations one has to make in order to calculate the structure of a system, the value of a certain thermodynamic quantity will depend on the thermodynamic path one has chosen. This deficiency is also known in the literature as thermodynamic inconsistency. Some of the reasons of this effect are:

- the approximate character of the theories used to calculate the correlation functions of a system (for instance, the closure relations mentioned in section 3.1 are only approximative relations);

- the correlation functions can only be computed up to a certain maximum distance. For example, in particular, near the spinodal in the phase diagram or in the critical region, these functions become long-ranged and we lose information by truncation.

To minimize these deficiencies, so called self-consistent liquid state theories have been developed during the past years. The self-consistent integral equation theories used in this thesis (see [48]) will be discussed in section 4.2. These concepts contain one or more self-consistency parameters (for instance in their closure relation) which can be adjusted in such a way that the various thermodynamic paths lead to the same result for one or more thermodynamic quantities. However, most of these methods are only partly self-consistent, meaning that in most cases only two thermodynamic routes lead to a self consistent result.

Chapter 4

Theoretical concepts

In this chapter we will describe the various theoretical concepts we have used in this thesis to obtain the thermodynamic properties and the structure functions (pair distribution functions and direct correlation functions) of the homogeneous and the inhomogeneous phase.

4.1 Perturbation theory

The basic idea of perturbation theories (PTs) is that the interparticle pair potential, $\phi(r)$, can in many cases be separated in a natural way into a short-range repulsion, $\phi_0(r)$, and a smoothly varying, long-range attraction, $\phi_1(r)$:

$$\phi(r) = \phi_0(r) + \phi_1(r). \quad (4.1)$$

In an additional plausible approximation the short-range forces can be modeled by the infinitely steep repulsion of the hard-sphere potential [49]. The properties of a given liquid can thus be related in a first step to those of a hard-sphere *reference system*, the attractive (or repulsive) long-range part of the potential being treated as a perturbation to the former. The choice of the hard-sphere fluid as a reference system is obvious, because the thermodynamic properties and structural functions are well known for this model. A physical justification can also be given: the thermodynamic properties and correlation functions are dominated by excluded volume effects, and this excluded volume results from the hard core.

The idea of representing a liquid as a system of hard spheres moving in an uniform, attractive potential well dates back to the ideas of van der Waals (van der Waals equation of state). Widom, for instance, gave the following equation of state in [50]

$$\frac{\beta p}{\rho} = \frac{\beta p_0}{\rho} - \beta \rho a,$$

where p is the pressure, p_0 is the pressure of the underlying hard-sphere system. The second term (where a is a positive constant) models the attractive part of the potential, resulting in a decrease of the pressure.

The calculation of the effect of the perturbation on the thermodynamic properties and structure functions of the system can, for instance, be done via a systematic expansion of the pair potential $\phi(r)$ in powers of the inverse temperature (“ λ -expansion”). In the λ -expansion one introduces

$$\phi_\lambda(r) = \phi_0(r) + \lambda\phi_1(r),$$

where λ is a *coupling parameter* varying from 0 (reference system only) to 1 (full perturbation):

$$\phi_{\lambda=0} = \phi_0(r) \quad ; \quad \phi_{\lambda=1} = \phi_0(r) + \phi_1(r) = \phi(r).$$

Thermodynamic and structural properties are then calculated from Taylor expansions of these quantities in terms of λ .

In this thesis we have used a hierarchy of PTs with increasing level of sophistication. In the following, we give a brief overview of these concepts (including their respective advantages or disadvantages).

- The high temperature approximation (HTA) corresponds to the lowest level in the λ -expansion: the expansion of the thermodynamic properties (Helmholtz free energy A) is truncated after the first term: no corrections of the structure of the fluid due to the perturbation are made.
- The random phase approximation (RPA) goes one step beyond the HTA. The thermodynamic properties are now given by the thermodynamic properties of the reference system plus the HTA term and the RPA term. From the diagrammatic derivation of the RPA we can calculate the structure properties of the system, namely

$$c(r) = c_0(r) - \beta\phi_1(r)$$

and

$$g(r) = g_0(r) + g_1(r),$$

where $g_1(r)$ is the correction to $g_0(r)$ due to the perturbation. However, the RPA leads to pair distribution functions that are nonzero inside the core, a clear violation of the conditions imposed by the hard-sphere reference system.

- The optimized random phase approximation (ORPA) is a refined version of the RPA: due to an additional condition, the pair distribution function now *has* to fulfill the core condition of the hard-sphere reference system. This refinement leads to significantly better results in comparison, for instance, with computer simulation results (than those from the RPA).
- The exponential approximation (EXP) goes beyond the ORPA. The EXP is a diagrammatic expansion of the pair distribution function $g(r)$ which is exact in the low density limit [6]. The EXP leads to a pair distribution function $g(r)$ having the form

$$g(r) = g_0(r)e^{g_1(r)}.$$

Although the EXP was originally proposed as an improvement over the RPA, Andersen and Chandler [7] have shown that the usage of the EXP together with the ORPA minimizes the errors made in the diagrammatic expansions of $g(r)$.

4.1.1 Basic ideas of the ORPA

The total system (reference+perturbation) is described by the potential $\phi(r)$ and correlation functions:

$$\begin{aligned} \phi(r) &= \phi_0(r) + \phi_1(r), \\ h(r) + 1 = g(r) &= g_0(r) + g_1(r) = h_0(r) + 1 + g_1(r), \end{aligned} \quad (4.2)$$

$$c(r) = c_0(r) + c_1(r), \quad (4.3)$$

where the subscript $_0$ denotes the reference part and the subscript $_1$ the perturbation part. Both the correlation functions of the reference and of the total system have to fulfill the OZ equation:

$$\begin{aligned} \tilde{h}_0(k) &= \tilde{c}_0(k) + \rho \tilde{h}_0(k) \tilde{c}_0(k), \\ \tilde{h}(k) &= \tilde{c}(k) + \rho \tilde{h}(k) \tilde{c}(k), \end{aligned} \quad (4.4)$$

If one uses the HS potential as a reference potential (as we do in this thesis), this implies that $g(r)$ has to be zero inside the core (both for the reference and the total system):

$$g_0(r) = 0 \quad \text{and} \quad g_1(r) = 0 \quad \text{for} \quad r < \sigma,$$

where σ is the hard-core diameter. The closure relation of the RPA (which is also used for the ORPA and the EXP) is that the perturbation potential $\phi_1(r)$ is taken into account by setting

$$c_1(r) = -\beta \phi_1(r) \quad \forall \quad r. \quad (4.5)$$

This equation acts, beside the core condition for $g(r)$, as a boundary condition for the algorithm which calculates the correlation functions of the system. We summarize the boundary conditions as

$$c_1(r) = \begin{cases} ? & ; \quad r < \sigma \\ -\beta \phi_1(r) & ; \quad r \geq \sigma \end{cases} \quad (4.6)$$

$$g_1(r) = \begin{cases} 0 & ; \quad r < \sigma \\ ? & ; \quad r \geq \sigma \end{cases}. \quad (4.7)$$

4.1.2 Structure for the one component system

In the case of the RPA one simply ignores (4.7) and only uses (4.6) [with an expansion for $c_1(r)$ inside the core, for instance $c_1(r < \sigma) = c_1(\sigma)$ or $c_1(r < \sigma) = 0$]. The pair distribution function $g(r) = g_0(r) + g_1(r)$ is then simply calculated using the OZ equation for the total system. However, as stated before, $g(r)$ is (in most cases) nonzero inside the core for the total system.

To avoid the problems of the RPA, the concept of the ORPA was introduced. By inserting (4.2) and (4.3) into (4.4) we get

$$\tilde{g}_1(k) = \tilde{c}_1(k) + \rho \left[\tilde{h}_0(k) \tilde{c}_1(k) + \tilde{h}_1(k) \tilde{c}_0(k) + \tilde{h}_1(k) \tilde{c}_1(k) \right] \quad (4.8)$$

and hence

$$\tilde{g}_1(k) = \frac{S_0(k)\tilde{c}_1(k)S_0(k)}{1 - \rho S_0(k)\tilde{c}_1(k)}, \quad (4.9)$$

the so called residual OZ equation. If we define the functional

$$F[c_1] = -\frac{1}{\rho(2\pi)^3} \int_{\mathbb{R}^3} d^3k \{ \rho S_0(k)\tilde{c}_1(k) + \ln[1 - \rho S_0(k)\tilde{c}_1(k)] \}, \quad (4.10)$$

its functional derivative with respect to c_1 evaluates to

$$\frac{\delta F[c_1]}{\delta \tilde{c}_1(k)} = \frac{1}{\rho(2\pi)^3} \frac{\rho^2 S_0(k)\tilde{c}_1(k)S_0(k)}{1 - \rho S_0(k)\tilde{c}_1(k)} = \frac{\rho}{(2\pi)^3} \tilde{g}_1(k), \quad (4.11)$$

and after Fourier transformation we get

$$\frac{\delta F[c_1]}{\delta c_1(r)} = \rho g_1(r). \quad (4.12)$$

One can see that the core condition for $g(r)$ can be interpreted as an extremum condition for the functional F (the first derivative of F being equal to zero) with respect to variations of c_1 inside the core ($r < \sigma$). Further, one can show that the functional (4.10) is a convex functional of $c_1(r)$, i.e., it has exactly *one* extremum which represents its unique solution [51].

From a numeric point of view, the ORPA reduces to a search of the minimum of the functional F . Its gradient (4.11) can easily be evaluated via the residual OZ relation. The correlation functions are discretized (both in r and k space) on a grid. For details on the discretization we refer to appendix B.1. For the numerical solution of the ORPA one proceeds as follows:

1. Define a starting value for $c_1(r)$ inside the core.
2. Fourier transformation (from r to k space) of $c_1(r)$ to get $\tilde{c}_1(k)$.
3. Insert this $\tilde{c}_1(k)$ into the residual OZ equation (4.9) to get $\tilde{g}_1(k)$.
4. Fourier transformation (from k to r space) of $\tilde{g}_1(k)$ to get $g_1(r)$.
5. Check if $g(r)$ satisfies the core condition. For applications it is sufficient to stop this iteration as soon as the largest value of $g(r)$ inside the core is below a given threshold:

$$\max_{r < \sigma} |g(r)| < \varepsilon \rightarrow \text{stop iteration.} \quad (4.13)$$

6. Use this $g_1(r)$ to correct $c_1(r)$ inside the core. This can be done using various techniques, the simplest and most common one is the method of steepest descents.
 7. Take the new $c_1(r)$ and go back to step (2).
-

One has to be careful at the numerical implementation of this algorithm: especially the Fourier transform of $\tilde{g}_1(k)$ from k to r space can cause some problems, because the resulting $g_1(r)$ is not steady at contact. The solution of this problem requires a little trick. Obviously, the term in square brackets in equation (4.8) is a convolution and therefore a continuous function. Before the Fourier transformation, we simply subtract $\tilde{c}_1(k)$ from $\tilde{g}_1(k)$, after Fourier transformation we add $c_1(r)$, obtaining thus $g_1(r)$:

$$g_1(r) = \frac{1}{(2\pi)^3} \int_{\mathbb{R}^3} d^3k e^{-i\vec{k}\vec{r}} [\tilde{g}_1(k) - \tilde{c}_1(k)] + c_1(r).$$

In some cases, in particular for strongly attractive perturbation potentials, $g(r)$ can become negative for some ranges of r . To address this behavior some modifications of the ORPA were proposed, for example the EXP [7] and the LEXP (linearized version of the EXP) [52].

The EXP starts from a diagrammatical analysis of the approximative expression for the pair distribution function which leads to the following form

$$g(r) = g_0(r)e^{g_1(r)}.$$

The EXP is, in contrast to the HTA or the ORPA, exact in the low-density limit [6]. By expanding of the exponential function for small $g_1(r)$ and discarding all terms beyond first order we get the LEXP:

$$g(r) = g_0(r)[1 + g_1(r)].$$

4.1.3 Structure for the binary system

For a binary system the correlation functions $g_{ij}(r)$ and $c_{ij}(r)$ are split into reference and perturbation parts

$$g_{ij}(r) = g_{0;ij}(r) + g_{1;ij}(r) \quad ; \quad c_{ij}(r) = c_{0;ij}(r) + c_{1;ij}(r).$$

Using the closure

$$c_{ij}(r) = c_{0;ij}(r) - \beta\phi_{1;ij}(r)$$

the defining equations for the ORPA (4.7) and (4.6) become

$$c_{1;ij}(r) = \begin{cases} ? & ; r < \sigma_{ij} \\ -\beta\phi_{1;ij}(r) & ; r \geq \sigma_{ij} \end{cases} \quad (4.14)$$

$$g_{1;ij}(r) = \begin{cases} 0 & ; r < \sigma_{ij} \\ ? & ; r \geq \sigma_{ij} \end{cases} . \quad (4.15)$$

We also define matrices similar to (3.9):

$$\mathcal{H} = \mathcal{H}_0 + \mathcal{H}_1 \quad ; \quad \mathcal{C} = \mathcal{C}_0 + \mathcal{C}_1.$$

After introducing these definitions we get the binary residual OZ relation

$$\begin{aligned} \mathcal{H}_1 &= \mathcal{C}_1 + \mathcal{C}_0 \cdot \mathcal{H}_1 + \mathcal{C}_1 \cdot \mathcal{H}_0 + \mathcal{C}_1 \cdot \mathcal{H}_1 \\ \mathcal{H}_1 &= (\mathbb{I} - \mathcal{C}_0 - \mathcal{C}_1)^{-1} \mathcal{C}_1 (\mathbb{I} + \mathcal{H}_0), \end{aligned}$$

where $\mathbb{1}$ is the 2x2 unity matrix. Introducing the static structure factor of the reference system, \mathcal{S}_0 (3.12), we get finally for \mathcal{H}_1 [see also (4.9)]:

$$\mathcal{H}_1 = (\mathcal{S}_0^{-1} - \mathcal{C}_1)^{-1} \mathcal{C}_1 \mathcal{S}_0.$$

The definition of the functional (4.10) can be generalized for the binary case in a straightforward way:

$$F[\mathcal{C}_1] = -\frac{1}{\rho(2\pi)^3} \int_{\mathbb{R}^3} d^3k \{ \text{tr} [\mathcal{C}_1 \mathcal{S}_0] + \ln [\det (\mathbb{1} - \mathcal{C}_1 \mathcal{S}_0)] \}. \quad (4.16)$$

The functional derivatives from this equation with respect to $\tilde{C}_{ij}(k)$ are

$$\frac{\delta F[\mathcal{C}_1]}{\delta \tilde{C}_{ij}(k)} = -\frac{\rho}{(2\pi)^3} \tilde{H}_{1;ij}(k).$$

The implementation of the optimization algorithm for the binary case is similar to the one described in the previous subsection.

4.1.4 Thermodynamic properties

The calculation of the thermodynamic quantities for the PTs described in the previous subsection are described in detail in [53]. Some of these thermodynamic quantities can be calculated using the expressions summarized in section 3.2.

- Internal energy U
- Chemical potential μ (using the Helmholtz free energy from this subsection)
- Isothermal compressibility χ_T

For the others, the pressure p and Helmholtz free energy A , the expressions which are based on the ORPA formalism will be derived in the following subsections.

4.1.4.1 Pressure p

The calculation of the pressure requires derivatives of the potential $\phi(r)$ with respect to the r , which - for the case of a hard sphere reference potential - can be circumvented by introducing the function $y(r)$, which, for most liquid state theories, is a continuous function. In the ORPA, $y(r)$ turns out to be discontinuous where the potential $\phi(r)$ is discontinuous. In the following we will derive an expression which can cope with such a discontinuity in general.

At first we have to rewrite those parts of the integral (3.18) which are concerned. Let us assume that $y(r)$ [and hence $\phi(r)$ and $\phi_1(r)$] have discontinuities at $r = \gamma$ and that these functions are continuous elsewhere. We start from equation (3.19):

$$p_{ex} = \frac{2\pi}{3} \frac{N}{V\beta} \rho \underbrace{\int_0^\infty dr r^3 \frac{d\phi(r)}{dr} y(r)}_I = \frac{2\pi}{3} \frac{N}{V\beta} \rho [I^S + I^D],$$

where the integral I is split into two parts, I^S and I^D . The integral I^S consists of all the continuous parts of I , whereas I^D takes into account the N jumps discarded of the integrand of I :

$$I^D = \sum_{i=1}^N I_i^D,$$

where I_i^D is the integral across the i th discontinuity.

$$\begin{aligned} I_i^D &= \int_{\gamma_-}^{\gamma_+} dr r^3 \frac{de(r)}{dr} y(r) = \int_{\gamma_-}^{\gamma_+} dr r^3 \frac{g(r)}{e(r)} \frac{de(r)}{dr} = \int_{\gamma_-}^{\gamma_+} dr r^3 g(r) \frac{d \ln e(r)}{dr} \\ &= \int_{\gamma_-}^{\gamma_+} dr r^3 g(r) \frac{d(-\beta\phi(r))}{dr} = \int_{\gamma_-}^{\gamma_+} dr r^3 g(r) \frac{dc_1(r)}{dr} \end{aligned} \quad (4.17)$$

using the ORPA closure. Now we “model” $c_1(r)$ near the discontinuity

$$c_1(r) = \varepsilon_0 + \Delta\varepsilon\theta(r - x),$$

where ε_0 is the value of $c_1(r)$ on the left side of the discontinuity and $\varepsilon_1 = \varepsilon_0 + \Delta\varepsilon$ is the value of $c_1(r)$ on the right side of the discontinuity. Using this ansatz for $c_1(r)$ near the discontinuity we introduce a continuous function $\hat{g}(r)$ around γ (because from the OZ equation we know that $g(r) - c(r)$ is a convolution and therefore continuous):

$$\hat{g}(r) = g(r) - c_1(r).$$

Inserting this into equation (4.17) for I_i^D leads to

$$\begin{aligned} I_i^D &= \int_{\gamma_-}^{\gamma_+} dr r^3 [\hat{g}(r) + c_1(r)] \frac{dc_1(r)}{dr} \\ &= \int_{\gamma_-}^{\gamma_+} dr r^3 \hat{g}(r) \frac{dc_1(r)}{dr} + \frac{1}{2} \int_{\gamma_-}^{\gamma_+} dr r^3 \frac{dc_1^2(r)}{dr}. \end{aligned}$$

Now we can integrate and using $\theta^2(r - x) = \theta(r - x)$ we get

$$I_i^D = \gamma^3 \left[\hat{g}(\gamma) \Delta\varepsilon + \frac{2\varepsilon_0 \Delta\varepsilon + (\Delta\varepsilon)^2}{2} \right].$$

We can replace $\hat{g}(\gamma)$ with the left- or right-side limit of $g(r)$; to eliminate ε_0 from the final equation we set

$$\hat{g}(\gamma) = \frac{g(\gamma_-) - \varepsilon_0 + g(\gamma_+) - \varepsilon_0 - \Delta\varepsilon}{2},$$

so finally the integral I_i^D evaluates to

$$I_i^D = \gamma^3 \frac{\Delta\varepsilon}{2} [g(\gamma_-) + g(\gamma_+)].$$

This result is identical to the one obtained in [53], but the proof is now more general.

4.1.4.2 Helmholtz free Energy A

The free energy A is calculated from

$$A = A_{ref} + A_{pert}, \quad (4.18)$$

where A_{ref} is the free energy of the reference system and A_{pert} is the free energy due to the perturbation. We assume that the free energy of the reference system (in our case a hard-sphere system) is well known. The perturbation free energy A_{pert} is calculated using equation (3.24):

$$\frac{A_{pert}(T_1)}{T_1} - \frac{A_{pert}(T_0)}{T_0} = \int_{\frac{1}{T_0}}^{\frac{1}{T_1}} d\frac{1}{T} U_p(T),$$

where U_p is the internal energy due to the perturbation potential. By setting T_0 to ∞ (ideal gas), T_1 to the actual temperature and substituting $\alpha = T_1/T$ we get

$$\frac{A_{pert}}{T_1} = \frac{1}{T_1} \int_0^1 d\alpha U_p(\alpha),$$

where $U_p(\alpha)$ is similar to (3.16) except that the $g(r)$ is now α -dependent:

$$A_{pert} = \rho \frac{N}{2} \int_0^1 d\alpha \int_{\mathbb{R}^3} d^3r g_\alpha(r) \phi_1(r). \quad (4.19)$$

Here $g_\alpha(r)$ is the pair distribution function for a system that is characterized by a potential $\phi_\alpha(r)$:

$$\phi_\alpha(r) = \phi_0(r) + \alpha \phi_1(r).$$

For the pair distribution function $g_\alpha(r)$ we assume the ansatz

$$g_\alpha(r) = g_0(r) + g_1(r; \alpha).$$

Inserting this into (4.19) leads us to

$$A_{pert} = \rho \frac{N}{2} \left[\int_{\mathbb{R}^3} d^3r g_0(r) \phi_1(r) + \int_0^1 d\alpha \int_{\mathbb{R}^3} d^3r g_1(r; \alpha) \phi_1(r) \right]. \quad (4.20)$$

The first term of this equation is the HTA. This approximation can be used if the perturbation potential has nearly no effect on the pair distribution function ($g_1(r; \alpha) \approx 0$). The second term can be calculated in the framework of the RPA by using the residual OZ equation (4.9) to express $\tilde{g}_1(k; \alpha)$ via

$$\tilde{g}_1(k; \alpha) = \frac{S_0(k) \tilde{c}_1(k; \alpha) S_0(k)}{1 - \rho S_0(k) \tilde{c}_1(k; \alpha)} = \frac{S_0(k) \alpha \tilde{c}_1(k) S_0(k)}{1 - \rho S_0(k) \alpha \tilde{c}_1(k)},$$

inserting the Fourier transformed of this equation into (4.20) leads to

$$A_{RPA} = \rho \frac{N}{2} \int_0^1 d\alpha \int_{\mathbb{R}^3} d^3r \phi_1(r) \frac{1}{(2\pi)^3} \int_{\mathbb{R}^3} d^3k e^{-i\vec{k}r} \frac{S_0(k) \alpha c_1(k) S_0(k)}{1 - \rho S_0(k) \alpha c_1(k)}.$$

Integrating over α and using the RPA closure (4.5) together with Parseval's theorem (see appendix B.3) we get finally

$$A_{RPA} = \frac{N}{2\rho\beta} \frac{1}{(2\pi)^3} \int_{\mathbb{R}^3} d^3k \{ \rho S_0(k) \tilde{c}_1(k) + \ln [1 - \rho S_0(k) \tilde{c}_1(k)] \}.$$

The result for the A_{RPA} is in fact the functional F (4.10) with an adequate prefactor. Inserting the optimized $c_1(r)$, A_{RPA} becomes A_{ORPA} :

$$A_{ORPA} = -\frac{N}{2\beta} F[c_1].$$

These two terms, A_{HTA} and A_{ORPA} , can be rearranged using the OZ relation and the fact that for any PT with a hard sphere reference system $h(r=0) = -1$:

$$c(r=0) = -1 - \rho \int_{\mathbb{R}^3} d^3r_1 c(r_1) h(r_1). \quad (4.21)$$

The last equation is valid both for the reference (c_0, h_0) and the total $(c = c_0 + c_1, h = h_0 + h_1)$ system. Using equation (4.5) we can write

$$\begin{aligned} A_{HTA} + A_{ORPA} &= \\ &= \frac{N}{2\beta} \left[-\rho \int_{\mathbb{R}^3} d^3r g_0(r) c_1(r) + \frac{1}{\rho (2\pi)^3} \int_{\mathbb{R}^3} d^3k \{ \rho S_0(k) \tilde{c}_1(k) + \ln [1 - \rho S_0(k) \tilde{c}_1(k)] \} \right] \\ &= \frac{N}{2\beta} \left[-\rho \tilde{c}_1(k=0) - \rho \int_{\mathbb{R}^3} d^3r h_0(r) c_1(r) + \frac{1}{(2\pi)^3} \int_{\mathbb{R}^3} d^3k [1 + \rho \tilde{h}_0(k)] \tilde{c}_1(k) \right] + \bar{A}_{ORPA}. \end{aligned} \quad (4.22)$$

where \bar{A}_{ORPA} is defined as

$$\bar{A}_{ORPA} = \frac{N}{2\beta \rho} \frac{1}{(2\pi)^3} \int_{\mathbb{R}^3} d^3k \ln [1 - \rho S_0(k) \tilde{c}_1(k)].$$

Using Parseval's theorem the last two integrals in (4.22) cancel. With (4.21) we get

$$\begin{aligned}
A_{HTA} + A_{ORPA} &= \frac{N}{2\beta} [-\rho\tilde{c}_1(k=0) + c_1(r=0)] + \bar{A}_{ORPA} \\
&= \frac{N\rho}{2\beta} [-\tilde{c}_1(k=0) - (h * c)(r=0) + (h_0 * c_0)(r=0)] + \bar{A}_{ORPA} \\
A_{HTA} + A_{ORPA} &= \bar{A}_{HTA} + \bar{A}_{ORPA}.
\end{aligned} \tag{4.23}$$

The graph theoretical analysis leading to the EXP brings along an additional term to the free energy [6]. Due to historic reasons, it is called B_2 term and is given by:

$$B_2 = -\frac{\rho N}{2\beta} \int_{\mathbb{R}^3} d^3r \left[g_0(r) (e^{g_1(r)} - g_1(r) - 1) - \frac{g_1(r)^2}{2} \right].$$

To conclude, the expressions used in this thesis for the Helmholtz free energy are given, according to the level of sophistication, by the following terms:

$$\begin{aligned}
A &= \underbrace{A_{id} + A_{ref,ex}}_{REF} + A_{HTA} + A_{ORPA} + B_2. \\
&\quad \underbrace{\hspace{10em}}_{HTA} \\
&\quad \underbrace{\hspace{15em}}_{RPA,ORPA} \\
&\quad \underbrace{\hspace{20em}}_{EXP}
\end{aligned} \tag{4.24}$$

For binary systems we can follow similar lines, the free energy is formally given by an expression similar to the one of equation (4.24). The first two terms are given by equation (3.27) and, depending on the reference system, equation (4.33), (4.34) or (4.35). The three remaining terms read

$$\begin{aligned}
A_{HTA} &= \rho \frac{N}{2} \sum_{i,j=1}^2 c_i c_j \int_{\mathbb{R}^3} d^3r g_{0;ij}(r) \phi_{1;ij}(r) \\
A_{ORPA} &= -\frac{N}{2\beta} F[\mathcal{C}_1] \\
B_2 &= -\frac{\rho N}{2\beta} \sum_{i,j=1}^2 c_i c_j \int_{\mathbb{R}^3} d^3r \left[g_{0;ij}(r) (e^{g_{1;ij}(r)} - g_{1;ij}(r) - 1) - \frac{g_{1;ij}(r)^2}{2} \right].
\end{aligned}$$

Finally \bar{A}_{HTA} and \bar{A}_{ORPA} are given by

$$\begin{aligned}
\bar{A}_{HTA} &= \frac{N}{2\beta\rho} \left[-\sum_{i,j=1}^2 \rho_i \rho_j \tilde{c}_{1;ij}(k=0) + \sum_{i=1}^2 \rho_i c_{1;ii}(r=0) \right] \\
\bar{A}_{ORPA} &= \frac{N}{2\beta\rho} \frac{1}{(2\pi)^3} \int_{\mathbb{R}^3} d^3k \ln [\det (\mathbb{I} - \mathcal{C}_1 \mathcal{S}_0)].
\end{aligned}$$

4.1.4.3 Chemical potential μ

In the ORPA (and related perturbation theories) the chemical potential μ can be calculated directly from the structure functions (i.e. no numerical derivatives are needed). The chemical potential is calculated using equation (3.28):

$$\mu_{ORPA} = \mu - \mu_{id} - \mu_{ref,ex} = \left(\frac{\partial [A_{HTA} + A_{ORPA}]}{\partial N} \right)_{T,V} = \frac{1}{V} \left(\frac{\partial [A_{HTA} + A_{ORPA}]}{\partial \rho} \right)_{T,V}.$$

Using equation (4.23) and Parseval's theorem leads to

$$\mu_{ORPA} = \frac{1}{2\beta} \frac{\partial}{\partial \rho} \left[-\rho^2 \tilde{c}_1(k=0) + \frac{1}{(2\pi)^3} \int_{\mathbb{R}^3} d^3k \left\{ \rho \tilde{c}_1(k) + \ln \frac{1 - \rho [\tilde{c}_0(k) + \tilde{c}_1(k)]}{1 - \rho \tilde{c}_0(k)} \right\} \right],$$

where all the structure functions are density dependent. Taking the derivative with respect to the density and after doing some cumbersome algebra we get

$$\begin{aligned} \mu_{ORPA} = & \frac{\rho}{2\beta} \left[-2\tilde{c}_1(k=0) - \rho \frac{\partial}{\partial \rho} \tilde{c}_1(k=0) \right. \\ & \left. - \frac{1}{(2\pi)^3} \int_{\mathbb{R}^3} d^3k \left\{ \tilde{c}_1(k) \tilde{h}(k) + \tilde{h}_1(k) \left[\tilde{c}_0(k) + \rho \frac{\partial}{\partial \rho} \tilde{c}_0(k) \right] + \rho \tilde{h}(k) \frac{\partial}{\partial \rho} \tilde{c}_1(k) \right\} \right]. \end{aligned}$$

Using Parseval's theorem again and rearranging the terms leads to

$$\begin{aligned} \mu_{ORPA} = & \frac{\rho}{2\beta} \left[-2\tilde{c}_1(k=0) - \rho \int_{\mathbb{R}^3} d^3r g(r) \frac{\partial}{\partial \rho} c_1(r) \right. \\ & \left. - \int_{\mathbb{R}^3} d^3r \left\{ c(r) h(r) - c_0(r) h_0(r) + h_1(r) \rho \frac{\partial}{\partial \rho} c_0(r) \right\} \right]. \end{aligned}$$

The integral in the first line is equal to zero because outside the core (where $g(r)$ is not equal to zero) the variation of $c_1(r)$ with respect to ρ is zero. The final result for the chemical potential μ is

$$\mu = \mu_{id} + \mu_{ref,ex} + \frac{1}{\beta} \left[-\rho \tilde{c}_1(k=0) + \frac{1}{2} c_1(r=0) + \frac{\rho^2}{2} \int_{\mathbb{R}^3} d^3r h_1(r) \frac{\partial}{\partial \rho} c_0(r) \right]. \quad (4.25)$$

The integral in the above equation is zero if $c_0(r)$ for the reference system is zero outside the core. However, if one uses the Verlet-Weis parameterization for the reference system (and $c_0(r)$ being nonzero outside the core), the integral will not vanish and has to be calculated explicitly. Using the Gibbs-Duhem relation (3.29) one can calculate the pressure

p from this chemical potential μ .

This evaluation of μ can also be done for binary systems. We start from

$$\mu_{i;ORPA} = \mu_i - \mu_{i;id} - \mu_{i;ref,ex} = \frac{1}{V} \left(\frac{\partial [A_{HTA} + A_{ORPA}]}{\partial \rho_i} \right)_{T,V},$$

and finally arrive, using similar arguments as above, at

$$\begin{aligned} \mu_i = \mu_{i;id} + \mu_{i;ref,ex} &+ \frac{1}{\beta} \left[- \sum_{j=1}^2 \rho_i \tilde{c}_{1;ij}(k=0) + \frac{1}{2} c_{1;ii}(r=0) \right. \\ &\left. + \frac{1}{2} \sum_{l,m=1}^2 \rho_l \rho_m \int_{\mathbb{R}^3} d^3r h_{1;lm}(r) \frac{\partial}{\partial \rho_i} c_{0;lm}(r) \right]. \end{aligned}$$

4.1.4.4 Simple perturbation theory for A in the fluid state

A simple perturbation scheme to evaluate the Helmholtz free energy A of a one component system in the fluid state (for the solid state see subsection 4.4) starts from the following general expression [see also equation (4.18)]:

$$A(\rho) = A_{ref}(\rho) + A_p(\rho),$$

where $A(\rho)$ is the free energy of the system with the potential $\phi(r) = \phi_0(r) + \phi_1(r)$, $A_{ref}(\rho)$ is the free energy of the reference system with potential $\phi_0(r)$ and $A_p(\rho)$ is the contribution to the free energy coming from the perturbation potential $\phi_1(r)$. In the fluid state, the explicit form of $A_p(\rho)$ is equal to the HTA term of equation (4.20):

$$A_p(\rho) = \frac{N}{2} \rho \int_{\mathbb{R}^3} d^3r g_0(r) \phi_1(r), \quad (4.26)$$

where $g_0(r)$ is the pair distribution function of the reference system. In this work we will refer to this approach as the perturbation approximation (PA).

4.1.5 Mean spherical approximation

The mean spherical approximation (MSA) was first proposed by Lebowitz and Percus [54] as a generalization of the mean-spherical model for Ising spin systems. The MSA applied to systems with a hard core and an adjacent perturbation potential is given in terms of the pair distribution function and direct correlation function by

$$\begin{aligned} g(r) &= 0 && ; && r < \sigma \\ c(r) &= -\beta\phi(r) && ; && r \geq \sigma. \end{aligned} \quad (4.27)$$

Together with the OZ relation these expressions yield an integral equation for $g(r)$ and $c(r)$. The first expression in (4.27) is exact, while the second extends the asymptotic

behavior of $c(r)$ to all $r \geq \sigma$ and is clearly an approximation.

The MSA can also be solved numerically in the framework of a perturbation theory, which is formally identical to the ORPA. For the reference system one uses the PY solution for HS, whereas the second expression of equation (4.27) is the ansatz of the ORPA for $c_1(r)$ outside the core [second expression of equation (4.6)]. To improve the quality of the solution, thermodynamic properties for the reference HS system are being calculated using the Carnahan-Starling equation of state [22]. Because the structure of the reference system implies $c(r) = 0$ outside the core, one can use equation (4.25) for the chemical potential.

4.1.6 Reference system (one component case)

As a reference system in the ORPA and the MSA we have used the HS system. To calculate its structure and thermodynamic properties we have used the analytical solution of the PY closure or the semi empirical parameterization of computer simulation results due to Verlet and Weis [23] (VW).

In the PY approximation the solution for the direct correlation function $c(r)$ at a given packing fraction η is found to be [55, 56]:

$$c(r; \eta) = \begin{cases} a + br + \frac{1}{2}\eta ar^3 & ; \quad r < \sigma \\ 0 & ; \quad r \geq \sigma \end{cases}, \quad (4.28)$$

where the two parameters a and b are defined as

$$a = -\frac{(1+2\eta)^2}{(1-\eta)^4} \quad ; \quad b = 6\eta \frac{(1+\frac{\eta}{2})^2}{(1-\eta)^4}.$$

Analytic expressions for the pair correlation function in the intervals $\sigma \leq r \leq 6\sigma$ are given in a paper by Smith and Henderson [57].

The PY solution for the HS system leads to the virial pressure (3.19) given by

$$p^{*v} = \frac{1 + 2\eta + 3\eta^2}{(1-\eta)^2}$$

and to the pressure we get from the compressibility equation (3.32)

$$p^{*c} = \frac{1 + \eta + \eta^2}{(1-\eta)^3}.$$

From these expressions it is obvious that the PY solution is thermodynamically inconsistent. Calculating the Helmholtz free energy using equation (3.25) from these two expressions for the pressure yields

$$\begin{aligned} A_{ex}^{*v} &= 6 \left(\frac{1}{1-\eta} - 1 \right) + 2 \ln(1-\eta) \\ A_{ex}^{*c} &= \frac{3}{2} \left(\frac{1}{(1-\eta)^2} - 1 \right) - \ln(1-\eta). \end{aligned} \quad (4.29)$$

The PY solution for HS systems has a few weak points (see [23]):

- The contact values of the pair distribution functions $g(r)$ calculated using this direct correlation function are too low. This leads to an increasing discrepancy between the prediction from the PY solution and the results from simulations as η increases.
- The maximum of the static structure factor $S(k)$ is too high because of the oscillations of the pair distribution functions for large r (these oscillations are also slightly out of phase with respect to computer simulations).
- The cavity function $y(r)$ is too small inside the core ($r < \sigma$).

To overcome these deficiencies, Verlet and Weis [23] have proposed a semi-empirical parameterization of the pair distribution function $g(r)$ which is used in combination with the empirical parameterization of the equation of state due to Carnahan and Starling (CS) [22]

$$p_{CS}^* = \frac{1 + \eta + \eta^2 - \eta^3}{(1 - \eta)^3} = \frac{1}{3}p^{*v} + \frac{2}{3}p^{*c}. \quad (4.30)$$

This expression for the pressure fits the results of computer simulations nearly perfectly. For the free energy, one finds

$$A_{ex;CS}^* = \eta \frac{4 - 3\eta}{(1 - \eta)^2}. \quad (4.31)$$

The VW parameterization for the pair distribution function $g(r)$ is given by

$$g\left(\frac{r}{\sigma}; \eta\right) = \begin{cases} 0 & ; r < \sigma \\ g_0\left(\frac{r}{\sigma_0}; \eta_0\right) + \frac{C}{r} e^{-m(r-\sigma)} \cos[m(r-\sigma)] & ; r \geq \sigma \end{cases}, \quad (4.32)$$

where σ_0 is the HS diameter and η_0 the packing fraction of a suitable chosen reference HS system in the PY approximation. These two parameters are found to be

$$\sigma_0 = \sigma \sqrt[3]{1 - \frac{\eta}{16}} \quad ; \quad \eta_0 = \eta \left(1 - \frac{\eta}{16}\right).$$

The pair distribution function (4.32) now has two contributions: a reference part stemming from a HS system with a slightly smaller packing fraction η_0 and an additional exponentially damped oscillating part. The two parameters C and m have to be determined so that the results for the pressure from the virial and compressibility equations agree and, in addition, are equal to the CS pressure (4.30). Relations for the two parameters C and m in equation (4.32) were derived by Grundke and Henderson [24].

4.1.7 Reference system (binary case)

The concept used for the description of the HS reference system can easily be generalized to the binary case. In the PY approximation, the direct partial correlation functions $c_{ij}(r)$ of a HS system [58] with density ρ are given analytically by [59]:

$$-c_{ij}(r) = \begin{cases} \frac{\pi}{2} \left[\frac{a}{3}\sigma_i^3 + b\sigma_i^2 + \chi^2 \xi_2 \sigma_i \right] & r < \nu_{ij} \\ \chi + \frac{1}{r} (a_{ij} + b_{ij}r + d_{ij}r^2 + f_{ij}r^4) & \nu_{ij} \leq r \leq \sigma_{ij} \\ 0 & \sigma_{ij} < r \end{cases}$$

where $\chi = 1/(1 - \eta)$ and

$$\begin{aligned}\eta &= \eta_1 + \eta_2 = \eta(c_1 + c_2) = \frac{\pi}{6}\rho \\ \sigma_{ij} &= \frac{1}{2}(\sigma_i + \sigma_j) \quad ; \quad \nu_{ij} = \frac{1}{2}(\sigma_i - \sigma_j) \\ \xi_1 &= \rho \sum_{i=1}^2 c_i \sigma_i \quad ; \quad \xi_2 = \rho \sum_{i=1}^2 c_i \sigma_i^2\end{aligned}$$

and

$$\begin{aligned}a &= \chi^2 \left[\rho + \pi \xi_2 \chi \left(\xi_1 + \frac{\pi}{4} \xi_2^2 \chi \right) \right] \\ b &= \chi^2 \left[\xi_1 + \frac{\pi}{2} \xi_2^2 \chi \right] \\ a_{ij} &= -\frac{\pi}{4} \nu_{ij}^2 \left[\sigma_{ij}^2 a + \sigma_{ij} \frac{b}{2} + \xi_2 \chi^2 \right] \\ b_{ij} &= \frac{\pi}{4} \left[(\sigma_i^3 + \sigma_j^3) \frac{a}{3} + (\sigma_i^2 + \sigma_j^2) b + \sigma_{ij} \frac{\xi_2}{2} \chi^2 \right] \\ d_{ij} &= -\frac{\pi}{4} \left[(\sigma_i^2 + \sigma_j^2) \frac{a}{2} + \sigma_{ij} \frac{b}{2} + \xi_2 \chi^2 \right] \\ f_{ij} &= \frac{\pi a}{4 \cdot 3}.\end{aligned}$$

The thermodynamic properties of this system can be calculated as described in section 3.2; again, the results are, as in the one component system, thermodynamically inconsistent. The virial pressure p^v as calculated by equation (3.20) for binary systems is equal to

$$p^{*v} = \chi \left[1 + \frac{\pi \xi_2 \chi}{2 \rho} \left(\xi_1 + \frac{\pi}{6} \xi_2^2 \right) \right],$$

whereas the compressibility pressure p^{*c} , equation (3.32), is found to be

$$p^{*c} = \chi \left[1 + \frac{\pi \xi_2 \chi}{2 \rho} \left(\xi_1 + \frac{\pi}{6} \xi_2^2 \chi \right) \right],$$

the difference between the two pressures being equal to

$$p^{*c} - p^{*v} = \frac{\pi^2 \eta}{12 \rho} (\xi_2 \chi)^3.$$

The results for the free energy A (3.25) using the expressions for the compressibility and virial pressure are:

$$A_{ex}^{*c} = -\ln(1 - \eta) + \frac{\chi \pi \xi_2}{\rho} \left[\frac{\xi_1}{2} + \frac{\pi}{24} \xi_2^2 \chi \right] \quad (4.33)$$

$$A_{ex}^{*v} = A_{ex}^{*c} + \frac{\xi_2^3 \pi^2}{12 \eta \rho} \left[\left(1 - \frac{3}{2} \eta \right) \chi^2 + \frac{1}{\eta} \ln(1 - \eta) \right]. \quad (4.34)$$

The inconsistencies of the PY approximation lead to the same deficiencies as in the one component case. Grundke and Henderson [60] have proposed an improved parameterization of the partial pair distribution functions which is very similar to the one used in the one component case [23, 24] and of similar quality as the VW parameterization (4.32). The thermodynamic properties are calculated from an empirical equation of state due to Mansoori, Carnahan, Starling and Leland [61]:

$$\begin{aligned} p^{*MCSL} &= \frac{1}{3}p^{*v} + \frac{2}{3}p^{*c} = \chi \left[1 + \frac{\pi \xi_2 \chi}{2 \rho} \left(\xi_1 + \frac{\pi}{18} \xi_2^2 \chi (\eta - 3) \right) \right] \\ A_{ex}^{*MCSL} &= \frac{1}{3}A_{ex}^{*v} + \frac{2}{3}A_{ex}^{*c} = \ln(1 - \eta) \left[\frac{\xi_2^3 \pi^2}{36 \eta^2 \rho} - 1 \right] + \frac{\chi \pi \xi_2}{\rho} \left[\frac{\xi_1}{2} + \frac{\pi}{36 \eta \chi \xi_2^2} \right], \end{aligned} \quad (4.35)$$

For a more detailed description of the thermodynamic properties of a binary system we refer to [62].

4.1.8 Free volume approximation for A

Velasco *et al.* [63] have proposed a free-volume approach for the Helmholtz free energy of the HS solid, which is both valid for the fcc (face centered cubic lattice) and the bcc (body centered cubic lattice) phase. In this thesis we will refer to this approach as the free volume perturbation approximation (FVPA). The explicit expression for of the Helmholtz free energy per particle is

$$\frac{A\beta}{N} = -\ln \frac{V(\rho_s)}{\Lambda^3},$$

where ρ_s is the density of the solid and $V(\rho_s)$ is the accessible volume of a particle, which is the volume constrained by its neighbors, assuming that they are fixed at their lattice equilibrium sites. For the position dependent one-particle density in the solid the parameterization as given by equation (C.1) is used. The respective free volumes $V(\rho)$ are given by [63]

$$V_{fcc}(\rho_s) = \frac{8}{\sqrt{2}} [a(\rho_s) - 1]^3 \quad (4.36)$$

$$V_{bcc}(\rho_s) = \frac{32}{3\sqrt{3}} [a(\rho_s) - 1]^3, \quad (4.37)$$

where $a(\rho_s)$ is the (density dependent) nearest neighbor distance. As shown in [63], the localization parameter α can be calculated via the mean square displacement $r_{rms}^2 = \langle r^2 \rangle = \frac{3}{2\alpha}$ and the approximate accessible volume of a particle (which is equal to $V = \frac{4\pi}{3} r_{rms}^3$). Thus, α is equal to

$$\alpha = \frac{3}{2} \left(\frac{4\pi}{3V(\rho_s)} \right)^{\frac{2}{3}}.$$

Combining this equation with equations (4.36) and (4.37) leads to

$$\alpha_{fcc} = \frac{3}{2 [a(\rho_s) - 1]^2} \left(\frac{3\sqrt{2}}{\pi} \right)^{\frac{2}{3}}$$

$$\alpha_{bcc} = \frac{3}{2 [a(\rho_s) - 1]^2} \left(\frac{8\sqrt{3}}{\pi} \right)^{\frac{2}{3}}.$$

4.2 Integral equations

In this section we will give an overview of the integral equation theories (IETs) used in this thesis. For a general introduction in IET see, for instance, [6].

IETs represent an alternative approach with respect to perturbation theories to calculate the structure and thermodynamic properties of a liquid. While in PTs one generally relates the properties of the system to those of a reference system and corrects for the (hopefully small) perturbations, IETs are based on the OZ equation, which is solved along with a suitable closure relation. These closures are derived from exact diagrammatic relations under simplifying approximations (the closure arise from exact diagrammatical expansions of the pair distribution function $g(r)$ in terms of the direct correlation function $c(r)$ but with certain classes of diagrams ignored). In general, the solution of the OZ equation in combination with a closure relation can be obtained only through numerical methods. However, for a few model potentials IETs can be solved analytically.

During the past years a large number of closure relations have been developed, which in some cases were constructed in order to satisfy particular requirements of the systems.

The closure relation can, in the general case, be written as

$$\overline{F}[c, h, \phi](r) = 0, \quad (4.38)$$

i.e., a functional relation between the direct correlation function $c(r)$, the total correlation function $h(r)$, and the pair potential $\phi(r)$. Alternative formulations of the closure relation can be given by introducing the *bridge function* $B(r)$ (consisting of all elementary diagrams that are not nodal, see [6]) via the exact relation

$$g(r) = h(r) + 1 = e^{-\beta\phi(r)+h(r)-c(r)+B(r)}. \quad (4.39)$$

For the solution of IETs, we use the following definitions. We define the continuous function

$$\gamma(r) = h(r) - c(r) = \rho(h * c)(r). \quad (4.40)$$

In order to yield the structure functions of a specific IE we have to solve the following two coupled integral equations:

$$\gamma(r) = \rho \int_{\mathbb{R}^3} d^3r_1 c(|\vec{r} - \vec{r}_1|) [\gamma(r_1) + c(r_1)] \quad (4.41)$$

$$c(r) = F^*[\gamma, \phi](r), \quad (4.42)$$

where $F^*[\gamma, \phi](r)$ denotes the explicit dependence of $c(r)$ from $\gamma(r)$ and $\phi(r)$. In general, it is numerically more convenient to use the OZ equation in k -space, which reads

$$\tilde{\gamma}(k) = \rho \frac{\tilde{c}(k)^2}{1 - \rho\tilde{c}(k)}. \quad (4.43)$$

Now we will introduce the various closures used in this thesis.

4.2.1 Percus-Yevick approximation

The Percus-Yevick (PY) approximation can be derived via graph theoretical analysis from an exact expression for the pair distribution function [10]. One obtains [see also equations (2.7) and (3.4)]

$$c(r) = [1 - e^{\beta\phi(r)}] g(r) = f(r)y(r),$$

or

$$F^*[\gamma, \phi](r) = c(r) = (e^{-\beta\phi(r)} - 1)(\gamma(r) + 1).$$

The bridge function in the PY approximation [see equation (4.39)] is given by

$$B_{PY}(r) = \ln[1 + \gamma(r)] - \gamma(r).$$

The PY approximation is known to give good results for short-ranged, repulsive interactions.

4.2.2 Hypernetted chain approximation

The hypernetted-chain (HNC) approximation [9] can also be obtained via graph theoretical methods and one obtains

$$g(r) = e^{-\beta\phi(r)+\gamma(r)},$$

i.e., the HNC bridge function vanishes. The functional F^* is given by

$$F^*[\gamma, \phi](r) = c(r) = e^{-\beta\phi(r)+\gamma(r)} - \gamma(r) - 1.$$

The HNC gives satisfactory results for long ranged interactions, such as the Coulomb potential.

4.2.3 Rogers-Young approximation

The Rogers-Young (RY) [11] closure relation is a so called ‘mixed closure’ relation. It interpolates via a mixing function $f(\alpha; r)$ between the PY and the HNC approximation. Via the mixing parameter α in the RY closure one can obtain self-consistency between two thermodynamic routes. The RY closure is defined as

$$F^*[\gamma, \phi](r) = c(r) = e^{-\beta\phi(r)} \left\{ 1 + \frac{\exp[\gamma(r)f(\alpha; r)] - 1}{f(\alpha; r)} \right\} - \gamma(r) - 1, \quad (4.44)$$

hence, the bridge function for the RY closure reads

$$B_{RY}(r) = \ln \left\{ 1 + \frac{\exp[\gamma(r)f(\alpha; r)] - 1}{f(\alpha; r)} \right\} - \gamma(r).$$

For $f(\alpha; r)$ one uses generally [11]

$$f(\alpha; r) = 1 - e^{-\alpha r} \quad ; \quad \alpha \in [0, \infty), \quad (4.45)$$

$f(\alpha; r)$ is a switching or mixing function with the following limiting behavior:

$$\begin{aligned} \lim_{r \rightarrow 0} f(\alpha; r) &= 0 \quad ; \quad \text{PY behavior for small distances} \\ \lim_{r \rightarrow \infty} f(\alpha; r) &= 1 \quad ; \quad \text{HNC behavior for large distances} \end{aligned}$$

It should be noted that these limits are independent of α . Similarly one finds

$$\begin{aligned} \lim_{\alpha \rightarrow 0} f(\alpha; r) &= 0 \quad ; \quad \text{PY behavior for small } \alpha \\ \lim_{\alpha \rightarrow \infty} f(\alpha; r) &= 1 \quad ; \quad \text{HNC behavior for large } \alpha, \end{aligned}$$

independent of r . In this thesis the self consistency requirement described in subsection 4.2.4.1 was used for the RY approximation.

4.2.4 Zero separation closure

The zero separation closure (ZSEP) was originally proposed by Verlet [64] and represents a direct approximation for the bridge function. One assumes the following form for the bridge function:

$$B_{ZSEP}(r) = -\frac{\alpha\gamma^2(r)}{2} \left[1 - \frac{\beta\gamma(r)}{1 + \delta\gamma(r)} \right] = B_{ZSEP}(r; [\gamma]), \quad (4.46)$$

where the three parameters α , β and δ are determined in such a way that the self-consistency between three different routes (described in the subsequent sections) is satisfied.

4.2.4.1 Virial and compressibility route

The first consistency requirement uses the inverse isothermal compressibility which can be calculated via (3.31). We compare

$$\frac{\chi_{T,id}}{\chi_T^c} = \left[1 + \rho \int_{\mathbb{R}^3} d^3r h(r) \right]^{-1}, \quad (4.47)$$

[χ_T^c is the isothermal compressibility calculated via the compressibility route, see equation (3.31)] with

$$\frac{\chi_{T,id}}{\chi_T^v} = \left(\frac{\partial \beta p^v}{\partial \rho} \right)_T; \quad (4.48)$$

p^v is the virial pressure (3.19) and χ_T^v the isothermal compressibility calculated via the virial route.

4.2.4.2 Gibbs-Duhem relation

The second consistency requirement uses the Gibbs-Duhem relation (3.29). This thermodynamic relation establishes the link between pressure p , chemical potential μ , and number density ρ . In our case we require that the virial pressure p^v satisfies

$$\left(\frac{\partial p^v}{\partial \mu}\right)_T = \rho. \quad (4.49)$$

In the framework of the ZSEP the excess chemical potential μ_{ex} can be calculated via Lee's star function approach [65] leading to [66]

$$\beta\mu_{ex} = \rho \int_{\mathbb{R}^3} d^3r \left[\ln y(r) - h(r) + \frac{1}{2}h(r)\gamma(r) + h(r)B_{ZSEP}(r) \right] - S^*, \quad (4.50)$$

we have used in the present case

$$\begin{aligned} S^* &= \rho \int_{\mathbb{R}^3} d^3r \frac{h(r)}{\gamma(r)} \int_0^{\gamma(r)} d\gamma' B_{ZSEP}(r; [\gamma']). \\ &= \rho \int_{\mathbb{R}^3} d^3r h(r) \frac{\alpha}{6\delta^2} \left[\frac{3\beta}{\delta} \left\{ 1 + \gamma(r)\delta \left(\frac{1}{3}\gamma(r)\delta - \frac{1}{2} \right) - \frac{\ln[1 + \gamma(r)\delta]}{\gamma(r)\delta} \right\} - \delta^2\gamma^2(r) \right]. \end{aligned}$$

Using (4.39), equation (4.50) can be written as

$$\beta\mu_{ex} = \rho \int_{\mathbb{R}^3} d^3r \left[\frac{1}{2}h(r)\gamma(r) + g(r)B_{ZSEP}(r) - c(r) \right] - S^*. \quad (4.51)$$

From the correlation functions we can thus evaluate the chemical potential μ to check if the Gibbs-Duhem relation (4.49) is fulfilled. This is done by calculating the pressure and chemical potential for various systems at different densities near ρ_0 . Then one calculates the virial pressure as a function of the chemical potential [$p^v = p^v(\mu)$], using, for instance, a cubic spline. The derivative of this function with respect to μ is then compared with the density ρ_0 .

4.2.4.3 Zero separation theorems for the cavity function

The value of the cavity distribution function $y(r)$ (3.4) at a given distance $r = R$ is equal to the energy required to insert a dimer of two particles separated by a distance R minus the work required to independently insert two monomers (of infinite dilution) [67]. The latter quantity is simply twice the chemical potential of the monomer. Hence, for $R = 0$ we have

$$\ln y(0) = \beta [2\mu_1 - \mu_2(\rho_2 = 0)], \quad (4.52)$$

where ρ_2 is the partial density of the dimers and $\beta\mu_1$ can be evaluated using (4.51). For $\beta\mu_2(\rho_2 = 0)$ we have to solve the corresponding binary OZ equations for the mixture of monomers (with ρ_1 finite) and infinitely diluted dimers ($\rho_2 \rightarrow 0$). To this end one first has to solve the OZ-equation together with the ZSEP closure for a set of parameters $[\alpha, \beta, \delta]$ to get the bulk fluid correlation functions. Then one has to solve the binary OZ equations [as shown in subsection 4.1.3] with $\phi_{12}(r) = 2\phi(r)$, and - in principle - with a different set of parameters $[\alpha', \beta', \delta']$ for the closure; in practice we take the same set of parameters as in the one component case. Once the correlation functions for the dimer are known we can evaluate the chemical potential μ_2 using the equation (4.51):

$$\beta\mu_{2,ex}(\rho_2 = 0) = \rho_1 \int_{\mathbb{R}^3} d^3r \left[\frac{1}{2} h_{12}(r) \gamma_{12}(r) + g_{12}(r) B_{12,ZSEP}(r) - c_{12}(r) \right] - S_{12}^*.$$

In the final step we compare the value of the cavity function as calculated by (4.52) with the value one gets from the ZSEP closure and the definition of the cavity function (3.4) together with the definition of the bridge function (4.39), i.e.,

$$\beta [2\mu_1 - \mu_2(\rho_2 = 0)] = h(0) - c(0) + B_{ZSEP}(0).$$

Summarizing, we outline the iterative procedure to get a solution for the ZSEP:

1. Choose an initial set of parameters $[\alpha_0, \beta_0, \gamma_0]$.
2. Solve the OZ equations for the monomer with this set of parameters.
3. Calculate derivatives with respect to ρ numerically.
4. Solve the binary OZ equations to get $\mu_2(\rho_2 = 0)$.
5. Check the three self consistency relations; if these equations are not fulfilled, modify the set of parameters $[\alpha, \beta, \gamma]$ and go back to step (2).

Especially step (5) is the most difficult part of this algorithm. It is therefore more convenient to scan, in a first step, the parameter space spanned by the three parameters.

4.2.5 Numerical algorithms

In the the next two subsections we will present the two algorithms to solve IEs numerically. We have used in this thesis the Broyles algorithm and the Labik-Malijevsky-Vonka algorithm.

4.2.5.1 Broyles algorithm

The scheme of the Broyles algorithm [68] is as follows:

1. We take an initial value (guess) for, $c(r)$, denoted by $c^0(r)$.
2. Fourier transform of $c^0(r)$ to obtain $\tilde{c}^0(k)$ and use equation (4.43) to get $\tilde{\gamma}^0(k)$.

3. Fourier transform of $\tilde{\gamma}^0(k)$ to get $\gamma^0(r)$.

4. Use the closure relation (4.42) with $\gamma^0(r)$ to get $c^1(r)$:

$$c^1(r) = F^* [\gamma^0(r), \phi(r)]$$

5. If the difference between $c^1(r)$ and $c^0(r)$ is small enough, we can stop this iteration:

$$\varepsilon = \max_{\forall r} |c^0(r) - c^1(r)| < \varepsilon_0 \rightarrow \text{solution found,}$$

where ε_0 is a given threshold (for example, 10^{-8}).

6. If the difference is too large, we have to obtain a new estimate of $c(r)$. This is done by ‘mixing’ $c^1(r)$ with the first guess, $c^0(r)$, to get $\bar{c}^1(r)$:

$$\bar{c}^1(r) = \alpha c^1(r) + (1 - \alpha)c^0(r),$$

where α is the mixing parameter ($\alpha \in (0, 1]$) which has to be chosen to achieve maximum stability of the algorithm. Instead of simply keeping α fixed one can modify α during the iterations: we start with $\alpha = \alpha_0$ (for example $\alpha_0 = 1$) and decrease α as soon as the convergence gets slower.

7. We restart the iteration with a new $c^0(r)$ at step (2) until the exit condition is satisfied.

4.2.5.2 Labik-Malijevsky-Vonka algorithm

The Labik-Malijevsky-Vonka (LMV) algorithm was proposed in [69] is based on two basic concepts:

- The closure relation $c(r) = F^*[\gamma, \phi](r)$ is linearized with respect to γ .
- Using the linearized closure, the OZ equation is solved *only* in k -space; hence less time consuming Fourier transforms from r - to k -space and back are needed.

Although during the process of finding the solution of equations (4.41) and (4.42) some linearized expressions are used, the algorithm is nevertheless solving the exact problem. In fact, this method can be interpreted as a Newton-Raphson algorithm (see section D.2). To simplify some of the equations used in this subsection we introduce the following functions:

$$\tilde{C}(k) = k\tilde{c}(k), \tag{4.53}$$

$$\tilde{\Gamma}(k) = k\tilde{\gamma}(k). \tag{4.54}$$

Using these definitions the two coupled equations (4.41) and (4.42) read as:

$$\begin{aligned} \tilde{\Gamma}(k) &= \rho \frac{\tilde{C}^2(k)}{k - \rho\tilde{C}(k)} = A[\tilde{C}](k), \\ \tilde{C}(k) &= \tilde{F}^+[\tilde{\Gamma}, \phi](k), \end{aligned} \tag{4.55}$$

where the first equation defines the operator A [which is the OZ equation using capitalized functions as defined in (4.53) and (4.54)]. The second equation defines the operator F^+ , which is the operator F^* (4.42) formulated for capitalized correlation functions [equations (4.53) and (4.54)]. Combining these two equations we get

$$0 = \tilde{\Gamma}(k) - A[\tilde{F}^+[\tilde{\Gamma}]](k) = \Psi[\tilde{\Gamma}](k).$$

We expand this functional in a Taylor expansion around the starting function $\tilde{\Gamma}^0(k)$, and truncate after the linear term [$\Delta\tilde{\Gamma}(k') = \tilde{\Gamma}(k') - \tilde{\Gamma}^0(k')$]:

$$\begin{aligned} 0 &= \Psi[\tilde{\Gamma}^0](k) + \left. \frac{d\Psi[\tilde{\Gamma}](k)}{d\tilde{\Gamma}(k')} \right|_{\tilde{\Gamma}=\tilde{\Gamma}^0} \Delta\tilde{\Gamma}(k') + O\left(\Delta\tilde{\Gamma}(k')^2\right) \\ \Psi[\tilde{\Gamma}^0](k) &= - \left\{ \frac{d\tilde{\Gamma}(k)}{d\tilde{\Gamma}(k')} - \frac{dA[\tilde{C}](k)}{d\tilde{C}(k'')} \frac{d\tilde{F}^+[\tilde{\Gamma}](k'')}{d\tilde{\Gamma}(k')} \right\}_{\tilde{\Gamma}=\tilde{\Gamma}^0} \Delta\tilde{\Gamma}(k') \\ &= -J(k, k')\Delta\tilde{\Gamma}(k'). \end{aligned} \quad (4.56)$$

To get an expression for \tilde{F}^+ suitable for this equation, we linearize the closure relation given by equation (4.42), using the functional derivative in r -space defined as

$$P^0(r) = \left. \frac{\delta F^*[\gamma, \phi](r)}{\delta\gamma(r)} \right|_{\gamma=\gamma^0}.$$

The Taylor expansion of $c(r)$ (truncated after the linear term) is

$$c(r) \approx c^0(r) + P^0(r) [\gamma(r) - \gamma^0(r)] = c^0(r) + P^0(r)\Delta\gamma(r),$$

in k -space this equation reads as

$$\tilde{c}(k) = \tilde{c}^0(k) + \frac{1}{(2\pi)^3} \int_{\mathbb{R}^3} d^3k' \Delta\tilde{\gamma}(k') \tilde{P}^0(\vec{k} - \vec{k}'). \quad (4.57)$$

By expressing $P^0(\vec{k} - \vec{k}')$ as the Fourier transformed of $P^0(r)$ we get

$$\tilde{c}(k) = \tilde{c}^0(k) + \frac{1}{k\pi} \int_0^\infty dk' k' \Delta\tilde{\gamma}(k') \int_0^\infty dr [\cos(r|k - k'|) - \cos(r|k + k'|)] P^0(r).$$

The last equation contains some cosine Fourier transforms (defined in appendix B.1). The linearized closure in k -space (written with capitalized functions) reads as

$$\tilde{F}^+[\tilde{\Gamma}](k) = \tilde{C}(k) = \tilde{C}^0(k) + \int_0^\infty dk \Delta\tilde{\Gamma}(k') \tilde{Q}^0(k, k'), \quad (4.58)$$

with $\tilde{Q}^0(k, k')$ being equal to

$$\tilde{Q}^0(k, k') = \frac{1}{\pi} \left[\tilde{P}_c^0(|k - k'|) - \tilde{P}_c^0(k + k') \right] = \frac{d\tilde{F}^+[\tilde{\Gamma}](k'')}{d\tilde{\Gamma}(k')}, \quad (4.59)$$

where the subscript $_c$ indicates a cosine Fourier transform. This equation can now be discretized, thus $\tilde{Q}^0(k, k')$ becomes a matrix:

$$\tilde{C}(k_i) = \tilde{C}^0(k_i) + \sum_{j=1}^N \tilde{Q}^0(k_i, k_j) \Delta\tilde{\Gamma}(k_j). \quad (4.60)$$

In this equation the upper index N is set to the index i where $\tilde{\Gamma}(k_i)$ is sufficiently zero (the Fourier transformed $\tilde{\Gamma}(k)$ has to decrease fast enough for increasing k , so that $\Gamma(r)$ is sufficiently described by setting $\tilde{\Gamma}(k)$ equal to zero beyond k_N). The final equation for $J(k, k')$ in (4.56) in its discretized form $J(k_i, k_j)$ ($k \rightarrow k_i, k' \rightarrow k_j$) is

$$J(k_i, k_j) = \delta_{ij} - \rho \tilde{C}(k_i) \frac{2k_i - \rho \tilde{C}(k_i)}{[k_i - \rho \tilde{C}(k_i)]^2} \tilde{Q}^0(k_i, k_j), \quad (4.61)$$

where $\tilde{C}(k_i)$ is evaluated by means of equation (4.60). The final step is to invert $J(k_i, k_j)$ and use the inverted matrix with (4.55) to get $\Delta\tilde{\Gamma}(k_j)$:

$$\Psi[\tilde{\Gamma}^0](k_i) = - \sum_{j=0}^N J(k_i, k_j) \Delta\tilde{\Gamma}(k_j) \quad (4.62)$$

The computational scheme consists of the following steps (consisting of two nested loops; the two constants ε_i and ε_o have to be set to appropriate values):

1. Take a first estimate (an initial guess) for $\Gamma^0(r)$. Fourier transform it to get $\tilde{\Gamma}^0(k)$.
2. Use the given closure [equation (4.55)] to evaluate $C^0(r)$ and $\tilde{C}^0(k)$.
3. Calculate $\tilde{Q}^0(k, k')$ using equation (4.59).
4. Take a first guess for $\tilde{\Gamma}(k)$ for the inner loop; in most cases one will take $\tilde{\Gamma}^0(k)$.
 - (a) From (4.58) calculate the (linearized estimate) $\tilde{C}(k)$.
 - (b) Insert this in (4.61) and invert the matrix $J(k, k')$ to get $J^{-1}(k, k')$.
 - (c) Use this inverted matrix to calculate $\Delta\tilde{\Gamma}(k)$ from (4.62) and furthermore a new estimate $\tilde{\Gamma}(k)$ using

$$\tilde{\Gamma}(k) + \Delta\tilde{\Gamma}(k) \rightarrow \tilde{\Gamma}(k).$$

- (d) If

$$\max |\Delta\tilde{\Gamma}(k)| < \varepsilon_i,$$

exit the inner loop, else go back to step (4a).

5. Calculate $\tilde{\Gamma}(k)$ for all k values that were excluded from the inner loop using a direct iteration.
6. Fourier transform $\tilde{\Gamma}(k)$ to get $\Gamma(r)$.
7. If the solution differs too much from the initial guess, one sets the actual solution to the initial guess and restarts the iteration at (2):

$$\max_{\forall r} |\Gamma_0(r) - \Gamma(r)| > \varepsilon_o \rightarrow \Gamma_0(r) = \Gamma(r) \quad ; \quad \tilde{\Gamma}_0(k) = \tilde{\Gamma}(k)$$

The numerical implementation of this algorithm has to be done very carefully. There are also numerous ways where one can improve the whole algorithm. For instance, the way a new estimate is calculated in the inner loop can be improved by using some kind of mixing (like in Broyles algorithm).

4.2.6 Thermodynamic properties

Most of the thermodynamic properties of IEs are calculated as described in section 3.2. These properties are the internal energy U , pressure p , chemical potential μ (via the derivative of the Helmholtz free energy) and the isothermal compressibility χ_T .

The Helmholtz free energy is in most IE approaches not directly accessible; it must hence be calculated via thermodynamic integration [using, for example, equation (3.25) or (3.26)]. Care has to be taken to avoid the coexistence region.

4.3 Classical density-functional theory

Classical density functional theory (DFT) is a very general approach to describe the structural and thermodynamic properties of homogenous and inhomogeneous systems; for an excellent introduction into DFT we refer to [4], Evans in [3] and [70]. The applications for DFT in liquid state physics are wide ranged: freezing, interface and surface problems [2], nucleation and others [71].

DFT is a general method of describing equilibrium properties of nonuniform fluids, it is a reformulation of statistical mechanics in terms of correlation functions and functionals. The Helmholtz free energy A is expressed as a functional of the inhomogeneous one-particle density $\rho(\vec{r})$:

$$A = A[\rho]. \tag{4.63}$$

In general, A can be split into an ideal and an excess part:

$$A[\rho] = A_{id}[\rho] + A_{ex}[\rho],$$

where $A_{id}[\rho]$ is given by

$$\beta A_{id}[\rho] = \int_{\mathbb{R}^3} d^3r \rho(\vec{r}) [\ln(\rho(\vec{r})\sigma^3) - 1] + 3N \ln \frac{\Lambda}{\sigma}. \tag{4.64}$$

A classical system with N particles can be described by the Hamiltonian H_N :

$$H_N = T + U + V.$$

It is the sum of the kinetic energy T of the N particles

$$T = \sum_{i=1}^N \frac{p_i^2}{2m},$$

where p_i is the momentum of the i th particle and m is its mass, the interaction potential U of the particles with each other (which may or may not be pair-wise additive) being given by

$$U = U(\vec{r}_1, \dots, \vec{r}_N),$$

where \vec{r}_i is the position of the i th particle, and the interaction V of the particles with an external potential

$$V = \sum_{i=1}^N V_{ext}(\vec{r}_i).$$

The key properties of the functional are:

- (i) The external potential $V_{ext}(\vec{r})$ is a unique functional of $\rho(\vec{r})$; i.e. it is uniquely determined by the equilibrium density $\rho_0(\vec{r})$ (see [4, 72]).
- (ii) The grand canonical potential $\Omega[\rho]$, defined as,

$$\Omega[\rho] = A[\rho] + \int_{\mathbb{R}^3} d^3r \rho(\vec{r}) V_{ext}(\vec{r}) - \mu \int_{\mathbb{R}^3} d^3r \rho(\vec{r}) \quad (4.65)$$

and $A[\rho]$ (4.63) are unique functionals of $\rho(\vec{r})$ (see Evans in [3], [2, 4]).

Another important property is the so called variational principle. The grand canonical potential $\Omega[\rho]$ (4.65) is minimized by the equilibrium density $\rho_0(\vec{r})$:

$$\Omega[\rho_0] < \Omega[\rho],$$

leading to the Euler-Lagrange equations

$$\left. \frac{\delta \Omega_V[\rho]}{\delta \rho(\vec{r})} \right|_{\rho=\rho_0} = 0 \quad ; \quad \left. \frac{\delta A[\rho]}{\delta \rho(\vec{r})} \right|_{\rho=\rho_0} + V_{ext}(\vec{r}) - \mu = 0$$

Further, the excess part of $A[\rho]$ (4.63) is the generating functional of a hierarchy of direct correlation functions $c^{(n)}(\vec{r}_1, \dots, \vec{r}_n; [\rho])$, defined via the n th functional derivate of $A_{ex}[\rho]$ with respect to $\rho(\vec{r})$:

$$c^{(n)}(\vec{r}_1, \dots, \vec{r}_n; [\rho]) = -\beta \frac{\delta^n A_{ex}[\rho]}{\delta \rho(\vec{r}_1) \dots \delta \rho(\vec{r}_n)}. \quad (4.66)$$

However, for a general system no exact expressions for the functionals are available (except for one-dimensional systems), hence approximations for these functionals are required. For an overview we refer to [3].

4.3.1 WDA and MWDA

A very common approximation for the density functional is the weighted density approximation (WDA) [73, 74] and its simplified version, the modified WDA (MWDA) [12]. In the WDA the DF is given by

$$A_{ex}^{WDA}[\rho] = \int_{\mathbb{R}^3} d^3r \rho(\vec{r}) f_0[\bar{\rho}(\vec{r})], \quad (4.67)$$

where f_0 denotes the excess free energy per particle of a uniform liquid and $\bar{\rho}(\vec{r})$ is the “weighted density”, defined as a weighted average of the true one-particle density $\rho(\vec{r})$ with respect to a weight function $w(r; \rho)$, according to

$$\bar{\rho}(\vec{r}) \equiv \int_{\mathbb{R}^3} d^3r' \rho(\vec{r}') w(\vec{r} - \vec{r}'; \bar{\rho}(\vec{r}')). \quad (4.68)$$

By this prescription the inhomogeneous system is mapped locally on a fluid of density $\bar{\rho}(\vec{r})$; $w(r; \rho)$ is determined to ensure that the approximation becomes exact in the limit of a uniform system [$\rho(\vec{r}) \rightarrow \rho_0$, where ρ_0 is the density of the uniform system]:

- (i) The weight function must satisfy the following normalization condition:

$$\int_{\mathbb{R}^3} d^3r' w(\vec{r} - \vec{r}'; \bar{\rho}(\vec{r})) = 1. \quad (4.69)$$

- (ii) A further specification of $w(r; \rho)$ follows from requiring that in the homogenous limit the two-particle direct correlation function [see equation (4.66)] is reproduced via the second functional derivative of $A_{ex}[\rho]$ with respect to $\rho(\vec{r})$. Explicitly, A_{ex}^{WDA} is required to satisfy the relation

$$c_0^{(2)}(|\vec{r} - \vec{r}'|; \rho_0) = -\beta \lim_{\rho \rightarrow \rho_0} \left[\frac{\delta^2 A_{ex}^{WDA}[\rho]}{\delta \rho(\vec{r}) \delta \rho(\vec{r}')} \right], \quad (4.70)$$

where $c_0^{(2)}(|\vec{r} - \vec{r}'|; \rho_0)$ is the two particle direct correlation function of the uniform system which, in general, is well known from standard liquid state theory. By inserting equation (4.67) into (4.70) one obtains a differential equation in k -space for w [73].

However, in general, the weight function $w(r; \rho)$ is not unique and the computational effort for the WDA is substantial.

Denton and Ashcroft [75] formulated a simplified version of the WDA, called the MWDA. Whereas the WDA is an approximation for the quantity $f(\vec{r}; [\rho])$, interpreted as the *local* excess free energy per particle, the new formulation focuses instead directly upon the *global* excess free energy per particle $A_{ex}[\rho]/N$. Now $A_{ex}[\rho]/N$ is position independent,

and hence the MWDA must necessarily involve a *position-independent* weighted density $\hat{\rho}$ ($\hat{\rho}$ represents the density of a liquid onto which the solid is mapped globally). So in the MWDA one assumes for $A_{s,ex}[\rho]$

$$\frac{A_{s,ex}[\rho_s]}{N} = \frac{A_{l,ex}(\hat{\rho})}{N}, \quad (4.71)$$

$\hat{\rho}$ is now defined by

$$\hat{\rho} \equiv \frac{1}{N} \int_{\mathbb{R}^3} d^3r \rho(\vec{r}) \int_{\mathbb{R}^3} d^3r' \rho(\vec{r}') \tilde{w}(\vec{r} - \vec{r}'; \hat{\rho}), \quad (4.72)$$

where we assign the symbol \tilde{w} to the weight function of the MWDA. From a comparison of equation (4.68) and (4.72) it is obvious that $\hat{\rho}$ can be interpreted as an additionally averaged density [over the weighted density $\bar{\rho}(\vec{r})$].

To ensure that the MWDA reproduces in the limit $\rho(\vec{r}) \rightarrow \rho_0$ the properties of the uniform system, \tilde{w} must also be normalized [see equation (4.69)]:

$$\int_{\mathbb{R}^3} d^3r' \tilde{w}(\vec{r} - \vec{r}'; \rho) = 1,$$

and A_{ex}^{MWDA} must satisfy an equation similar to (4.70). This results in the following expression for \tilde{w} :

$$\tilde{w}(|\vec{r} - \vec{r}'|; \rho_0) = -\frac{1}{2 \frac{d}{d\rho} \frac{A_{l,ex}(\rho)}{N}} \left[\frac{1}{\beta} c_0^{(2)}(|\vec{r} - \vec{r}'|; \rho_0) + \frac{1}{V} \rho_0 \frac{d^2}{d\rho^2} \frac{A_{l,ex}(\rho)}{N} \right]_{\rho=\rho_0}.$$

In k space this equation reads

$$\tilde{w}(k; \rho_0) = -\frac{1}{2 \frac{d}{d\rho} \frac{A_{l,ex}(\rho)}{N}} \left[\frac{1}{\beta} c_0^{(2)}(k; \rho_0) + \delta(k) \rho_0 \frac{d^2}{d\rho^2} \frac{A_{l,ex}(\rho)}{N} \right]_{\rho=\rho_0}. \quad (4.73)$$

The δ -function ensures that, for $k = 0$, the compressibility sum rule (3.34) is fulfilled. For $k \neq 0$ the Fourier transform of $\tilde{w}(k; \rho_0)$ is proportional to $\tilde{c}_0^{(2)}(k; \rho_0)$. Equations (4.71), (4.72) and (4.73) constitutes the MWDA.

We use the MWDA to explain how the solid state can be described in the DF formalism. The following parameterization for $\rho(\vec{r})$ [sum over Gaussian peaks localized at the lattice sites, see also equation (C.1)]:

$$\rho(\vec{r}) = \left(\frac{\alpha \sigma^2}{\pi} \right)^{\frac{3}{2}} \sum_{\{\vec{R}\}} e^{-\alpha(\vec{r} - \vec{R})^2}, \quad (4.74)$$

where the vectors $\{\vec{R}\}$ constitute the lattice \mathcal{G} , is used. If the localization parameter α is big enough ($\alpha > 50$), the Gaussian peaks have a negligible overlap.

At first, we keep α fixed and rewrite $A_{id}[\rho]$, equation (4.64), which becomes

$$\begin{aligned} A_{id}^* &= \frac{\beta A_{id}}{N} = \frac{\beta A_{id}(\alpha)}{N} = \int_{\mathbb{R}^3} d^3r \left(\frac{\alpha \sigma^2}{\pi} \right)^{\frac{3}{2}} e^{-\alpha r^2} \left[\frac{3}{2} \ln \left(\frac{\alpha \sigma^2}{\pi} \right) - \alpha r^2 - 1 \right] - \frac{3}{2} \ln T^* + C \\ &= \left[\frac{3}{2} \ln \left(\frac{\alpha \sigma^2}{\pi} \right) - \frac{5}{2} - \frac{3}{2} \ln T^* \right] + C, \end{aligned}$$

where the constant C collects all the parameters which are not necessary for the determination of the phase diagram. Because the excess free energy of the liquid fulfills the compressibility equation (3.34), using equation (4.72) and (4.73) one gets the following implicit equation for the weighted density $\hat{\rho}$ of the liquid (the subscript 0 for the liquid direct correlation function has been omitted) in k -space:

$$\hat{\rho} = \rho_s \left\{ 1 - \frac{1}{2 \frac{d}{d\hat{\rho}} A_{l,ex}^*(\hat{\rho})} \sum_{\{k\} \neq 0} e^{-\frac{k^2}{2\alpha} \tilde{c}(k; \hat{\rho})} \right\}, \quad (4.75)$$

where ρ_s is the density of the solid and $\tilde{c}(k; \hat{\rho})$ is the Fourier transform of the direct correlation function. The summation in this equation runs over all nonzero vectors of the reciprocal lattice of \mathcal{G} . Equation (4.75) has to be solved iteratively. If two solutions are found [the solutions are the intersections of a straight line (left side) and a convex shaped curve (right side)], one takes the lower $\hat{\rho}$ (because only the lower $\hat{\rho}$ approaches ρ_0 as α tends to 0).

The drawback of this equation is that, for high solid densities ρ_s , one has to sum over a large number of reciprocal lattice vectors to achieve convergence (high solid densities are leading to sharp density profiles and hence large localization parameters α). To avoid this (time consuming) summation, equation (4.75) can be transformed to r -space:

$$\begin{aligned} \hat{\rho} &= \rho_s \left[1 - \frac{\tilde{c}(k=0; \hat{\rho})}{2 \frac{d}{d\hat{\rho}} A_{l,ex}^*(\hat{\rho})} \right] \\ &\quad - \frac{1}{\hat{\rho} \frac{d}{d\hat{\rho}} A_{l,ex}^*(\hat{\rho})} \frac{1}{2N} \int_{\mathbb{R}^3} d^3r \int_{\mathbb{R}^3} d^3r' \rho(\vec{r}) \rho(\vec{r}') c(|\vec{r} - \vec{r}'|; \hat{\rho}). \end{aligned} \quad (4.76)$$

For our parameterization of the density, the double integral in (4.76) simplifies to (see appendix C.2):

$$\begin{aligned} &\frac{1}{2N} \int_{\mathbb{R}^3} d^3r \int_{\mathbb{R}^3} d^3r' \rho(\vec{r}) \rho(\vec{r}') c(|\vec{r} - \vec{r}'|; \hat{\rho}) = \\ &\quad \sqrt{\frac{\alpha}{2\pi}} \left\{ \alpha \int_0^\infty dr r^2 e^{-\frac{\alpha}{2} r^2} c(r; \hat{\rho}) + \frac{1}{2} \sum_{i=1}^\infty \frac{n_i}{R_i} \int_0^\infty dr r c(r; \hat{\rho}) \left[e^{-\frac{\alpha}{2}(r-R_i)^2} - e^{-\frac{\alpha}{2}(r+R_i)^2} \right] \right\}. \end{aligned}$$

Care has to be taken because the peaks in this parameterization can become very sharp for high α values. A simple Simpson algorithm is hardly sufficient unless the direct

correlation function $c(r)$ is discretized on an extremely fine mesh ($\Delta r \approx 10^{-6}$). In this thesis, we have used a rather time-consuming method to calculate this integral: first, the discretized direct correlation function $c(r)$ is interpolated by a set of cubic splines; with this interpolation the integral can be integrated analytically.

In the last step, the MWDA Helmholtz free energy is minimized with respect to the localization parameter α , to find the equilibrium density:

$$A(\rho_s; \alpha) = A_{id}(\rho_s; \alpha) + A_{l,ex}(\hat{\rho}(\rho_s, \alpha)). \quad (4.77)$$

4.3.2 cMWDA

One problem of the MWDA is that equation (4.75) does not necessarily have a solution in the density range, where a fluid exists ($0 < \hat{\rho} < \rho_{max}$, where ρ_{max} is typically $0.9\sigma^3 - 1.1\sigma^3$). This can be the case if the Helmholtz excess free energy of the fluid is a positive quantity, while the Helmholtz excess free energy of the solid is a negative quantity, for all the values of ρ and T that are of interest. Therefore, the mapping (4.71) cannot always be made. One reason for the above problems can be the attractive part of the interaction potential. To overcome this problem, Likos and Senatore [13] introduced the so called correlation MWDA (cMWDA).

One basic requirement of the cMWDA is, that one has to be able to split the potential in a reference and a perturbation part, the latter should contain the attractive contribution of the interaction potential:

$$\phi(r) = \phi_r(r) + \phi_p(r),$$

where $\phi_r(r)$ is the reference and $\phi_p(r)$ is the perturbation part (this splitting is very similar to the one used for PTs). At first we deal with the perturbation part in a high temperature approximation (HTA) manner, defining

$$A_{HTA}[\rho] = \frac{1}{2} \int_{\mathbb{R}^3} d^3r \int_{\mathbb{R}^3} d^3r' \rho(\vec{r}) \rho(\vec{r}') \phi_p(|\vec{r} - \vec{r}'|). \quad (4.78)$$

It should be noted that the authors of [13] called this term the Hartree contribution. Thus, we are led to a separation of the Helmholtz free energy $A[\rho]$ of the form

$$A[\rho] = A_{id}[\rho] + A_{r,ex}[\rho] + A_{HTA}[\rho], \quad (4.79)$$

which defines the reference excess free energy $A_{r,ex}[\rho]$ (in [13], this term was called the ‘correlation’ free energy). For the liquid phase this HTA-contribution simplifies to

$$A_{l,HTA}(\rho_l) = \frac{1}{2} N \rho^2 4\pi \int_0^\infty dr r^2 \phi_p(r).$$

For $A_{r,ex}$ the MWDA mapping is used

$$\frac{A_{s,r,ex}[\rho_s]}{N} = \frac{A_{l,r,ex}(\hat{\rho})}{N}, \quad (4.80)$$

and we get the following relation between the direct correlation function and the free energy (4.66)

$$\left. \frac{\delta^2 A_{s,r,ex}[\rho]}{\delta \rho(\vec{r}) \delta \rho(\vec{r}')} \right|_{\rho(\vec{r})=\rho_0} = -\frac{1}{\beta} c(|\vec{r} - \vec{r}'|; \rho_0) - \phi_p(|\vec{r} - \vec{r}'|),$$

and define

$$c_r(r; \rho) = c(r; \rho) + \beta \phi_p(r).$$

For the liquid the compressibility equation (3.34) is fulfilled:

$$\frac{d^2}{d\rho^2} A_{l,r,ex}^+(\rho) = -\tilde{c}_r(k=0; \rho).$$

The excess free energy of the liquid can simply be calculated by

$$A_{l,r,ex}(\rho) = A_{l,ex}(\rho) - A_{l,HTA}(\rho).$$

It should be noted that equations (4.75) and (4.76) are also valid for the cMWDA if one replaces all correlation functions with the reduced correlation functions and the Helmholtz excess free energies with the perturbation excess free energies. The Helmholtz free energy curve of the solid at a given temperature is obtained as follows:

- Calculate the properties of the liquid phase of the given system at a given temperature for a certain range of densities $[0, \rho_{max}]$.
- Replace the direct correlation functions ($\{c(\rho), \tilde{c}(\rho)\} \rightarrow \{c_p(\rho), \tilde{c}_p(\rho)\}$) and the Helmholtz free energy ($\{A_{l,ex}(\rho)\} \rightarrow \{A_{l,p,ex}(\rho)\}$) of the liquid.
- For every solid density ρ_s perform the following steps:
 - Start with a first guess for the localization parameter α .
 - Perform the mapping (4.80) to get the weighted density $\hat{\rho}$.
 - Calculate the total Helmholtz free energy for the solid defined by equation (4.79) and (4.78).
 - Reiterate the inner loop until the minimum of $A_s[\rho_s; \alpha]$ with respect to α has been found:

$$A_s(\rho_s) = \min_{\alpha} \{A_{s,id}(\rho_s; \alpha) + A_{l,p,ex}(\hat{\rho}(\rho_s, \alpha)) + A_{s,HTA}(\rho_s)\}$$

The resulting curve can be used in conjunction with the Helmholtz free energy curve of the liquid to determine the phase transitions at the given temperature.

4.3.3 Fundamental measure theory

A geometrically based fundamental measure free energy DF for hard spheres was first proposed by Rosenfeld [14]. The basic idea of the fundamental measure theory (FMT) is that these functionals can be constructed from fundamental geometrical properties of the particles. For the fluid phase of hard spheres, the FMT as applied in [14] produces the PY solution for the correlation functions and the Helmholtz free energy [compressibility route, see equation (4.29)].

The basic idea for a given system is to interpolate between the ‘ideal-liquid’ [76], high density limit where the pair correlation function is dominated by convolutions of single-particle geometries, i.e., overlap volume and overlap surface area, and the limit of low density where it is given by the pair exclusion volume. The key for the realization of this idea is the convolution decomposition of the excluded volume for a pair of convex hard bodies in terms of characteristic functions for the geometry of the two individual bodies. On the basis of a unique convolution decomposition for hard spheres, Rosenfeld [14] derived a fundamental measure free energy functional for a hard sphere mixture. It should be noted that for hard spheres the Mayer function is closely related to the geometric properties of the particles.

An important characteristic feature of present day FMT DFTs is that they give the correct dimensional crossover from three dimensions (3D) to lower ones. One may also start from the 0D case and construct the 3D functionals systematically [77, 78] using the idea of ‘functional interpolation’ between dimensions [78]. Thus the FMT generates the thermodynamic properties (free energy) from the very basic situation of a cavity that has the size of one particle; here, for hard spheres the occupation number is zero or 1, and one can calculate the excess free energy exactly [79].

4.3.3.1 Weight functions

FMT belongs to the weighted density DFTs. The weight functions are obtained from the convolution decomposition of the Mayer function. For hard spheres, the weight functions are characteristic functions of the geometry of the particles and can hence be obtained by the convolution decomposition of the excluded volume of a pair of particles. This excluded volume is equal to the Mayer function $f(r)$ (for hard spheres); so the weight functions are related to the $f(r)$ by

$$-\frac{1}{2}f(r) = w_0 \otimes w_3 + w_1 \otimes w_2 - \vec{w}_{v1} \otimes \vec{w}_{v2}, \quad (4.81)$$

where the \otimes denotes a three dimensional convolution product.

The set of weight functions is not unique. Here we use the following notation: we have three types of weight functions (scalar, vector and tensor weight functions), all weight functions can be constructed from the scalar weight function $w_3(r)$.

The scalar weight functions are defined by:

$$w_2(r) = -\frac{\partial w_3(r)}{\partial r} \quad (4.82)$$

$$w_1(r) = w_2(r) \frac{1}{4\pi r} \quad (4.83)$$

$$w_0(r) = w_1(r) \frac{1}{r}, \quad (4.84)$$

the vector weight functions are given by:

$$\vec{w}_{v2}(\vec{r}) = w_2(r) \frac{\vec{r}}{r} \quad (4.85)$$

$$\vec{w}_{v1}(\vec{r}) = w_1(r) \frac{\vec{r}}{r}, \quad (4.86)$$

and the tensor weight function is defined as

$$\mathcal{W}(\vec{r}) = w_2(r) \frac{\vec{r}\vec{r}}{r^2},$$

where $\vec{r}\vec{r}$ denotes a dyadic product. One can also define a traceless tensor weight function

$$\overline{\mathcal{W}}(\vec{r}) = w_2(r) \left(\frac{\vec{r}\vec{r}}{r^2} - \frac{\mathbb{I}}{3} \right), \quad (4.87)$$

where \mathbb{I} denotes the unity matrix in \mathbb{R}^3 . One can easily show that for a hard sphere system with diameter σ , $w_3(r)$ is given by

$$w_3^{HS}(r) = \Theta\left(\frac{\sigma}{2} - r\right).$$

4.3.3.2 Weighted densities

The Helmholtz excess free energy density functional for FMTs is calculated using

$$\frac{A_{ex}[\{\rho\}]}{k_B T} = \int_{\mathbb{R}^3} d^3r \Phi[\{n\}], \quad (4.88)$$

where the $n(\vec{r})$ are the (scalar, vector and tensor) weighted densities

$$n_\alpha(\vec{r}) = \int_{\mathbb{R}^3} d^3r' \rho(\vec{r}') w_\alpha(\vec{r} - \vec{r}') \quad ; \quad \alpha = 0, 1, 2, 3 \quad (4.89)$$

$$\vec{n}_{vi}(\vec{r}) = \int_{\mathbb{R}^3} d^3r' \rho(\vec{r}') \vec{w}_{vi}(\vec{r} - \vec{r}') \quad ; \quad i = 1, 2 \quad (4.90)$$

$$\mathcal{T}(\vec{r}) = \int_{\mathbb{R}^3} d^3r' \rho(\vec{r}') \mathcal{W}(\vec{r} - \vec{r}') \quad (4.91)$$

$$\overline{\mathcal{T}}(\vec{r}) = \int_{\mathbb{R}^3} d^3r' \rho(\vec{r}') \overline{\mathcal{W}}(\vec{r} - \vec{r}').$$

Φ is the Helmholtz excess-free energy density and a function of the weighted densities of the particles, which are dimensional quantities with the dimensions

$$[n_\alpha] = (\text{volume})^{(\alpha-3)/3} \quad ; \quad [\vec{n}_{vi}] = (\text{volume})^{(i-3)/3} \quad ; \quad [\mathcal{T}] = (\text{volume})^{-1/3},$$

and provide a functional basis set $\{\varphi_i\}$ for expanding the energy density Φ via

$$\Phi = \sum_{i=0}^6 A_i(n_3)\varphi_i \quad (4.92)$$

used in equation (4.88). This functional set is found to be (the dot denotes the scalar product)

$$\{\varphi_i\} = \left\{ n_0, n_1 n_2, \vec{n}_{v1} \cdot \vec{n}_{v2}, n_2^3, n_2 (\vec{n}_{v2} \cdot \vec{n}_{v2}), \vec{n}_{v2} \cdot \mathcal{T} \cdot \vec{n}_{v2}, n_2^\beta \text{tr} \mathcal{T}^{3-\beta} \right\} \quad (4.93)$$

For the HS system, the coefficients $A_i(n_3)$ as functions of the dimensionless weighted density n_3 are determined from the scaled particle differential equation (see [14])

$$-\Phi + \sum_{\alpha} n_{\alpha} \frac{\partial \Phi}{\partial n_{\alpha}} + n_0 = \frac{\partial \Phi}{\partial n_3}, \quad (4.94)$$

where the constants of integration can be fixed by known limits of thermodynamic properties (equation of state). The expression for Φ as derived in [14, 80] consists of three parts (see also subsection 4.3.4),

$$\Phi[\{n_\alpha\}] = \Phi_1 + \Phi_2 + \Phi_3,$$

where

$$\Phi_1 = -n_0 \ln(1 - n_3) \quad (4.95)$$

$$\Phi_2 = \frac{n_1 n_2 - \vec{n}_{v1} \cdot \vec{n}_{v2}}{1 - n_3} \quad (4.96)$$

$$\Phi_3 = \frac{n_2^3 - 3n_2 (\vec{n}_{v2} \cdot \vec{n}_{v2})}{24\pi (1 - n_3)^2}. \quad (4.97)$$

If one also incorporates the tensor weight function \mathcal{T} the contribution Φ_3 takes the form [78]

$$\Phi_3 = \frac{\vec{n}_{v2} \cdot \mathcal{T} \cdot \vec{n}_{v2} - n_2 \vec{n}_{v2} \cdot \vec{n}_{v2} - \text{tr} \mathcal{T}^3 + n_2 \text{tr} \mathcal{T}^2}{\frac{16\pi}{3} (1 - n_3)^2}, \quad (4.98)$$

where $\text{tr} \mathcal{A}$ denotes the Trace of the matrix \mathcal{A} . One can replace \mathcal{T} by $\overline{\mathcal{T}}$, leading to

$$\Phi_3 = \frac{\frac{1}{3} n_2^3 - n_2 \vec{n}_{v2} \cdot \vec{n}_{v2} + \frac{3}{2} [\vec{n}_{v2} \cdot \overline{\mathcal{T}} \cdot \vec{n}_{v2} - \text{tr} \overline{\mathcal{T}}^3]}{8\pi (1 - n_3)^2}.$$

This free energy density was derived for the HS system; its functional form has been used also for other systems: one simply has to insert the weighted densities for the corresponding potential.

4.3.4 Evaluation of Φ

Using the ansatz (4.92) together with the scaled particle differential equation (4.94) leads to the following differential equations for the coefficients $A_i(n_3)$:

$$\begin{aligned} n_0 & : -\frac{1}{1-n_3} = \frac{\partial A_0(n_3)}{\partial n_3} \\ n_1 n_2 & : A_1(n_3) = (1-n_3) \frac{\partial A_1(n_3)}{\partial n_3} \\ \vec{n}_{v1} \cdot \vec{n}_{v2} & : A_2(n_3) = (1-n_3) \frac{\partial A_2(n_3)}{\partial n_3} \\ n_2^3 & : 2A_3(n_3) = (1-n_3) \frac{\partial A_3(n_3)}{\partial n_3} \\ n_2 (\vec{n}_{v2} \vec{n}_{v2}) & : 2A_4(n_3) = (1-n_3) \frac{\partial A_4(n_3)}{\partial n_3}. \end{aligned}$$

These differential equations have the following *unique* solutions:

$$\begin{aligned} A_0(n_3) & = -\ln(1-n_3) \\ A_1(n_3) & = c_1 \frac{1}{1-n_3} \quad ; \quad A_2(n_3) = c_2 \frac{1}{1-n_3} \\ A_3(n_3) & = c_3 \frac{1}{(1-n_3)^2} \quad ; \quad A_4(n_3) = c_4 \frac{1}{(1-n_3)^2}. \end{aligned}$$

In the uniform HS liquid the excess free energy for hard spheres is hence given by [see also equation (4.102)]:

$$A_{ex}^*(\eta) = -\ln(1-\eta) + c_1 \frac{3\eta}{1-\eta} + c_3 \frac{36\pi\eta^2}{(1-\eta)^2}.$$

To determine the integration constants c_1 and c_3 one compares the pressure (by taking the derivative of the excess free energy defined by these coefficients) with the virial expansion for the HS pressure. Using

$$p_{ex}^*(\eta) = \eta \frac{dA_{ex}^*(\eta)}{d\eta}, \quad (4.99)$$

we obtain the Taylor expansion of $p_{ex}^*(\eta)$ for small η :

$$\begin{aligned} p_{ex}^*(\eta) & = (1+3c_1)\eta + (1+6c_1+72\pi c_3)\eta^2 + (1+9c_1+216\pi c_3)\eta^3 \\ & \quad + (1+12c_1+432\pi c_3)\eta^4 + O(\eta^5). \end{aligned}$$

With two parameters (c_1 and c_2) one can only reach equivalence with a given equation of state up to $O(\eta^2)$. For example, the ‘classical’ Rosenfeld solution for Φ reassembles the third virial coefficient for hard spheres [6]:

$$p_{ex;hs}^*(\eta) = 4\eta + 10\eta^2 + O(\eta^3).$$

Hence, the result for c_1 and c_3 is

$$c_1 = 1 \quad ; \quad c_3 = \frac{1}{24\pi}.$$

For the constants c_2 and c_4 , one has to take the quasi zero-dimensional limit of $\Phi = \Phi_1 + \Phi_2 + \Phi_3$, as shown in [79]. In this limit, the contributions of both Φ_2 and Φ_3 have to vanish. For Φ_2 to vanish, c_2 and c_4 have to fulfill the following relations (see [79]):

$$\begin{aligned} c_2 &= -c_1 \\ c_4 &= -3c_3. \end{aligned}$$

4.3.4.1 Uniform case

We will now check the uniform limit of the free energy density Φ . In this limit, equation (4.89) for the scalar weight functions becomes the defining relation for ξ_i

$$n_i = \rho \int_{\mathbb{R}^3} d^3r w_\alpha(\vec{r}) = \rho \tilde{w}_i(k=0) = \rho \xi_i. \quad (4.100)$$

The result of equation (4.90) evaluates to zero for the vector weight-functions (symmetric)

$$\vec{n}_{vi} = \vec{0}.$$

For the tensor weight function (4.91) we obtain:

$$\mathcal{T} = \frac{\rho}{3} \begin{pmatrix} 1 & 0 & 0 \\ 0 & 1 & 0 \\ 0 & 0 & 1 \end{pmatrix} \int_{\mathbb{R}^3} d^3r w_2(\vec{r}) = \frac{\rho}{3} \mathbb{I} \xi_2 = \frac{n_2}{3} \mathbb{I}.$$

The powers of \mathcal{T} and their traces become

$$\mathcal{T}^i = \left(\frac{n_2}{3}\right)^i \mathbb{I} \quad ; \quad \text{tr} \mathcal{T}^i = 3 \left(\frac{n_2}{3}\right)^i \quad ; \quad i = 1, 2, 3.$$

With these results we can find for the excess free energy in the uniform limit:

$$\begin{aligned} \Phi_1 &= -n_0 \ln(1 - n_3) \\ \Phi_2 &= \frac{n_1 n_2}{1 - n_3} \\ \Phi_3 &= \frac{n_2^3}{24\pi (1 - n_3)^2}, \end{aligned}$$

hence

$$\left. \frac{\beta}{V} A_{ex}[\rho] \right|_{\rho(\vec{r})=\rho} = \frac{\beta}{V} A_{ex}(\rho) = -n_0 \ln(1 - n_3) + \frac{n_1 n_2}{1 - n_3} + \frac{n_2^3}{24\pi (1 - n_3)^2}. \quad (4.101)$$

If we insert the uniform limits of the scalar weight functions for the hard sphere system with diameter σ (see equation (4.100), $\xi_3 = \frac{\pi}{6}\sigma^3$, $\xi_2 = \pi\sigma^2$, $\xi_1 = \frac{1}{2}\sigma$, $\xi_0 = 1$) the free energy reads as

$$A_{ex}^*(\eta) = -\ln(1 - \eta) + \frac{3}{2} \left[\frac{1}{(1 - \eta)^2} - 1 \right], \quad (4.102)$$

where $\eta = \xi_3$ is the packing fraction. This expression is the compressibility excess free energy of the PY equation for hard spheres (4.29).

The direct correlation function $c(r)$ can be calculated from the Helmholtz excess free energy using equation (4.66). For the FMT the two particle direct correlation function can be expressed as a sum over convolutions of weight functions:

$$c(\vec{r}_1, \vec{r}_2) = -\beta \frac{\delta^2 A_{ex}[\{\rho\}]}{\delta \rho_1(\vec{r}_1) \delta \rho_2(\vec{r}_2)} = - \int_{\mathbb{R}^3} d^3 r' \sum_{\alpha_1, \alpha_2} \phi_{\alpha_1, \alpha_2} w_{\alpha_1}(\vec{r}_1 - \vec{r}') \otimes w_{\alpha_2}(\vec{r}_2 - \vec{r}'),$$

where the position independent partial derivatives $\phi_{\alpha_1, \alpha_2}$ are defined as

$$\phi_{\alpha_1, \alpha_2} = \left. \frac{\delta^2 \Phi}{\delta n_{\alpha_1} \delta n_{\alpha_2}} \right|_{\{n_\alpha\} = \{n_\alpha(\vec{x})\}}.$$

For the three contributions (4.95), (4.96) and (4.98) to the excess free energy given in (4.101) the partial derivatives in the uniform case are:

- Φ_1 (4.95) :

$$\begin{aligned} \frac{\partial^2 \Phi_1}{\partial n_0 \partial n_3} &= \frac{\partial^2 \Phi_1}{\partial n_3 \partial n_0} = \frac{1}{1 - n_3} \\ \frac{\partial^2 \Phi_1}{\partial n_3 \partial n_3} &= \frac{n_0}{(1 - n_3)^2} \end{aligned}$$

- Φ_2 (4.96) :

$$\begin{aligned} \frac{\partial^2 \Phi_2}{\partial n_1 \partial n_2} &= \frac{\partial^2 \Phi_2}{\partial n_2 \partial n_1} = - \frac{\partial^2 \Phi_2}{\partial \vec{n}_{v1} \partial \vec{n}_{v2}} = - \frac{\partial^2 \Phi_2}{\partial \vec{n}_{v2} \partial \vec{n}_{v1}} = \frac{1}{1 - n_3} \\ \frac{\partial^2 \Phi_2}{\partial n_1 \partial n_3} &= \frac{\partial^2 \Phi_2}{\partial n_3 \partial n_1} = \frac{n_2}{(1 - n_3)^2} \\ \frac{\partial^2 \Phi_2}{\partial n_2 \partial n_3} &= \frac{\partial^2 \Phi_2}{\partial n_3 \partial n_2} = \frac{n_1}{(1 - n_3)^2} \\ \frac{\partial^2 \Phi_2}{\partial n_3 \partial n_3} &= 2 \frac{n_1 n_2}{(1 - n_3)^3} \end{aligned}$$

- Φ_3 (4.98) rewritten as

$$\begin{aligned} \Phi_3 &= \frac{\vec{n}_{v2} \mathcal{T} \vec{n}_{v2} - n_2 \vec{n}_{v2} \vec{n}_{v2} + \frac{2}{9} n_2^3}{\frac{16\pi}{3} (1 - n_3)^2} \\ \frac{\partial^2 \Phi_3}{\partial n_2 \partial n_2} &= - \frac{\partial^2 \Phi_3}{\partial \vec{n}_{v2} \partial \vec{n}_{v2}} = \frac{n_2}{4\pi (1 - n_3)^2} \\ \frac{\partial^2 \Phi_3}{\partial n_2 \partial n_3} &= \frac{\partial^2 \Phi_3}{\partial n_3 \partial n_2} = \frac{n_2^2}{8\pi (1 - n_3)^3} \\ \frac{\partial^2 \Phi_3}{\partial n_3 \partial n_3} &= \frac{n_2^3}{4\pi (1 - n_3)^4} \end{aligned}$$

Summarizing, the direct correlation function takes the form

$$\begin{aligned}
-c(r) = & \frac{1}{1-n_3} (w_0 \otimes w_3 + w_3 \otimes w_0 + w_1 \otimes w_2 + w_2 \otimes w_1 - \vec{w}_{v1} \otimes \vec{w}_{v2} - \vec{w}_{v2} \otimes \vec{w}_{v1})(r) \\
& + \left[\frac{n_1}{(1-n_3)^2} + \frac{n_2^2}{8\pi(1-n_3)^2} \right] (w_2 \otimes w_3 + w_3 \otimes w_2)(r) \\
& + \left[\frac{n_0}{(1-n_3)^2} + 2\frac{n_1 n_2}{(1-n_3)^3} + \frac{n_2^3}{4\pi(1-n_3)^4} \right] (w_3 \otimes w_3)(r) \\
& + \frac{n_2}{(1-n_3)^2} \left[(w_1 \otimes w_3 + w_3 \otimes w_1)(r) + \frac{1}{4\pi} (w_2 \otimes w_2 - \vec{w}_{v2} \otimes \vec{w}_{v2})(r) \right].
\end{aligned}$$

Using the symmetry relation

$$w_\alpha \otimes w_\beta = w_\beta \otimes w_\alpha$$

and the following partial derivatives of the free excess energy in the uniform limit (4.101)

$$\begin{aligned}
\beta \frac{\partial^2 A_{ex}(\rho)}{\partial n_0 \partial n_3} = \chi_0 &= \frac{1}{1-n_3} \\
\beta \frac{\partial^2 A_{ex}(\rho)}{\partial n_1 \partial n_3} = \chi_1 &= \frac{n_2}{(1-n_3)^2} \\
\beta \frac{\partial^2 A_{ex}(\rho)}{\partial n_2 \partial n_3} = \chi_2 &= \frac{n_1}{(1-n_3)^2} + \frac{n_2^2}{8\pi(1-n_3)^2} \\
\beta \frac{\partial^2 A_{ex}(\rho)}{\partial n_3 \partial n_3} = \chi_3 &= \frac{n_0}{(1-n_3)^2} + 2\frac{n_1 n_2}{(1-n_3)^3} + \frac{n_2^3}{4\pi(1-n_3)^4}
\end{aligned}$$

we get finally

$$\begin{aligned}
-c(r) = & 2 \left\{ \chi_2 (w_2 \otimes w_3)(r) + \chi_1 \left[(w_1 \otimes w_3)(r) + \frac{1}{8\pi} (w_2 \otimes w_2 - \vec{w}_{v2} \otimes \vec{w}_{v2})(r) \right] \right. \\
& \left. + \chi_0 (w_0 \otimes w_3 + w_1 \otimes w_2 - \vec{w}_{v1} \otimes \vec{w}_{v2})(r) \right\} + \chi_3 (w_3 \otimes w_3)(r). \quad (4.103)
\end{aligned}$$

For hard spheres this direct correlation function is equal to the direct correlation function one gets from the PY solution [see also section 4.1.6].

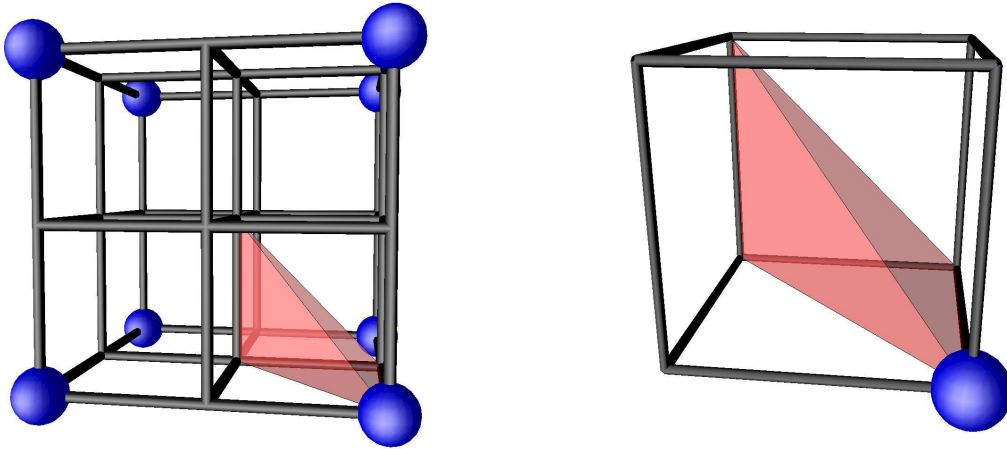
4.3.4.2 Nonuniform case

The first step towards the Helmholtz free energy in the nonuniform ordered solid state is the evaluation of the weighted densities for the position dependent one particle density. In this case the density of the solid is parameterized via equation (C.1). The superposition of the one particle density of equation (C.1) holds also for the weighted density. The weighted densities, defined as convolutions [see equations (4.89), (4.90) and (4.91)] in r -space, become products in k -space.

After the weighted densities are calculated, one has to evaluate equation (4.88) for a

given lattice. A simple and straightforward implementation for the fcc and bcc lattice is to discretize the simple cubic cell¹ using an equidistant three-dimensional mesh. For each point of this mesh one has to calculate the free energy density $\Phi[\{n(\vec{r})\}]$ by summing over all neighbors particles which contribute to the free energy density at this mesh point. This part of the evaluation can be sped up by using the various symmetry relations that hold for the chosen lattice. In figure 4.1 and 4.2 the smallest simplices (asymmetric unit, see

Figure 4.1: Simple cubic cell for the sc lattice; shown inside the cell is a smallest simplex (asymmetric unit) which was considered in the integrations; all other regions of the cell are obtained via mirroring from this simplex. Left side: cubic cell, right side: simple cubic cell.



[81]) are shown for the sc (simple cubic), fcc (face centered cubic) and bcc (body centered cubic) lattice. For an overview of the lattices used in this thesis we refer to appendix C.1. Those simplices are enclosing the volume for which one has to calculate the free energy density. The rest of the volume can be filled with mirrored versions of this simplex. The Helmholtz free energy is then calculated using, for instance, a three dimensional Simpson rule, integrating over the whole simple cubic cell.

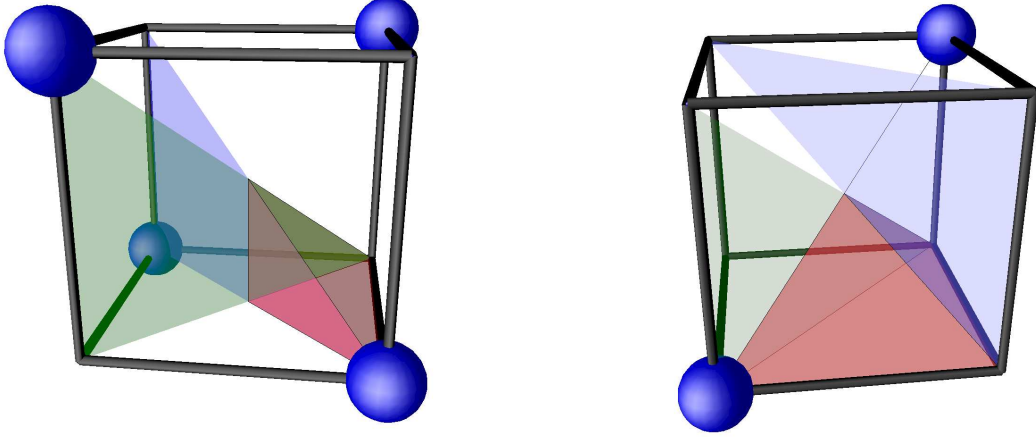
It should be noted that the evaluation of equation (4.88) represents the most time-consuming step of the evaluation of the Helmholtz free energy. The execution time of the algorithm scales with the third power of the number of mesh points in one dimension:

$$t \propto N^3.$$

$\Phi(\vec{r})$ can be a rapidly varying function of \vec{r} , so one has to choose the mesh very carefully. Most FMT calculations in this thesis were done using a cubic mesh with $N = 101$ mesh points along one side of the simple cube, leading to a total number of approximately 1000000 mesh points. Using the asymmetric unit as described above reduces this number for the fcc lattice to ≈ 43000 .

¹The simple cubic cell consists of one eighth of the cubic cell.

Figure 4.2: Simple cubic cell for the fcc and bcc lattice, shown inside the cell is a smallest simplex (asymmetric unit) which has to be calculated; all other regions of the cell can be mirrored from this simplex. Left side: fcc lattice cell, the two transparent triangles spanning the whole cell represent two symmetry planes. Right side: bcc lattice.



4.3.5 Roth's approach

It is clear that, using the Taylor expansion approach described in subsection 4.3.4, one is unable to recover a given equation of state *exactly*. Roth has introduced a method, which overcomes this deficiency. His method has the advantage that one can apply it to a larger class of equations of state.

The idea of his method is as follows: the excess free energy density Φ is constructed using the same principles as the original Rosenfeld approach. The parameter c_1 is set to one, whereas the parameter c_3 is now a function of η : $c_3(\eta)$ depends explicitly on the equation p_{eos}^* of state one wants to describe. $c_3(\eta)$ is calculated directly from the excess free energy relation for the considered equation of state:

$$A_{ex}^*(\eta) = -\ln(1-\eta) + \frac{3\eta}{1-\eta} + c_3(\eta) \frac{36\pi\eta^2}{(1-\eta)^2} = A_{ex,eos}^*(\eta) \rightarrow c_3(\eta) = f(A_{ex,eos}^*(\eta)).$$

Using this technique one can, for example, easily recover the CS equation of state [equation (4.30) and (4.31)] by setting $c_3(\eta)$ equal to

$$c_3(\eta) = \frac{\eta + (1-\eta)^2 \ln(1-\eta)}{36\pi\eta^2},$$

leading to a classic (i.e., missing the tensor contribution) expression for Φ_3 , which reads as:

$$\Phi_3 = \frac{[\eta + (1-\eta)^2 \ln(1-\eta)] [n_2^3 - 3n_2 (\vec{n}_{v2} \cdot \vec{n}_{v2})]}{36\pi\eta^2 (1-n_3)^2}. \quad (4.104)$$

4.3.6 Soft fundamental measure theory

Whereas the FMT was used for hard core interactions, the soft fundamental measure theory (SFMT) deals with soft interactions. The SFMT is, like the FMT, built on well-defined limiting cases, where the behavior of the exact free energy functional is known. These cases are the virial expansion of the pressure and the 0D limit of the free energy.

4.3.6.1 Deconvolution equation

The deconvolution equation (4.81) is reformulated using the defining ‘hierarchy’ (4.82-4.84) of the scalar weight functions to

$$-\frac{1}{2}f(r) = \frac{1}{4\pi} \left[-\frac{w'_3(r)}{r^2} \otimes w_3(r) + \frac{w'_3(r)}{r} \otimes w'_3(r) - \frac{w'_3(r)}{r^2} \vec{r} \otimes \vec{r} \frac{w'_3(r)}{r} \right] \quad (4.105)$$

where the prime denotes differentiation with respect to r . This equation, an integro-differential equation of first order in the unknown function $w_3(r)$, has to be solved for $w_3(r)$ using a given Mayer function $f(r)$ [and hence a pair potential $\phi(r)$]. A direct numerical solution of this equation via iterative algorithms turns out to be unstable and hence impossible (small changes for $w_3(r)$ become completely washed out under the convolution operation).

However, it is possible to construct an explicit solution. The Mayer function and the weight function $w_2(r)$ obey the simple relation derived by Schmidt [15]

$$\frac{\partial f(r)}{\partial r} = \int_{-\infty}^{\infty} dr' w_2(r') w_2(r - r'), \quad (4.106)$$

where we can formally set $w_2(r < 0) = 0$ to simplify the limits of the integration. This equation reads in reciprocal space [for the definition of the Fourier transforms see equations (B.3) and (B.4)]:

$$ik\tilde{f}(k) = \tilde{w}_2^2(k) \quad \longrightarrow \quad \tilde{w}_2(k) = \pm \sqrt{ik\tilde{f}(k)}. \quad (4.107)$$

However, numerically it is more stable to Fourier transform the derivative of the Mayer function instead of the doing the derivative in k space; further, one has to be careful of the singularities in $f'(r)$. We find

$$\mathcal{F}(k) = \widetilde{f'(r)} = \int_{-\infty}^{\infty} dr \frac{\partial f(r)}{\partial r} e^{ikr} = \widetilde{f'_S(r)} + \sum_{i=1}^N v_i e^{ikr_i},$$

where $f_S(r)$ represents the smooth part of the Mayer function and the r_i (with $i = 1, \dots, N$) are the positions where $f(r)$ has a discontinuity of height v_i . It should be noted that $f(r) = 0$ for $r < 0$ and hence the lower integral bound is zero [in contrast to equation (B.3)]. The Fourier transformed derivative of the Mayer function, $\mathcal{F}(k)$, is defined on $k \in (-\infty, \infty)$ with the following symmetry relations:

$$\Re[\mathcal{F}(-k)] = \Re[\mathcal{F}(k)] \quad ; \quad \Im[\mathcal{F}(-k)] = -\Im[\mathcal{F}(k)], \quad (4.108)$$

where \Re and \Im denote the real and imaginary part of the argument. Now we have to take the root in (4.107)

$$\tilde{w}_2(k) = \pm \sqrt{\mathcal{F}(k)}$$

for all k . It should be noted that one has to be careful with the sign in this equation. It may change depending on the value of k . As a physically meaningful prescription we choose a continuous and differentiable function in k space.

In this thesis we choose the following algorithm to implement the discretized version of equation (4.107):

1. Take $k = 0$ (index $j = 0$) as the starting point.
2. For the actual index j , calculate the square roots $\mathcal{R}^j = R_r^j + iR_i^j$ of the complex value $\mathcal{F}(k_j)$. This root is not unique, in fact, both $\mathcal{R}_1^j = \mathcal{R}^j$ and $\mathcal{R}_2^j = -\mathcal{R}^j$ are possible solutions. For $k = 0$ we take the positive root.
3. Compare these two roots with the estimated result \mathcal{R}'^j calculated using the two previous roots \mathcal{R}^{j-2} and \mathcal{R}^{j-1} using, for example, a simple linear extrapolation; whereas for $j = 1$ one can use $\mathcal{R}'^1 = \mathcal{R}^0$.
4. Take the root with the smaller difference to the predicted value as the result, $\tilde{\mathcal{W}}_2(k_j) = \mathcal{R}^j$.
5. Go to the next index j and continue at step (2).

The resulting complex valued function $\tilde{\mathcal{W}}_2(k) = \tilde{w}_2^R(k) + i\tilde{w}_2^I(k)$ consists of a real and an imaginary part for all k . Using equation (B.4) and the symmetry relations (4.108) [which also apply to $\mathcal{W}_2(k)$] for the retransformation we get for the real part:

$$w_2^R(r) = \frac{1}{\pi} \left[\int_0^\infty dk \tilde{w}_2^R(k) \cos(kr) + \int_0^\infty dk \tilde{w}_2^I(k) \sin(kr) \right],$$

whereas the imaginary part evaluates to zero. This equation can be calculated using the one dimensional cosine (B.5) and sine (B.6) Fourier transforms.

The weight function $w_3(r)$ can be calculated from $w_2(r)$ via a simple integration with respect to r [see also equation (4.82)]. One has to make sure that $w_3(r)$ fulfills the boundary condition $w_3(r \rightarrow \infty) = 0$. If the potential (and also the Mayer function) of the system has a core, $w_3(r)$ has a discontinuity at $r = \frac{\sigma}{2}$. This discontinuity is hard to reproduce numerically, so in this case one can use a ‘second boundary condition’ by requesting that $w_3(r < \frac{\sigma}{2}) = 1$.

For some potentials the deconvolution equation (4.81) is analytically solvable. Solutions of the SFMT for various potentials will be presented in the next subsections. One should note that the solution of the SFMT for the hard sphere potential yields the well known result $w_2(r) = \delta(r - \sigma/r)$ and $w_3(r) = \Theta(\sigma/2 - r)$, i.e., the weight functions as proposed by Rosenfeld.

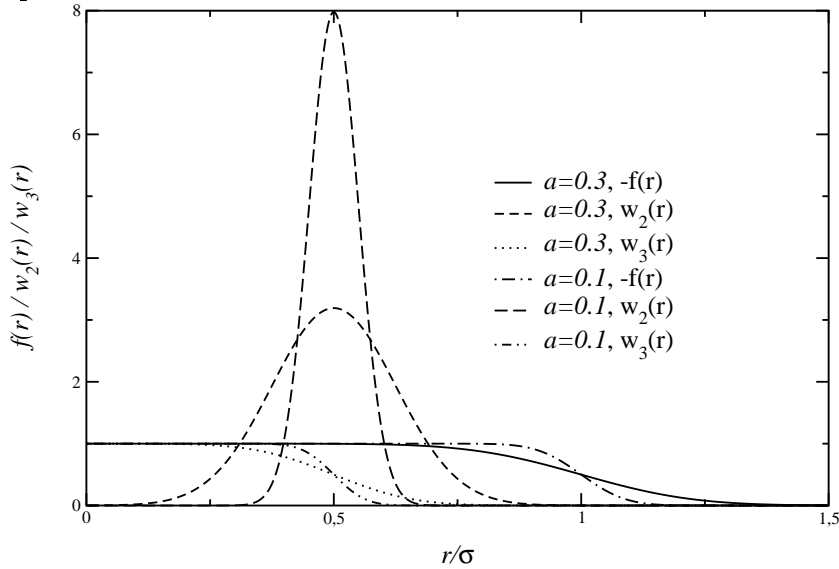
4.3.6.2 SFMT for the error function potential

For the ERF potential as presented in section 2.2.8 there exists an analytical solution for $w_2(r)$ under the restriction that $f(r=0) = -1$ (valid for $\frac{a}{\sigma} \leq 0.3$). The derivative of the Mayer function is equal to

$$\frac{\partial f(r)}{\partial r} = \frac{1}{a\sqrt{\pi}} \exp \left[- \left(\frac{r - \sigma}{a} \right)^2 \right],$$

and after doing some algebra (the self convolution of a Gaussian function is again a Gaussian function with shifted maximum and increased width) we get for $w_2(r)$

Figure 4.3: Mayer function $f(r)$ and weight functions $w_2(r)$ and $w_3(r)$ for SFMT for the error function potential with $a = 0.1$ and $a = 0.3$.



$$w_2(r) = \frac{1}{a} \sqrt{\frac{2}{\pi}} \exp \left[- \left(\frac{r - \frac{\sigma}{2}}{\frac{a}{\sqrt{2}}} \right)^2 \right]$$

and for $w_3(r)$

$$w_3(r) = \frac{1}{2} \left[1 - \operatorname{erf} \left(\frac{r - \frac{\sigma}{2}}{\frac{a}{\sqrt{2}}} \right) \right].$$

In figure 4.3, the weight functions $w_2(r)$ and $w_3(r)$ are shown together with the Mayer function $f(r)$ for $a = 0.1$ and $a = 0.3$. Obviously, softer potentials are leading to a broadening in the weight functions. The according pair distribution functions $g(r)$ for these values of a are shown in figures 4.4 ($a = 0.1$) and 4.5 ($a = 0.3$). For $a = 0.1$, the SFMT solution without the test particle limit (TPL) applied (the TPL is explained in section 4.3.7) yields a result where for $r < 0.5$ the core condition is violated; hence $g(r)$

Figure 4.4: Pair distribution functions $g(r)$ for the error-function fluid with $a = 0.1$ at $\eta = 0.3$, the analytical SFMT solution presented in this subsection (with and without the TPL as discussed in the next session) and the result of the RY approximation ($\alpha \approx 0.38081$).

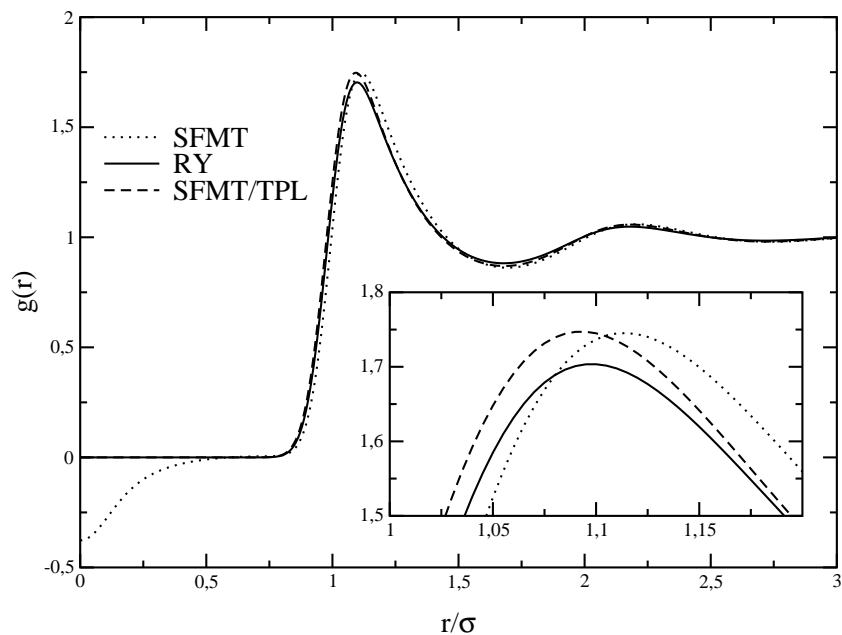
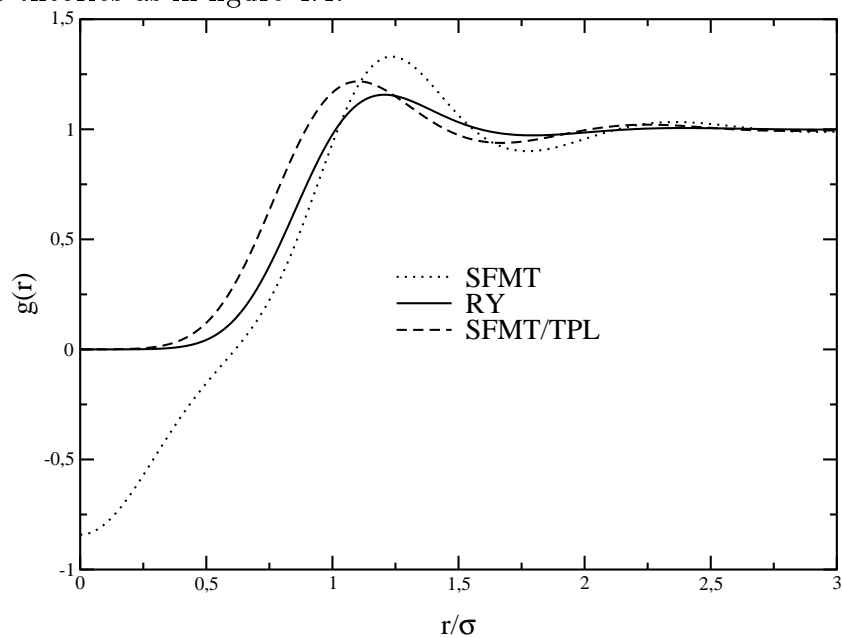


Figure 4.5: Pair distribution functions $g(r)$ for the error-function fluid with $a = 0.3$ at $\eta = 0.3$, same theories as in figure 4.4.



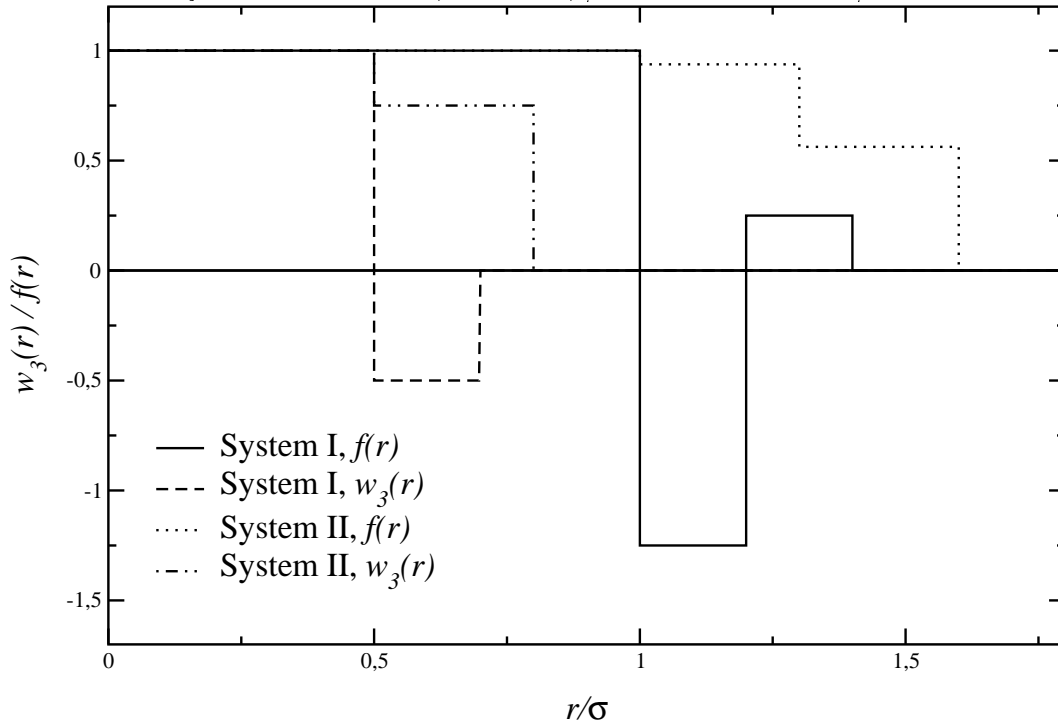
is in fact unusable. By the employment of the TPL, the result is consistent with the core region. For such small values of a , the results one gets using the SFMT together with the TPL are of comparable quality as the solutions from the RY approximation. For $a = 0.3$, the pair distribution function one gets from the SFMT is unphysical. The application of the TPL repairs the core violation of the SFMT, but obviously the result is still very different from the RY solution.

Summarizing, we can say that the analytical solution of the SFMT for the error function potential yields satisfactory results when the ‘softness’ of the core is small ($a \leq 0.1$) and if the TPL is used to correct the unphysical behavior of $g(r)$ inside the core region.

4.3.6.3 SFMT for the double square well potential

The SFMT for the double square well potential (parameters see subsection 2.2.2.1) has an analytical solution, if the ratios between ε_1 and ε_2 and λ_1 and λ_2 fulfill certain conditions.

Figure 4.6: Mayer function $f(r)$ and weight function $w_3(r)$ for SFMT for the double square-well/square-shoulder potential. System I: $\lambda_1 = 1.2$, $\lambda_2 = 1.4$, $\beta\varepsilon_1 = 0.810930$ and $\beta\varepsilon_2 = -0.28769$. System II: $\lambda_1 = 1.3$, $\lambda_2 = 1.6$, $\beta\varepsilon_1 = -2.7726$ and $\beta\varepsilon_2 = -0.82668$.

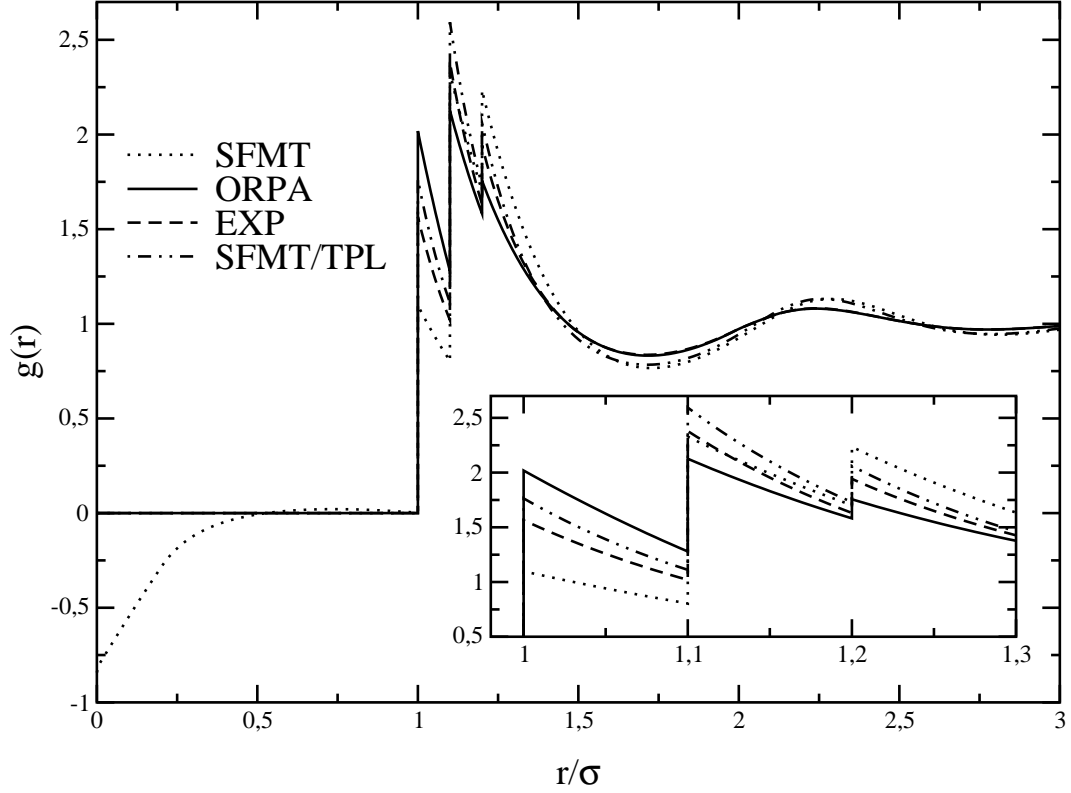


To derive these conditions we start with the derivative of the Mayer function:

$$\frac{df(r)}{dr} = e^{\beta\varepsilon_1} \delta(r - \sigma) + (e^{\beta\varepsilon_2} - e^{\beta\varepsilon_1}) \delta(r - \sigma\lambda_1) + (1 - e^{\beta\varepsilon_2}) \delta(r - \sigma\lambda_2).$$

This function can be deconvoluted numerically. We present here an elegant solution of equation (4.105). The basic idea is that the self convolution of a function with two δ -singularities leads to a function with three delta peaks. So we make the following ansatz

Figure 4.7: Pair distribution functions $g(r)$ for a double square-shoulder fluid with $\lambda_1 = 1.1$, $\lambda_2 = 1.2$ at $\eta = 0.3$, $T^* = 0.9788$ (left shoulder), $\varepsilon_r = 0.1707$ for the analytical SFMT solution presented in this subsection (with and without the TPL as discussed in the next session), ORPA and EXP. The inset shows the region around $r = \sigma$.



for $w_2(r)$ with the two parameters v_1 and v_2 :

$$w_2(r) = v_1 \delta\left(r - \frac{\sigma}{2}\right) + (1 - v_1) \delta(r - v_2).$$

Inserting $w_2(r)$ into (4.106) leads to this two equations for v_2 :

$$v_2 = \sigma \left(\lambda_1 - \frac{1}{2} \right) \quad \text{and} \quad v_2 = \sigma \frac{\lambda_2}{2},$$

so the condition for λ_1 and λ_2 is:

$$2\lambda_1 = 1 + \lambda_2.$$

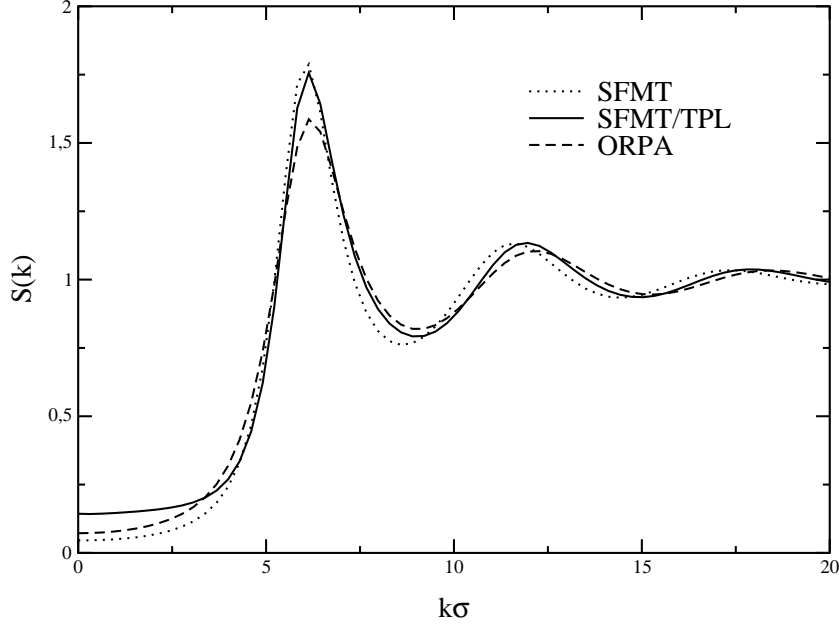
For v_1 one gets three equations:

$$e^{\beta\varepsilon_1} = v_1^2 \quad ; \quad e^{\beta\varepsilon_2} - e^{\beta\varepsilon_1} = 2v_1(1 - v_1) \quad \text{and} \quad 1 - e^{\beta\varepsilon_2} = (1 - v_1)^2,$$

hence $\beta\varepsilon_1$ and $\beta\varepsilon_2$ are connected via the following condition:

$$\sqrt{e^{\beta\varepsilon_1}} = 1 \pm \sqrt{1 - e^{\beta\varepsilon_2}};$$

Figure 4.8: Static structure factor $S(k)$ for a double square-shoulder fluid with $\lambda_1 = 1.1$, $\lambda_2 = 1.2$ at $\eta = 0.3$, $T^* = 0.9788$ (left shoulder), $\varepsilon_r = 0.1707$ for the analytical SFMT solution presented in this subsection (with and without the TPL as discussed in the next session) and ORPA.

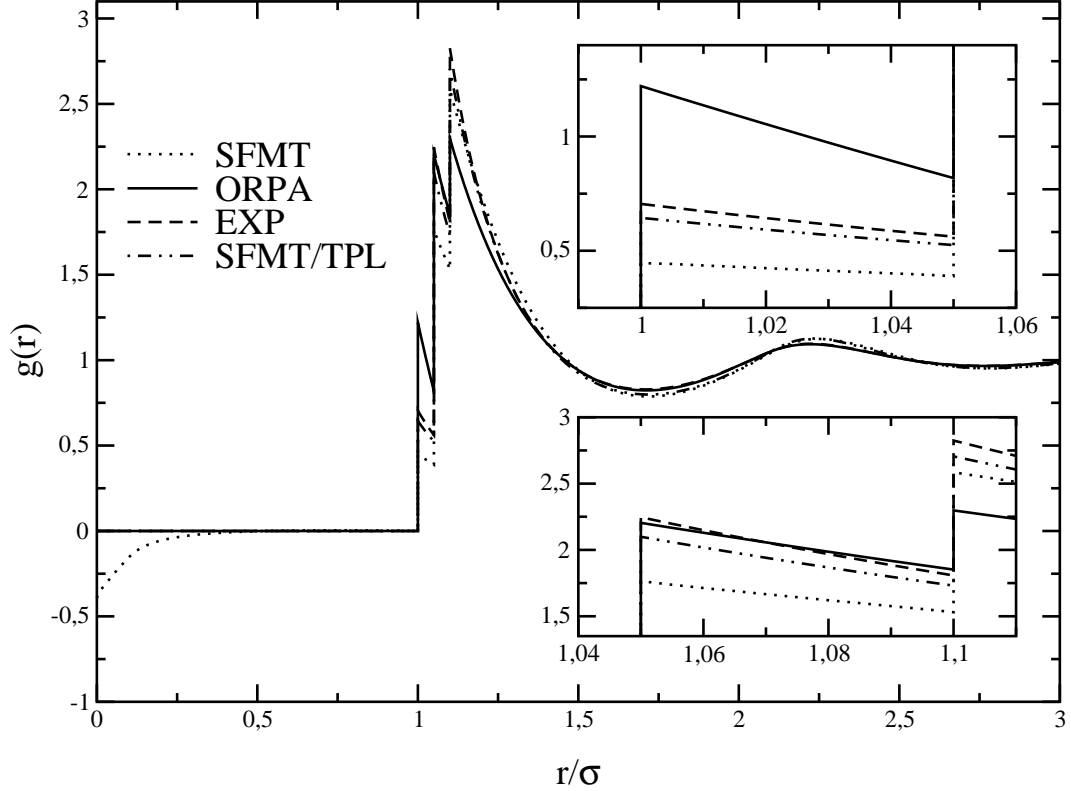


this equation has, beside the simple solution $\varepsilon_1 = \varepsilon_2 = 0$, only a meaningful solution if $\beta\varepsilon_2$ is less than zero. In other words the second potential step must be a shoulder.

Although the field of application for this special solution of the SFMT is very limited, it is still interesting to see how good the results of the SFMT for this potential are when compared with other theories described in this thesis. In figure 4.7 and 4.9, We compare the SFMT (with and without test particle limit applied) to the ORPA and the EXP results for two double square-shoulder potentials. From these figures, it is clear that the (pure) SFMT yields unphysical results (violation of the core condition) for this type of potentials. By applying the TPL to the SFMT results, the quality improves significantly. For narrow perturbations (figure 4.9), the solution of the SFMT/TPL is nearly as good as the EXP results. A problem both the SFMT and SFMT/TPL results are suffering from, is that both theories are predicting long-range oscillations with an amplitude that is too high when compared with the EXP; hence the first peak of the static structure factor of the SFMT and SFMT/TPL is also too high (figure 4.8 shows the static structure factor $S(k)$ for figure 4.7).

Summarizing, we can say that the analytic solution of the SFMT for this potential type yields only satisfactory results if the perturbation of the hard-core behavior is small and the TPL is applied to the SFMT results. However, the employment of the TPL is very time consuming and convergence is hard to achieve if the perturbation part of the potential is too big.

Figure 4.9: Pair distribution functions $g(r)$ for a double square-shoulder fluid with $\lambda_1 = 1.05$, $\lambda_2 = 1.1$ at $\eta = 0.3$, $T^* = 0.5457$ (left shoulder), $\varepsilon_r = 0.2435$ for the analytical SFMT solution presented in this subsection (with and without the test particle limit as discussed in the next session), ORPA and EXP. The inset shows the region around the first and the second shoulder.



4.3.6.4 SFMT for the square-well/square-shoulder potential

For the square-well/square-shoulder potential a semi analytical solution of the SFMT can be derived. For this solution, no restrictions are imposed on the potential. However, it should be noted that the solution (fluid structure and thermodynamic properties) is not always physical.

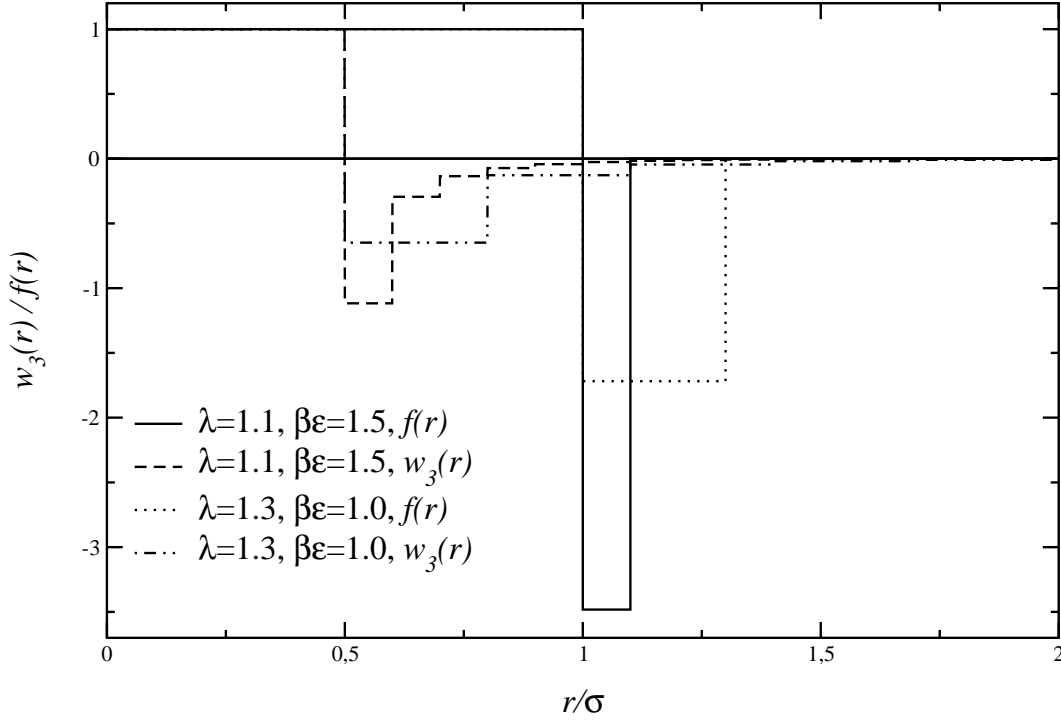
We start from the derivative of the Mayer function:

$$\frac{\partial f(r)}{\partial r} = e^{\beta\varepsilon} \delta(r - \sigma) + (1 - e^{\beta\varepsilon}) \delta(r - \lambda\sigma). \quad (4.109)$$

From the form of this function it is clear that it is not possible to find a simple solution like for the double square-well potential. We start with a general ansatz for $w_2(r)$ consisting of an infinite number of delta peaks:

$$w_2(r) = \sum_{i=1}^{\infty} p_i \delta(r - x_i) \quad \text{with} \quad x_1 < x_2 < \dots \quad (4.110)$$

Figure 4.10: Mayer function $f(r)$ and SFMT weight function $w_3(r)$ for a square well potential, $\lambda = 1.1$ and 1.3 , $\beta\varepsilon = 1.0$ and 1.5 .



We also impose that the sequence of p_i tend towards zero for large i . The self convolution of this ansatz leads to

$$\frac{\partial f(r)}{\partial r} = \sum_{i=1}^{\infty} p_i \delta(r - 2x_i) + 2 \sum_{\substack{i=1 \\ j>i}}^{\infty} p_i p_j \delta(r - x_i - x_j). \quad (4.111)$$

We focus on the positions x_i of the delta peaks by comparing equations (4.109) and (4.111). For the first two delta peaks at x_1 and x_2 one finds

$$x_1 = \sigma \frac{1}{2} \quad ; \quad x_2 = \sigma \left[\frac{1}{2} + \lambda - 1 \right].$$

Similarly, we find

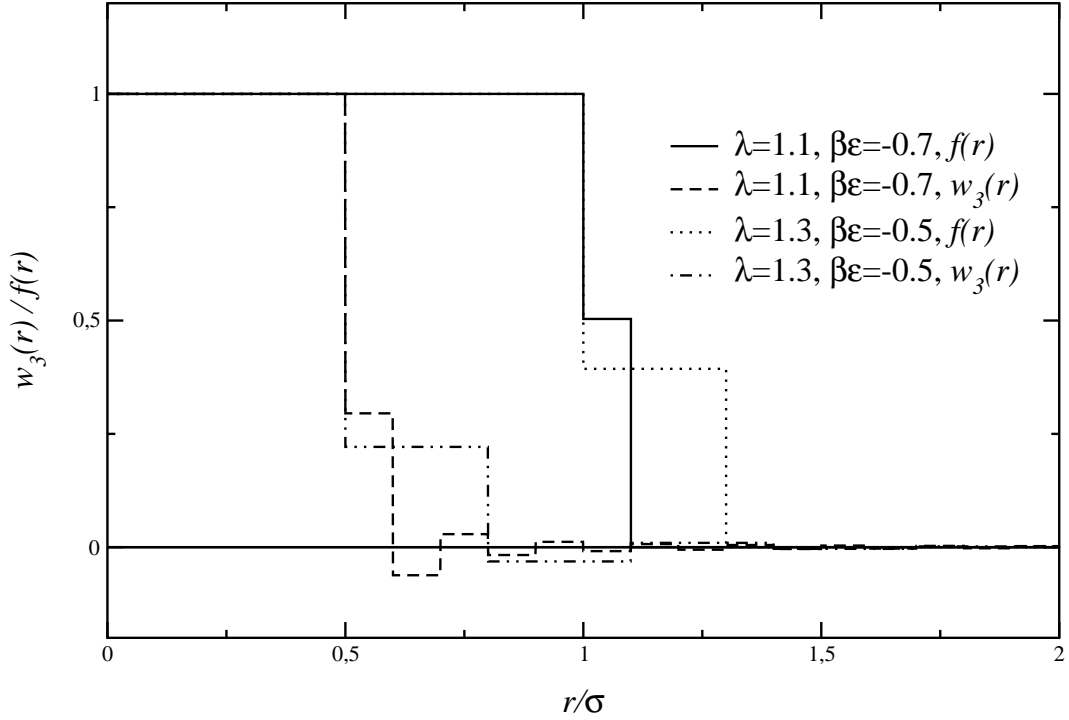
$$x_3 = 2x_2 - x_1 = \sigma \left[\frac{1}{2} + 2(\lambda - 1) \right].$$

The same arguments apply to the next resulting peak at $x_2 + x_3$ and so on. The peaks of $w_2(r)$ are hence positioned at

$$x_i = \sigma \left[\frac{1}{2} + (i - 1)(\lambda - 1) \right].$$

The number of source peaks [stemming from $w_2(r)$] contributing to the resulting destination peaks [of $\frac{\partial f(r)}{\partial r}$] is equal to the index of the source peak (the numbers inside the

Figure 4.11: Mayer function $f(r)$ and weight function $w_3(r)$ for SFMT for a square shoulder potential, $\lambda = 1.1$ and 1.3 , $\beta\varepsilon = -0.5$ and -0.7 .



parentheses are equal to the indices of the source peaks which have to be convoluted):

- 1.(at σ) \rightarrow (1, 1)
- 2.(at $\lambda\sigma$) \rightarrow (1, 2) + (2, 1)
3. \rightarrow (1, 3) + (2, 2) + (3, 1)
4. \rightarrow (1, 4) + (2, 3) + (3, 2) + (4, 1).

It should be noted that all peaks with index higher than two have to vanish, so an increasing number of contributing source peaks is necessary to make the destination peak vanish. The evaluation of the peak heights p_i is now straightforward. For the first and second peak we find

$$p_1 = \sqrt{e^{\beta\varepsilon}} \quad ; \quad p_2 = \frac{1 - e^{\beta\varepsilon}}{2p_1}. \quad (4.112)$$

For p_3, p_5 and, in general for odd coefficients, the results are

$$p_3 = -\frac{p_2^2}{2p_1} \quad ; \quad p_5 = -\frac{\frac{1}{2}p_3^2 + p_2p_4}{p_1} \quad ; \quad p_i = -\frac{1}{p_1} \left[\frac{1}{2}p_{\frac{i+1}{2}} + \sum_{j=2}^{\frac{i-1}{2}} p_j p_{i+1-j} \right].$$

For the even coefficients we get:

$$p_4 = -\frac{p_2p_3}{p_1} \quad ; \quad p_6 = -\frac{1}{p_1} (p_2p_5 + p_3p_4) \quad ; \quad p_i = -\frac{1}{p_1} \sum_{j=2}^{\frac{i-1}{2}} p_j p_{i+1-j}.$$

Figure 4.12: Pair distribution functions $g(r)$ for the square-shoulder fluid with $\lambda = 1.05$ at $\eta = 0.3$, $T^* = 2$ for the analytical SFMT solution present in this subsection (with and without the test particle limit as discussed in the next session), ORPA, EXP and Nezbeda's semi-analytical solution of the PY approximation. The inset shows the region around $r = \sigma$.

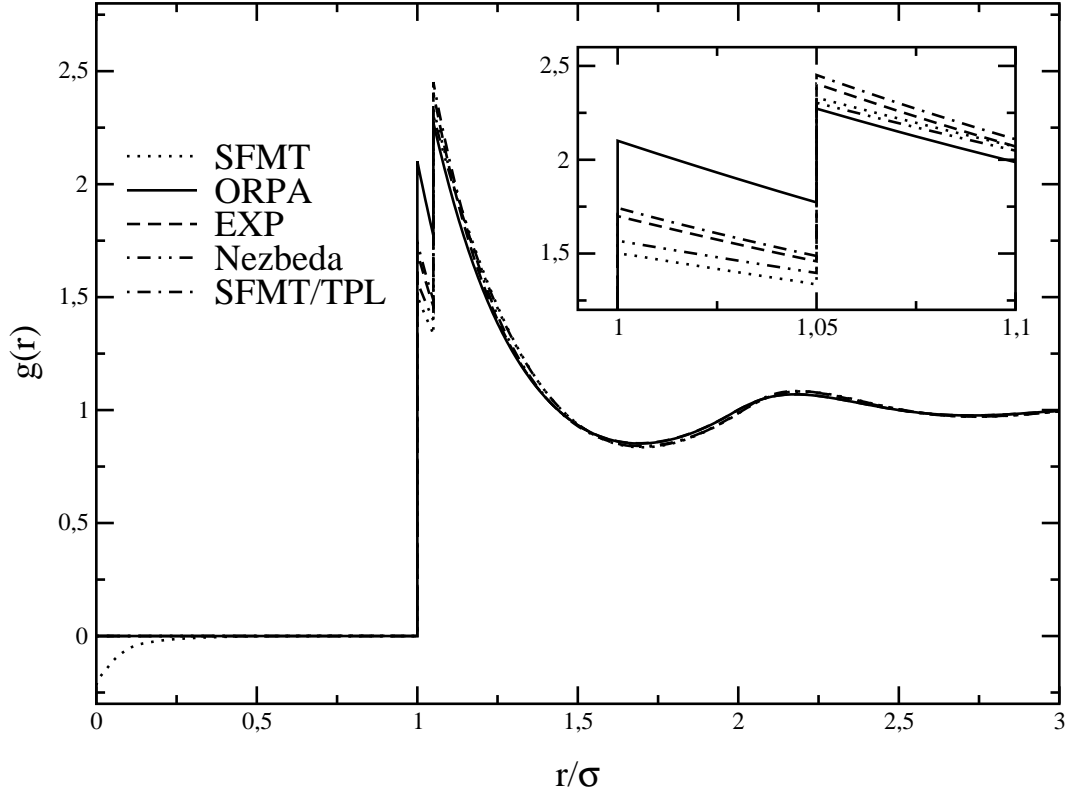
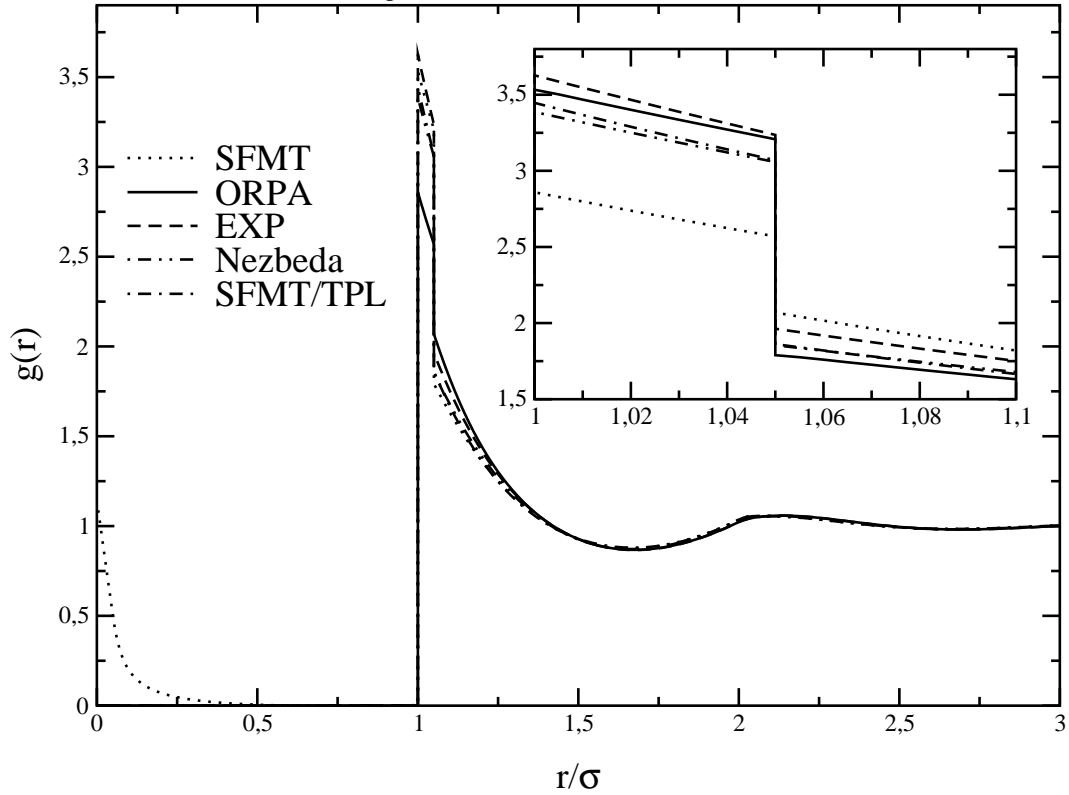


Figure 4.10 and 4.11 shows the solutions $w_3(r)$ for different square well and square shoulder potentials. It should be noted that the ansatz (4.110) does not always lead to a convergent solution ($|p_{i+1}| < |p_i|$); problems emerge for square-shoulder systems with $\beta\varepsilon < -0.7$, because under those circumstances the series p_i diverges with increasing i . In particular, the SFMT for square-shoulder potentials is unable to recover the limit of $\beta\varepsilon \rightarrow -\infty$, i.e., a HS system with diameter $\lambda\sigma$ and the solution $w_2(r) = \delta(r - \frac{\lambda\sigma}{2})$: here p_1 tends to zero whereas p_2 tends to plus infinity [of equation (4.112)]. Beside the results we present in section 6.4, the result for a square-shoulder fluid with $\lambda = 1.05$ at $\eta = 0.3$ and $T^* = 2$ is shown in figure 4.12. Obviously, the analytic SFMT solution predicts a completely unphysical behavior inside the core, where $g(r)$ has to be equal to zero (in contrast to the SFMT solution). This deficiency can be repaired by applying the TPL presented in the next section. For $r \geq \sigma$, the results are all of comparable quality, only the ORPA is overestimating the attractive part of the potential, hence the contact value of $g_{ORPA}(r)$ is too high. It should be noted, that for these two systems (figures 4.12 and 4.13), the (p_i) are nearly equal to zero ($|p_i| < 10^{-12}$) for $r \approx 2.0$. If the perturbation potential width is increased to $\lambda = 1.5$, the analytic SFMT solution fails completely to

Figure 4.13: Pair distribution functions $g(r)$ for the square-well fluid with $\lambda = 1.05$ at $\eta = 0.3$, $T^* = 2$. Symbols as in figure 4.12.



predict the structure of the fluid, as shown in figure 4.14.

Summarizing, the analytic solution of the SFMT for the square-well/square-shoulder potential suffers from the same problems as discussed in the subsection for the error function potential and the double square-well/square-shoulder potential (violation of the core condition). Small perturbations of the hard-sphere potential yield good results (if the SFMT is combined with the TPL).

4.3.7 Test particle limit

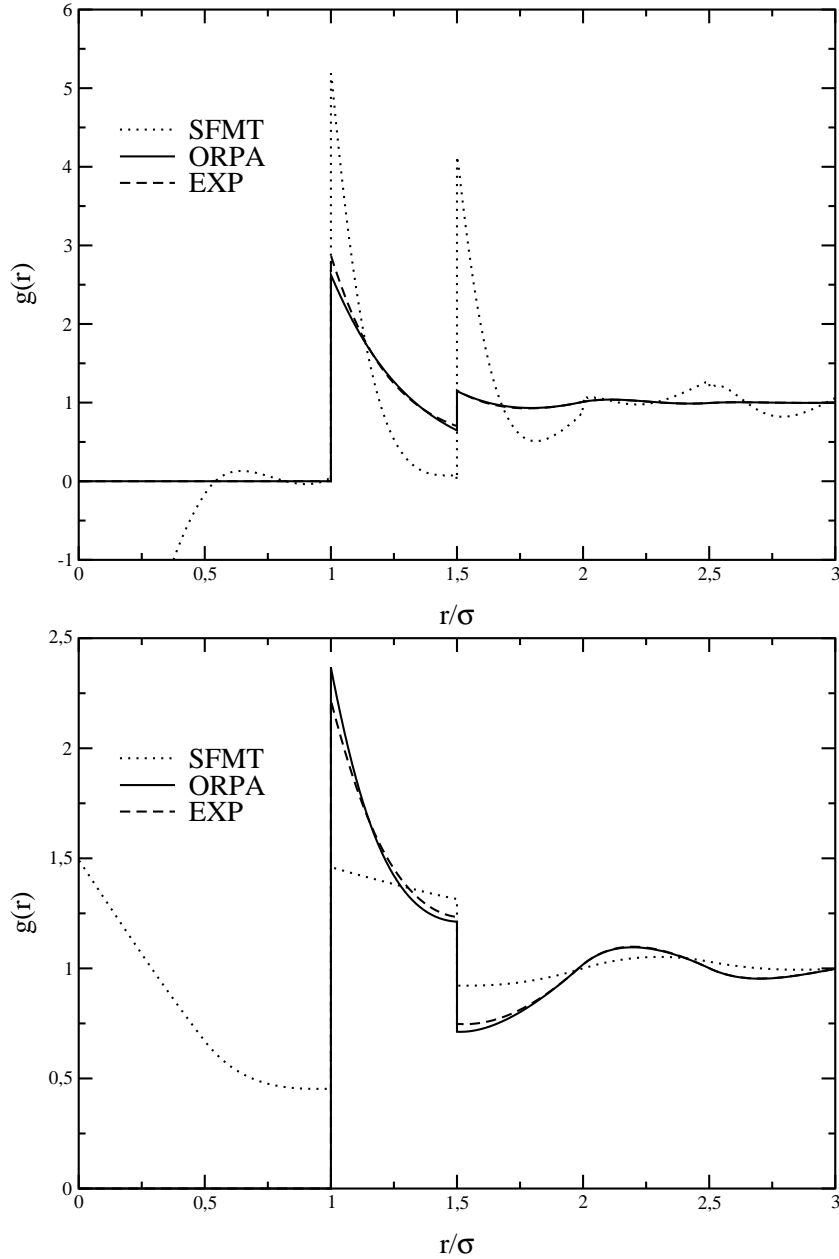
The pair distribution function $g(r)$ one gets in the framework of the SFMT for a given pair potential violates in general the core condition in the fluid phase, i.e. the pair distribution function is nonzero where the potential is infinity. To overcome this deficiency, Rosenfeld [16] proposed the so called test-particle limit (TPL); this approach was introduced by Henderson [17] for the statistical mechanics of fluids.

We start again from the Euler-Lagrange equation

$$\frac{\delta\Omega[\rho]}{\delta\rho(\vec{r})} = 0,$$

here the grand potential $\Omega[\rho]$ of a system subject to an external potential $V_{ext}(\vec{r})$ is minimized with respect to the one particle density $\rho(\vec{r})$. In the framework of the TPL

Figure 4.14: Pair distribution functions $g(r)$ for the square-well (lower graph) and the square-shoulder (upper graph) fluid with $\lambda = 1.5$ at $\eta = 0.3$, $T^* = 2$ for the analytical SFMT solution presented in this subsection, ORPA and EXP. The negative tail of the SFMT solution in the square-shoulder graph goes down to about -10 for $r = 0$.



the external potential $V_{ext}(\vec{r})$ is the pair potential $\phi(r)$ of the test particle situated at the origin and the density profile $\rho(\vec{r})$ induced by this particle is connected to the pair distribution function via

$$\rho(\vec{r}) = \rho g(\vec{r}).$$

The grand potential is then given as

$$\Omega[\{\rho\}] = A_{id}[\{\rho\}] + A_{ex}[\{\rho\}] + \int_{\mathbb{R}^3} d^3r \rho(\vec{r}) [\phi(\vec{r}) - \mu_0], \quad (4.113)$$

where $A_{id}[\{\rho\}]$ is given by equation (4.64) and μ_0 is the chemical potential of the bulk fluid (subscript $_0$) defined by equation (3.28) which can be split into

$$\mu_0 = \mu_{0,id} + \mu_{0,ex} = \mu_{0,ex} + \frac{1}{\beta} \ln \rho + C,$$

where the constant C contains the remaining system parameters. The functional derivative of equation (4.113) with respect to $\rho(r) = \rho(\vec{r})$ is equal to

$$0 = k_B T \ln [\rho(r) \sigma^3] + \frac{\delta A_{ex}[\{\rho\}]}{\delta \rho(r)} + [\phi(r) - \mu_0].$$

This relation connects the pair distribution function $g(r)$ with the one particle direct correlation function $c^{(1)}(r)$ defined as [see equation (4.66)]

$$c^{(1)}(r) = -\beta \mu_{ex}[r; \{\rho\}] = -\beta \frac{\delta A_{ex}[\{\rho\}]}{\delta \rho(r)}$$

via

$$g(r) = \exp [\beta \mu_{0,ex} + c^{(1)}(r) - \beta \phi(r)].$$

In the framework of the FMT the one particle direct correlation function $c^{(1)}(r)$ can be expressed using the weight functions and weighted densities:

$$c^{(1)}(r') = - \int_{\mathbb{R}^3} d^3r \frac{\partial \Phi[\{n\}]}{\partial \rho} \Big|_{\rho=\rho(\vec{r})} = - \int_{\mathbb{R}^3} d^3r \sum_{\alpha} \frac{\partial \Phi[\{n\}]}{\partial n_{\alpha}(r)} w_{\alpha}(|\vec{r}' - \vec{r}'|). \quad (4.114)$$

In this equation the index α also incorporates the vector weight functions. To calculate $c_1(r)$, the derivative of Φ with respect to the n_{α} have to be calculated. These are given by:

$$\begin{aligned} \frac{\partial \Phi}{\partial n_0} &= -\ln(1 - n_3) \\ \frac{\partial \Phi}{\partial n_1} &= \frac{n_2}{1 - n_3} \\ \frac{\partial \Phi}{\partial n_2} &= \frac{n_1}{1 - n_3} + \frac{1}{8\pi} \frac{n_2^2 - \vec{n}_{v2}^2}{(1 - n_3)^2} \\ \frac{\partial \Phi}{\partial n_3} &= \frac{n_0}{1 - n_3} + \frac{n_1 n_2 - \vec{n}_{v1} \vec{n}_{v2}}{(1 - n_3)^2} + \frac{1}{12\pi} \left(\frac{n_2}{1 - n_3} \right)^3 - \frac{1}{4\pi} \frac{n_2 \vec{n}_{v2}^2}{(1 - n_3)^3} \\ \frac{\partial \Phi}{\partial \vec{n}_{v1}} &= -\frac{\vec{n}_{v2}}{1 - n_3} \\ \frac{\partial \Phi}{\partial \vec{n}_{v2}} &= -\frac{\vec{n}_{v1}}{1 - n_3} - \frac{1}{4\pi} \frac{n_2 \vec{n}_{v2}}{(1 - n_3)^2}. \end{aligned}$$

The weighted densities $n_\alpha(r)$ are calculated using the convolutions defined by equations (4.89) and (4.90). Since $\rho(r)$ is nonzero for $r \rightarrow \infty$, in the TPL one has to rewrite this equation for the scalar weight functions:

$$n_i(r) = \int_{\mathbb{R}^3} d^3r' \rho(r') w_i(|\vec{r} - \vec{r}'|) = \rho \int_{\mathbb{R}^3} d^3r' h(r') w_i(|\vec{r} - \vec{r}'|) + \rho \xi_i,$$

where ξ_i is defined in equation (4.100). This reformulation is not necessary for the vector weight functions, because $\tilde{w}_\alpha(k=0) = 0$.

The bulk fluid excess chemical potential $\mu_{0,ex}$ is calculated via

$$\mu_{0,ex} = -\frac{1}{\beta} c^{(1)}(r) \Big|_{\rho(r)=\rho_0} = -\frac{\rho}{\beta} \sum_{i=0}^3 \frac{\partial \Phi}{\partial n_i} \xi_i,$$

where in the partial derivatives of Φ one sets $n_i = \xi_i$ and $\vec{n}_\alpha = 0$.

4.4 Simple perturbation theory for A in the solid state

In this subsection we will present a simple perturbation theory for the evaluation of the Helmholtz free energy A in the solid state (for the same theory in the fluid state see subsection 4.1.4.4). As stated there, we start from

$$A[\rho] = A_{ref}[\rho] + A_p[\rho],$$

where $A[\rho]$ is the free energy of the system with the potential $\phi(r) = \phi_0(r) + \phi_1(r)$, $A_{ref}[\rho]$ is the free energy of the reference system with potential $\phi_0(r)$ and $A_p[\rho]$ is the contribution to the free energy coming from the perturbation potential $\phi_1(r)$. The explicit form of $A_p[\rho]$ [up to first order of the perturbation potential $\phi_1(r)$] is

$$A_p[\rho] = \frac{1}{2} \int_{\mathbb{R}^3} d^3r \int_{\mathbb{R}^3} d^3r' \rho(\vec{r}) \rho(\vec{r}') g_0(\vec{r}, \vec{r}') \phi_1(|\vec{r} - \vec{r}'|), \quad (4.115)$$

where $g_0(\vec{r}, \vec{r}')$ is the pair distribution function of the reference system. For the nonuniform solid phase, equation (4.115) can be treated in two ways. One can, similar to the uniform phase, use a suitable approximation for the pair distribution function $g_0(\vec{r}, \vec{r}')$ in the solid. The second approach is to use equation (4.115) as a simple mean-field approximation by setting $g_0(\vec{r}, \vec{r}')$ equal to one.

For the first case, $\rho(\vec{r}) \rho(\vec{r}') g_0(\vec{r}, \vec{r}')$ can be approximated using a parameterization for the pair distribution function of hard spheres in the solid [Rascon *et al.* [82, 83], equation (C.4)]. This leads to

$$A_p[\rho] \Big|_{\rho(\vec{r})=\rho_s} = \frac{N}{2} \rho_s \int_{\mathbb{R}^3} d^3r g_{0,hs}(r) \phi_1(r), \quad (4.116)$$

where ρ_s is the density of the solid. Although this equation looks formally the same as equation (4.26), its numerical treatment is much more difficult because $g_{0,hs}(r)$ consists of an infinite sum of Gaussians. Equation (4.116) can be solved using equation (C.4) with a slightly modified version of (C.3) (because the first peak of $g_{0,hs}(r)$ is parameterized with other parameters).

In the case of the mean field approximation, using a radially symmetric perturbation potential $\phi_1(r)$ and the parameterization (C.1) for the density $\rho(\vec{r})$ one gets

$$A_p[\rho] = \frac{N}{2} \int_{\mathbb{R}^3} d^3r \int_{\mathbb{R}^3} d^3r' \rho(\vec{r}) \rho(\vec{r}') \phi_1(|\vec{r} - \vec{r}'|). \quad (4.117)$$

Together with equation (C.3), this leads to

$$A_p[\rho] = \frac{N}{2} \sqrt{\frac{\alpha}{2\pi}} \int_0^\infty dr \phi_1(r) \left[2\alpha r^2 e^{-\frac{\alpha}{2}r^2} + \sum_{i=1}^\infty \frac{n_i}{R_i} r \left(e^{-\frac{\alpha}{2}(r-R_i)^2} - e^{-\frac{\alpha}{2}(r+R_i)^2} \right) \right],$$

where the parameters n_i and R_i are defined in appendix C.3.

4.5 Einstein model for the solid

The Einstein model [84] is based on the Gibbs-Bogoliubov (GB) inequality [6] which states that the Helmholtz free energy A of a system (with a Hamiltonian \mathcal{H}) is related to the Helmholtz free energy A_0 of the reference system (with a Hamiltonian \mathcal{H}_0) via

$$A \leq A_0 + \langle \mathcal{H} - \mathcal{H}_0 \rangle_0, \quad (4.118)$$

where the canonical average on the right-hand side is taken in the reference system. The model is useful only for soft interactions where a harmonic approximation for the solid is justified. The Einstein model was adopted for the GCM in [46].

Application of the GB inequality is useful if

- a sufficiently simple Hamiltonian \mathcal{H}_0 can be chosen, which physically corresponds to a situation close enough to the ‘real’ Hamiltonian, and where A_0 and the average $\langle \mathcal{H} - \mathcal{H}_0 \rangle_0$ can be calculated without too much effort and
- this Hamiltonian contains at least one variational parameter which can be chosen to minimize the right hand side of equation (4.118), obtaining in this way a lower upper bound for the free energy of the given system.

For a harmonic solid, the Einstein solid characterized by the Hamiltonian

$$\mathcal{H}_0 = \sum_{i=1}^N \left[\frac{\vec{p}_i^2}{2m} + \frac{k}{2} (\vec{r}_i - \vec{R}_i)^2 \right], \quad (4.119)$$

is a reasonable reference system. In this equation, \vec{p}_i is the canonical momentum of a particle of mass m positioned at \vec{r}_i , k is the ‘spring constant’ which plays the role of a

variational parameter and the set $\{\vec{R}_i\}$ forms a Bravais lattice. The Einstein model of the solid is based on the assumption that the crystal with N particles consists of N uncoupled three-dimensional isotropic oscillators, all having the same frequency (therefore, k is the same for every lattice site).

For the Hamiltonian \mathcal{H} we assume the following form

$$\mathcal{H} = \sum_{i=1}^N \frac{\vec{p}_i^2}{2m} + \frac{1}{2} \sum_{i \neq j}^N \phi(|\vec{r}_i - \vec{r}_j|) = \sum_{i=1}^N \frac{\vec{p}_i^2}{2m} + V(\{\vec{R}_i\}).$$

By introducing the two-particle density operator

$$\hat{\rho}^{(2)}(\vec{r}, \vec{r}'; \{\vec{R}_i\}) = \sum_{i \neq j} \delta(\vec{r} - \vec{R}_i) \delta(\vec{r}' - \vec{R}_j)$$

we can write

$$V(\{\vec{R}_i\}) = \frac{1}{2} \int_{\mathbb{R}^3} d^3r \int_{\mathbb{R}^3} d^3r' \phi(|\vec{r} - \vec{r}'|) \hat{\rho}^{(2)}(\vec{r}, \vec{r}'; \{\vec{R}_i\}).$$

By taking the ensemble average in the reference system we get

$$\langle V(\{\vec{R}_i\}) \rangle_0 = \frac{1}{2} \int_{\mathbb{R}^3} d^3r \int_{\mathbb{R}^3} d^3r' \phi(|\vec{r} - \vec{r}'|) \rho_0^{(2)}(\vec{r}, \vec{r}'; \{\vec{R}_i\}).$$

For the Einstein model of the solid, the one-particle density $\rho_0^{(1)}(\vec{r})$ is a sum of Gaussians; hence $\rho_0^{(2)}(\vec{r}, \vec{r}')$ is also a product of Gaussian sums:

$$\rho_0^{(2)}(\vec{r}, \vec{r}'; \{\vec{R}_i\}) = \rho(\vec{r}) \rho(\vec{r}')$$

where $\rho(\vec{r})$ is the parameterization of the one-particle density in the solid as described by (C.1) using the set of lattice vectors $\{\vec{R}_i\}$. Using equation (C.2) and by omitting the innermost ($i = 0$) shell we get for $\langle V(\{\vec{R}_i\}) \rangle_0 = \langle V(\alpha) \rangle_0$

$$\langle V(\alpha) \rangle_0 \frac{\beta}{N} = \frac{1}{2} \sqrt{\frac{\alpha}{2\pi}} \sum_{i=1}^{\infty} \frac{n_i}{R_i} \int_0^{\infty} dx x \beta \phi(x) \left(e^{-\frac{\alpha}{2}(x-R_i)^2} - e^{-\frac{\alpha}{2}(x+R_i)^2} \right). \quad (4.120)$$

The calculation of $\langle \mathcal{H} - \mathcal{H}_0 \rangle_0$ finally yields

$$\langle \mathcal{H} - \mathcal{H}_0 \rangle_0 \frac{N}{\beta} = \langle V(\alpha) \rangle_0 - \frac{3}{2}$$

The calculation of the Helmholtz free energy A_0 of the Einstein solid is straightforward and gives

$$A_0 = \frac{3N}{2\beta} \ln \left(\frac{\alpha \sigma^2}{\pi} \right) + 3 \frac{N}{\beta} \ln \left(\frac{\Lambda}{\sigma} \right)$$

where α is related to the parameter k of the Hamiltonian (4.119) by

$$\alpha = \frac{\beta k \sigma^2}{2}.$$

The final result for $A(\alpha)$ is

$$A(\alpha) \frac{\beta}{N} \leq \frac{3}{2} \left[\ln \left(\frac{\alpha}{\pi} \right) - 1 \right] + 3 \ln \left(\frac{\Lambda}{\sigma} \right) + \langle V(\alpha) \rangle_0.$$

The term $3 \ln(\Lambda/\sigma)$ is α -independent. The righthand side of this relation to be minimized with respect to α to yield a lowest upper bound for the Helmholtz free energy. Optimization is possible because of the two competing contributions to the free energy $A(\alpha)$. The term with $\ln \frac{\alpha}{\pi}$ favors $\alpha \rightarrow 0$. This can be seen quite easily: for this ‘ideal’ term the free energy is equal to $A_{id} = U_{id} - TS_{id}$ (where U_{id} is a constant), therefore the entropy is proportional to $-\ln(\frac{\alpha}{\pi})$. So the entropy will be maximized by decreasing α towards zero. In contrast to that, the ‘excess’ term $\langle V(\alpha) \rangle_0$ favors $\alpha \rightarrow \infty$, because by doing so the interaction between the particles will be minimized [as can be seen from equation (4.120)].

Chapter 5

Phase equilibria

In this chapter we will present the methods used in this thesis to obtain a phase diagram of a one-component or binary system. A phase coexistence between two phases at a fixed temperature T is taking place, if the two phases have the same pressure p and the same chemical potential μ (or, for binary systems, the two particle species have the same partial chemical potentials μ_i with $i = 1, 2$). There are numerous papers dealing with phase transitions of various systems; for an overview we refer to [18].

5.1 One Component systems

5.1.1 Binodals

To find a phase equilibrium (binodals) for a one component system one has to solve two coupled, non-linear equations:

$$p(\rho_1) = p(\rho_2) \quad (5.1)$$

$$\mu(\rho_1) = \mu(\rho_2), \quad (5.2)$$

where ρ_i (with $i = 1, 2$) are the coexistence densities. Using the Maxwell relations (3.22) and (3.28) one can rearrange these two equations to get the so called double-tangent construction. This procedure can be carried out using the Helmholtz free energy reduced to the number of particles, A^* , as a function of the inverse number density $\frac{1}{\rho}$. In this thesis, we have used the second method which uses the Helmholtz free energy reduced to the volume A^+ as a function of the number density ρ . Using this convention we get for the reduced pressure p^* and chemical potential μ^* :

$$p^*(\rho) = \rho \frac{dA^+(\rho)}{d\rho} - A^+(\rho)$$
$$\mu^*(\rho) = \frac{dA^+(\rho)}{d\rho}.$$

These two equations can be interpreted as a straight line with equation $y(x) = kx + d$ with $k = \mu^*(\rho)$ and $d = -p^*(\rho)$. A phase transition occurs if one can find a common

tangent which touches the isothermal A^+ curve in two points (hence a double tangent). To calculate the phase transitions for a given temperature T one has to do the following steps:

- Calculate the free energy curves of all possible phases [vapor/liquid phase, solid phases (sc, fcc, bcc)] to get $A_i(\rho)$ where $\rho \in [\rho_{i,start}, \rho_{i,end}]$ and $i = 1 \dots N$ (N is the number of phases).
- Draw all the curves using the chosen reduction (A^* vs. $\frac{1}{\rho}$ or A^+ vs. ρ). However, the second reduction has to be preferred because the ρ -range is limited to $[0, \rho_{max}]$.
- Find all the double tangents that can occur in this graph:

$$(\{\rho_{c1}, \rho_{c2}\}) = \sum_{i=1}^N \sum_{j=i}^N \text{dte}(A_i, A_j),$$

where the indices c_1 and c_2 denote the coexistence densities and dte stands for the double tangent construction. One has to be careful because it is possible to find more than one phase transition for a given pair of (A_i, A_j) .

- These phase transitions have to be sorted into *stable* and *metastable* ones. Metastable phase transitions are those that are covered by other (stable) phase transitions and hence will never occur. A procedure to distinguish between stable and metastable phase transitions is explained below.
 1. Mark all phase transitions as stable. Start with the first phase transition ($i = 1$) in the list (the list has not to be sorted with respect to the densities of the coexistence).
 2. Iterate over all phase transitions $j \neq i$ which are marked as stable. If $\rho_{j,c1}$ or $\rho_{j,c2} \in [\rho_{i,c1}, \rho_{i,c2}]$ then
 - (a) If $A_i(\rho_{j,c1/c2}) < A_j(\rho_{j,c1/c2})$, mark the phase transition j as metastable, else mark phase transition i as metastable.
 - (b) If i is marked as metastable, exit the iteration.
 3. Search the next stable phase transition i . Go back to step (2)

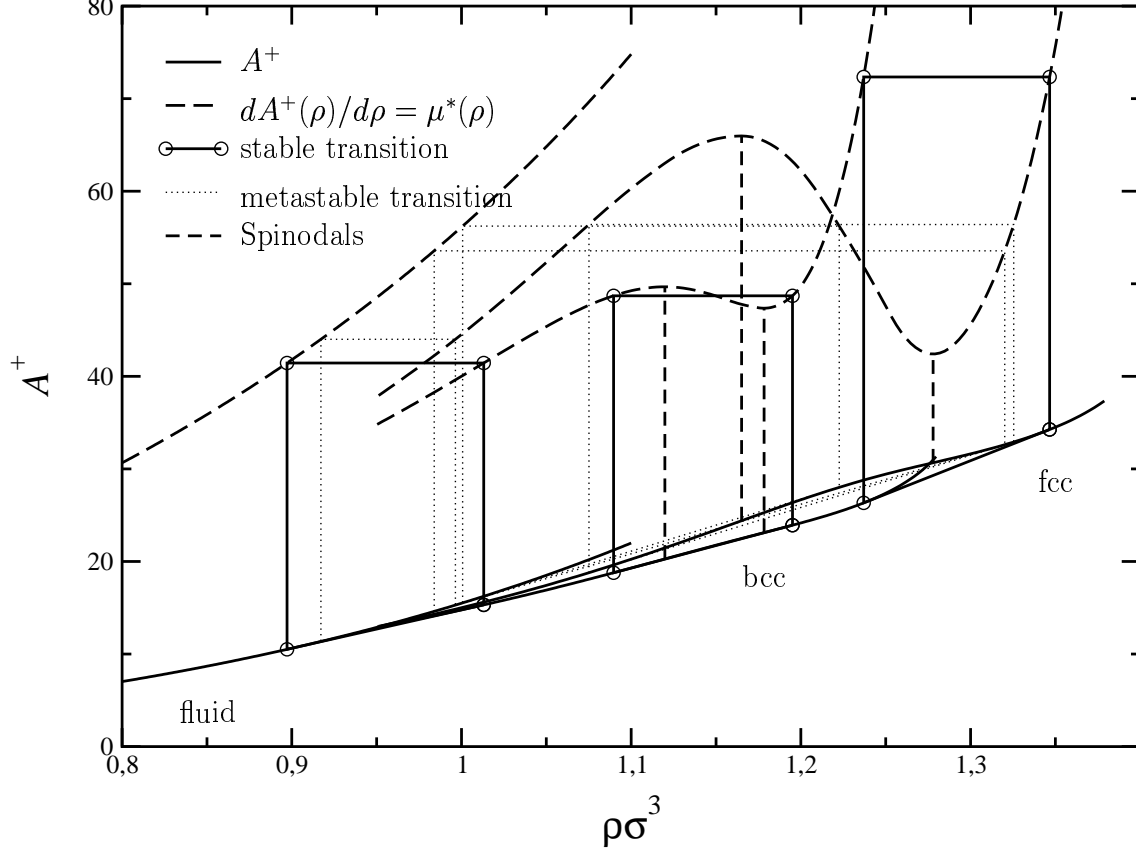
In figure 5.1 we give an example for the complexity of possible phase transitions for a one component system.

5.1.2 Spinodals

Besides the binodals one can also calculate the so called spinodals. The spinodal line consists of all points where the isothermal compressibility diverges and includes thus the critical point(s). Using equation (3.31) the condition for a spinodal reads

$$\frac{\chi_{T,id}}{\chi_T} = 0 = \frac{1}{1 + \rho \tilde{h}(k=0)} = 1 + \rho \tilde{c}(k=0).$$

Figure 5.1: Stable vs metastable phase points. Square-shoulder potential with $\lambda = 1.12$, $T^* = 0.3$. The Helmholtz free energy curves are calculated for the fluid phase, an fcc and a bcc crystal. The according $\mu^*(\rho)$ are, at $\rho = 1$ from top to bottom: fluid, fcc and bcc.



Using equation (3.34) and

$$\frac{d^2 A_{id}^+(\rho)}{d\rho^2} = \frac{1}{\rho}$$

this can be rewritten to

$$\begin{aligned} \tilde{c}(k=0; \rho) &= \frac{1}{\rho} = -\frac{d^2 A_{ex}^+(\rho)}{d\rho^2} = -\frac{d^2 [A^+(\rho) - A_{id}^+(\rho)]}{d\rho^2} \\ \frac{1}{\rho} &= -\frac{d^2 A^+(\rho)}{d\rho^2} + \frac{1}{\rho} \\ 0 &= -\frac{d^2 A^+(\rho)}{d\rho^2}. \end{aligned}$$

So the spinodal points at a given temperature T are the inflection points of the Helmholtz free energy reduced to the volume.

5.2 Binary systems

In this thesis we constrain ourselves to symmetric binary systems (see section 2.1.2). Because we have not examined the solid state for binary systems, according to [85] our phase diagrams consists of up to four different phases:

Mixed vapor/Mixed liquid: Both species have the same concentration (due to the symmetry of the system); these two phases are essentially the same (the only difference being the density where they occur) and can only be distinguished if a phase transition between them happens (which terminates in a critical point).

Demixed liquid: In the demixed liquid there is coexistence between a species-one rich component (with $c_1 > 0.5$) and, due to the symmetry of the system, a species-two rich component (with $c_2 > 0.5$).

For a general binary system we have to solve the following equations for each temperature (so we have omitted the temperature as a parameter) to obtain the coexistence densities and coexistence concentrations:

$$\mu_1(\rho^I, c_1^I) = \mu_1(\rho^{II}, c_1^{II}) \quad (5.3)$$

$$\mu_2(\rho^I, c_1^I) = \mu_2(\rho^{II}, c_1^{II}) \quad (5.4)$$

$$p(\rho^I, c_1^I) = p(\rho^{II}, c_1^{II}), \quad (5.5)$$

where $i = I, II$ denotes the two phases, the ρ^i are the coexistence densities and the c_1^i are the coexistence concentrations. Due to the symmetry of the system, the following relations are always fulfilled:

$$\mu_1(\rho, c_1) = \mu_2(\rho, 1 - c_1) \quad ; \quad p(\rho, c_1) = p(\rho, 1 - c_1), \quad (5.6)$$

for all ρ and c_1 . By combining the symmetry relation for μ_1 and μ_2 with the coexistence conditions (5.3) and (5.4), one gets the following equation:

$$\mu_2(\rho^I, c_1^I) = \mu_2(\rho^{II}, c_1^{II}) = \mu_1(\rho^{II}, 1 - c_1^{II}) = \mu_1(\rho^I, 1 - c_1^I).$$

So a phase transition can only occur at the intersection of the two surfaces $\mu_1(\rho, c_1)$ and $\mu_2(\rho, c_2)$ as show in figure 5.2. This intersection is projected onto the (ρ, c_1) -plane, where it becomes one (or more) curves $c_1^i(\rho)$, with $i = 0, \dots, N$. By using these functions $c_1^i(\rho)$ together with the coexistence equations (5.3), (5.4) and (5.5) one gets

$$\mu_1(\rho^I, c_1^i(\rho^I)) = \mu_1^i(\rho^I) = \mu_1^j(\rho^{II}) = \mu_1(\rho^{II}, c_1^j(\rho^{II})) \quad (5.7)$$

$$p(\rho^I, c_1^i(\rho^I)) = p^i(\rho^I) = p^j(\rho^{II}) = p(\rho^{II}, c_1^j(\rho^{II})). \quad (5.8)$$

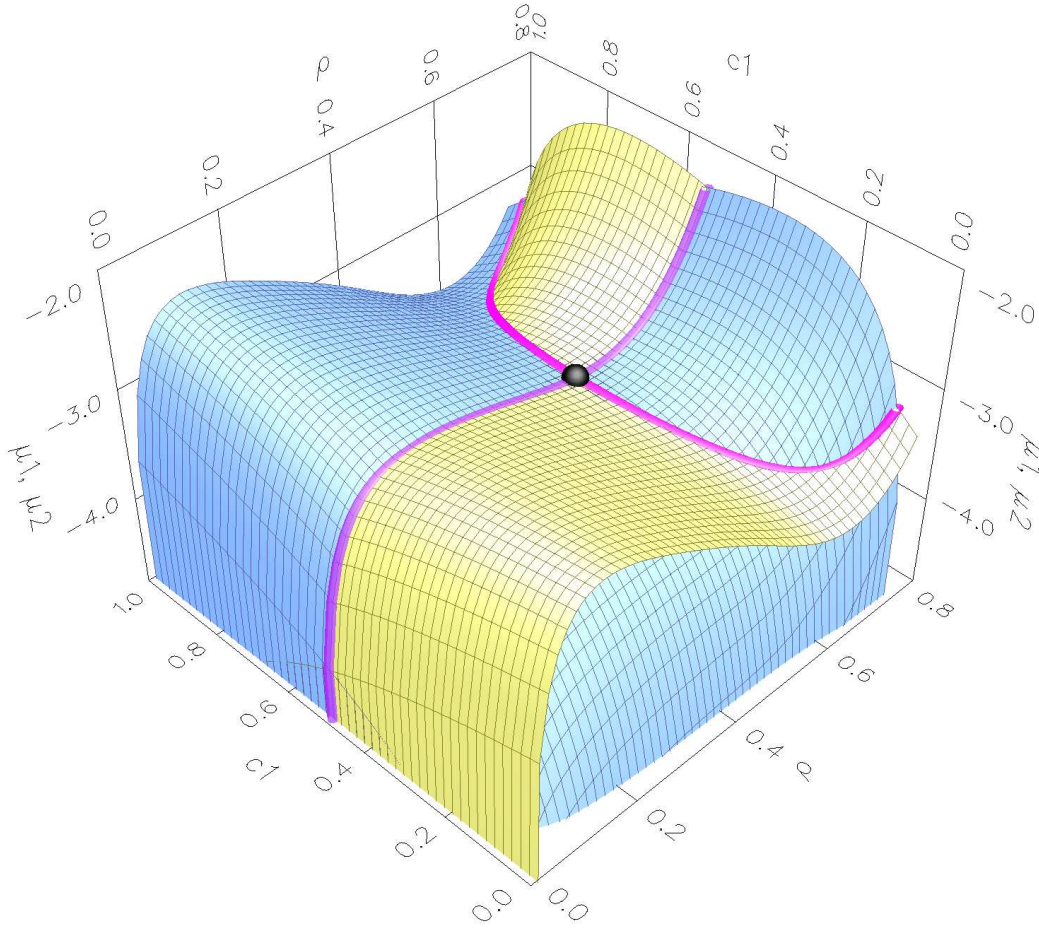
In our case there are only two curves, where the first one corresponds to $c_1^0(\rho) = 0.5$. Equations (5.7) and (5.8) can be easily solved, leading to phase transitions specified by

$$[\rho^I, c_1^i(\rho^I); \rho^{II}, c_1^j(\rho^{II})].$$

These phase transitions can occur between any of the three phases described above:

- $i = j = 0$; $c_1^{i,I}(\rho^I) = c_1^{j,II}(\rho^{II}) = 0.5$: mixed vapor-mixed liquid,

Figure 5.2: μ_1, μ_2 as functions of c_1 and ρ for a symmetric binary tHSY system calculated using the ORPA, the reference system are HS in the PY approximation. System parameters (as defined in subsection 2.2.3.1) are as follows: $\sigma_i = 1, \kappa_{ij} = 2.5, \lambda_{ij} = 2.5, T^* = 0.65$. Due to the symmetry of the system, the three interparticle potentials are related via $\phi_{11}(r) = \phi_{22}(r), \phi_{12}(r) = \phi_{21}(r) = \varepsilon_r \phi_{11}(r)$ with $\varepsilon_r = 0.7$ (see also figure 6.92 in section 6.8). The consolute point is denoted by the black sphere.

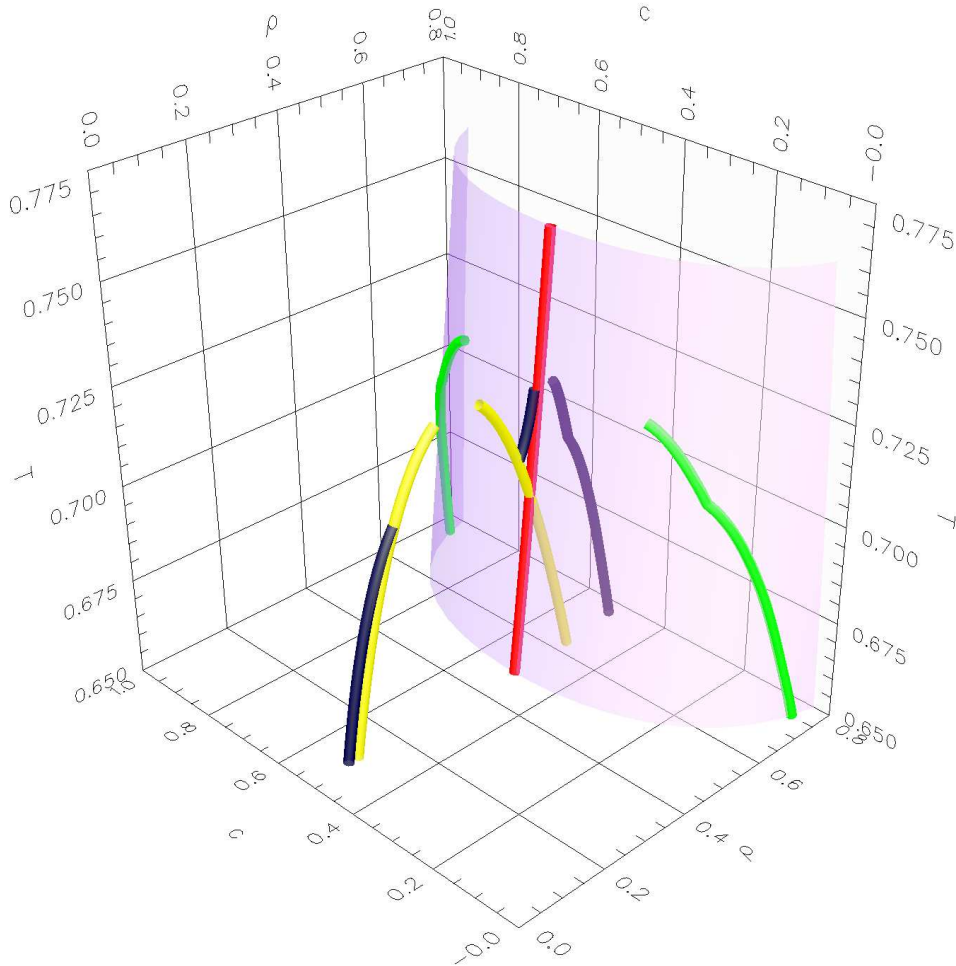


- $i = 0, j = 1; c_1^{iI}(\rho^I), \rho^I < \rho_c, c_1^{jII}(\rho^{II}) \neq 0.5$: mixed vapor-demixed liquid,
- $i = 0, j = 1; c_1^{iI}(\rho^I), \rho^I > \rho_c, c_1^{jII}(\rho^{II}) \neq 0.5$: mixed liquid-demixed liquid,

where ρ_c is the density of the mixed vapor-mixed liquid critical point.

In figure 5.3, the curved surface consists of all curves $c_1^1(\rho)$ (demixing plane). The nearly vertical line on this plane is the λ line. In the $c_1 = 0.5$ plane one can see the mixed vapor-mixed liquid and mixed vapor/mixed liquid-demixed liquid phase transition. The curves on the demixing plane are the concentrations $c_1^{1II}(\rho^{II})$ for the demixed liquid.

Figure 5.3: Phase diagram of a symmetric binary tHSY system calculated using the ORPA, the reference system are HS in the PY approximation. For the system parameters see figure 5.2.



5.3 Entropy and freezing

Beside the standard double-tangent mechanism to construct the phase equilibria as described above, we also adopted an approach originally proposed in [86] to locate the onset of freezing by monitoring the behavior of the multiparticle residual entropy, defined as

$$\Delta s \equiv s_{ex} - s_2.$$

In this equation s_{ex} is the excess entropy per particle of the system in units of the Boltzmann constant k_B and s_2 is defined as

$$s_2 = -\frac{\rho}{2} \int_{\mathbb{R}^3} d^3r \{g(r) [\ln g(r) - 1] + 1\}.$$

s_{ex} is being calculated using

$$A = U - TS \quad ; \quad A_{ex} = U_{ex} - Ts_{ex}Nk_B = U_{ex} - s_{ex} \frac{N}{\beta},$$

using reduced units for A_{ex} and U_{ex} we get

$$s_{ex} = \frac{\beta}{N} [U_{ex} - A_{ex}] = \frac{3}{2} U_{ex}^* - A_{ex}^*.$$

According to previous results reported in the literature [86, 87], it turns out that the vanishing of Δs acts as a quite sensitive indicator of the freezing transition in several one-component fluids.

Chapter 6

Results

6.1 Gaussian core model

In this section we will present the results for the Gaussian core model (GCM) as presented in subsection 2.2.5. The GCM is of great importance as an excellent approximation of the interaction potential acting between the centers of mass of two polymer chains in a solvent. The properties of such a system were first analyzed by Stillinger *et al.* in the late seventies [33, 34, 35, 37, 37]. Simulations on the fluid state structure of this system have been recently performed by Watzlawek *et al.* [46, 88]. For a review of the formal properties of the GCM we refer to [18].

6.1.1 Structure

In this section we will present the structure factor $S(k)$ and pair distribution function $g(r)$ for the GCM for various densities ρ calculated via integral equations (see section 4.2) using the RY, HNC and ZSEP closure. These results will be compared with Monte Carlo (MC) simulations performed by Martin Watzlawek.

We focus our attention on temperature $T^* = 0.01$ (see subsection 2.1.1) for two reasons: on the one hand, according to the approximate phase diagram [89], at $T^* = 0.01$ the system remains fluid at all densities and therefore we can study the development of the correlation functions with density for an unlimited range of the latter, without entering a region where the fluid is metastable. On the other hand, this temperature is low enough so that significant structure is expected for the correlation functions of the fluid and hence the integral equation theories can be given a strong test. We present the results so obtained in figures 6.1, 6.2 and 6.3 and discuss them below.

We begin with the RY closure. When the packing fraction η is not large enough, typically $\eta \leq 0.50$ at this temperature, the RY closure gives results which are in very good agreement with simulations, as can be seen in figures 6.1 and 6.2. However, above $\eta \approx 0.50$, the $g(r)$ from simulations starts *penetrating* towards $r = 0$, which means physically that the probability of finding two particles ‘sitting on top of each other’ is finite and there is no ‘correlation hole’ in $g(r)$. This is to be expected for a system with a bounded interaction. However, as can be seen from figure 6.3(a), the RY closure fails to capture precisely the penetration phenomenon, yielding $g(r)$ s that are *too low* at small separation and making

the erroneous prediction that a correlation hole exists.

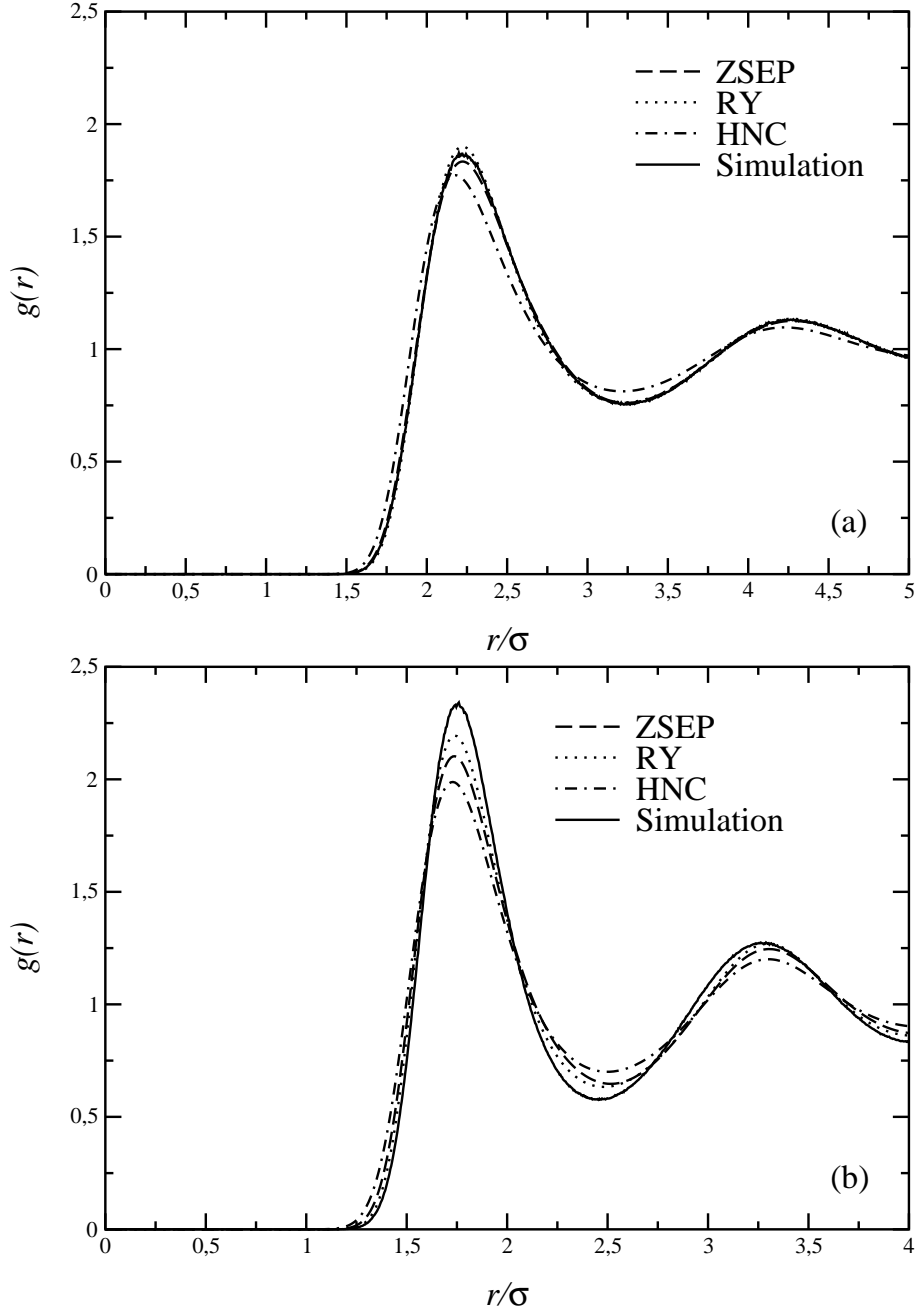
The reason for the behavior can be traced back in the construction of the RY closure, equations (4.44) and (4.45), where it can be seen that the RY closure always looks like the PY closure at small separations. The latter is however inaccurate for a long-range interaction lacking a hard core. We attempted to modify the RY closure by employing mixing functions yielding a HNC-like small- r behavior and a PY-like large- r behavior. However, this did not yield self-consistency parameters for the whole range of densities. Despite its inability to correctly describe the high-density penetration of $g(r)$, the standard RY closure yields nevertheless a self-consistency parameter α for all densities considered here. In addition, this parameter grows with density, thus pointing to a tendency of RY closure to reduce to the HNC closure at high packings.

In view of the failure of the RY closure, we are led to consider the ZSEP closure which has *precisely* the property that in its implementation the value of $g(r)$ at zero separation plays an important role and is determined self-consistently. In fact, the resounding success of the ZSEP closure in describing the $g(r)$ of the penetrable spheres model (PSM) (also a bounded interaction) has been mainly attributed to this property [67]. As can be seen from figures 6.1 and 6.2(a), the ZSEP closure performs only slightly less well than the RY closure up to a packing fraction $\eta \approx 0.25$. The self-consistency parameters α , β and γ of the ZSEP closure are displayed in figure 6.4. The parameter α which appears as an overall factor in the parameterization of the bridge function [see equation (4.46)] decreases with density and close to $\eta = 0.25$ it is small enough and the ZSEP closure practically reduces to the HNC closure.

However, at packing fractions $\eta > 0.25$, a *second branch* of solutions appears, which is denoted by the dashed lines in figure 6.4. This branch is disconnected from the first and hence it causes the $g(r)$ to behave discontinuously at this packing fraction, a result which is clearly unphysical. This second branch produces $g(r)$ s that show *too much penetration* and too little structure, when compared with simulation results. The reason for this unphysical behavior can be traced to the fact that this second branch corresponds to bridge functions which are *positive* at small separations r . Indeed, from equation (4.46), and taking into account that $\gamma(r) = h(r) - c(r) \gg 1$ at small separation, we can see that $B_{ZSEP}(r)$ has the sign of the product $\alpha(\beta - \gamma)/\gamma$. For the first, physical branch (solid lines in figure 6.4) this combination is *negative* because $\beta < \gamma$. For the second, unphysical branch, this combination is positive because $\beta > \gamma$ there. A positive bridge function acts then as an additional ‘attractive potential’ in equation (4.39) and causes the overpenetration of $g(r)$ mentioned above.

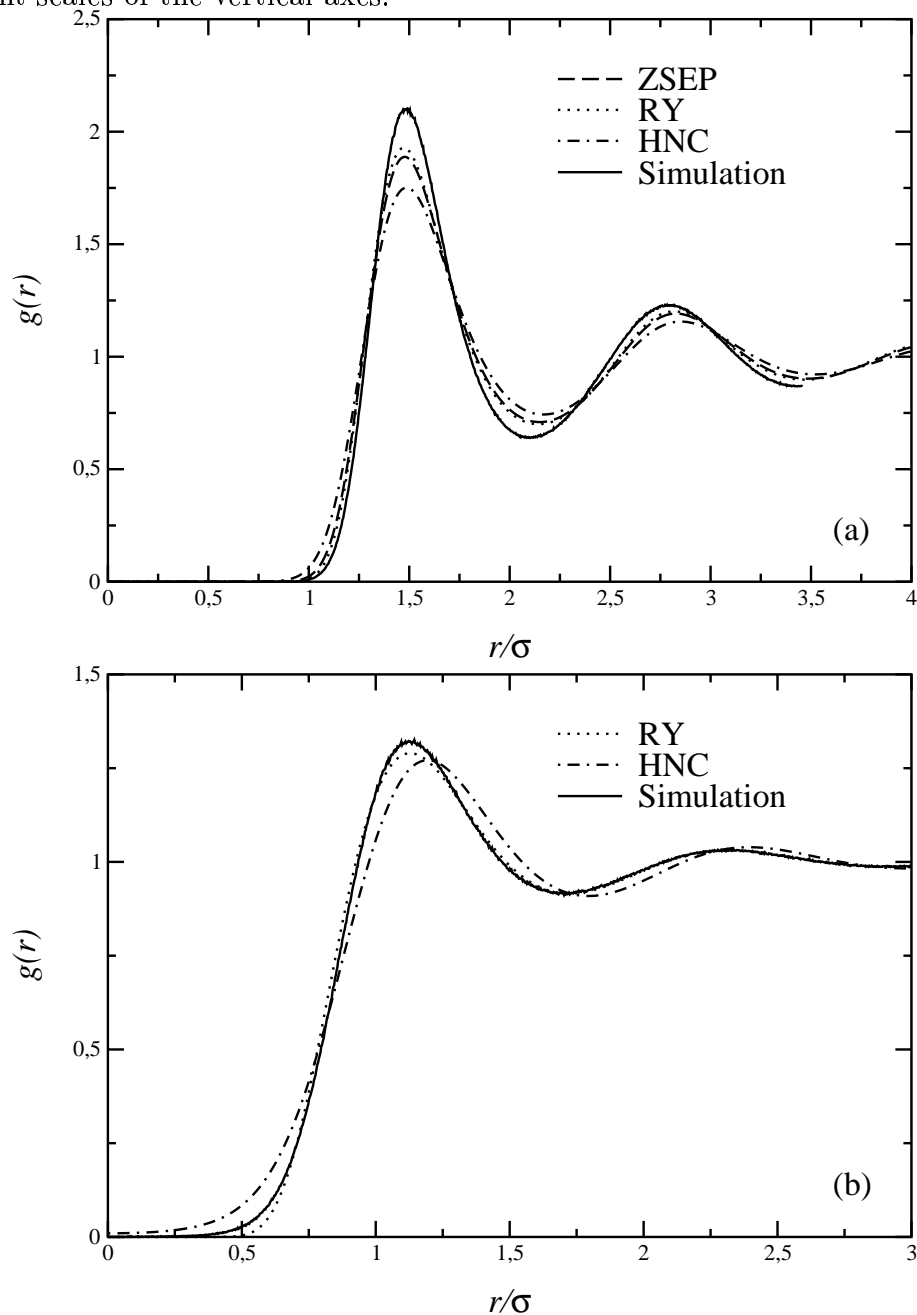
The appearance of a branch of the solution of the ZSEP closure for which the bridge function is positive is a sign of internal inconsistency of the closure and in this sense the ZSEP closure signals its own limits of applicability. Indeed, the bridge function of any system has been shown to be a quasi-universal function, which can always be mapped onto the bridge function of a suitably defined hard-sphere system having a hard-sphere diameter that depends on the characteristics of the interaction and the thermodynamic point under consideration [90]. The bridge function of the HS system is, however, practically exactly known and it is essentially a negative function for all r . Hence, a positive bridge function is physically unacceptable and the second branch of solutions of the ZSEP closure has to be discarded. The results from this second branch come again into very good agreement

Figure 6.1: Comparison of the radial distribution function $g(r)$ between the simulation results and those obtained from the various closures, at $T = 0.01$ and at small values of the packing fraction. (a) $\eta = 0.05$; (b) $\eta = 0.12$.



with simulation at packing fractions above $\eta \approx 1.00$ because, as seen in figure 6.4, the parameter α is already very small there and the bridge function has a negligible contribution to $g(r)$; even the unphysical branch reduces to the HNC approximation at high densities. However, there is no way to bridge the physical solutions at packings $\eta \leq 0.25$

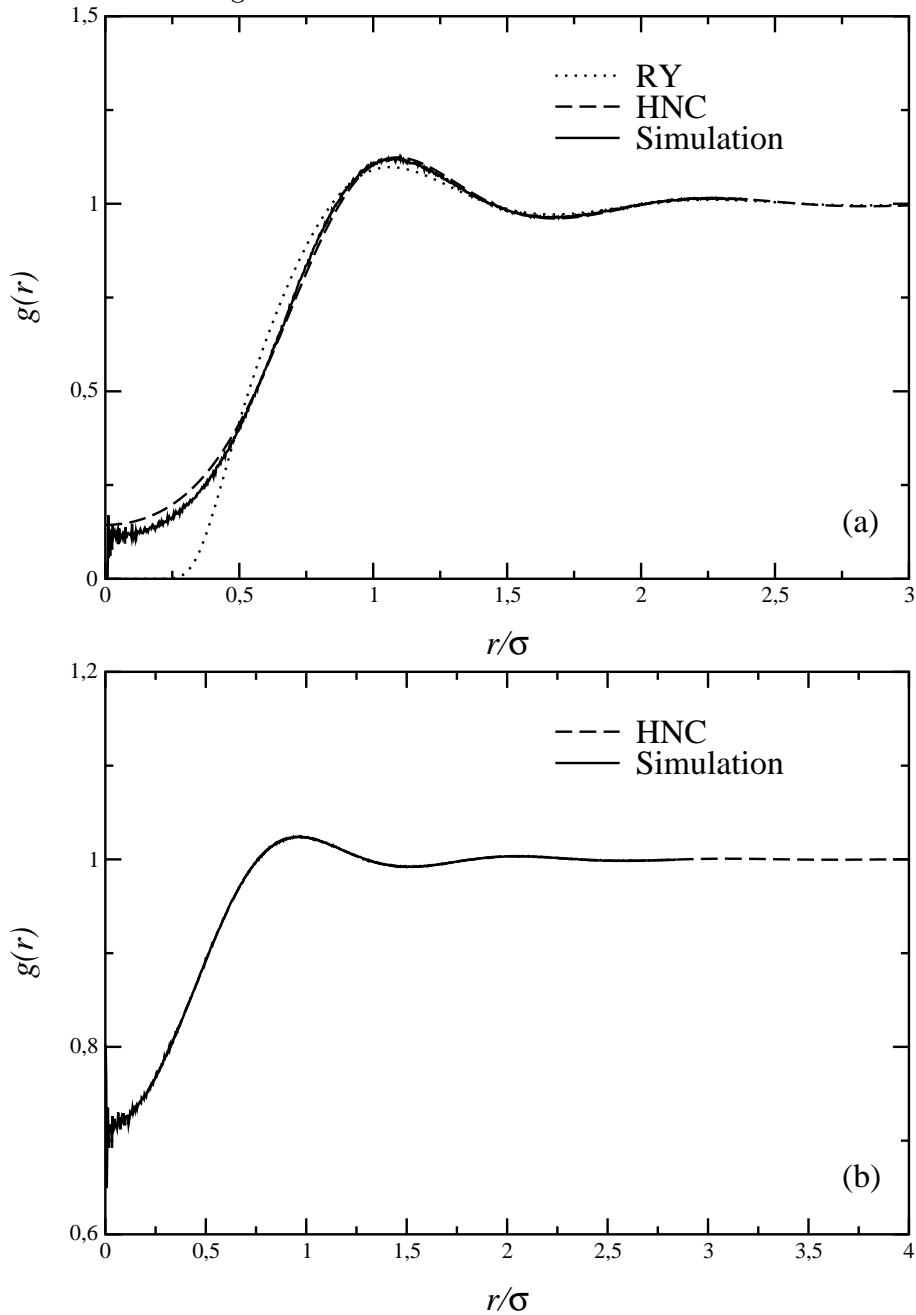
Figure 6.2: As figure 6.1, but for intermediate packings. (a) $\eta = 0.20$; (b) $\eta = 0.50$. Note the different scales of the vertical axes.



with the HNC-like solutions *within* the ZSEP closure, that is without having to compare with independently produced simulation results.

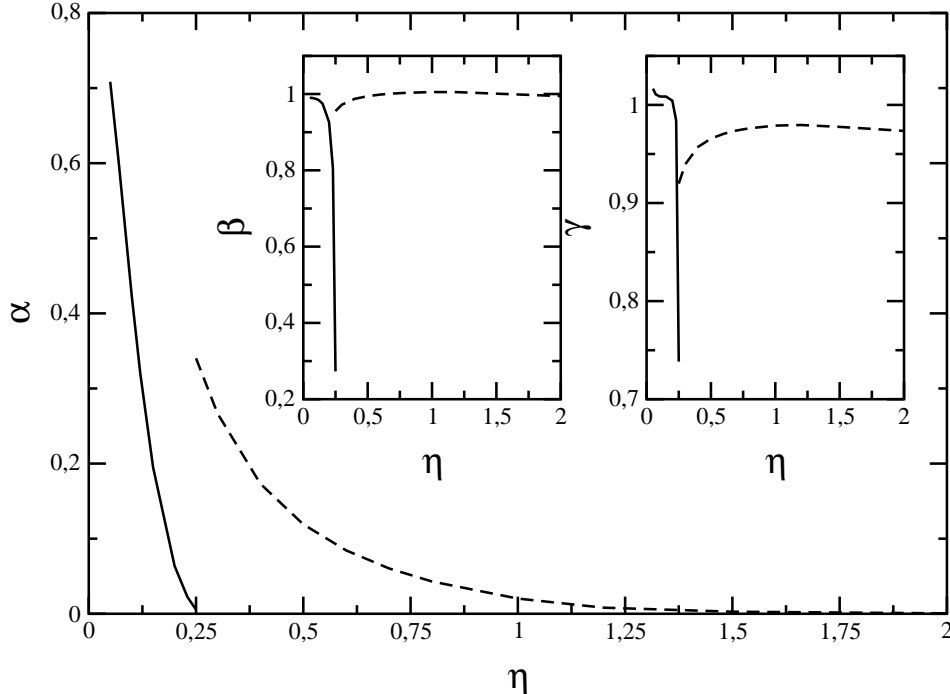
We comment next on the quality of the HNC closure. As can be seen from figures 6.1-6.3, the HNC closure underestimates the structure at small-to-intermediate packings but yields otherwise reasonable results. It does not suffer from any of the problems of the

Figure 6.3: As figure 6.1, but for high packings. (a) $\eta = 1.00$; (b) $\eta = 6.00$, where the simulation result is indistinguishable from the HNC result.



more sophisticated closures and, in fact, it seems to be the best at high densities. In order to further explore this property (which is supported by the fact that the other two closures tend to the HNC at this limit), we also solved this closure at *extremely high* packing fractions. Here, the highest packing at which we simulated was $\eta = 6.00$, due to time constraints. In view of the fact that the HNC closure gives results which coincide

Figure 6.4: The self-consistency parameters of the ZSEP closure applied to the GCM at reduced temperature $T = 0.01$ as functions of the packing fraction η . The solid lines denote the physical branch and the dashed lines the unphysical branch.

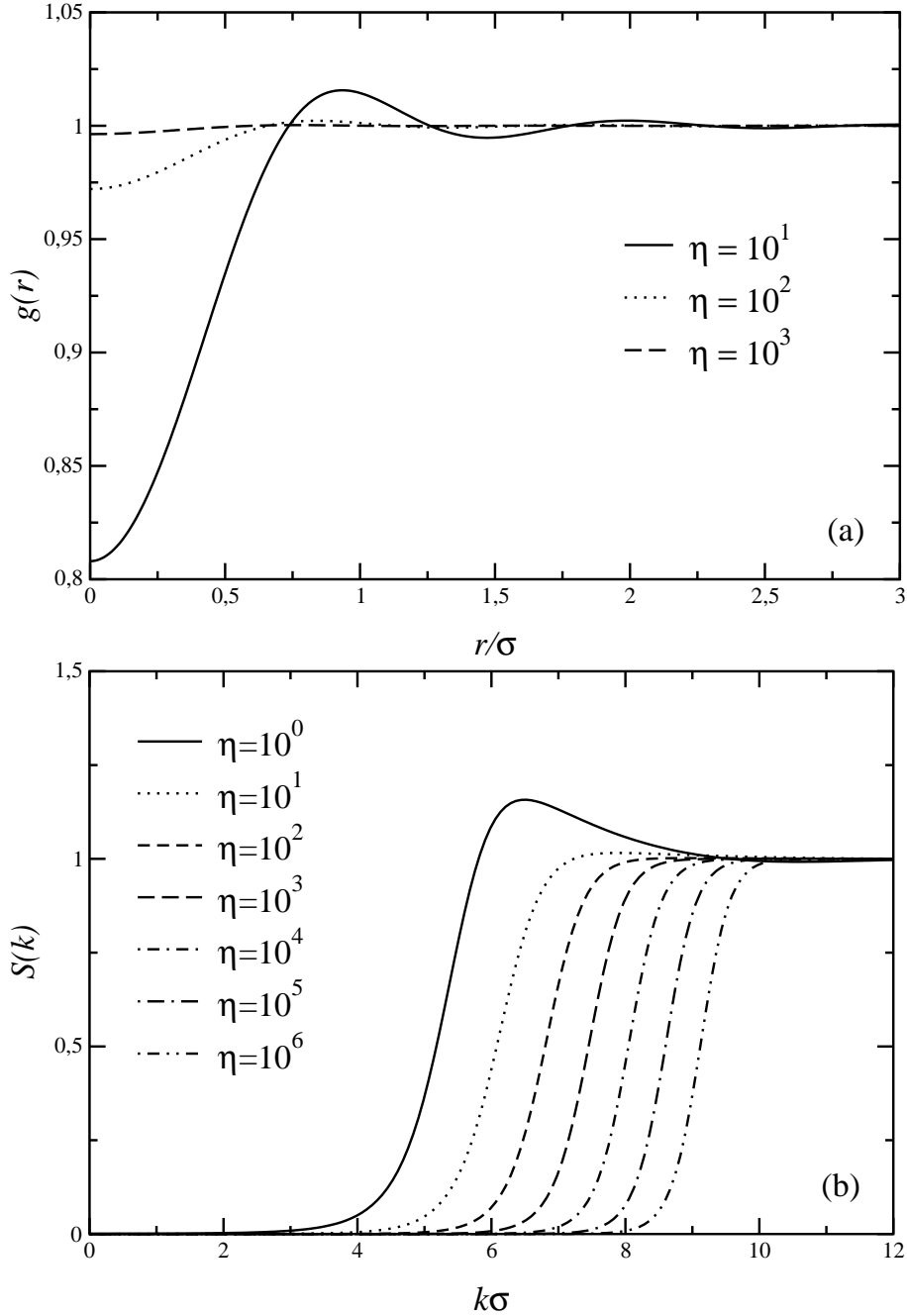


with those from Monte Carlo simulation at $\eta = 6.00$ [see figure 6.3(b)], we gain confidence at this closure and apply it for arbitrarily high densities, in order to obtain information on the structure of the very dense fluid. In figure 6.5(a), we show results for $g(r)$, where it can be seen that at very high packings $g(r)$ tends to unity and hence $h(r) = g(r) - 1$ tends to zero. However, this does not mean that the structure factor $S(k)$ tends to unity as well, as a naive guess based on the definition $S(k) = 1 + \rho \tilde{h}(k)$ would imply. The quantity $\tilde{h}(k)$ tends to zero, but at the same time the prefactor ρ diverges, thus giving rise to a non-trivial $S(k)$.

Results for the corresponding structure factor $S(k)$ are shown in figure 6.5(b). It can be seen that, for high densities, the peak of $S(k)$ disappears and the latter looks like a ‘smoothed step function’ with values ranging from zero to one. The value of k at which the crossover occurs does not scale as a power law of the density but rather shifts to the right almost a constant every time the packing fraction is increased by an order of magnitude. This dependence is described in section 6.2.

The liquid-state correlation functions of the GCM display an anomalous behavior in comparison with that of ‘normal’ liquids, interacting by means of hard, unbounded interactions. For the latter, the structure grows monotonically with increasing density and eventually the system freezes. Here, the structure grows monotonically up to a packing fraction $\eta \simeq 0.12$ at $T = 0.01$ and for higher densities it becomes weaker again. To demonstrate this phenomenon, we show in figure 6.6 the structure factors obtained from

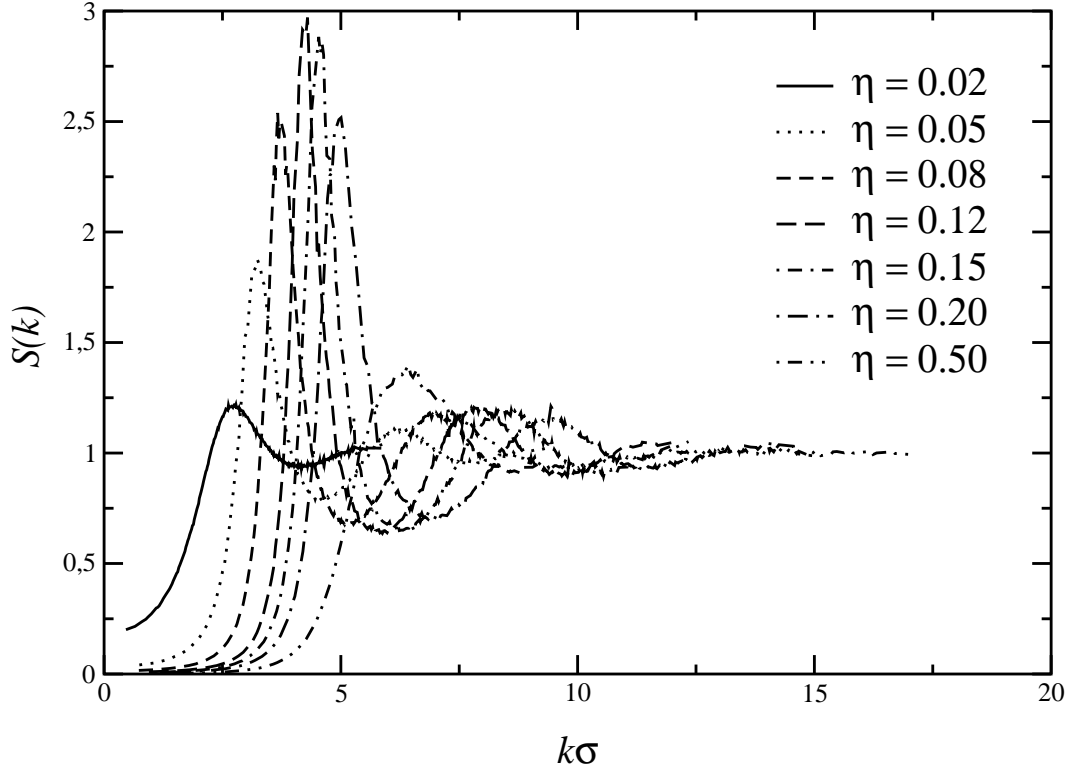
Figure 6.5: (a) The radial distribution function $g(r)$ and (b) the structure factor $S(k)$ as obtained by the HNC closure for extremely high values of the packing fraction η .



the MC simulations for a wide range of densities, where it can be seen that the height of the peak of $S(k)$ attains its maximum value at $\eta \simeq 0.12$.

This behavior of $S(k)$ is closely related to re-entrant melting [91]. Indeed, the height of the maximum of $S(k)$ is a diagnostic tool for the freezing transition. According to the Hansen-Verlet criterion [92, 93], a liquid crystallizes when $S(k)$ at its highest peak has the

Figure 6.6: The structure factor $S(k)$ of the GCM at $T = 0.01$ for different packing fractions, as obtained by Monte Carlo simulations



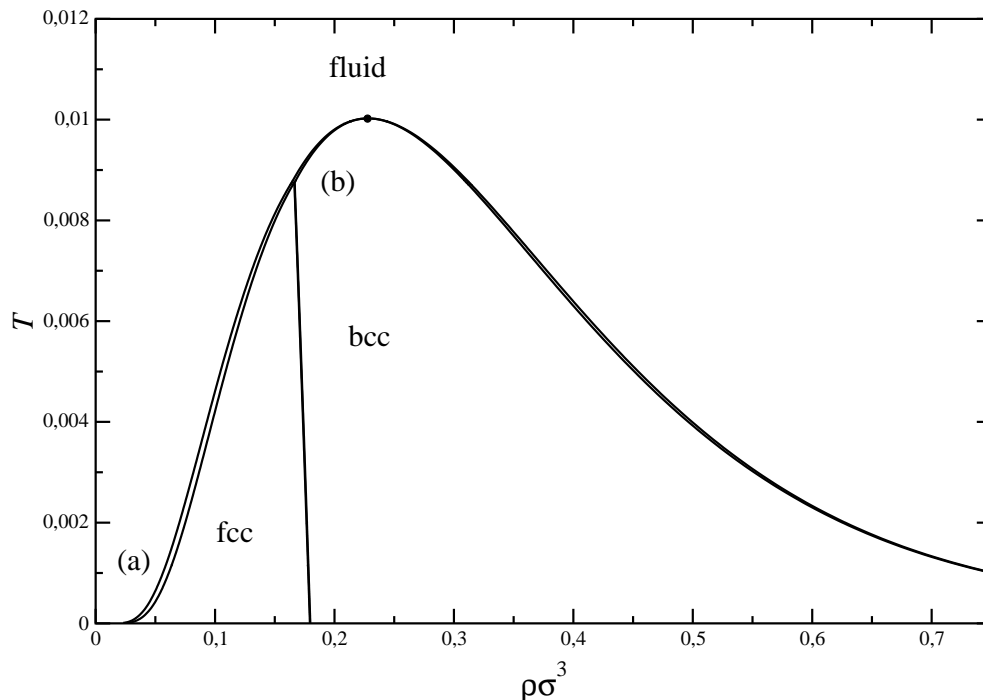
quasi-universal value 2.85. At higher values of the peak the system is solid and at lower values it is fluid. The evolution of $S(k)$ with density shown in figure 6.6 in conjunction with the Hansen-Verlet value, implies that at this temperature the system barely freezes and that $T = 0.01$ is very close to the upper freezing temperature. We will confirm this prediction in the next chapter, where we will also use the structural results obtained here in order to calculate the free energy of the fluid.

Finally, we have performed MC simulations and solved the HNC closure at much higher temperatures, $T = 1.00$, corresponding to the physical domain for the effective interactions between polymer chains. There, we found that the HNC closure accurately reproduces the simulation results at all densities and that the liquid has very little structure, a result which can be easily understood in view of the fact that the thermal energy, which is equal to the interaction strength here, washes out the correlation effects caused by the interactions.

6.1.2 Phase diagram

Figure 6.7 shows the quantitative phase diagram for the GCM. The structure of the fluid phase was calculated using the HNC (see section 4.2.2), the Helmholtz free energy was calculated using the virial route (3.23), because at low densities the compressibility route (3.24) yields free energies that are too low, leading to the erroneous result that the HS-like

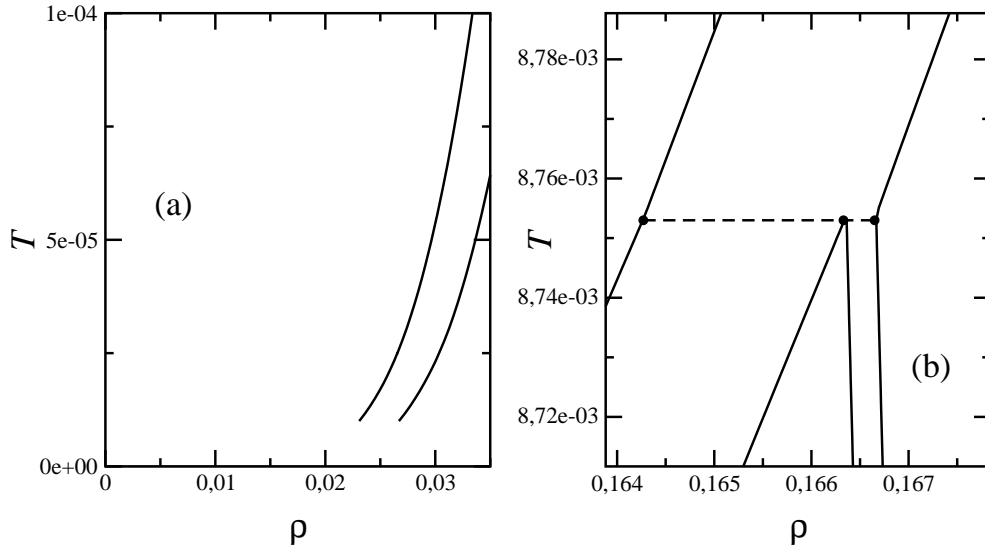
Figure 6.7: Phase diagram of the Gaussian core model. The fluid-fcc, bcc-fcc and fcc-fluid transitions are all double lines but only some of them can be resolved on the scale of the figure because the gaps (especially the fcc-bcc gap) are very small. The full dot marks the point at which the fluid-bcc coexistence curve turns around.



freezing of the Gaussian fluid into a fcc lattice does not take place. There are two factors playing an important role here: on the one hand, the predicted isothermal compressibilities are too high, causing a fluid free energy which is too low, and on the other hand, the solid free energy, being a product of the variational procedure outlined in section 4.5, is unavoidably higher than the true one [see equation (4.118)]. It is therefore pertinent to follow the HNC virial route in calculating the fluid free energy. The latter leads in fact to an overestimation of the fluid free energy, but this compensates for the overestimation of the solid free energy and leads to the physical correct picture of freezing into an fcc solid at the low-density part of the phase diagram. We have thus calculated the fluid free energies through the HNC virial route for a range of temperatures $10^{-5} \leq T \leq 0.015$ for a range of densities $0 \leq \rho \leq 1.0$ and performed the common-tangent construction on the Helmholtz free energies for the fluid and solid phases (fcc and bcc) as described in section 5.

The resulting phase diagram (figures 6.7 and 6.8) is very similar to the approximate one drawn by Stillinger and Stillinger [89]. It shows the sequence of freezing, structural (fcc \rightarrow bcc) and remelting transitions as well as the upper freezing temperature T_u associated with the corresponding density ρ_u . The coordinates of this point, where the fluid-bcc coexistence lines turn around, are $(T_u, \rho_u) = (0.0102, 0.2292)$. This is in perfect agreement with the preliminary results from section 6.1.1, where at $T = 0.01$ the structure factor at $\eta = 0.12$, corresponding to $\rho = 0.2292$, was found to slightly exceed the Hansen-Verlet

Figure 6.8: Insets for the phase diagram of the GCM (see figure 6.7). (a) In the neighborhood of zero densities and temperatures. (b) In the neighborhood of the fluid-fcc-bcc triple temperature, with the dashed line denoting the triple line between these coexisting phases.



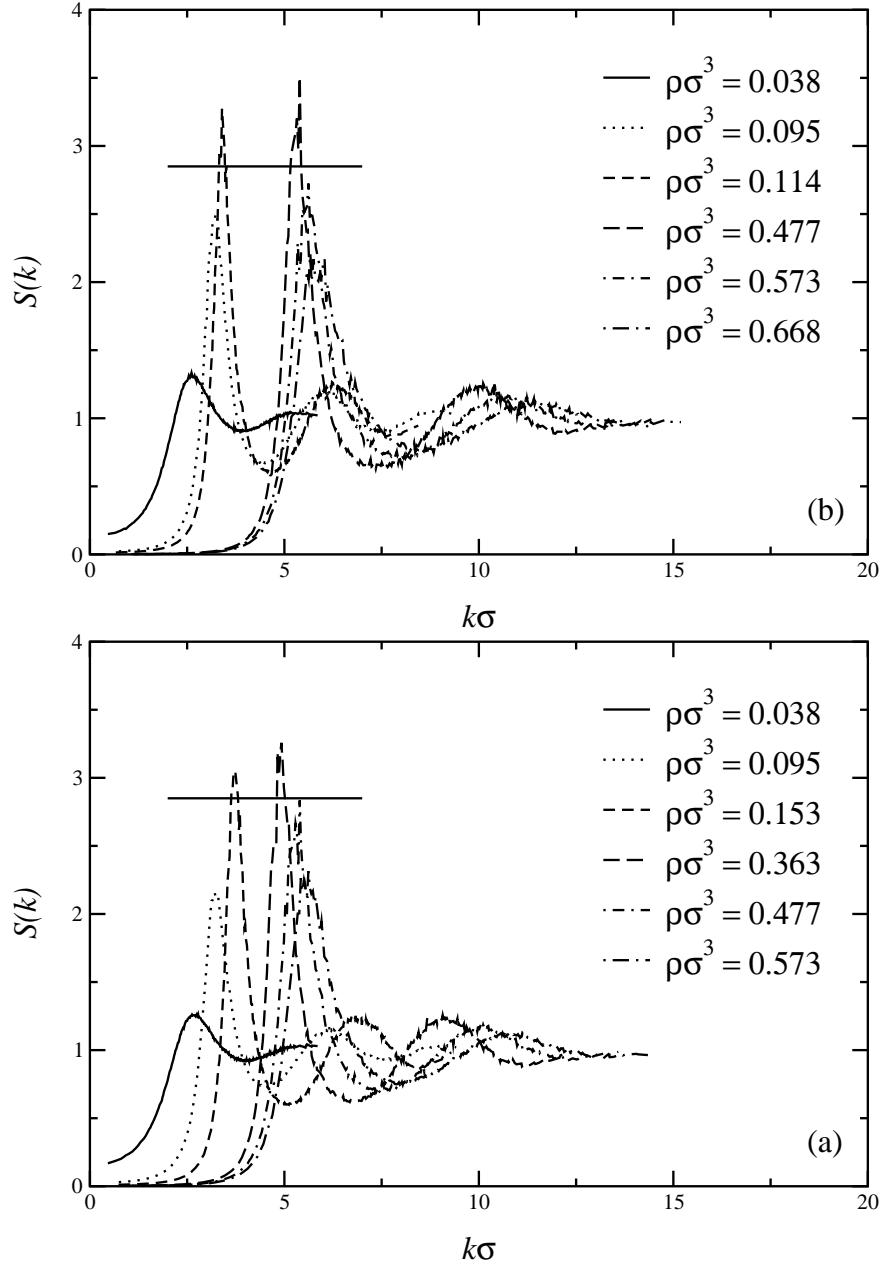
value. The fcc-bcc coexistence lines run linearly from the points $\rho_{fcc} = 0.17941$ and $\rho_{bcc} = 0.17977$ at $T = 0$ to the points $\rho_{fcc} = 0.15531$ and $\rho_{bcc} = 0.16667$ at the triple temperature $T_t = 8.753 \times 10^{-3}$. The density gap between the fcc and bcc coexisting densities remains constant and equal to $\Delta\rho = 3.6 \times 10^{-4}$. The density of the coexisting fluid at the triple temperature is $\rho_{fluid} = 0.16431$.

It should be emphasized that, notwithstanding its deceptive appearance in figure 6.7, the point (T_u, ρ_u) is *not* a critical point. At (T_u, ρ_u) , two common tangents between the fluid and bcc solid free energies, one lying on the low-density side and the other on the high-density side of it, coalesce into this single point. No susceptibility diverges and all Helmholtz free energy-density curves remain strictly concave up.

It is now pertinent to ask whether the Hansen-Verlet freezing criterion is satisfied for both the low- and the high- density crystallization of the system. To this end, M. Watzlawek has performed additional MC simulations at temperatures below T_u and in figure 6.9 we show structure factors at two such temperatures, $T = 0.007$ and $T = 0.005$, for increasing values of the density. It can be seen that the Hansen-Verlet criterion is indeed valid for both freezing transitions.

It is of course also possible to calculate the exact free energies of the various candidate phases in a simulation by means, e.g., of the virial route in the fluid state and by employing an appropriate method for the solid state. However, the latter is very time consuming. The very good agreement between the phase boundaries obtained from the approximate theory presented here and the MC results regarding the height of the peak of $S(k)$ and the spontaneous crystallization of the system in the simulation box give us confidence that the phase diagram of figure 6.7 is quantitatively correct.

Figure 6.9: Structure factors of the GCM at (a) $T = 0.007$ and (b) $T = 0.005$ obtained from MC simulations. The densities are indicated in the keys. The straight line marks the Hansen-Verlet value 2.85. The corresponding structure factors in the regions $0.153 \leq \rho \leq 0.363$ for $T = 0.007$ and $0.114 \leq \rho \leq 0.477$ for $T = 0.005$ show Bragg peaks, indicating that the GCM has to be in the solid state for these densities.



6.2 Phase behavior of bounded potentials

In this section we will discuss the phase behavior of bounded potentials like, for example, the Gaussian core potential (see subsection 2.2.5), the penetrable spheres model (see subsection 2.2.7) or the Fermi distribution potential (see subsection 2.2.6). The mechanisms leading to a phase transition in a system which consists of particles interacting via a finite potential are, for example, discussed in [18]. As a short preface to the subsequent subsections, we introduce the following definitions.

Clustering Clustering means the tendency of particles to form composite particles (clusters) in which a number of particles sit on top of each other. This mechanism creates ‘free space’ and is therefore able to stabilize, for example, solid phases [18].

Reentrant melting With ‘reentrant melting’ one describes the tendency of certain pair potentials [Gaussian core model (GCM, see subsection 2.2.5)] to remelt at densities above their respective freezing density. This effect can happen more than once at a fixed temperature, for example star polymers are displaying a very rich phase diagram [91].

These behaviors have, as stated above, been encountered for potentials that are very similar to each other. In fact, the Fermi distribution model (FDM, see subsection 2.2.6) can show up both types of phase behavior (depending on the potential parameter ξ , see subsection 6.2.4).

6.2.1 Clustering versus reentrant melting behavior

In this section we will, as stated above, in full generality discuss the phase behavior of systems whose particles interact by means of potentials which do not diverge at the origin, are free of attractive parts and decay fast enough to zero as the interparticle separation r goes to infinity. We will establish a criterion which determines whether a given system freezes at all temperatures or if it will display reentrant melting and an upper freezing temperature by employing a mean field-density functional theory (which is shown to become exact at high temperature and/or densities).

Bounded interatomic potentials arise naturally as *effective interactions* between the center of mass of soft, flexible macromolecules such as polymer chains [45] etc. Indeed, the centers of mass of two macromolecules can coincide without violation of excluded volume conditions, hence bringing about a bounded interaction (like, for example, the GCM in section 2.2.5). Because bounded potentials can be tuned by applying the same mechanisms as for unbounded potentials (solvent quality, temperature, chain length, salt concentration etc.), it appears to be useful to consider bounded potentials in some generality in order to draw conclusions about the expected phase behavior of systems interacting by means of such interactions.

The basic question that should be answered in this chapter is the following: Given a non attractive and bounded pair potential which satisfies the following requirements guaranteeing stability and the existence of the thermodynamic limit:

- it is bounded;

- it is positive definite;
- it decays fast enough to zero at large separations, so that it is integrable and its Fourier transform exists;
- it is free of attractive parts;

to which topology (clustering or reentrant melting) belongs the phase diagram of the system?

6.2.2 The model and the mean-field limit

We will work with a general interaction

$$\phi(r) = \varepsilon \phi^*\left(\frac{r}{\sigma}\right),$$

which satisfies the requirements put forward above. ε and σ are an energy and a length scale and $\phi^*(r)$ is some dimensionless function. This function does not have to be analytic, i.e. discontinuities in the potential or its derivatives are allowed. Without loss of generality, we assume

$$\phi^*(0) = 1.$$

Let us call $\tilde{\phi}^*(k)$ the Fourier transform of the interaction potential. For more concreteness (and for purposes of demonstration) we use in the Fermi distribution model (FDM) as defined in section 2.2.6. This potential represents the family of bounded interaction $\phi_\xi(r)$ depending on a tunable parameter ξ .

The key idea for examining the high temperature and/or high density limit of such model systems is the following. We consider in general a spatially modulated density profile $\rho(\vec{r})$ which does not vary too rapidly on the scale σ set by the interaction. At high densities, $\rho\sigma^3 \gg 1$, the average interparticle distance $a \equiv \rho^{-1/3}$ becomes vanishingly small, and it holds $a \ll \sigma$, i.e., the potential is extremely long range. Every particle is simultaneously interacting with an enormous number of neighboring molecules and in the absence of short-range excluded volume interactions the excess free energy of the system [94] can be approximated by a simple mean-field term, equal to the internal energy of the system:

$$A_{ex}[\rho] \cong \frac{1}{2} \int_{\mathbb{R}^3} d^3r \int_{\mathbb{R}^3} d^3r' \rho(\vec{r}) \rho(\vec{r}') \phi(|\vec{r} - \vec{r}'|), \quad (6.1)$$

with the approximation becoming more accurate with increasing density. Then, equation (6.1) immediately implies that in this limit the direct correlation function $c(r)$ of the system, defined as in equation (4.70), becomes independent of the density and is simply proportional to the interaction potential, namely

$$c(r) = -\beta\phi(r) = -\frac{1}{T^*}\phi^*(r). \quad (6.2)$$

Using the last equation together with the OZ equation, we obtain an analytic expression for the structure factor $S(k)$ of the system as

$$S(k) = \frac{1}{1 + \rho \frac{1}{T^*} \tilde{\phi}^*(k)}. \quad (6.3)$$

This mean-field approximation (MFA) has been put forward and examined in detail in the context of the Gaussian core model independently by Lang *et al.* [46] and by Louis *et al.* [95]. The model is particularly relevant from the physics point of view, due to its connection to the theory of effective interactions between polymer chains [45]. Here, we establish the validity of the MFA at high densities for bounded, positive-definite interactions *in general* and we examine its implications for the global phase behavior of such systems.

6.2.3 Spinodal instability and freezing

We employ the MFA as a physically motivated *working hypothesis* for now and, by direct comparison with simulation results, we will show later that it is indeed valid. Within the framework of the theory, an exact criterion can be formulated, concerning the stability of the liquid phase at high temperatures and densities. The function $\phi^*(r)$ was assumed to be decaying monotonically from unity at $r = 0$ to zero for $r \rightarrow \infty$. For the function $\tilde{\phi}^*(k)$, there are two possibilities:

1. It has a monotonically decay from the value

$$\tilde{\phi}^*(k = 0) = \int_{\mathbb{R}^3} d^3r \phi^*(r) > 0$$

to the value $\tilde{\phi}^*(k) = 0$ for $k \rightarrow \infty$. We call such potentials k^+ -potentials. Obviously, the Gaussian interaction belongs to this class.

2. It has oscillatory behavior at large k , with the implication that it is a non monotonic function of k , attaining necessarily negative values for certain ranges of the wavenumber k . We call such potentials k^\pm -potentials. Long-range oscillations in k -space imply that $\phi^*(r)$ changes more rapidly from unity at $r = 0$ to zero at $r \rightarrow \infty$ in the k^\pm -class than in the k^+ one. Moreover, let us call k_* the value of k at which $\tilde{\phi}^*(k)$ attains its minimum, negative value.

If we are dealing with a k^\pm -potential equation (6.3) implies that $S(k)$ has a maximum at precisely the wave-vector k_* where $\tilde{\phi}^*(k)$ attains its negative minimum, $-\tilde{\phi}^*(k_*)$ and this maximum becomes a *singularity* at the ‘spinodal line’ $\rho\beta|\tilde{\phi}^*(k_*)| = 1$. The theory has a divergence, implying that the underlying assumption of a uniform liquid is not valid and the system must reach a crystalline state. Indeed, on the basis of the fluctuation-dissipation theorem, $S(k)$ can be interpreted as a response function of the density to an infinitesimal external modulating field at wavenumber k [6] and a diverging value of

this response function clearly signals an instability. If the Fourier transform of $\phi^*(r)$ has negative Fourier components, then an increase in temperature can be compensated by an increase in density in the denominator of equation (6.3), so that $S(k_*)$ will have a divergence at all β . We thus conclude that *k^\pm -systems freeze at all temperatures*.

If we are dealing with a k^+ -potential [$\tilde{\phi}^*(k)$ monotonic], then equation (6.3) implies that $S(k)$ is also a monotonic function of k at high densities [46]. For such potentials, one can always find a temperature high enough, so that the assumptions of equation (6.1) hold and then equation (6.3) forces the conclusion that freezing of the system is impossible at such temperatures. This does not imply, of course, that such systems do not freeze at all; one simply has to go to a low enough temperature and density, so that the mean-field assumption does not hold and the interaction is much larger than the thermal energy. Then, the system will display a hard-sphere type of freezing, to be discussed more explicitly below. An upper freezing temperature T_u^* must exist for k^+ -potentials, implying that such systems must remelt at $T^* < T_u^*$ upon increase of the density. Hence, we reach the conclusion that *k^+ -systems display an upper freezing temperature and reentrant melting*. The criterion says nothing about the crystal structure of the solid, however, which always depends on the details of the interaction as well as the density [46, 89].

For potential of the k^+ -class, the mean-field arguments presented above hold not only at high temperatures but also at low ones, provided that the requirement $\rho\sigma^3 \gg 1$ is satisfied, because these are molten at high densities for all nonzero temperatures. The validity of the mean-field theory for k^+ -type systems, even at very low temperatures, was confirmed recently by direct comparison with simulation results for the particular case of the Gaussian potential ([46], see also section 6.1). If the potential is in the k^\pm -class, the mean field approximation holds provided that the system is not already frozen, as we will confirm shortly. Moreover, both kinds of systems display an unusual kind of ‘high-density ideal gas’ limit. Indeed, taking the expression (6.3) for $S(k)$ and using the relations $S(k) = 1 + \rho\tilde{h}(k)$, where $\tilde{h}(k)$ is the Fourier transform of the total correlation function $h(r)$ of the uniform fluid, we obtain:

$$\tilde{h}(k) = -\frac{\frac{1}{T^*}\tilde{\phi}^*(k)}{1 + \rho\frac{1}{T^*}\tilde{\phi}^*(k)}. \quad (6.4)$$

At low ks , where $\tilde{\phi}^*(k)$ is of order unity, the term proportional to the density in the denominator dominates in the limit of high densities and $\tilde{h}(k)$ scales as $-\frac{1}{\rho} \rightarrow 0$. At high ks , the Fourier transform $\tilde{\phi}^*(k)$ in the numerator is itself small, with the result that $\tilde{h}(k)$, and hence also the correlation function $h(r)$, is approaching zero. This, in turn, means that the radial pair distribution function $g(r) = h(r) + 1$ is very close to unity in this limit and deprived of any significant structure for all values of r and it only has some small structure at small r , which is in fact more pronounced for k^\pm -potentials than for k^+ ones. In this limit, the hypernetted chain (HNC) closure (see subsection 4.2.2) becomes exact, as the exact relation

$$g(r) = \exp [\beta\phi(r) + h(r) - c(r) - B(r)],$$

combined with the limits

$$g(r) \rightarrow 1 \quad ; \quad h(r) \rightarrow 0 \quad \text{and} \quad c(r) \rightarrow -\beta\phi(r)$$

forces the bridge function $B(r)$ to vanish. Moreover, equation (6.3) and (6.4) reveal that the systems obey a scaling law, namely that the functions $S(k)$ and $T^*h(r)$ do not depend on ρ and T^* separately but only on the ratio $\frac{\rho}{T^*}$.

Systems in the k^\pm -class freeze before the spinodal is reached. In order to make quantitative predictions, we invoke the empirical Hansen-Verlet freezing criterion [92, 93], which states that a system crystallizes when $S(k)$ at its main peak attains, approximately, the value $S(k_*) = S_m = 2.85$. Although this criterion was originally put forward for hard, atomic interactions (HS, Lennard-Jones etc.), recent detailed analysis have demonstrated that it holds for the freezing and the remelting of the non diverging Gaussian interaction [46]. Hence, we assume that it is valid for the general case of systems we consider here and combining it with equation (6.3), we obtain the equation of the freezing line $T_f^*(\eta)$ as

$$T_f^*(\eta) = \eta \frac{6 \left| \tilde{\phi}^*(k_*) \right|}{\pi \left(1 - \frac{1}{S_m} \right)} \approx 2.864\eta \left| \tilde{\phi}^*(k_*) \right|. \quad (6.5)$$

The value of $\left| \tilde{\phi}^*(k_*) \right|$ determines the slope of the freezing line at the high (T^*, η) part of the phase diagram.

6.2.4 Comparison with simulations

We now wish to put these arguments in a strong test, using the concrete family of the Fermi distribution model (FDM, see subsection 2.2.6). First of all, we have calculated the Fourier transform of the potential (2.10) numerically, establishing that member of the FDM with $\xi < \xi_c$ belong to the k^\pm class and members with $\xi > \xi_c = 0.49697$ to the k^+ class. The GCM is also a member of the latter class.

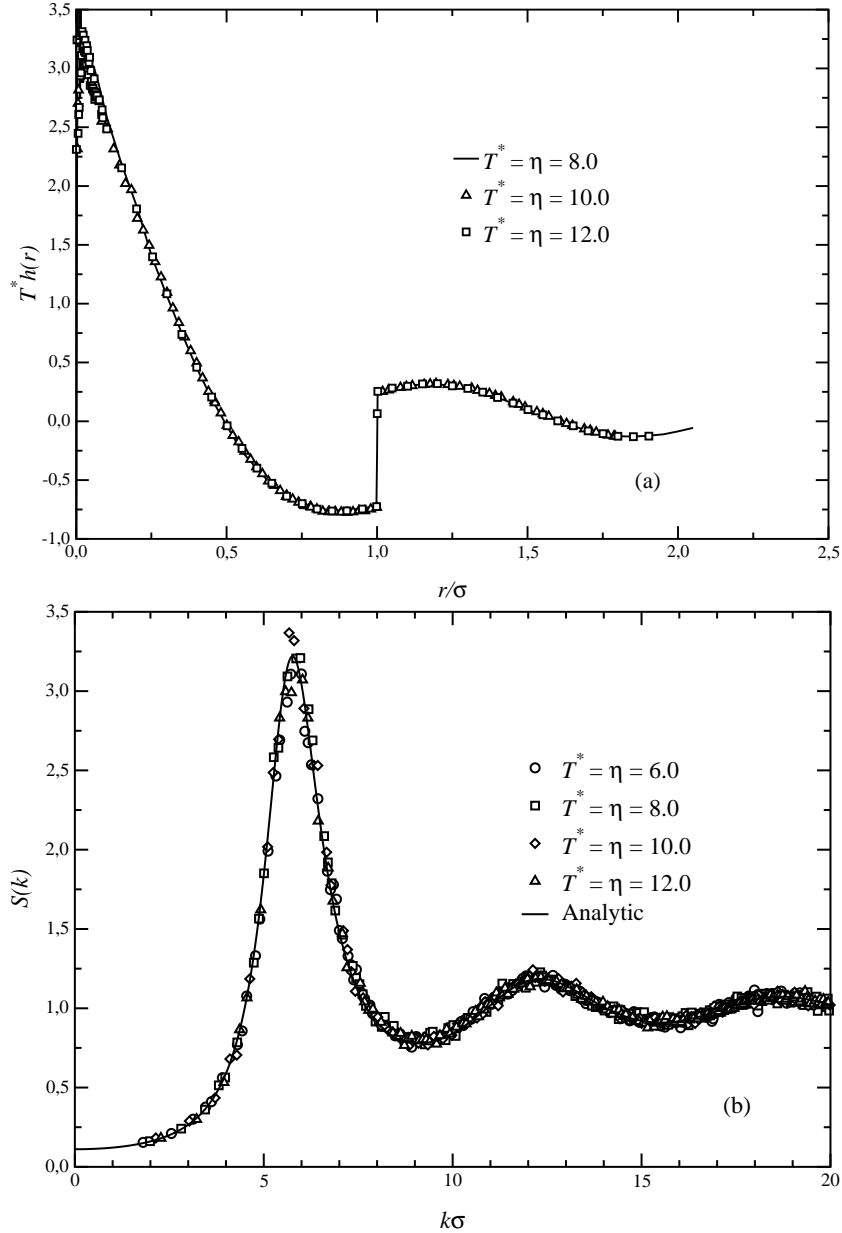
6.2.4.1 Systems displaying clustering

As examples of systems displaying clustering transitions, we have taken the extreme (and by now well-studied) case $\xi = 0$ (the PSM) as well as the case $\xi = 0.1$ of the FDM. We have performed standard Monte Carlo (MC) NVT simulations for a large number of values for the temperature and density. We begin with the PSM for which the static structure factor $S(k)$ takes the form [using equations (6.1) and (6.3)]

$$S(k) = \left[1 + 24 \frac{\eta}{T^*} \frac{\sin(k) - k \cos(k)}{k^3} \right]^{-1}. \quad (6.6)$$

The high temperature-high density freezing line of equation (6.5) takes for this choice of ξ the form $T_f^*(\eta) = 1.033\eta$. To test the analytical expression of equation (6.6), we move along the ‘diagonal’ $T^* = \eta$, a combination that lies almost on the Hansen-Verlet estimate for the location of the freezing line. In figure 6.10 we show the comparison of the analytical results with those obtained from the MC simulations for $S(k)$ and we also demonstrate the validity of the mean-field approximation for the PSM. In order to further investigate the validity of the MFA, we have performed MC simulations in a variety of

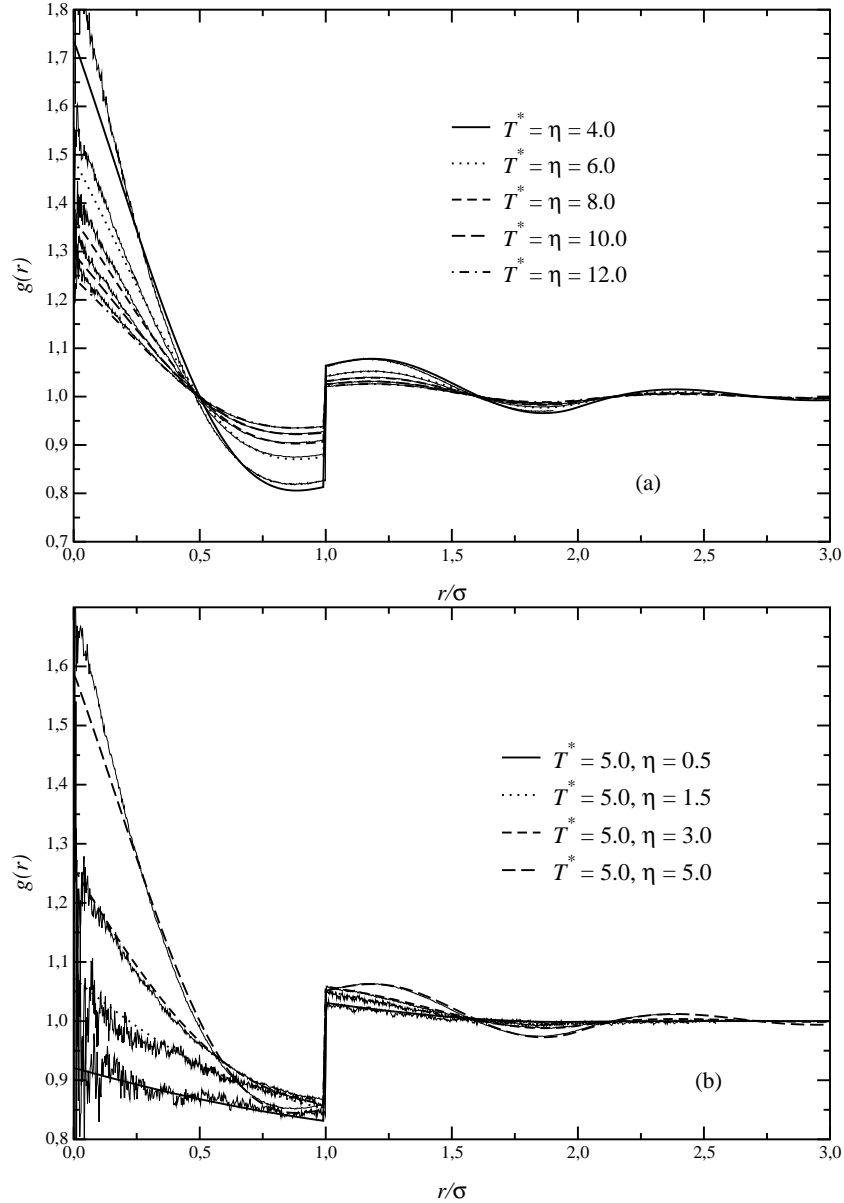
Figure 6.10: (a) The product $T^*h(r)$ for an FDM with $\xi = 0$ (PSM), along the diagonal $T^* = \eta$ at high packing fractions, as obtained from MC simulations. The results close to $r = 0$ are noisy due to poor statistics there. All results collapse onto a single curve. (b) The corresponding structure factors $S(k)$, shown together with the analytical result of equation (6.6).



thermodynamic points and we present a selection of the obtained results in figures 6.11 and 6.12 and discuss them below.

In figure 6.11(a) we show a comparison between the MC and MFA results for the pair distribution function $g(r)$ along the ‘diagonal’ $T^* = \eta$. It can be seen that the agreement

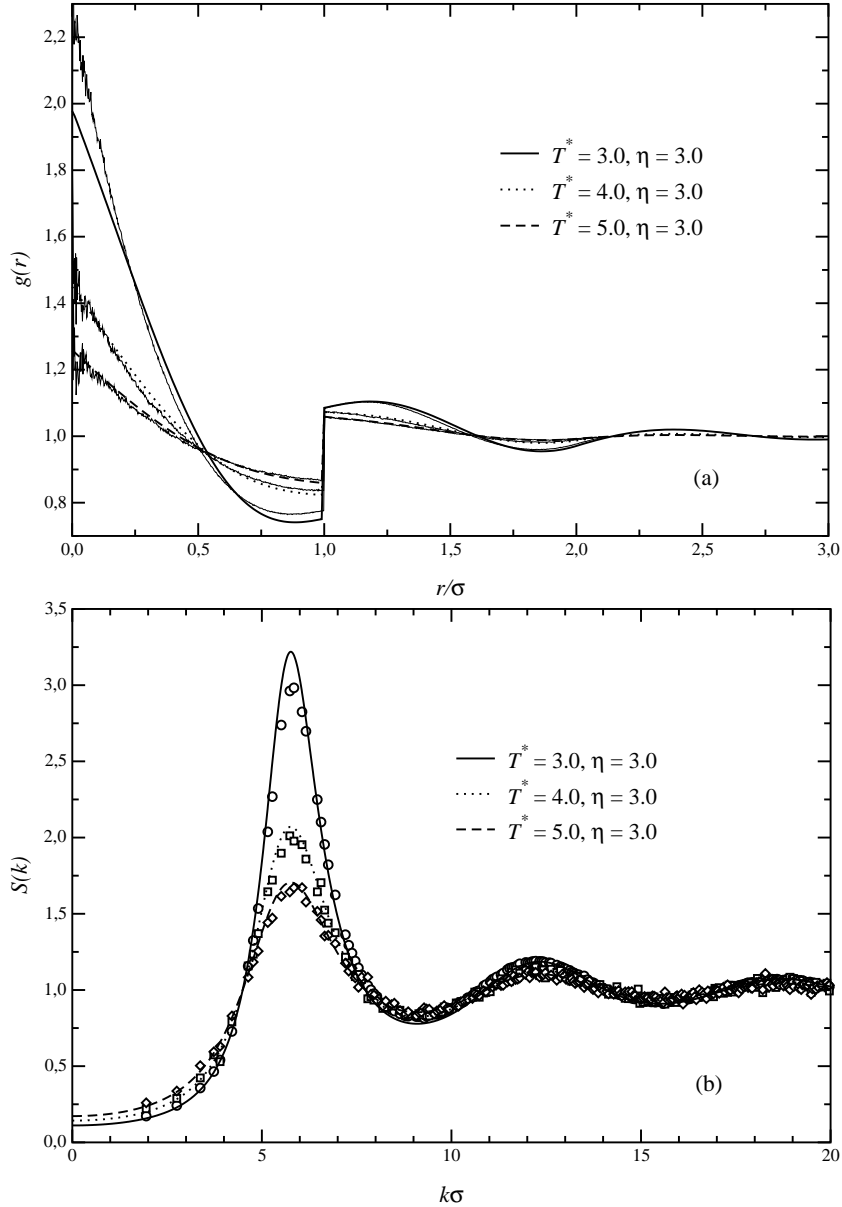
Figure 6.11: (a) The function $g(r)$ of the PSM for the selected points along the ‘diagonal’ $T^* = \eta$ as obtained from theory (thick lines) and simulation (thin lines). (b) Same but now for fixed temperature $T^* = 5$ and increasing packing fraction η .



between the two is already very good at $T^* = \eta = 4.0$ and thereafter it improves markedly with increasing temperature and density. The results obtained from the present theory are of the same quality as those obtained by Feraud *et al.* [67], who used the sophisticated zero-separation closure (ZSEP, see section 4.2.4) to investigate the liquid structure of the system.

In figure 6.11(b) we perform the same comparison but now at *fixed temperature* $T^* = 5.0$ and increasing packing fraction η . As can be seen, at this temperature, the MFA, which

Figure 6.12: (a) Same as figure 6.11(b) but now for fixed $\eta = 3.0$ and increasing temperature. (b) The structure factors at the thermodynamic points of (a), comparison between theory (lines) and simulation (symbols).



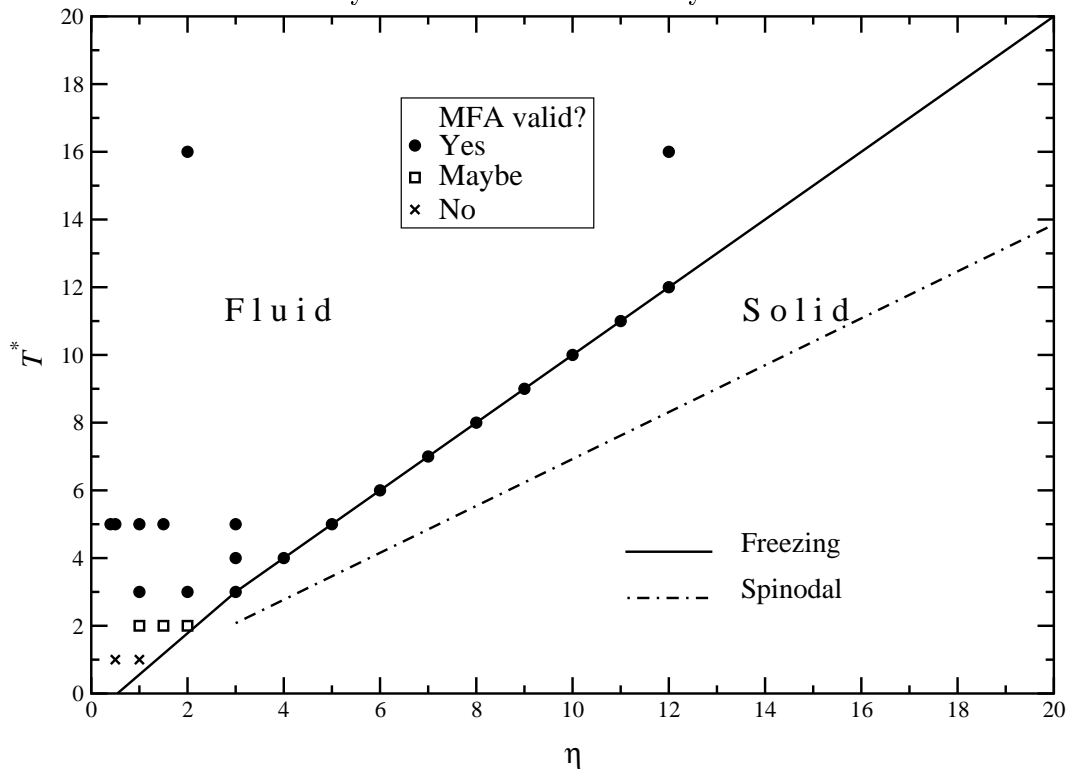
was originally formulated as a high-density approximation, proves to perform extremely well even at intermediate packing fractions, $\eta = 0.5$ for instance. This is a direct consequence of the boundedness of the interaction combined with a temperature $T^* \gg \varepsilon$. Indeed, for small densities, the direct correlation function $c(r)$ tends to the Mayer function $f(r)$, $c(r) \approx e^{-\beta\phi(r)} - 1$ [6]. If we are dealing with a bounded interaction at high temperatures, we can linearize the exponential, obtaining $c(r) \approx -\beta\phi(r)$ at low densities, which matches the MFA expression (6.2) at high densities, thus leading to the conclusion

that the MFA is an excellent approximation at *all densities*. For unbounded interactions the linearization of the exponential is evidently impossible.

In Figure 6.12 we present a comparison between MC and MFA at *fixed packing fraction* $\eta = 3.0$ and increasing temperature. As can be clearly seen, the validity of the MFA improves with increasing temperature. For bounded interactions, an increasing temperature implies a ‘washing-out’ of the correlation effects caused by the (increasingly weak) interaction effects and a tendency of the system towards a particular ‘high-density ideal gas’ limit characterized by the tendency of the function $g(r)$ towards unity. However, it is an interesting peculiarity of these systems that unlike the usual ideal gas, the limit $g(r) \rightarrow 1$ (or, equivalently, $h(r) \rightarrow 0$) does *not* imply a corresponding limit $S(k) \rightarrow 1$. Though the Fourier transform of $h(r)$, $\tilde{h}(k)$, tends to zero as ρ^{-1} , this is compensated by the large density ρ , so that the structure factor $S(k) = 1 + \rho\tilde{h}(k)$ displays the signature of strong ordering through the pronounced peaks seen in figures 6.10(b) and 6.12(b).

Further, we performed MC simulations at selected points deeply inside the region $T^* < T_f^*(\eta)$, finding that the obtained structure factors displayed Bragg peaks and hence confirming the prediction that the system is frozen there. Putting all our results together, we draw in figure 6.13 a semi-quantitative phase-diagram of the PSM, accompanied by an assessment of the validity of the MFA at selected thermodynamic points. The MFA appears

Figure 6.13: The phase diagram of the PSM, along with the points where the mean field theory brings excellent agreement with simulation (filled circles), fairly good agreement (empty squares) and no good agreement (X-symbols). These symbols should help delineate the domain of validity of the mean-field theory.



to be an excellent approximation at all densities above the temperature $T^* = 3.0$. Hence, we take as an estimate for the freezing line above $T^* = 3.0$ the MFA-Hansen-Verlet line $T_f^* = 1.033\eta \approx \eta$; for lower temperatures, we simply connect the point $(\eta, T^*) = (3.0, 3.0)$ with the point $(\eta, T^*) = (0.5, 0.0)$, which comes from the consideration that at $T^* = 0$ the PSM reduces to the hard sphere system which is known to freeze at a fluid density $\eta_{HS} \approx 0.5$. The monotonic shape of the freezing curve for low temperatures arises from detailed considerations there, which can be found in [96].

Next we present in figure 6.14 a comparison for the FDM with $\xi = 0.1$. For this choice of ξ , the Hansen-Verlet based freezing line takes the form $T_f^* = 0.712\eta$. The selected points lie in the fluid region and the comparison indicates once more the excellent accuracy of the MFA both for $g(r)$ and for $S(k)$. The pair distribution function $g(r)$ of this model is deprived of the jump at $r = \sigma$ seen in the PSM; the latter is caused by the discontinuity of the PSM potential there. However, a similarity between the $g(r)$'s of the $\xi = 0$ and $\xi = 0.1$ models is that they both attain their maximum values at full overlaps between the particles $r = 0$ and thereafter they decay rapidly, featuring a depletion region around $r \approx \sigma$. This is a characteristic pointing to a strong *clustering* property in the fluid phase, a property thereafter inherited by the incipient thermodynamically stable crystal; the number of particles 'sitting on top of each other' and thereby occupying the same crystal site scales linearly with density. In order to corroborate this claim, we can argue in two different ways, using the liquid as a reference point.

First, let us consider the number of particles N_c in the fluid phase whose centers are, on average, within a distance σ from the given particle. The number N_c is given by the formula:

$$N_c = 1 + 4\pi\rho \int_0^\sigma dr r^2 g(r). \quad (6.7)$$

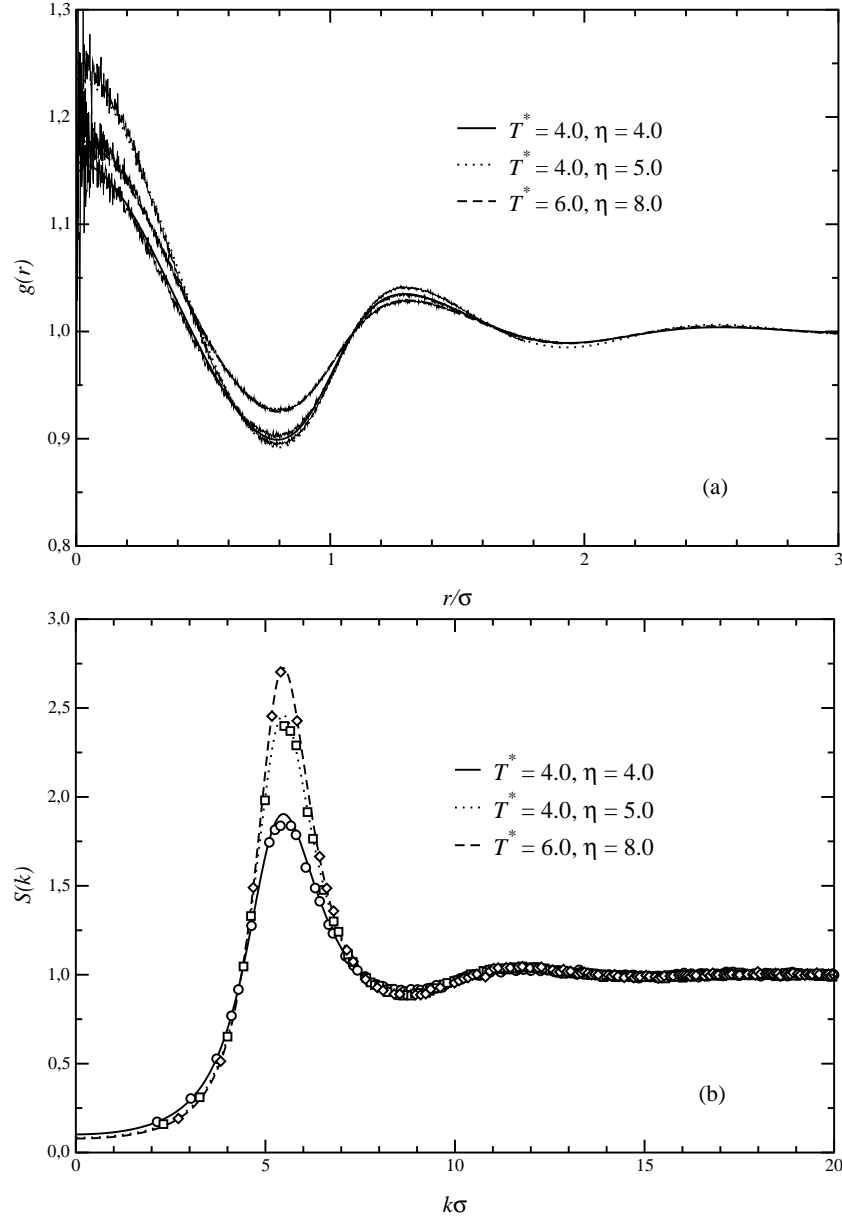
In figure 6.15 we show the function $4\pi r^2 g(r)$ within a particle diameter σ for a sequence of points along the freezing line of the PSM. As all these curves tend to a common limit with increasing density, the integral $N_c - 1$ tends to a constant and hence $N_c \propto \rho$ at high densities, where the second term on the right hand side of equation (6.7) dominates.

Second, we can use the wave vector k_* at which the fluid structure factor has a maximum in order to estimate for the lattice constant a of the incipient crystal through the relation $a \propto \frac{1}{k_*}$. For the models at hand, this maximum is entirely determined by the pair potential; unlike in usual fluids featuring diverging interactions, for which k_* scales as $\rho^{\frac{1}{3}}$, in our case k_* knows nothing about the density. Thus, all post-freezing crystals have the same lattice constant, although their average density is a linear function of the temperature. This clearly shows that clustering must take place in the crystal: by allowing more particles to occupy the same lattice site, a practically constant *effective density* of clusters is maintained in the crystal, thus leading to a density-independent lattice constant.

6.2.4.2 Systems displaying reentrant melting

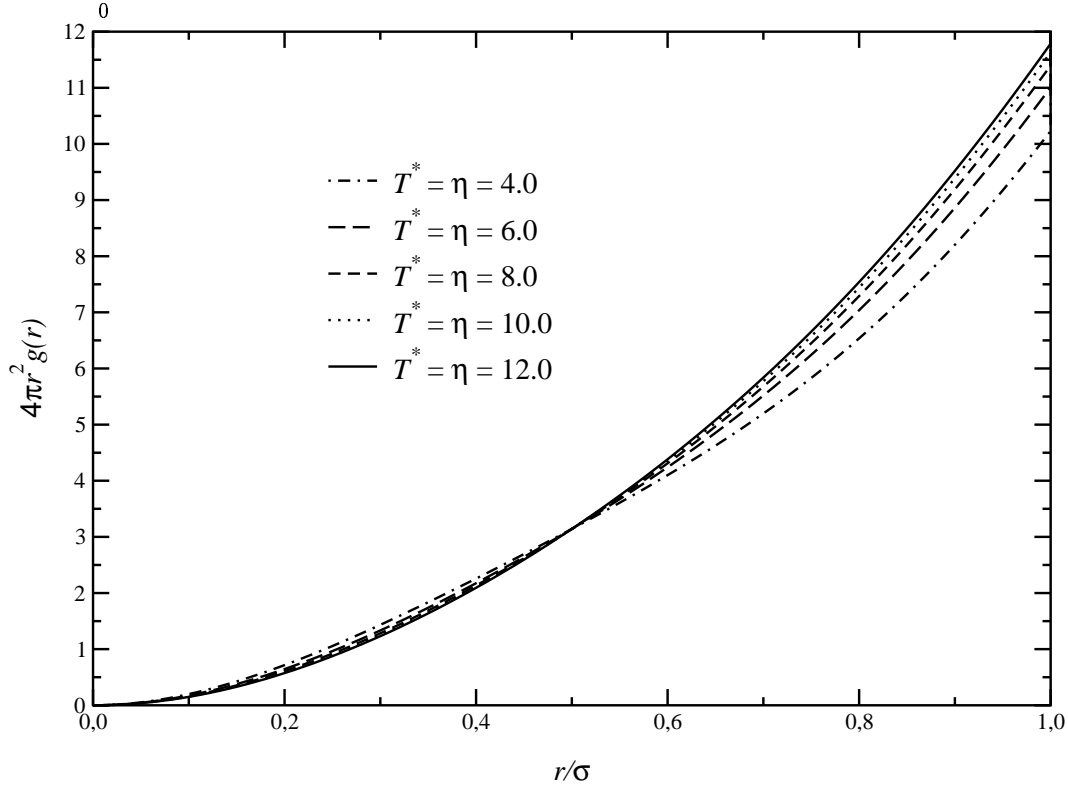
We now turn our attention to the opposite case, namely pair potentials $\phi(r)$ belonging to the k^+ -class. As an example within the FDM family, we have taken the model with

Figure 6.14: (a) Comparison between theory (thick lines) and simulation (thin lines) results for $g(r)$ of a FDM system $\xi = 0.1$. (b) Comparison for the structure factors (lines: theory, symbols: simulation) for the same system at the thermodynamic points of (a).



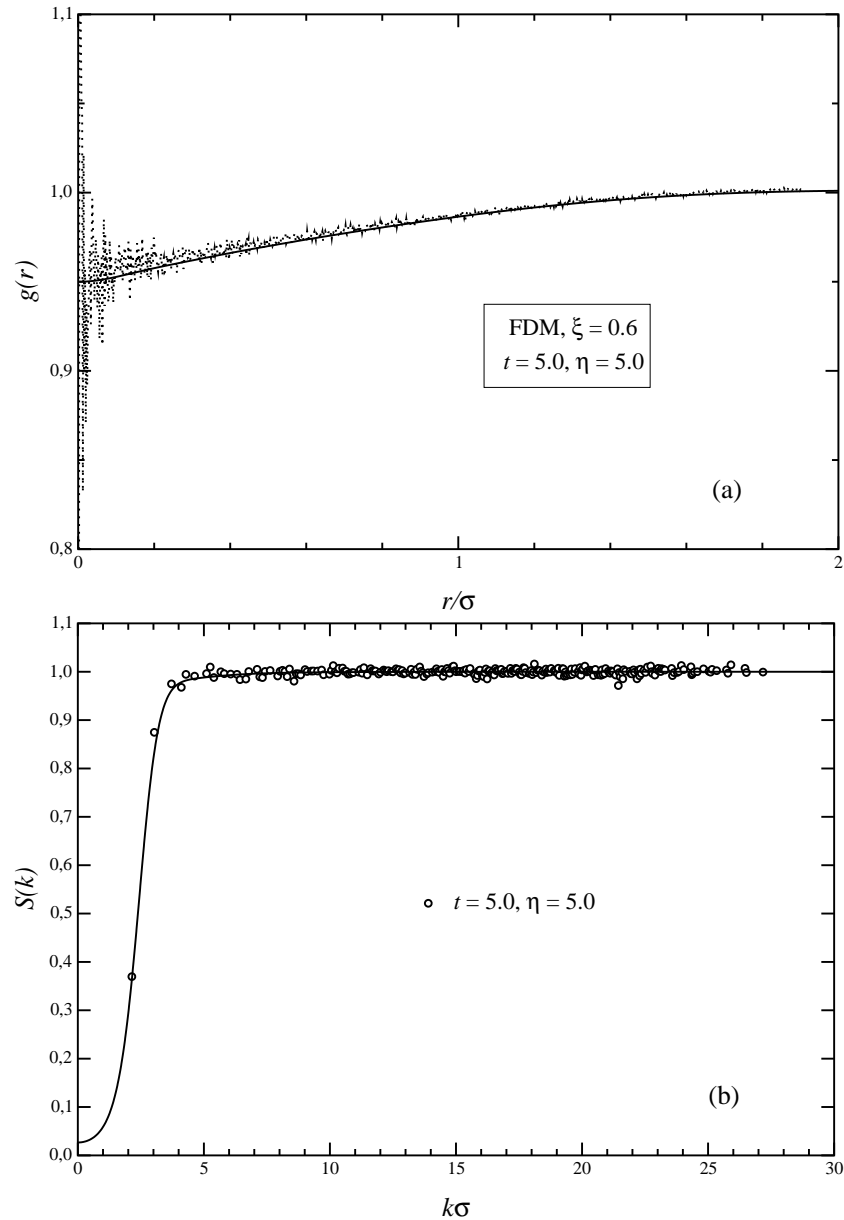
parameter $\xi = 0.6$ and performed a comparison between MC and MFA results. A characteristic example is shown in figure 6.16. As can be seen in figure 6.16(a), unlike the case of k^\pm -class potentials, the radial distribution function is completely deprived of any structure, although the thermodynamic parameters are in the same regime as those present in figures 6.11, 6.12 and 6.14. In fact, in the present case, $g(r)$ has a minimum at $r = 0$, not a maximum. This complete lack of structure is reflected in the shape of $S(k)$, shown in figure 6.16(b).

Figure 6.15: The quantity $4\pi r^2 g(r)$ within the diameter σ of the PSM along the freezing line $T^* = \eta$. All the curves converge to a single one at high densities, indicating that the integral $4\pi\rho \int_0^\sigma dr r^2 g(r)$ scales linearly with density ρ .



These characteristic features for the k^+ -class are not an artifact of the relatively high temperature chosen in the results of figure 6.16. They persist even at extremely low temperatures, provided the density is high enough. This has been amply demonstrated recently for the case of the Gaussian core model, another member of the k^+ -class [46]. In order to stress this point we present in figure 6.17 the $g(r)$ and $S(k)$ of the GCM at $T^* = 0.01$ and $\eta = 6.0$. Though $g(r)$ displays some structure up to $r \approx 2\sigma$, the structure factor $S(k)$ shows no signature of some kind of ordering. At any arbitrary small but finite temperature, a high enough density can be found for which the MFA is valid and then the assumption that a uniform phase exists leads consistently to a fluid which has ideal-gas behavior, i.e., vanishingly small correlations. These liquids are different from usual ideal gases in that, e.g., their pressure p and isothermal compressibility χ_T scale respectively as $p \sim \rho^2$ and $\chi_T \sim T^* \rho^{-2}$. Nevertheless, they are thermodynamically stable. Hence, for potentials in the k^+ -class, the equilibrium phase for sufficiently high densities at arbitrarily small but finite temperatures is the uniform fluid.

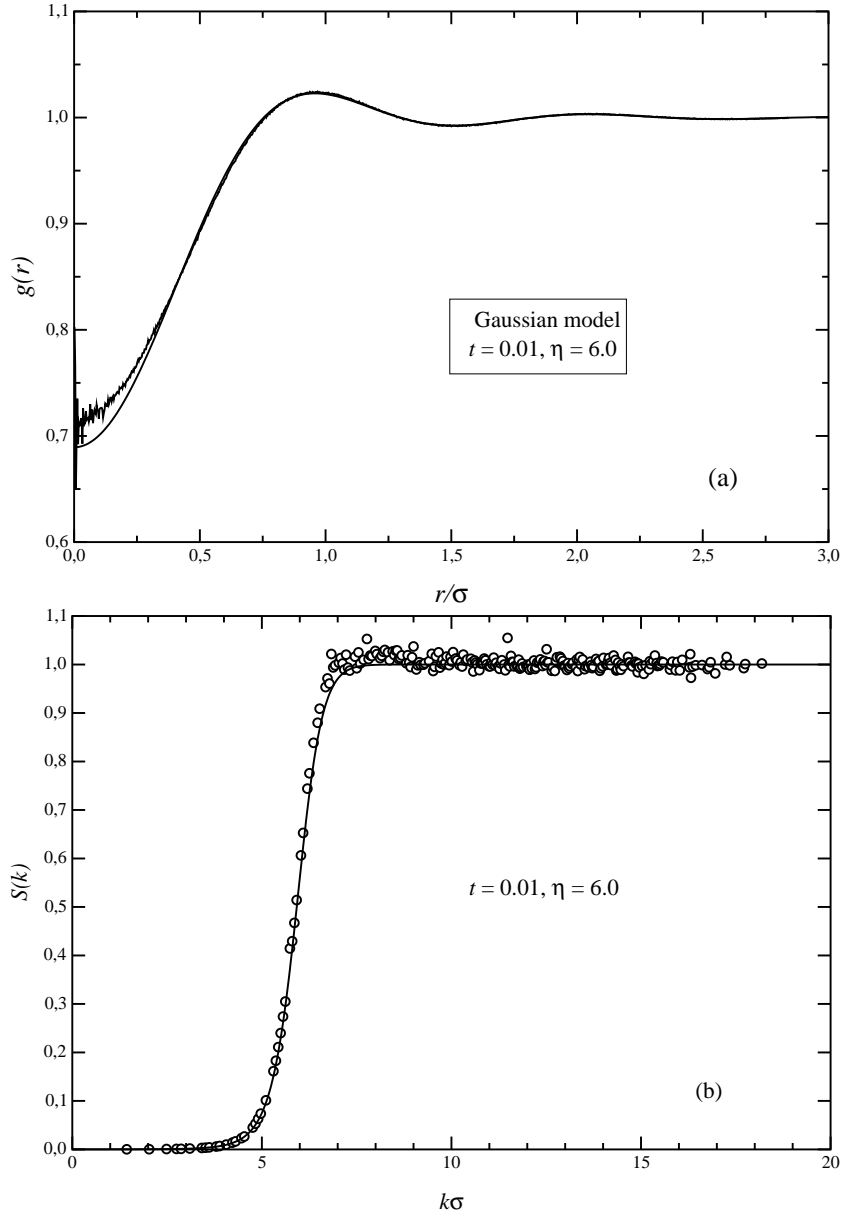
Figure 6.16: (a) Comparison between theory (thick lines) and simulation (thin lines) results for $g(r)$ of a FDM system with $\xi = 0.6$. (b) Comparison for the structure factor $S(k)$ (lines: theory, symbols: simulation) for the same system at the thermodynamic point of (a).



6.2.4.3 Generic phase diagrams

We now turn to the opposite limit of the low temperature-low density part of the phase diagram. There, following the original ideas of Stillinger [33], a HS mapping can be performed as follows. The Boltzmann factor $e^{-\beta\phi(r)}$ of the potential varies monotonically from the value $e^{-\beta\epsilon} \approx 0$ (since $\beta\epsilon \gg 1$ there) at $r = 0$ to unity at $r \rightarrow \infty$ and has a close

Figure 6.17: (a) Comparison between theory (thick lines) and simulation (thin lines) results for $g(r)$ of the GCM. (b) Comparison for the structure factor $S(k)$ (lines: theory, symbols: simulation) for the same system at the thermodynamic point of (a).



resemblance to that of a hard sphere system. We can thus define an effective hard sphere diameter σ_{HS} through the relation:

$$e^{-\beta\phi(\sigma_{HS}/\sigma)} = \frac{1}{2}. \quad (6.8)$$

Writing $\phi(r) = \varepsilon\phi^*(r)$ and using the fact that $\phi(r)$ is a monotonic function in order to establish that the inverse function $\phi^{-1}(r)$ exists, we can rewrite equation (6.8) as:

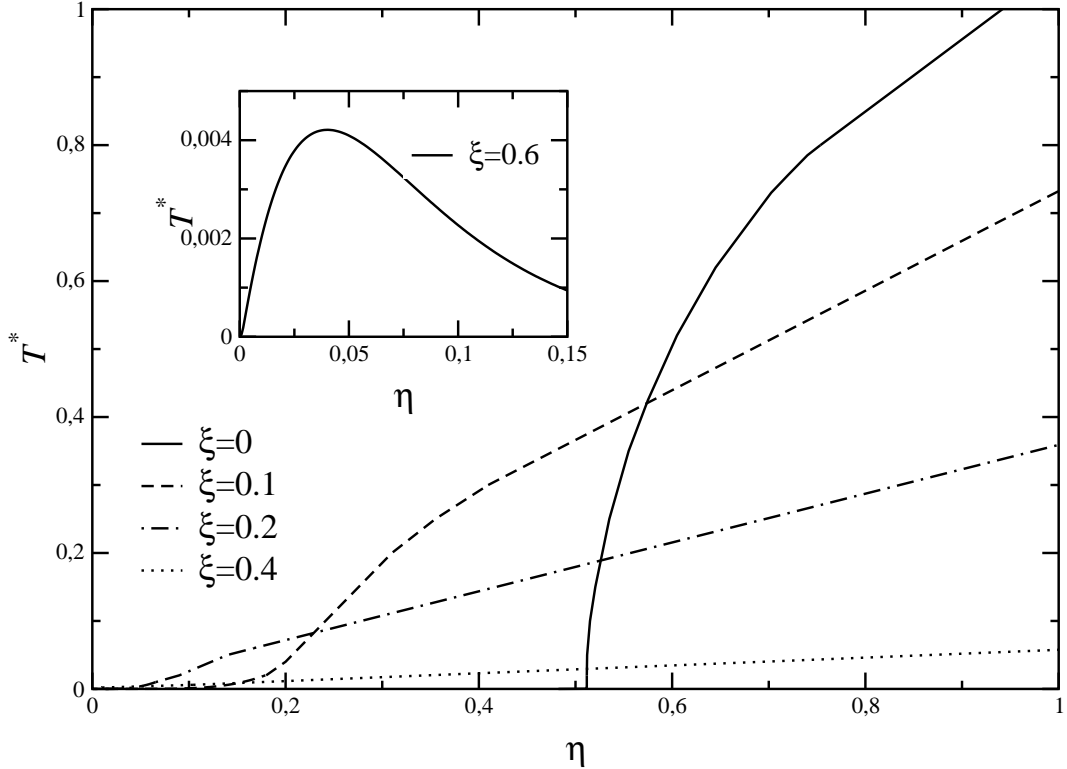
$$\sigma_{HS} = \sigma\phi^{-1}(T^* \ln 2). \quad (6.9)$$

We now use the known fact that hard spheres freeze at $\eta_{HS} \approx 0.5$ together with equation (6.9) above in order to obtain the low temperature-low density freezing line of the system as

$$T_f^*(\eta) = \frac{1}{\ln 2} \phi \left((2\eta)^{-\frac{1}{3}} \right). \quad (6.10)$$

As the limit $\phi(r) \rightarrow 0$ is attained for $r \rightarrow \infty$ only, it follows that the low temperature-low

Figure 6.18: Evolution of the phase diagram of k^\pm -FDM's with $\xi < \xi_c$. To the right of the freezing lines the system is solid and to the left fluid. Inset: the phase diagram of a k^+ -FDM with $\xi > \xi_c$, obtained by solving the HNC and employing the Hansen-Verlet criterion. Below the bell-shaped curve the system is solid and above fluid.



density freezing line of the system goes to $\eta = 0$ at $T_f^* = 0$. Equation (6.10) is valid for *all* potentials we consider here; however, for k^+ -potentials, combining the HS-like freezing at low temperatures and low densities with the fact that at high densities the fluid has to be stable, derived in the preceding subsection, we can draw the conclusion that such a system must display reentrant melting and an upper freezing temperature.

We have now taken equation (6.10) for the low- T^* and low- η freezing line of the FDM and combined it with the analytic expression at the opposite limit, (6.5), in order to

draw schematically the evolution of the phase diagram of the FDM as a function of ξ , for $\xi < \xi_c$. The results are shown in Figure 6.18. With increasing ξ , the slopes of the high- T^* freezing line decrease; at the limit $\xi \rightarrow 0$, corresponding to the PSM, the low- T^* freezing line approaches the horizontal axis vertically, as is dictated by the fact that the PSM becomes equivalent to the HS system there [33]. In the inset of figure 6.18, we show the phase diagram for a system with $\xi = 0.6 > \xi_c$, showing reentrant melting behavior. The evolution of the phase diagram from a clustering to a reentrant melting behavior can be easily visualized from this picture.

Finally, it is important to point out that Stillinger has proven that any system interacting by means of a potential which

- is differentiable at least four times,
- vanishes strongly enough at infinity to be integrable and
- is +1 at the origin,

will inevitably lead to a reentrant melting phase diagram *under the assumption* that the competing crystal structures have *single lattice site occupancy* [33]. We can therefore now complete the statement and say that if a potential belongs to the k^+ -class, then it will freeze into crystals of single occupancy and then remelt upon increase of the density. But if it belongs to the k^\pm -class, then it will freeze into a clustered solid at any temperature. Clustering appears therefore to be the crucial mechanism for crystal stabilization in these systems.

6.3 One component hard sphere system

The one component hard sphere (HS) system has been the object of intensive investigations from a lot of different theoretical approaches. In this section we will compare the results we obtained for the fluid and solid structure and liquid-solid transition for the one component hard-sphere system using various techniques described in this thesis.

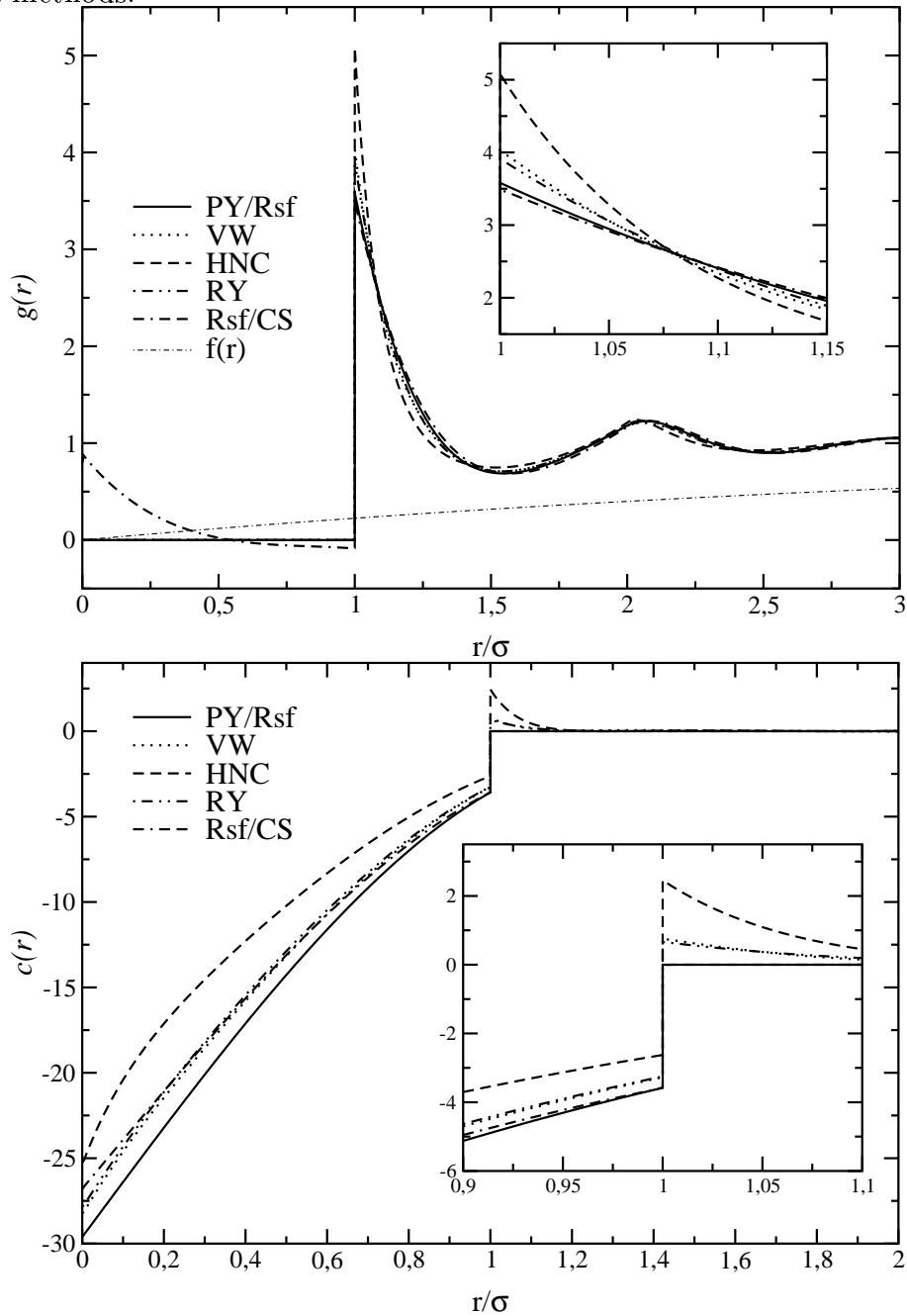
6.3.1 Fluid structure

In this section we will present results for the structure of the HS system at two different densities, $\rho = 0.2$ and $\rho = 0.8$. We applied the RY approximation and the Rosenfeld functional (with some new, yet unpublished expressions for the excess free energy density Φ introduced in section 4.3.5) for the hard sphere potential. In Figure 6.19, the pair correlation functions $g(r)$ and the direct correlation functions $c(r)$ for a hard sphere fluid at $\rho = 0.8$ calculated using various methods are shown. The abbreviations are standing for: PY/Rsf denotes the Percus-Yevick result (equal to the classical Rosenfeld (Rsf) functional for hard spheres), VW denotes the Verlet-Weiss parameterization, HNC is the Hypernetted chain approximation, RY denotes the Rogers-Young approximation (with $\alpha = 0.249$) and Rsf/CS is the Rosenfeld functional where for Φ_3 equation (4.104) is used. The insets are showing the contact value of $g(r)$ and the behavior of $c(r)$ around $r = \sigma$. From this figure, it is obvious that the pair distribution function $g(r)$, calculated using the version of the Rosenfeld functional which reassembles the Carnahan-Starling equation of state, violates the core condition $g(r) = 0 \forall r < \sigma$. Additionally, the contact value of this $g(r)$ is the lowest one of all five examined theories, lying even below the PY result. The HNC overestimates the contact value, whereas the RY approximation reveals its interpolating character (between the PY and the HNC), leading to a contact value which is nearly identical to the one of the VW parameterization (this can also be seen for $c(r)$), where the RY result also shows a exponential decreasing tail for $r > \sigma$.

Figure 6.20 shows the static structure factor $S(k)$ for the various theories; the two insets display the region for $k \rightarrow 0$ and the region around the first peak. This figure also shows the very good agreement between the RY solution and the VW parameterization; these two curves are enclosed by the PY and the HNC solution. For the compressibility $\chi_T/\chi_{T,id} = S(k=0)$ (see subsection 3.2.5), the VW and the Rsf/CS solution are nearly identical. This is obvious, because both methods are leading to the same Helmholtz free energy, which is directly related to the static structure factor at $k = 0$ using equation (3.34). However, the results still differ from the exact result, because the VW parameterization reproduces the CS free energy by adjusting the contact value and the long-range oscillations of $g(r)$, whereas the Rsf/CS method uses the CS equation of state as a direct input for its free energy. The results one gets for the correlation functions (especially for the tail $r > \sigma$) are somehow constrained by the weight functions (which are nonzero only for $r \leq \frac{\sigma}{2}$) and are therefore unable to reconstruct the exact value for $k = 0$.

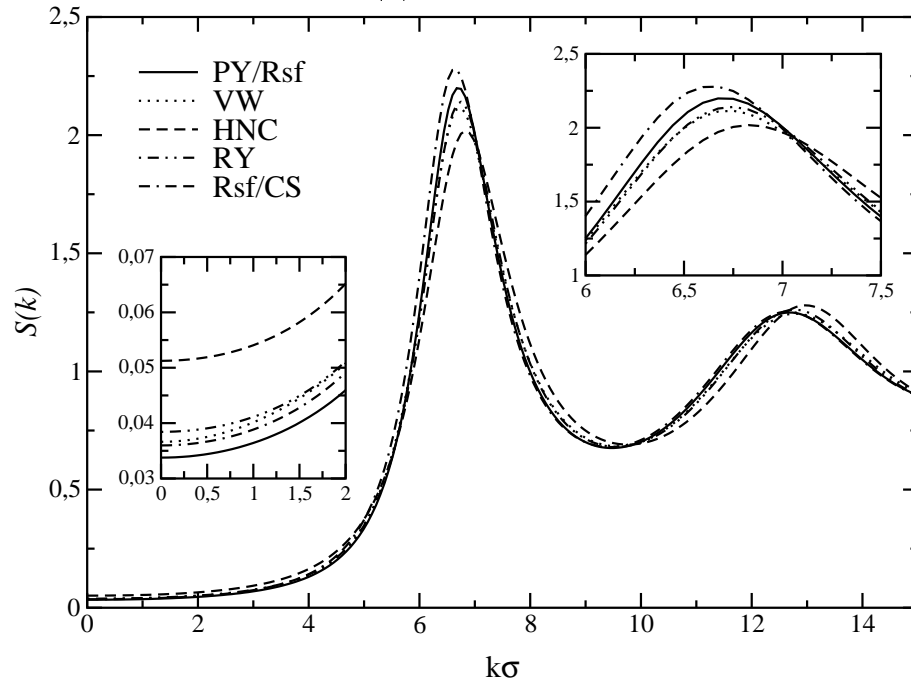
In figures 6.21 and 6.22, we present the corresponding results for $\rho = 0.2$. Although the density is now significantly lower than for figures 6.19 and 6.20, the basic trends (as discussed for $\rho = 0.8$) are still present; for example the core violation of the Rsf/CS solution. For $g(r)$ and $c(r)$, the results of the VW parameterization and the RY approximation are

Figure 6.19: Pair distribution functions $g(r)$ and Rogers-Young mixing function $f(r)$ (upper part) and direct correlation functions $c(r)$ (lower part) for the HS fluid at $\rho = 0.8$ for various methods.



now nearly indistinguishable, hence for the insets of figure 6.21 we have marked the VW solution with an additional plus sign.

As for the Rsf/CS method, we can say that this theory is useless for the study of the uniform HS fluid, due to the inability to recover the basic requirements for $g(r)$.

Figure 6.20: Static structure factor $S(k)$ for the HS fluid at $\rho = 0.8$ for various methods.

6.3.2 Thermodynamic properties of the fluid

Figure 6.23 shows the Helmholtz excess free energy for the HS fluid. The curves were calculated using various methods: PY/c and HNC/c: Percus-Yevick resp. Hypernetted-chain solution, compressibility route (3.33); PY/v and HNC/c: PY and HNC solution, virial route (3.25); CS and RY: Carnahan-Starling parameterization and Rogers-Young approximation, equation (3.33) and (3.25) yield the same result. The RY result is nearly identical to the CS result, which was introduced as an approximation for the results from computer simulations. Interestingly, the PY and HNC results fulfill the following relation:

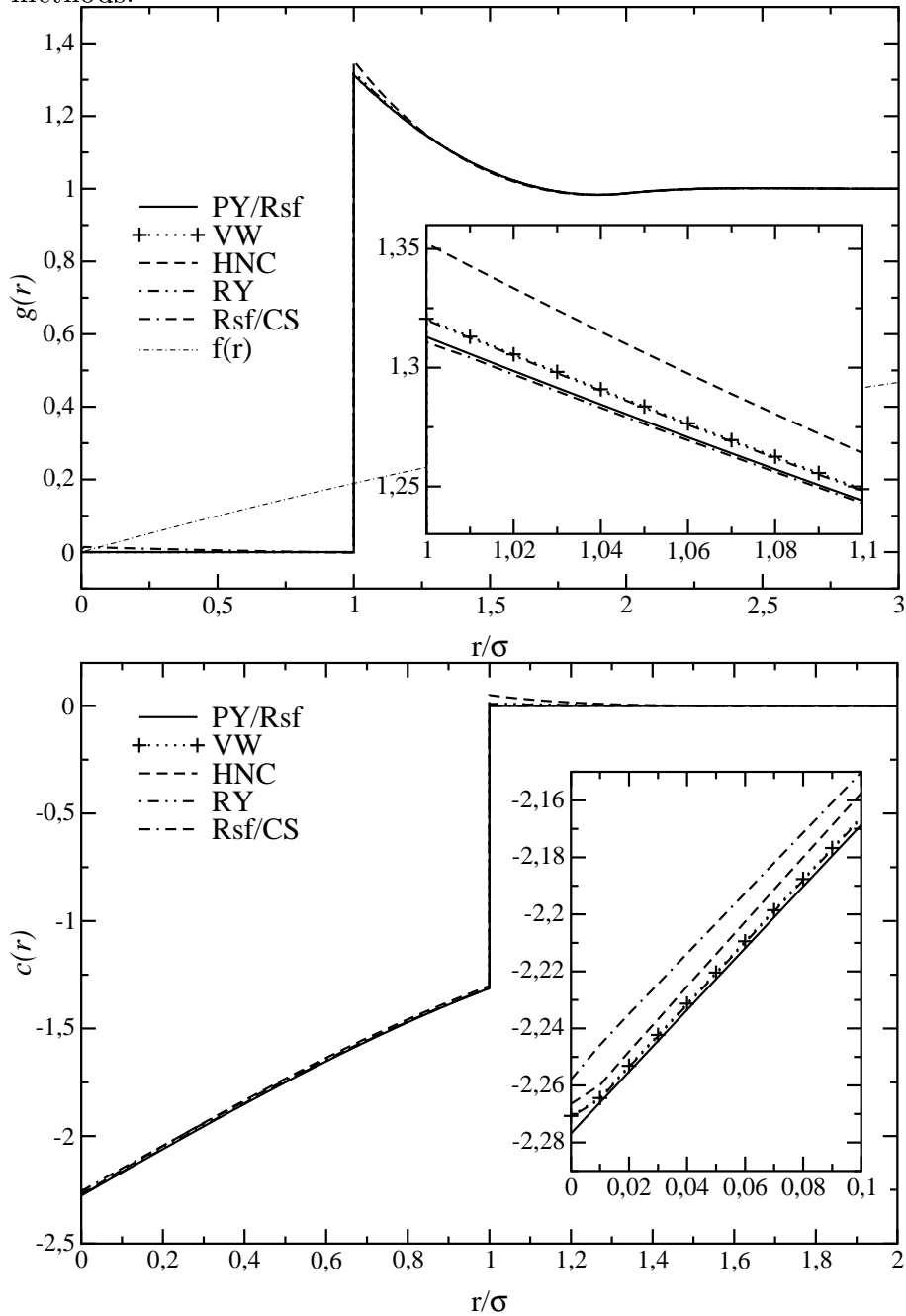
$$A_{HNC/c}(\rho) < A_{PY/v}(\rho) < A_{CS}(\rho) < A_{PY/c}(\rho) < A_{HNC/v}(\rho).$$

So the PY result for $A(\rho)$ is for both the virial and compressibility route a better solution than the HNC result. The rather high results for $A_{HNC/v}(\rho)$ are clear from figure 6.24, where the virial pressure $p^*(\rho)$ for the various methods is shown; the too low results for $A_{HNC/c}(\rho)$ can be justified by the high value for the static structure factor $S(k)$ for $k = 0$ (see figure 6.20):

$$A_{ex}^+(\rho) = \int_0^\rho d\rho' \left(\frac{\rho'}{\rho} - 1 \right) \left[1 - \frac{1}{S(k=0; \rho')} \right]$$

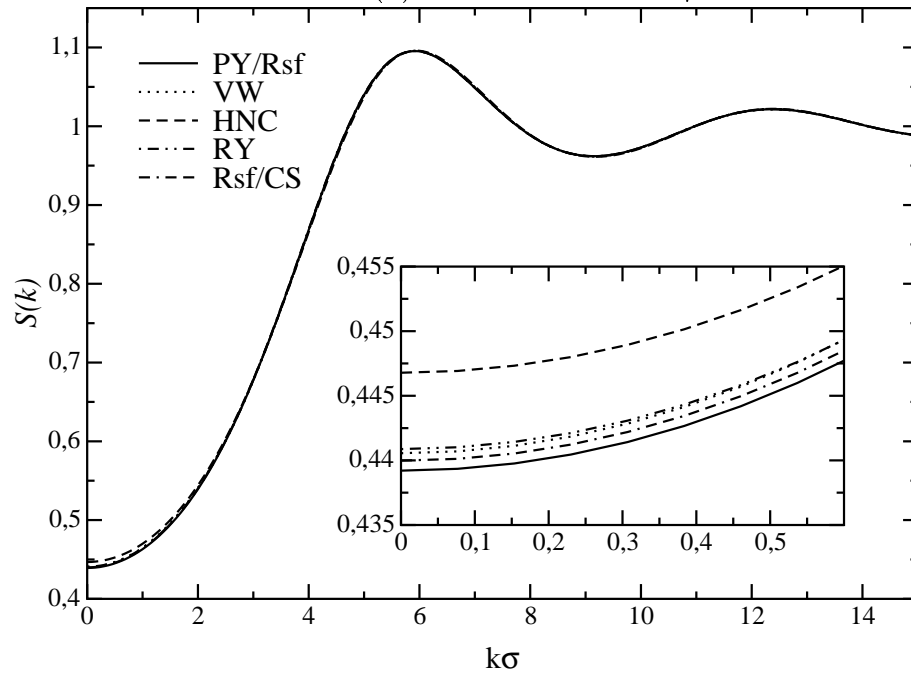
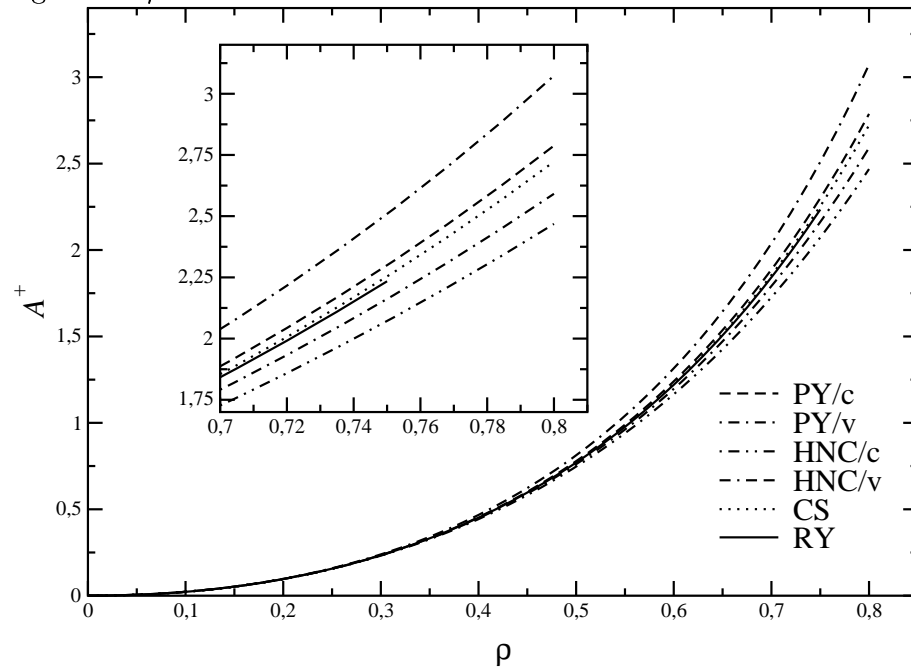
In figure 6.24 one can see, again, the good results one gets from the RY approximation (when compared with the CS results). However, the computational effort for RY approximation is substantially higher (mainly due to the requirement that the structure functions have to be evaluated for more than one density to evaluate the self consistency parameter)

Figure 6.21: Pair distribution functions $g(r)$ and Rogers-Young mixing function $f(r)$ (upper part) and direct correlation functions $c(r)$ (lower part) for the HS fluid at $\rho = 0.2$ for various methods.



than for the VW parameterization (which is given analytically).

Figure 6.25 shows the density dependent optimization parameter $\alpha(\rho)$. This parameter is a slowly varying function of ρ (and not a constant, as stated in [11]). The value for $\rho = 0$ was extrapolated, because for $\rho = 0$ the self consistency relation is fulfilled for all

Figure 6.22: Static structure factor $S(k)$ for the HS fluid at $\rho = 0.2$ for various methods.Figure 6.23: Helmholtz free energy $A_{ex}^+(\rho)$ for the HS fluid for various methods. The inset shows the region for $\rho > 0.7$.

parameters α . Interestingly, $\alpha(\rho)$ is not a strictly monotonic function of ρ . It can be

Figure 6.24: Virial pressure $p^*(\rho)$ for the HS fluid for various methods. The inset shows the region for $\rho > 0.7$.

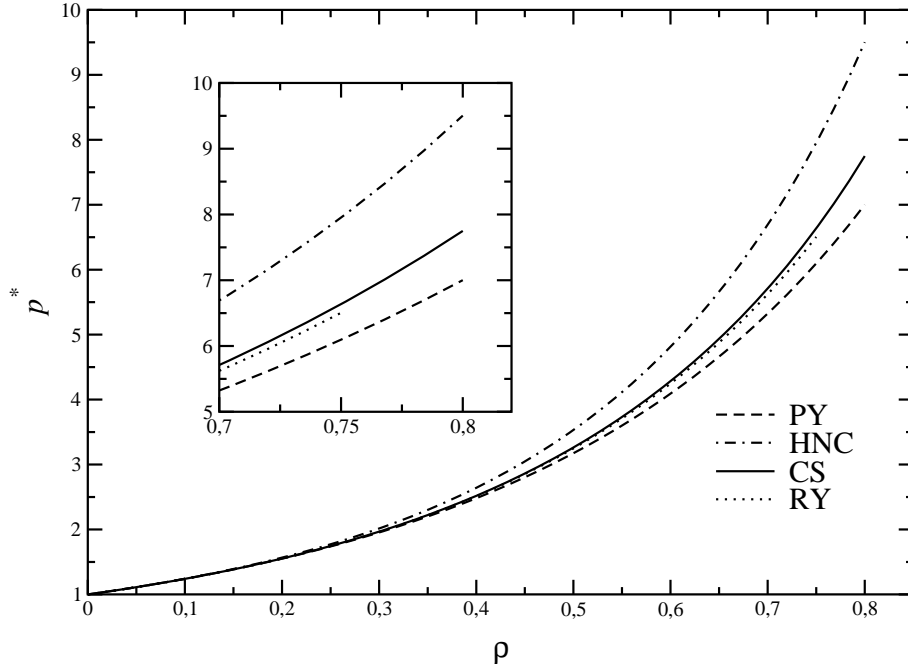
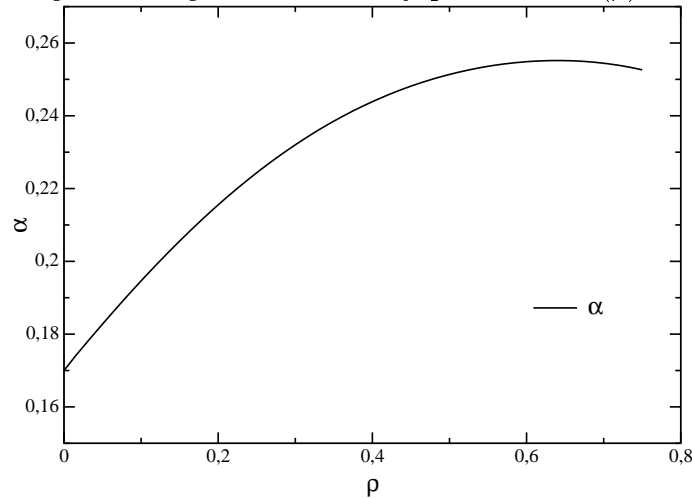


Figure 6.25: Rogers-Young self consistency parameter $\alpha(\rho)$ for the HS fluid.



easily seen from figures 6.25 and 6.19, that for small densities and distances r the PY part of the closure is in favor of the HNC part. This dominance decreases a little bit until $\rho \approx 0.635$, where the HNC part has its maximum contribution with $\alpha \approx 0.255$. Beyond this point, the HNC part loses ground against the PY part. However, it should be noted that for the whole ρ -range the PY part is always the dominating part of the closure for small distances r . In table 6.1, some numerical values for the pressure and the isothermal

Table 6.1: Numerical comparison between the CS parameterization and RY approximation results for the pressure $p^*(\rho)$ and the isothermal compressibility $\chi^*(\rho)$ of the HS fluid.

ρ	p_{RY}^*	p_{CS}^*	ε_p	χ_{RY}^*	χ_{CS}^*	ε_χ
0.08	1.1865	1.1865	0.0 %	8.9705	8.9702	0.003 %
0.16	1.4173	1.4174	-0.007 %	3.2376	3.2364	0.037 %
0.24	1.7043	1.7048	-0.029 %	1.5649	1.5628	0.134 %
0.32	2.0627	2.0645	-0.087 %	0.8533	0.8505	0.329 %
0.40	2.5129	2.5180	-0.203 %	0.4969	0.4936	0.669 %
0.48	3.0824	3.0946	-0.394 %	0.3011	0.2977	1.142 %
0.56	3.8084	3.8349	-0.691 %	0.1872	0.1839	1.794 %
0.64	4.7423	4.7961	-1.122 %	0.1182	0.1152	2.604 %
0.72	5.9568	6.0606	-1.713 %	0.0752	0.0726	3.581 %

compressibility for the HS fluid are shown together with their relative errors defined as

$$\varepsilon_X = \frac{X_{RY}^* - X_{CS}^*}{X_{CS}^*}.$$

Summarizing, we can say that the RY solution of HS and the CS approximation give results that are in good agreement (both thermodynamically and with respect to the structure) with the computer simulation results. The PY and the HNC solutions are both yielding results that are in fairly good agreement with the simulation data, but to a lesser extent than the two former theories.

6.3.3 Fluid-solid phase transition for the HS system

In this subsection we will present the results we obtained for the fluid-solid phase transition of the HS system. This (entropy driven) transition from a liquid to an fcc-solid has been extensively studied [97, 98, 99, 100, 101]. In table 6.2, the fluid-solid coexistence densities for various different methods (both for the fluid and the solid phase) are shown. $\Delta\rho$ is equal to $\rho_s - \rho_l$ and the error ε is defined as

$$\varepsilon = \frac{|\rho_l - \rho_{l,MC}|}{\rho_{l,MC}} + \frac{|\rho_s - \rho_{s,MC}|}{\rho_{s,MC}}, \quad (6.11)$$

where $\rho_{x,MC}$ is the respective liquid or solid density of the (Monte-Carlo) computer simulation. In this table, FVPA denotes the free volume perturbation approximation (see subsection 4.1.8) and Rsf/CS denotes the approach of Roland Roth, where the Carnahan-Starling equation of state is reproduced by a reformulation of the Rosenfeld (Rsf) free energy density Φ (see subsection 4.3.5). Figure 6.26 and 6.27 shows the double tangent construction for the fluid-solid phase transition for most of the methods of table 6.2. Remember that, for the fluid phase, the PY/compressibility gives the same results as the

¹Verlet-Weis parameterization for the fluid excess free energy, PY correlation functions used as input to the MWDA [75].

Table 6.2: Coexistence densities for the fluid-solid phase transition of the HS system.

Fluid method	Solid method	ρ_l	ρ_s	$\Delta\rho$	error ε
PY, compressibility route	MWDA	0.877	1.018	0.141	8.18 %
PY, virial route	MWDA	0.961	1.061	0.100	4.25 %
VW	MWDA	0.880	1.030	0.150	7.34 %
VW	MWDA/PY ¹	0.910	1.036	0.130	3.58 %
PY, compressibility route	FVPA	0.901	1.032	0.131	4.92 %
PY, virial route	FVPA	1.074	1.149	0.075	24.73 %
VW	FVPA	0.940	1.060	0.120	1.92 %
Rsf	Rsf	0.892	0.985	0.093	10.39 %
Rsf/CS	Rsf/CS	0.934	1.023	0.089	2.27 %
Computer simulation [100]		0.940	1.040	0.100	0 %

Rosenfeld functional and the VW parameterization is equal to the Rosenfeld/CS functional. The caption means the following:

PY/c: MWDA with Percus-Yevick correlation functions, excess free energy calculated using the compressibility route as input.

PY/v: MWDA with Percus-Yevick correlation functions, excess free energy calculated using the virial route as input.

VW/CS: MWDA with Verlet-Weis parameterization for the correlation functions as input.

Rsf: Rosenfeld functional using the ‘classical’ Φ (see subsections 4.3.3 and 4.3.4.2).

Rsf/CS: Rosenfeld functional where the free energy reproduces the Carnahan-Starling (CS) equation of state for the fluid phase (see subsection 4.3.5).

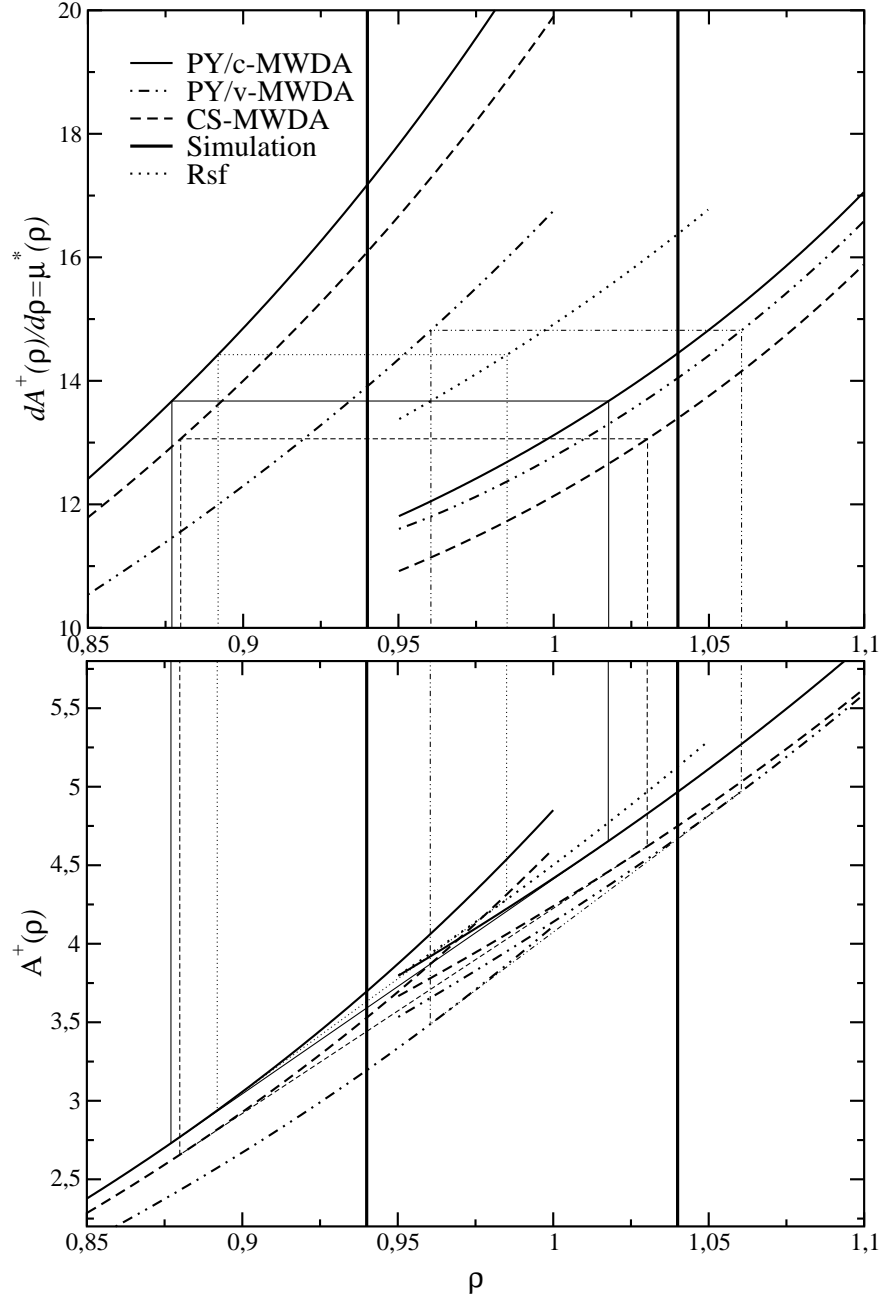
FVPA: Free volume approximation (see subsection 4.1.8).

By taking the error defined in equation (6.11) as a measure of the quality of the results, the VW-FVPA theory is the best approximation of the computer simulation data, followed by the Rosenfeld/CS approximation. The VW parameterization gives a very good result for the solid density, whereas the fluid density is a bit too low; however, the free energy for the fluid reproduces the CS equation of state which is a very good approximation for the free energy from computer simulations.

Interestingly, for the solid phase the result of the original Rosenfeld functional and the Rosenfeld/CS functional in figure 6.26 and 6.27 are nearly identical. One can see from figure 6.28 (where the localization parameter $\alpha(\rho)$ of the one-particle density parameterization (C.1) for the various theories is shown), that $\alpha(\rho)$ for the Rsf/CS functional (in the density range $0.95 \leq \rho \leq 1.05$) is related to $\alpha(\rho)$ of the original Rsf functional by

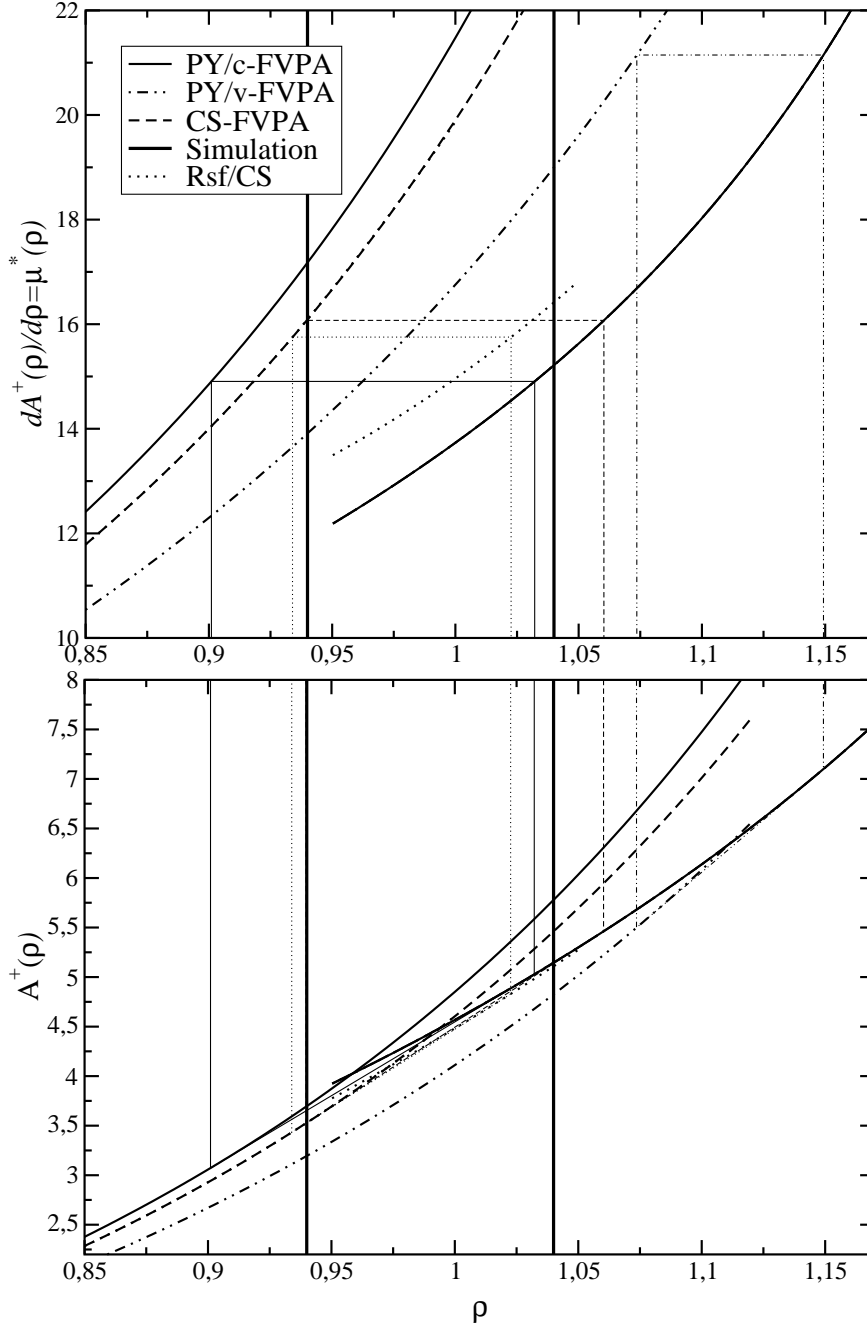
$$\alpha_{Rsf}(\rho) \approx \alpha_{Rsf/CS}(\rho) + 5,$$

Figure 6.26: The double tangent construction for the fluid-solid phase transition of the HS system. Lower graph: free Energy A^+ as a function of ρ ; upper graph: derivative of free energy $A^+(\rho)$ with respect to ρ (=chemical potential μ^*)



thus leading to an ideal free energy for the Rsf/CS functional that is always lower than the ideal free energy for the Rsf functional. Because of this relation, the density profile (and so the weighted densities) of the solid calculated using the Rsf functional are slightly sharper than the ones predicted by the Rsf/CS functional. Thus, the overlap of the various weighted densities from the different lattice sites is bigger for the Rsf/CS, resulting in an

Figure 6.27: The double tangent construction for the fluid-solid phase transition of the HS system. Lower graph: free Energy A^+ as a function of ρ ; upper graph: derivative of free energy $A^+(\rho)$ with respect to ρ ($=$ chemical potential μ^*)



increased free energy density Φ in the areas where the overlap occurs. So the excess free energy of the Rsf/CS functional is higher (and, as can be seen from figure 6.26 and 6.27) by approximately the same amount as the ideal energy is lower. The behavior of the excess free energy $A_{ex}^+(\rho)$ for the various methods is shown in figure 6.29. By comparing

Figure 6.28: Localization parameter $\alpha(\rho)$ for the various methods used to evaluate the solid phase of the HS system.

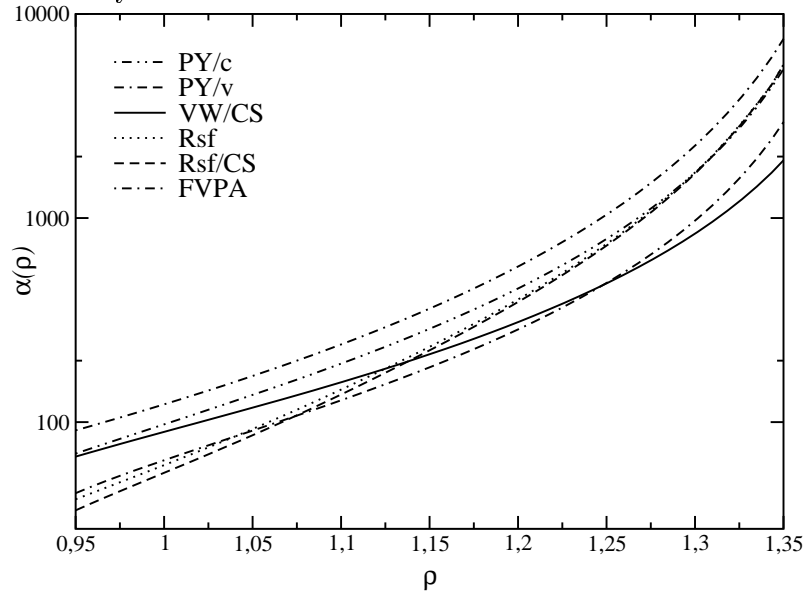


Figure 6.29: Excess free energy $A_{ex}^+(\rho)$ of the HS system for the fcc solid.

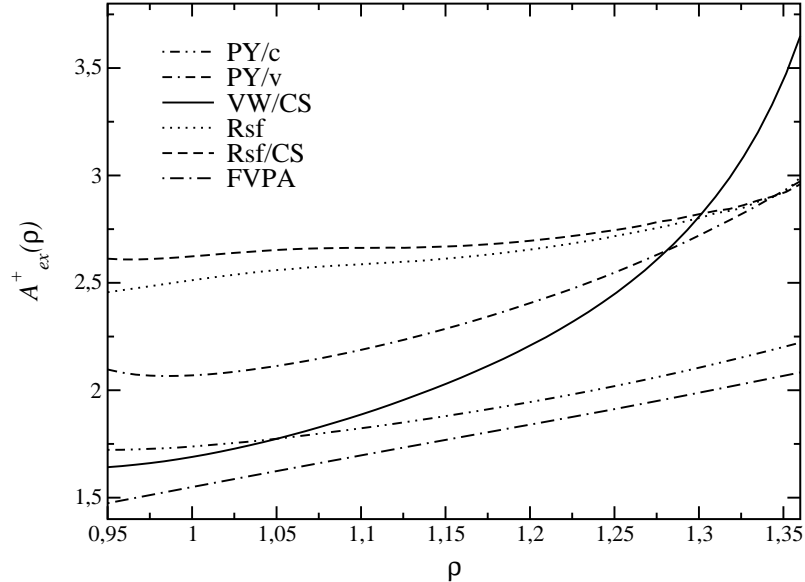
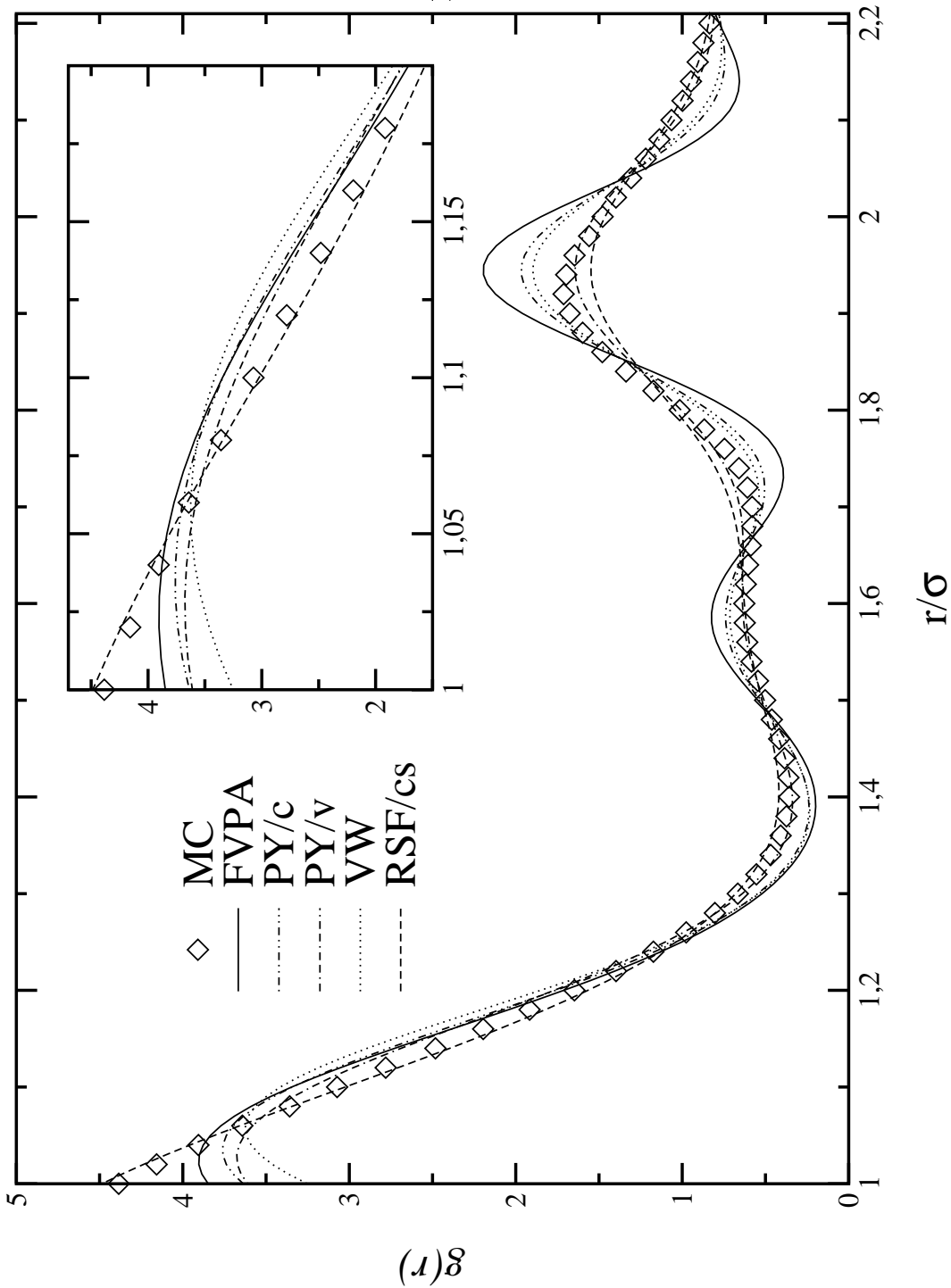
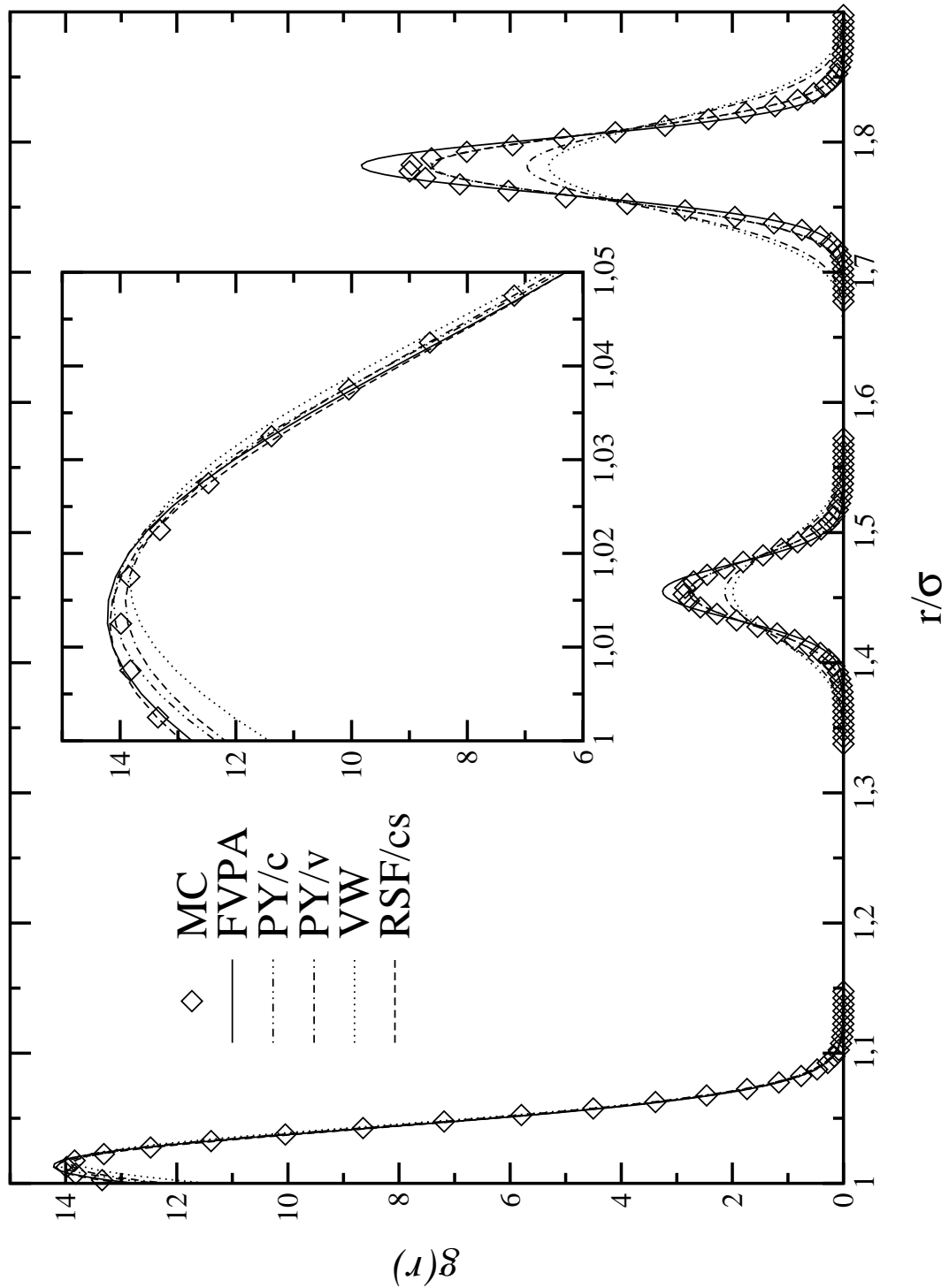


figure 6.28 and 6.29, the following basic trend emerges (up to $\rho_s \approx 1.04$): The lower the localization parameter α is for a given theory, the higher the excess free energy is for the same theory. α tries to compensate the lower ideal free energy by increasing the overlap of the particles at the lattice sites as discussed above.

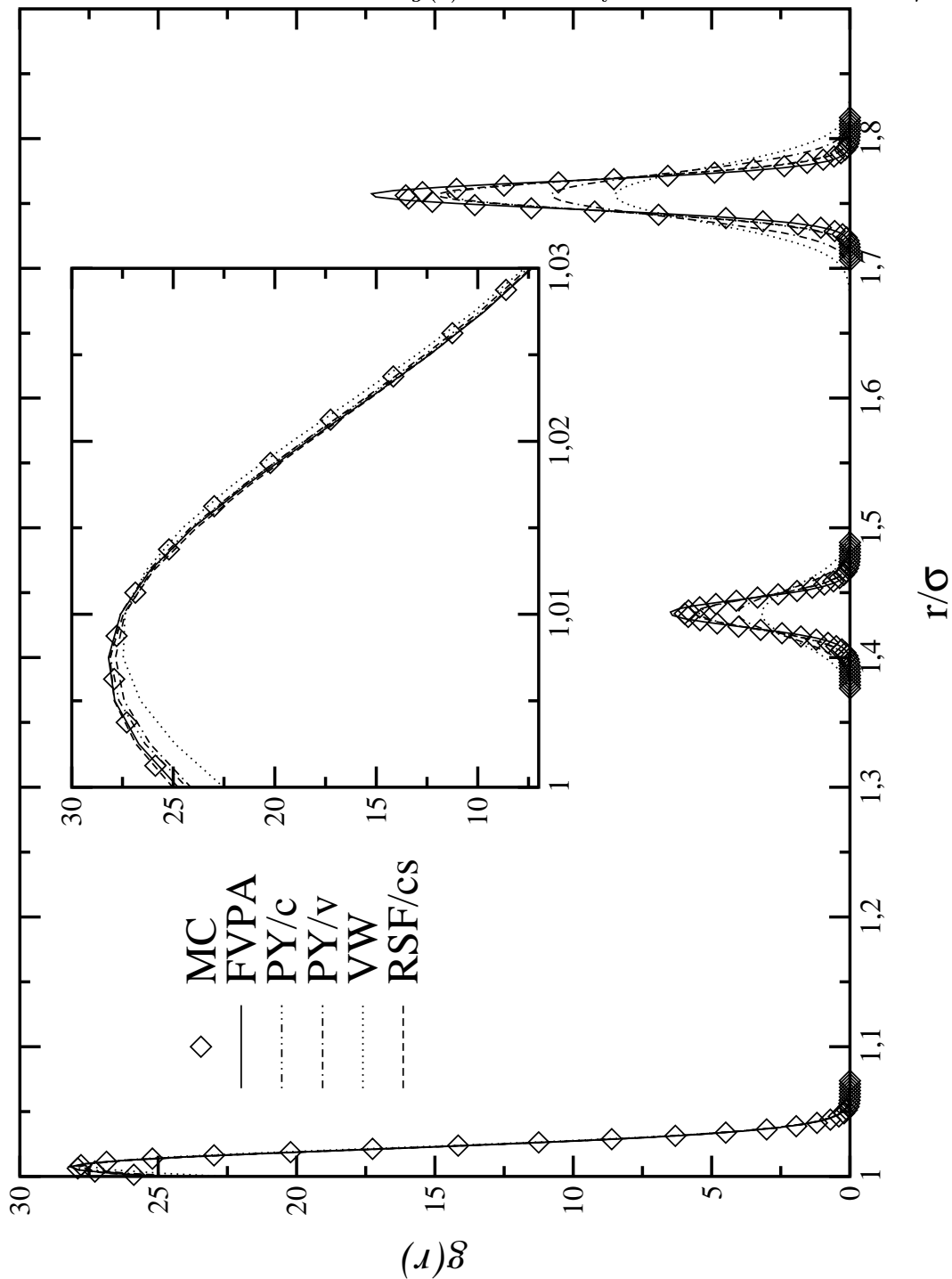
Figure 6.30: Pair distribution function $g(r)$ of the HS system for the fcc solid at $\eta = 0.52$.

6.3.4 Solid structure

Using the parameterization of the pair distribution function $g(r)$ as defined in section C.3, we have calculated the $g(r)$ for the solid packing fractions $\eta = 0.52$, 0.68 and 0.71 using

Figure 6.31: Pair distribution function $g(r)$ of the HS system for the fcc solid at $\eta = 0.68$.

various theories in order to be able to compare them with the computer simulation results from [102].

Figure 6.32: Pair distribution function $g(r)$ of the HS system for the fcc solid at $\eta = 0.71$.

For $\eta = 0.52$ (figure 6.30, $\rho = 0.9931$), the Rsf/CS functional is the only theory that predicts the first peak correctly (in the framework of our used parameterization of $g(r)$ [82, 83]). All other theories are showing a peak that is too small when compared with

the computer simulation results. If one looks at the second and third peak (at $r \approx 1.6$ and $r \approx 1.95$), it is clear that the FVPA, the PY/c and the VW results are exaggerating the oscillations of $g(r)$ (because their $\alpha(\rho)$'s are too low), whereas the PY/v result gives a very good approximation in this range of r . Overall, the Rsf/CS functional gives the best result, being a slightly worse approximation to the computer simulation $g(r)$ than the PY/v result for outside the first peak ($r > 1.3$).

For $\eta = 0.68$ (figure 6.31, $\rho = 1.2987$), the picture changes a little bit. For the first peak, the Rsf/CS result is still the best approximation; the FVPA now gives a comparable result for this range of r . The PY/c, PY/v and VW results are too low (with the same 'ranking' as for $\eta = 0.52$). For the second and third peak, the FVPA still predicts too narrow values (which is clear from the according curve in figure 6.28), and the VW result is still too low (as predicted by 6.28). In contrast to figure 6.30, the PY/v result now gives a result that is of similar quality as the VW parameterization. The PY/c and the Rsf/CS result are nearly identical and are offering a very good approximation to the computer simulation data.

For $\eta = 0.71$ (figure 6.32, $\rho = 1.3560$) the behavior is very similar to $\eta = 0.68$. Now the difficulties of the VW and the PY/v approximations are obvious; both of them are predicting peaks that are too broad. For the first peak, the Rsf/CS functional comes once again very close to the computer simulation, with the FVPA solution only slightly worse. The VW parameterization fails badly at the first peak, even when compared to the other theories. For peak two and three, the FVPA now gives the best approximation of the simulation results.

This leads us to the following conclusions:

- The localization parameter $\alpha(\rho)$ fitted to the computer simulation results lies somewhere between $\alpha_{Rsf/CS}(\rho)$ and $\alpha_{FVPA}(\rho)$, where the former dominates for smaller ρ and the latter is dominating the region towards the closed packing limit.
- The VW parameterization predicts, albeit its satisfactory result for the location of the fluid-solid phase transition, for high densities a solid structure where the localization of the particles around their lattice sites is underestimated.
- The Rsf/CS functional is the theory which gives the best overall agreement with the computer simulation results, both for the structure and the fluid-solid phase transition.
- The Rsf functional gives a solid structure which is comparable to the Rsf/CS functional, but the predicted fluid-solid phase transition occurs at densities that are too low.
- The FVPA gives a remarkably good approximation for the fluid-solid phase transition. The FVPA also gives a good result for the solid pair distribution function for densities near the closed packing limit.

Finally, in figures 6.33 to 6.37 we have visualized¹ the free energy density $\Phi(\vec{r})$ for the solid HS system (fcc lattice) at various densities ($\rho_s = 0.95, 1.0, 1.05, 1.1$); two results for

¹Using IBM's visual data explorer (dx).

Figure 6.33: Iso-surface plot of the free energy density $\Phi(\vec{r})$ for the HS system, fcc lattice with $\rho_s = 0.95$. Shown is the result for the Rosenfeld functional.

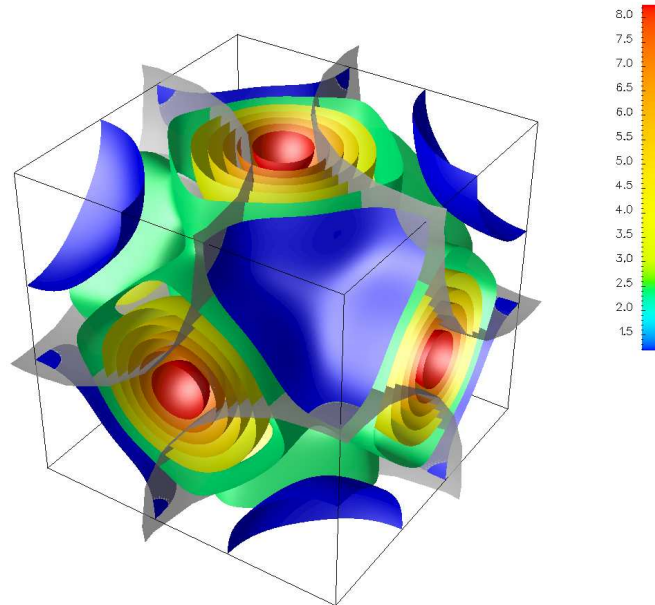
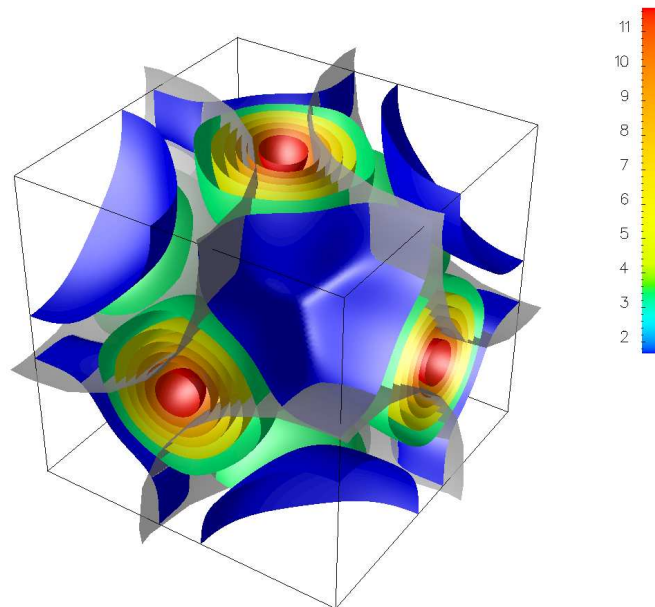


Figure 6.34: Iso-surface plot of the free energy density $\Phi(\vec{r})$ for the HS system, fcc lattice with $\rho_s = 1.0$. Shown is the result for the Rosenfeld functional.



the bcc lattice are presented in figure 6.38 ($\rho_s = 1.0$) and 6.39 ($\rho_s = 1.2$). Shown are the results we got using the (classical) Rosenfeld functional; the Rosenfeld/CS results are looking identical on this length scale. The hard sphere particles are displayed as quarter-

Figure 6.35: Iso-surface plot of the free energy density $\Phi(\vec{r})$ for the HS system, fcc lattice with $\rho_s = 1.05$. Shown is the result for the Rosenfeld functional.

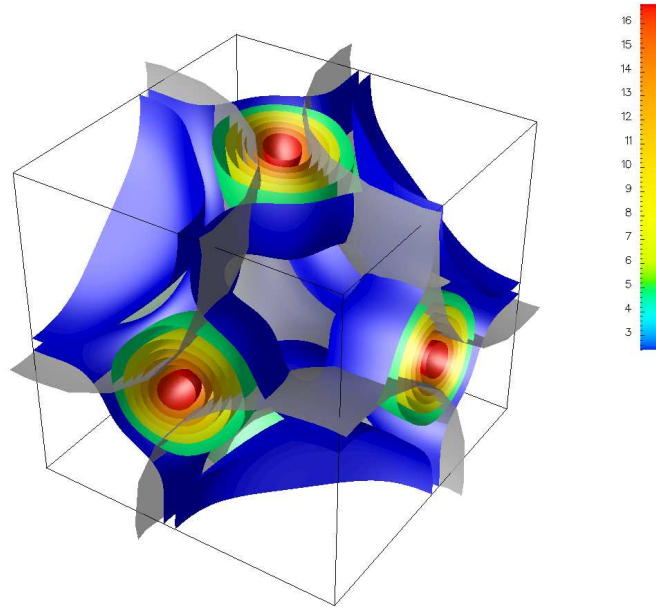
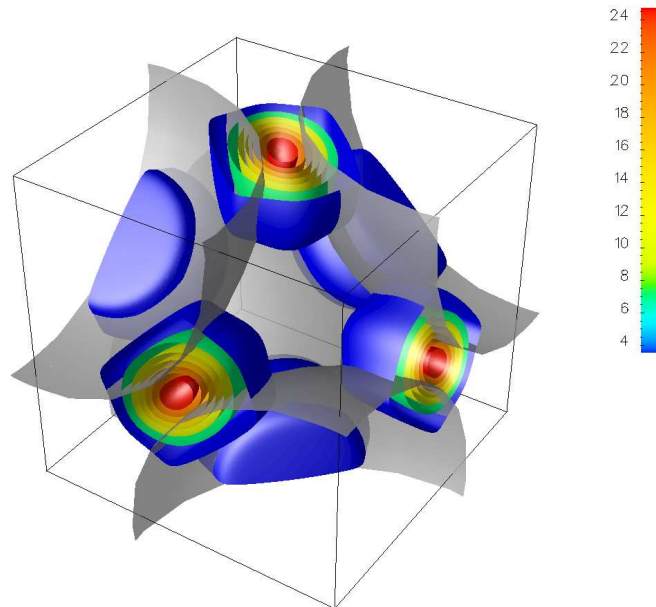


Figure 6.36: Iso-surface plot of the free energy density $\Phi(\vec{r})$ for the HS system, fcc lattice with $\rho_s = 1.1$. Shown is the result for the Rosenfeld functional.



spheres at their respective lattice positions.

For $\rho_s = 0.95$ (figure 6.33) and $\rho_s = 1.0$ (figure 6.34), the free energy density $\Phi(\vec{r})$ is a slowly varying function of \vec{r} . The maximum of $\Phi(\vec{r})$, $\sigma^3\Phi_{max}(\vec{r}) \approx 8 - 10$, occurs in

Figure 6.37: Iso-surface plot of the free energy density $\Phi(\vec{r})$ for the HS system, fcc lattice with $\rho_s = 1.2$. Shown is the result for the Rosenfeld functional.

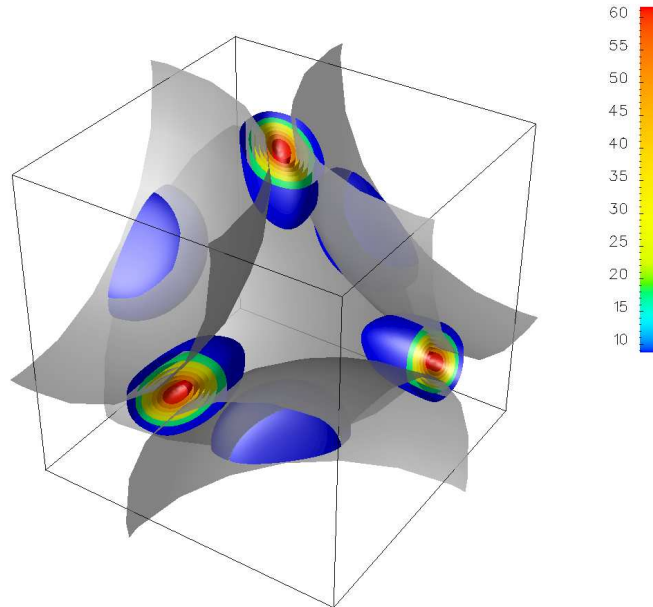
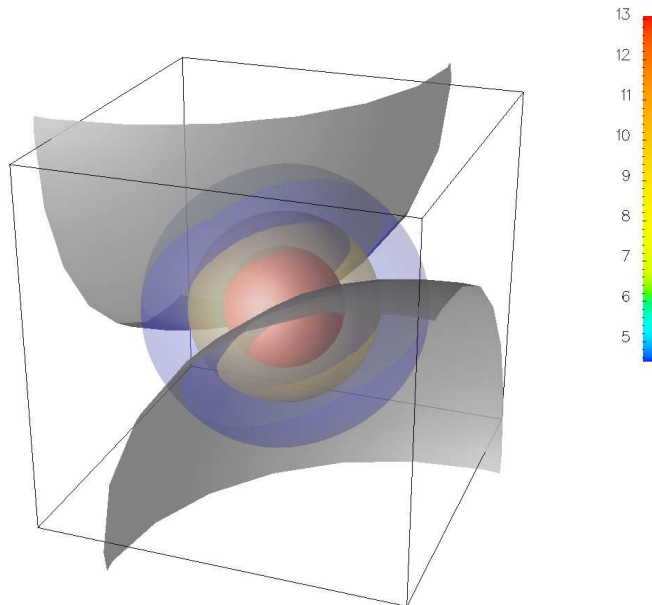
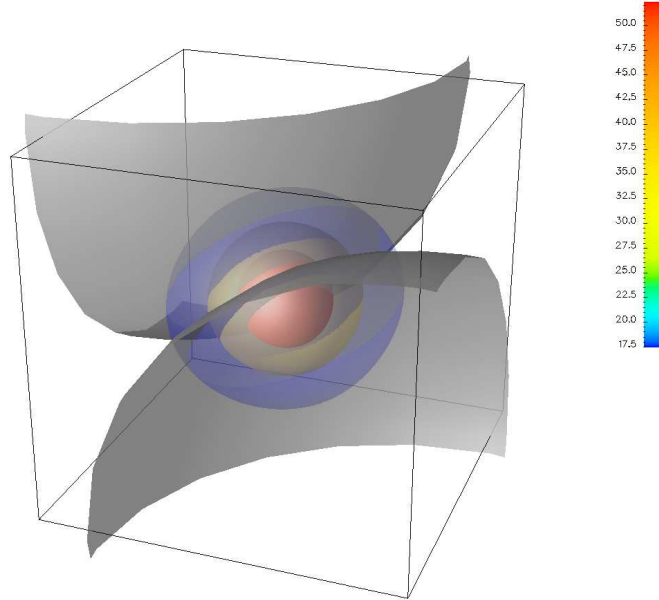


Figure 6.38: Iso-surface plot of the free energy density $\Phi(\vec{r})$ for the HS system, bcc lattice with $\rho_s = 1.0$. Shown is the result for the Rosenfeld functional.



the region where two sphere surfaces have their smallest distance to each other. Interestingly, for these two figures the free energy density is also nonzero inside the particles; for instance for $\rho_s = 0.95$ there is an iso-surface at about the half particle radius. This

Figure 6.39: Iso-surface plot of the free energy density $\Phi(\vec{r})$ for the HS system, bcc lattice with $\rho_s = 1.2$. Shown is the result for the Rosenfeld functional.



iso-surface is being pushed towards the outside of the particles at figure 6.34.

For $\rho_s = 1.05$ (figure 6.35), the free energy density is nonzero outside the core only for the regions around the maxima of $\Phi(\vec{r})$; this maxima are becoming sharper with increasing density and are now at $\sigma^3\Phi_{max}(\vec{r}) \approx 16$. The free energy forms some kind of ‘bonds’ between the particles. The iso-surface inside the particles mentioned above has also been pushed even more towards the particle surface.

For $\rho_s = 1.1$ (figure 6.36), the regions where the free energy density is nonzero are not connect anymore. $\Phi(r)$ is now being nearly completely pushed outside the particles, forming radially symmetric connections between the particles and their nearest neighbors. This ‘pushing out’ has further increased for $\rho_s = 1.2$ (figure 6.37). The maxima are now very sharp (with $\sigma^3\Phi_{max}(\vec{r}) \approx 60$), and the free energy density is zero for nearly the whole volume.

For the bcc crystal, the behavior of $\Phi(\vec{r})$ as a function of the solid density ρ_s is similar. However, it can be seen from figure 6.38 ($\rho_s = 1.0$) and 6.39 ($\rho_s = 1.2$) that the sharp localization of $\Phi(\vec{r})$ does not take place (albeit the close packing limit of the bcc crystal happens at a density that is lower than the close packing limit of the fcc crystal). Nevertheless, the maximum values of $\Phi(\vec{r})$ for the bcc crystal are comparable to the maxima of the fcc crystal. This behavior is subject to ongoing investigations.

6.4 Square well and square shoulder systems

In this section we will present the results for the one component square-well/square-shoulder potentials (partly published in [103]).

6.4.1 Fluid structure

Here, we will present the results for the pair distribution function $g(r)$. The thermodynamic parameters for which the various theories has been solved for the square-well fluid are shown in table 6.3. We begin with the square-well fluid having a potential width

Table 6.3: Thermodynamic parameters and theories for which the square-well system has been solved.

λ	T^*	ρ	Theories
1.5	1.0	0.8	EXP, ORPA, HNC, PY, MC (Simulation [103])
1.03	1.0	0.8	Nezbeda [25], EXP, ORPA, RY ($\alpha = 0.16667$), Rsf, Rsf/TPL
1.03	0.5	0.8	Nezbeda [25], EXP, ORPA, PY, HNC

$\lambda = 1.5$. In figure 6.40, we show results for $g(r)$ at $T^* = 1.0$. As can be seen from the left inset, the EXP yields the best contact value when compared to the simulation data; however, it is seriously inaccurate at $r = \lambda\sigma$. The ORPA also yields results which are in good agreement with simulation data; they are actually superior to the EXP approximation.

The situation with the RY closure is completely different. At density $\rho = 0.8$, there is no thermodynamically self-consistent solution to this closure at $T^* = 1.0$. This failure was also observed earlier in a different closure for the same system, by Bergholtz *et al.* [104]. They used the so called HMSA closure [105] (the HMSA closure equation interpolates continuously between the soft core, mean spherical approximation (SMSA) at short interparticle distances and the hypernetted chain closure (HNC) at larger interparticle distances). The reason of the lack of existence of a solution is the following: the RY closure is a mixture of the PY and the HNC closures. In a case where it works (for example hard spheres), the difference between the ‘fluctuation’ compressibility [see equations (3.31) and (4.47)] and the ‘virial’ compressibility [see equations (3.30) and (4.48)], has opposite signs for the HNC and the PY closure. In particular, the PY closure typically predicts virial compressibilities which are too high, so the quantity $\chi_T^c - \chi_T^v$ is negative. On the other hand, the HNC predicts too low virial compressibilities with the result that the the quantity $\chi_T^c - \chi_T^v$ is positive. With reference to figure 6.40, we now see that the major discontinuity in $g(r)$ (at $r = \sigma$), whose magnitude gives the dominant contribution to the virial pressure, turns out to be *higher* than the simulation result in *both* the PY and the HNC closures. Hence, both yield a positive value for the difference $\chi_T^c - \chi_T^v$ and a self-consistent solution of the RY closure does not exist. This is the same mechanism that brings about the failure of the HMSA closure (see above) of Bergholtz *et al.* [104] The self consistency parameter α of the RY closure cannot attain negative values, as is clear

Figure 6.40: Pair distribution functions $g(r)$ for the square-well fluid with $\lambda = 1.5$ at $\rho = 0.8$, $T^* = 1$ for various theories. The insets show the regions around $r = \sigma$ and $r = \lambda\sigma$.

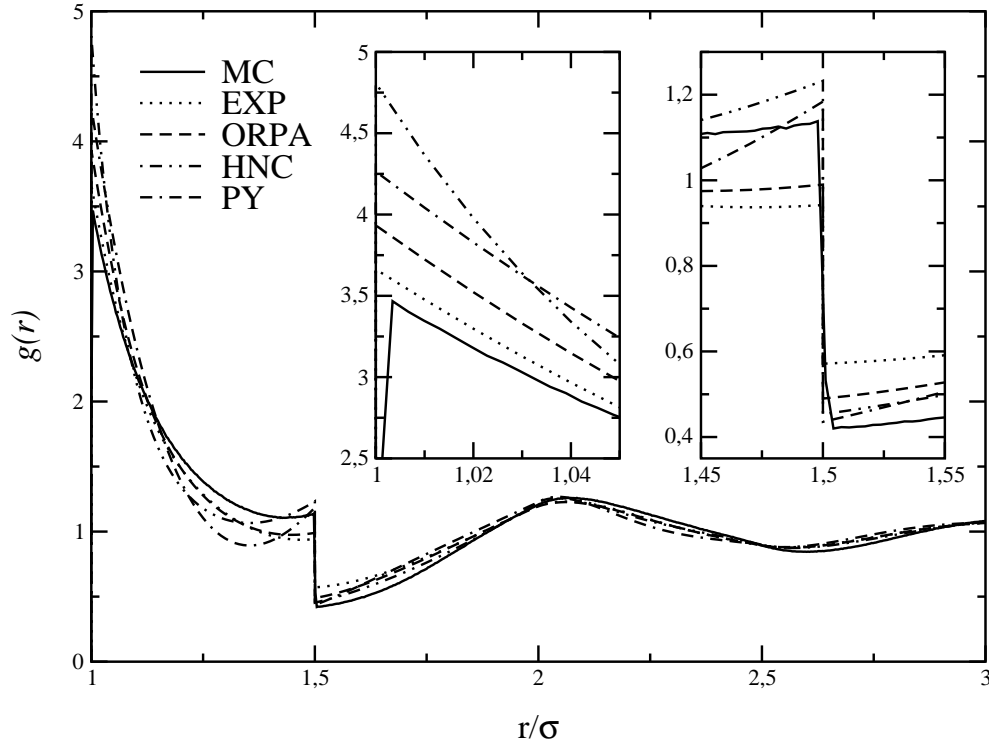


Figure 6.41: Rogers-Young self consistency parameter α as a function of inverse temperature for the square-well fluid with $\lambda = 1.5$ at various densities.

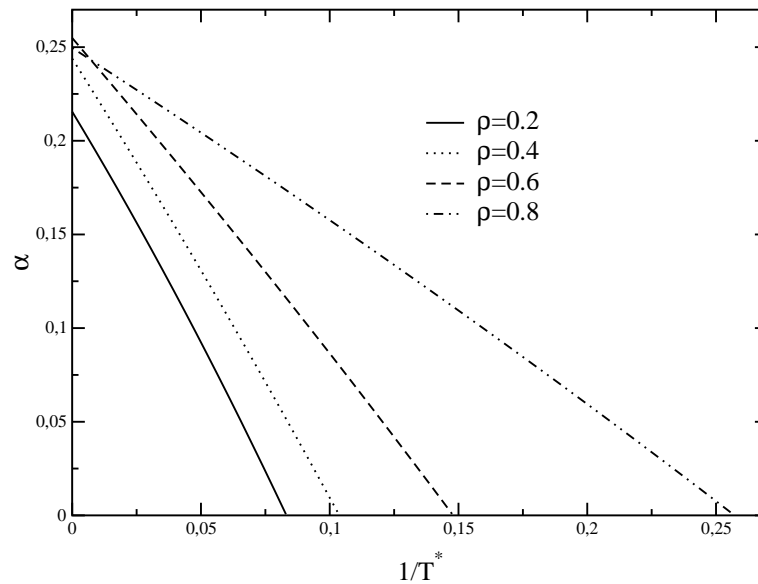
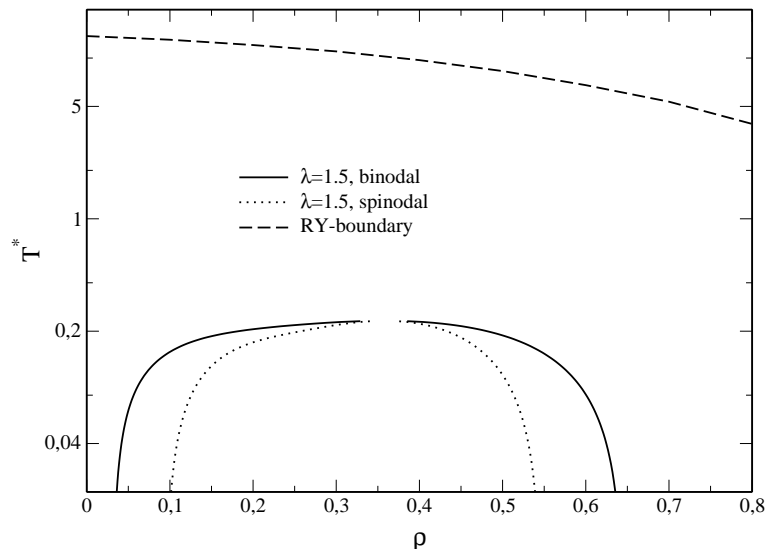


Figure 6.42: The fluid part of the phase diagram of the $\lambda = 1.5$ square-well fluid as calculated within the ORPA and the locus of points where we were unable to find a self-consistent solution of the RY closure (i.e., α tends to be smaller than zero). Below this boundary, $\alpha < 0$ and the RY closure has no self-consistent solution.

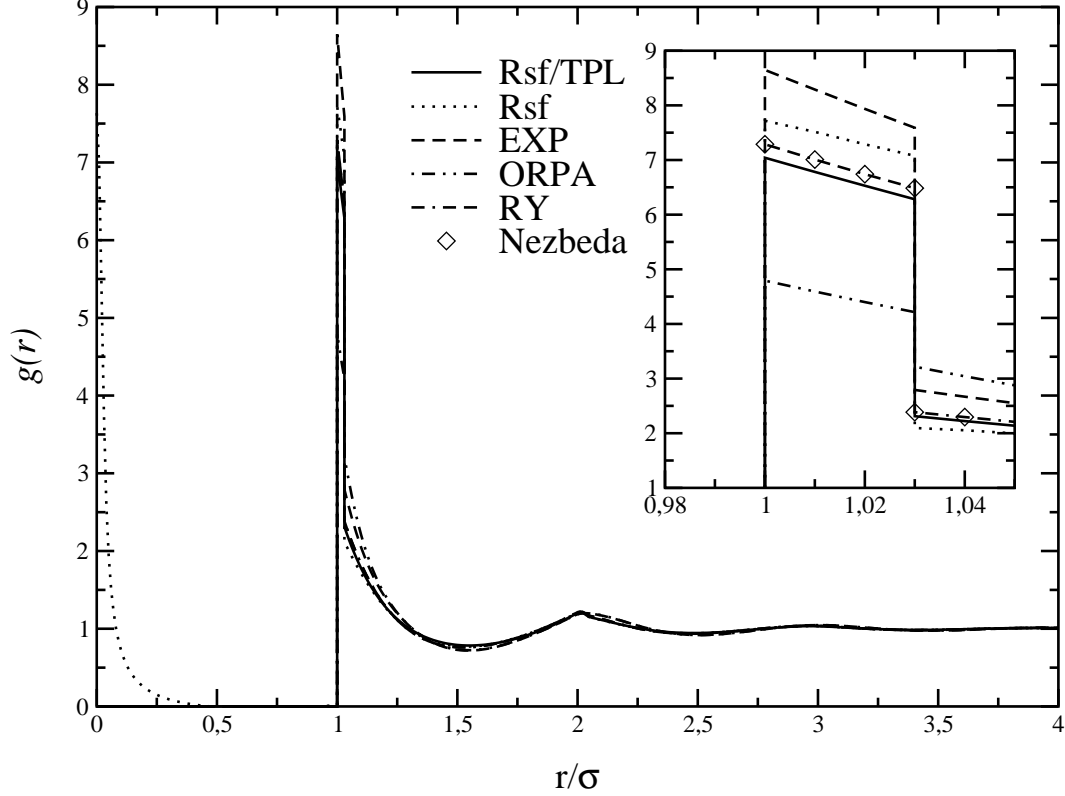


from equation (4.45). We can, therefore, trace out the domain in thermodynamic space where the RY closure fails, by keeping track of the value α as a function of density and temperature and working out the locus of points where $\alpha = 0$. In figure 6.41 we show the parameter α as a function of inverse temperature for the square-well fluid with $\lambda = 1.5$ for a number of reduced densities. It can be seen that with decreasing temperature the mixing parameter decreases for all values of the reduced density. Beyond the point where $\alpha = 0$, the solution of the RY closure is no longer self consistent. In figure 6.42 the locus of points $\alpha = 0$ in conjunction with the fluid part of the phase diagram of the system, as calculated within the ORPA, is shown.

For narrow square-well systems ($\lambda = 1.03$), the solution of the RY closure is unproblematic. In figure 6.43 we show results for various theories, including the Rosenfeld (Rsf, with and without the test particle limit (TPL) applied) and the Nezbeda solution (see subsection 2.2.2 and [25]). The Nezbeda solution is an approximate analytic solution for the direct correlation function $c(r)$ within the PY approximation. The Nezbeda approximation is valid for short range wells or shoulders, typically $\lambda \leq 1.05$ *only*; its advantage is that all the parameters that enter the expressions for the correlation functions can be given analytically as functions of density and temperature, for a summary see [13].

In figure 6.43, the simulation result is practically indistinguishable for the RY result and is thus not shown. The Rsf result without the TPL shows a violation of the core condition. If one applies the TPL to the Rsf functional, the quality of the result increases significantly. The ORPA and the EXP approximations, however, predict too low and too high values for $g(r)$ in the narrow well. In figure 6.44, the results for $T^* = 0.5$ are shown. Although the solutions of the PY and the HNC closure yield both results which are very close to the Nezbeda solution (which is in a very good agreement with the simulation

Figure 6.43: Pair distribution functions $g(r)$ for the square-well fluid with $\lambda = 1.03$ at $\rho = 0.8$, $T^* = 1$ for various theories. The insets show the regions around $r = \sigma$ and $r = \lambda\sigma$.



results), we were unable to find a mixing parameter α for which the RY solution is self consistent.

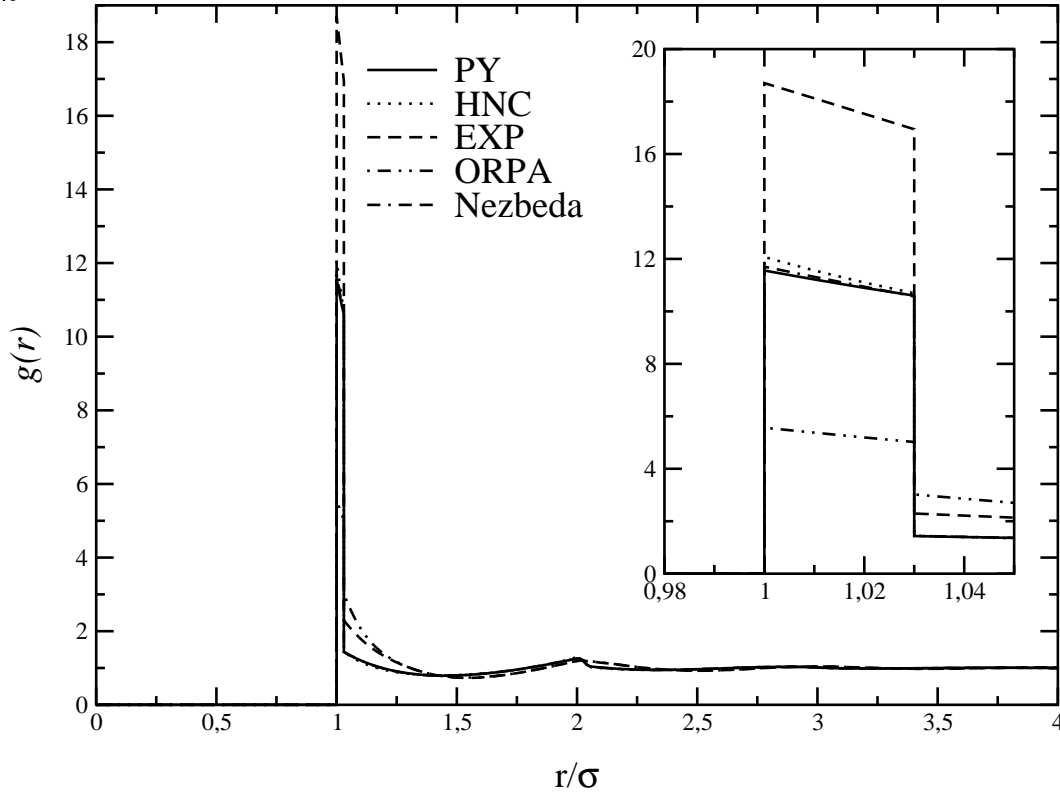
The thermodynamic parameters for which the various theories have been solved for the square-shoulder fluid are shown in table 6.4. Results for $g(r)$ are shown in figures 6.45

Table 6.4: Thermodynamic parameters and theories for which the square-shoulder system has been solved. The Monte-Carlo (MC) results were taken from [103].

λ	T^*	η	Theories
1.5	1.0	0.4	EXP, ORPA, RY ($\alpha = 1.0651$), MC (Simulation)
1.5	0.5	0.4	EXP, ORPA, RY ($\alpha = 1.6581$), MC (Simulation)
1.2	1.0	0.4	EXP, ORPA, RY ($\alpha = 0.6316$), MC (Simulation)
1.2	0.5	0.4	EXP, ORPA, RY ($\alpha = 0.7832$), MC (Simulation)

($\lambda = 1.5$) and 6.46 ($\lambda = 1.2$). It can now be seen that the RY closure delivers results which are in perfect agreement with simulation. We have further explored the thermodynamic space and was always able to find a self-consistent solution [$\alpha \in (0, \infty)$] of the

Figure 6.44: Pair distribution functions $g(r)$ for the square-well fluid with $\lambda = 1.03$ at $\rho = 0.8$, $T^* = 0.5$ for various theories. The insets show the regions around $r = \sigma$ and $r = \lambda\sigma$.



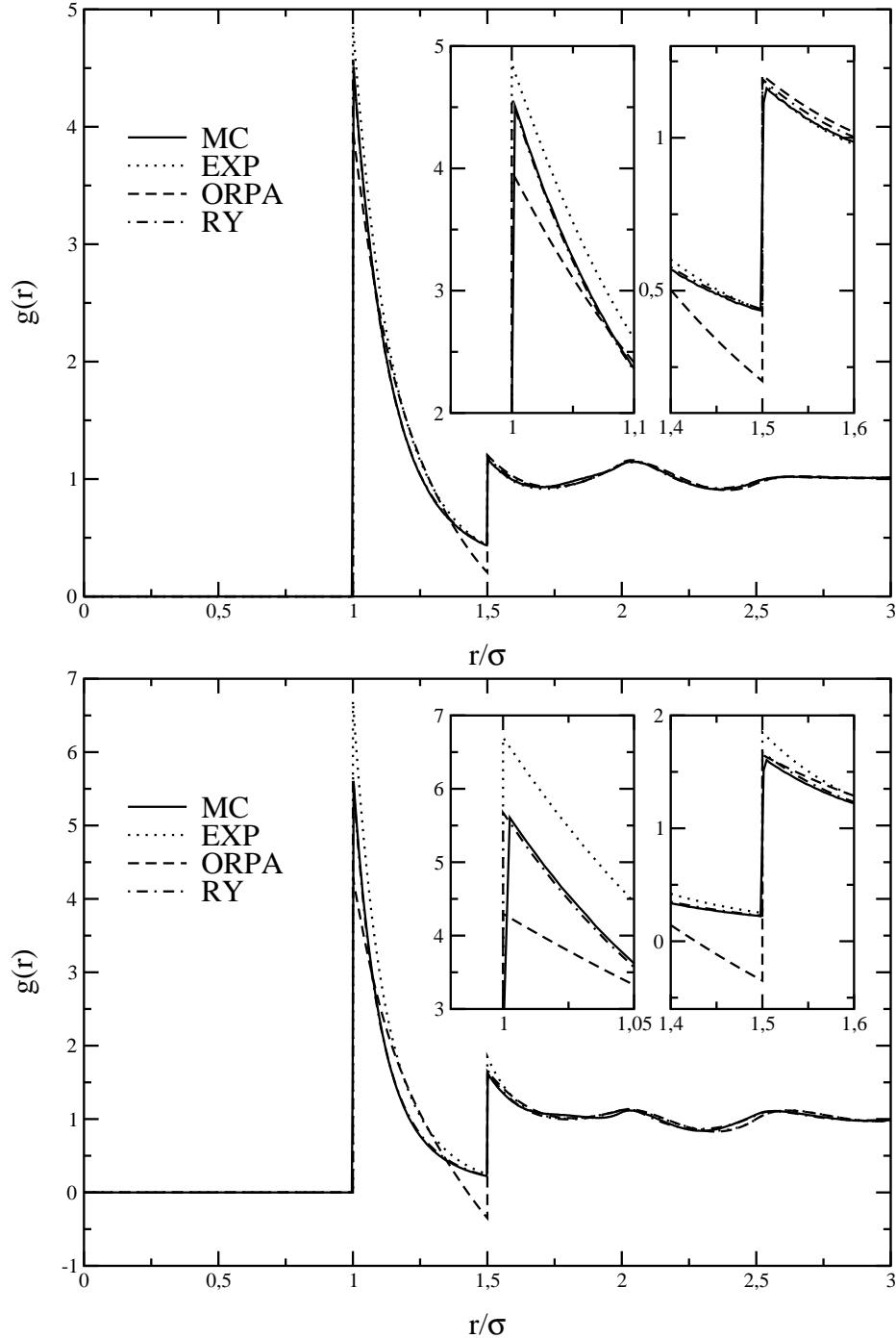
RY closure. We conclude, therefore, that *for purely repulsive potentials* the RY closure is problem free and, in addition, yields results of excellent quality in comparison with the simulation data.

The ORPA and the EXP approximation, on the other hand, do not yield satisfactory agreement with simulation. In one case, $\lambda = 1.5$, $T^* = 0.5$ and $\eta = 0.4$, the ORPA even predicts a region where $g(r)$ is negative (lower graph of figure 6.45), a clearly unphysical solution. The reason for this failure can be traced back to the perturbative nature of the ORPA. Indeed, from the defining equations for the ORPA [see equation (4.5)] it is clear that the latter is a high-temperature approximation which is bound to fail at sufficiently low temperatures as the quantity $-\beta\phi_1(r)$ will tend to minus infinity for the case of the square-shoulder potential. In figures 6.47 and 6.48 we delineate the region in the density-temperature plane where the ORPA leads to negative $g(r)$ in the case of the square-shoulder systems with $\lambda = 1.5$ and $\lambda = 1.2$, respectively.

6.4.2 Thermodynamic properties

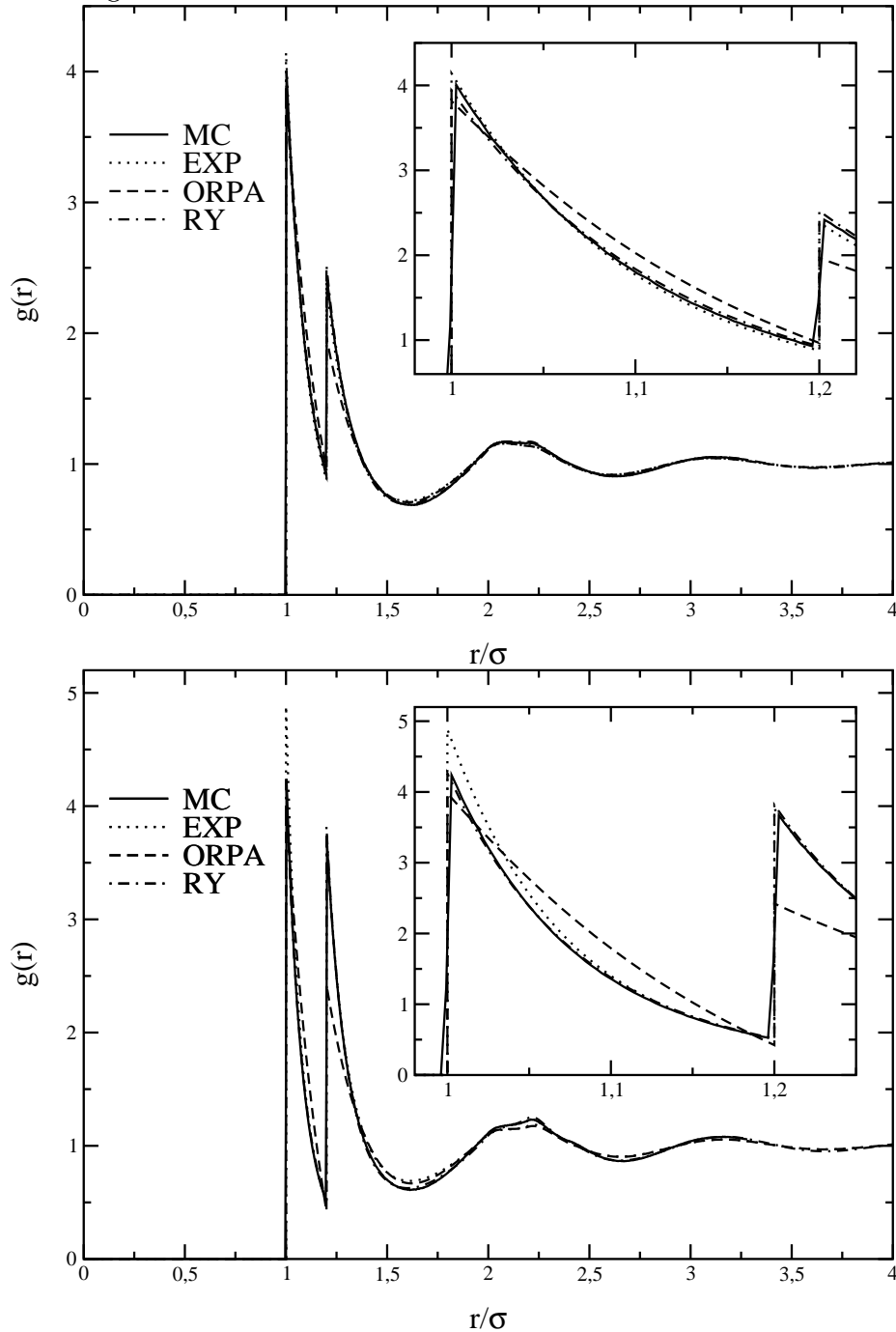
We have examined the thermodynamic properties for the square-well and square-shoulder potential for a number of parameters, shown, together with the results, in tables 6.5

Figure 6.45: Pair distribution functions $g(r)$ for the square-shoulder fluid with $\lambda = 1.5$ at $\eta = 0.4$, $T^* = 1$ (upper graph) and $T^* = 0.5$ (lower graph) for various theories. The insets show the regions around $r = \sigma$ and $r = \lambda\sigma$.



and 6.6. The calculation was carried out using the ORPA and EXP approximations. Remarkable is the thermodynamic inconsistency of the pressure (with an error of $\approx 200\%$)

Figure 6.46: Pair distribution functions $g(r)$ for the square-shoulder fluid with $\lambda = 1.2$ at $\eta = 0.4$, $T^* = 1$ (upper graph) and $T^* = 0.5$ (lower graph) for various theories. The insets show the regions around $r = \sigma$ and $r = \lambda\sigma$.



for the pressure self-consistency of the $\lambda = 1.03$ and $T^* = 0.5$ square-well system. In figure 6.49 we plot the results for the pressure, obtained via the virial and the energy route within the EXP for a square-well system of range $\lambda = 1.5$ and three different tem-

Figure 6.47: The region of failure for the ORPA, square-shoulder potential with $\lambda = 1.5$. The region is denoted by dots.

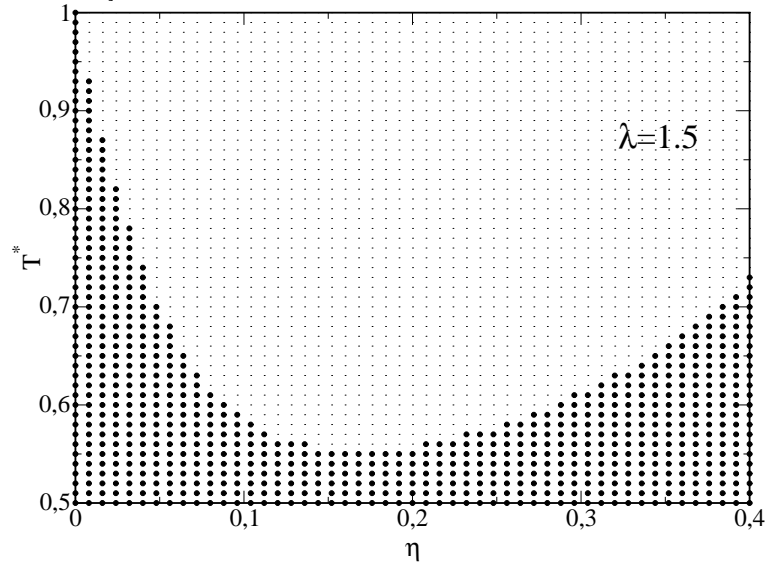
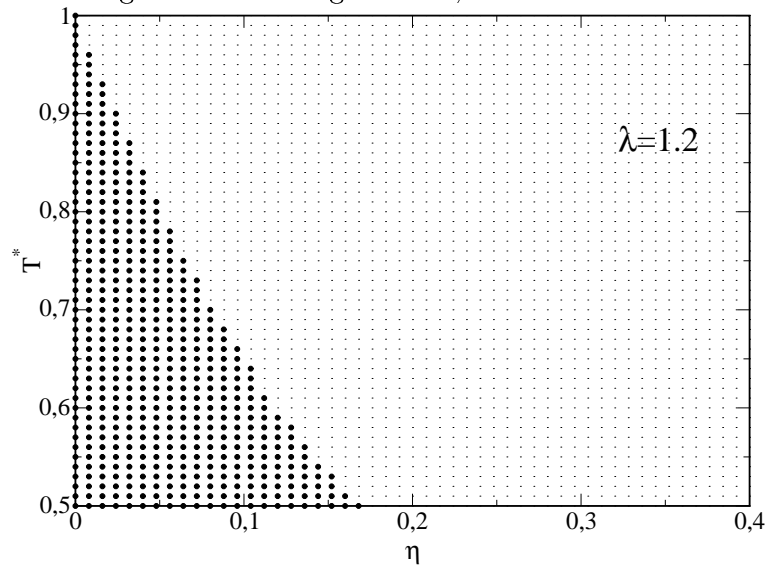


Figure 6.48: As figure 6.47, but for $\lambda = 1.2$.



peratures T^* ; the error bars indicate the difference between two different thermodynamic routes for the pressure and hence the degree of thermodynamic inconsistency. Figure 6.50 present similar results for a square-shoulder system with $\lambda = 1.2$. We observe that the thermodynamic self-consistency gets worse as the temperature decreases.

Table 6.5: Thermodynamic properties for various square-well fluids at density $\rho = 0.8$. p_v^* and p_c^* denote the pressure calculated by the virial [see equation (3.19)] and compressibility routes; U_{ex}^* and $U_{e,ex}^*$ are the excess internal energy per particle calculated by the virial [equation (3.16)] and energy routes; χ_T^c and χ_T^v denote the ‘compressibility’ and ‘virial’ isothermal compressibilities, respectively.

λ	T^*	p_v^*	p_c^*	U_{ex}^*	$U_{e,ex}^*$	χ_c^T	χ_v^T
ORPA							
1.50	1.0	3.1576	2.5810	-3.11786	-3.11666	0.07154	0.05054
1.03	1.0	2.2251	6.1576	0.53433	0.53573	0.05037	0.18271
1.03	0.5	-4.3965	4.4958	-0.09446	-0.08885	0.05571	-0.08456
EXP							
1.50	1.0	2.2680	2.8667	-2.98020	-3.07134	0.07154	0.05200
1.03	1.0	6.7050	5.7104	0.16009	0.22626	0.05037	0.05237
1.03	0.5	5.5124	2.3045	-2.69078	-2.19607	0.05571	0.05887

Table 6.6: Thermodynamic properties for various square-shoulder fluids at packing fraction $\eta = 0.4$. Symbols as for table 6.5.

λ	T^*	p_v^*	p_c^*	U_{ex}^*	$U_{e,ex}^*$	χ_c^T	χ_v^T
ORPA							
1.50	1.0	11.164	12.0939	4.12697	4.12880	0.03811	0.04856
1.03	1.0	10.749	8.2087	1.26262	1.26395	0.05143	0.03297
1.03	0.5	13.537	9.4209	1.37030	1.37562	0.04713	0.02379
EXP							
1.50	1.0	12.8124	12.3074	4.45280	4.16482	0.03811	0.04367
1.03	1.0	8.0333	7.9292	1.15479	1.16115	0.05143	0.04687
1.03	0.5	9.4576	8.4402	1.14153	1.11314	0.04713	0.03760

6.4.3 Phase diagrams

The phase diagram of square-well potentials has, due to its attractive parts in the interaction potential, a vapor-liquid phase separation terminating in a critical point. The position of this critical point in the (ρ, T^*) plane depends on the width of the perturbation potential in a strongly monotonic way; the critical temperature T^* increases with width. In figures 6.51 to 6.54 the results for vapor-liquid transition of the square-well fluid at $\lambda = 1.25$ (figure 6.51), 1.5 (figure 6.52), 1.75 (figure 6.53) and 2.0 (figure 6.54) for various theories are shown. The EXP and PA (perturbation approximation, see subsection 4.1.4.4) results were calculated using a VW parameterization. Due to its simple treatment of the perturbation, the PA consequently overestimates the temperature of the critical point. The EXP also has some problems to predict the (estimated) critical

Figure 6.49: Reduced dimensionless pressure p^* calculated for a square-well system of range $\lambda = 1.5$ for three different temperatures T^* as indicated, calculated via the virial and the energy route. The lines indicate the average of the values for the two routes and the error bars the difference between these two values.

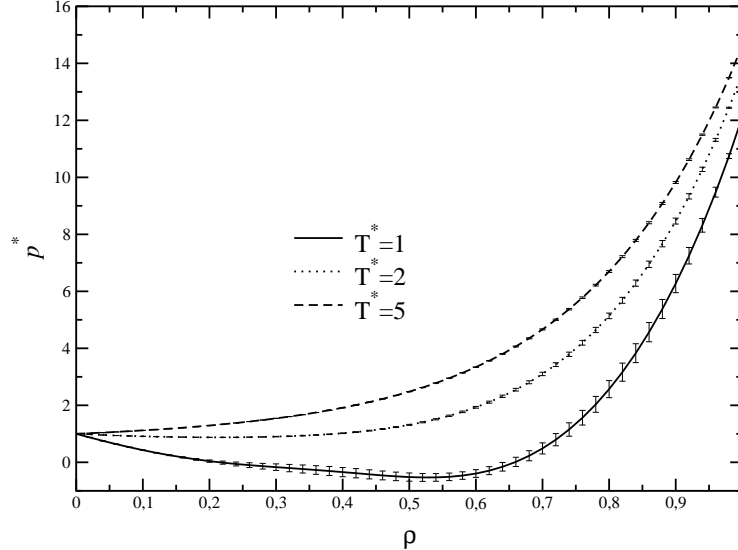
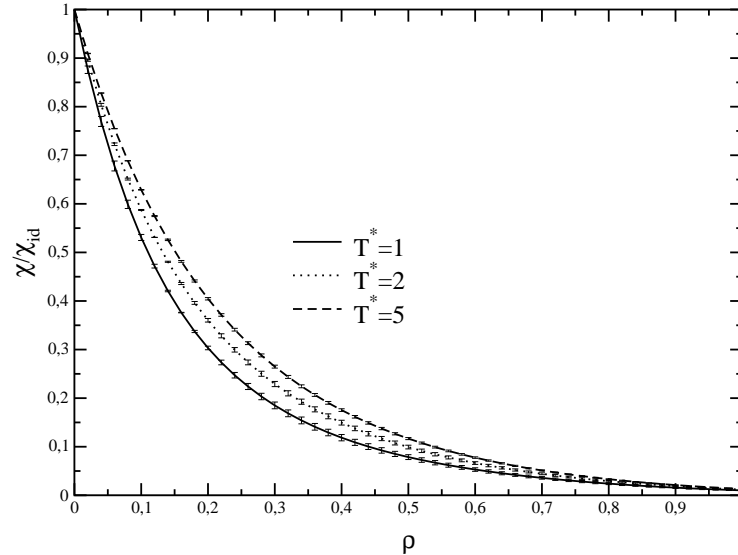
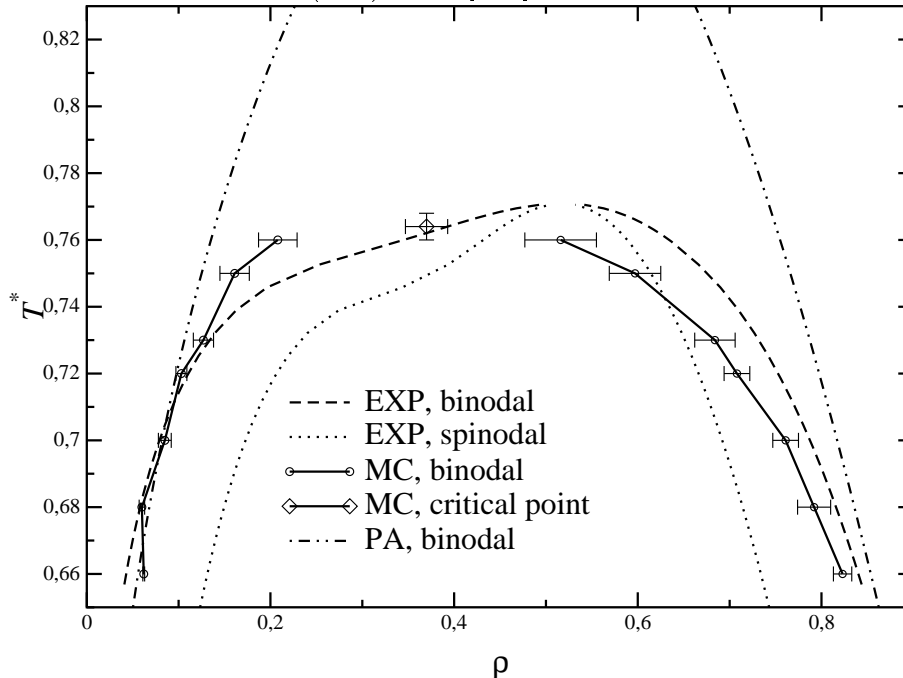


Figure 6.50: Reduced isothermal compressibility χ/χ_{id} ($\chi_{id} = \beta/\rho$) calculated for a square-shoulder system of range $\lambda = 1.2$ for three different temperatures T^* as indicated, calculated via the compressibility and the virial route. The lines denote the average of the values for the two routes and the error bars the difference between these two values.



point from the computer simulations exactly. For intermediate ranges of $\lambda \approx 1.5$ (see figure 6.52) this theory is able to fit the vapor-liquid phase transition from computer simulation data very precisely.

Figure 6.51: Vapor-liquid phase transition of the square-well fluid with $\lambda = 1.25$. Shown are the results for the EXP, for the simple perturbation theory discussed in section 4.1.4.4 and computer simulation results (MC) from [106].



In table 6.7, we have summarized the numerical values for the critical point coordinates for the vapor-liquid phase transition of the four systems mentioned above.

The absence of attractive parts in the interaction potential of the square-shoulder system

Table 6.7: Critical point coordinates (ρ, T^*) for the vapor-liquid phase transition of the square-well fluid for different λ -values (see figures 6.51 to 6.54).

	MC	EXP
$\lambda = 1.25$	(0.370, 0.764)	(0.526, 0.772)
$\lambda = 1.5$	(0.299, 1.219)	(0.358, 1.258)
$\lambda = 1.75$	(0.284, 1.811)	(0.295, 1.834)
$\lambda = 2.0$	(0.225, 2.764)	(0.277, 2.707)

brings along that there exists *only one* fluid phase, i.e., there is no liquid-gas separation. Both, square well and square shoulder systems, freeze at high densities. Additionally, for narrow wells and shoulders there appears in the solid region of the phase diagram a new type of phase coexistence, namely an *isostructural* fcc-fcc phase transition, terminating in a critical point. This transition was discovered in simulation work by Bolhuis and Frenkel (for square-well systems in [107] and for square-shoulder systems in [108]). This isostructural transition was studied recently in the framework of density functional theory by Denton and Löwen [109]. There, a perturbative approach was employed, where the

Figure 6.52: Vapor-liquid phase transition of the square-well fluid with $\lambda = 1.5$. Symbols see figure 6.51.

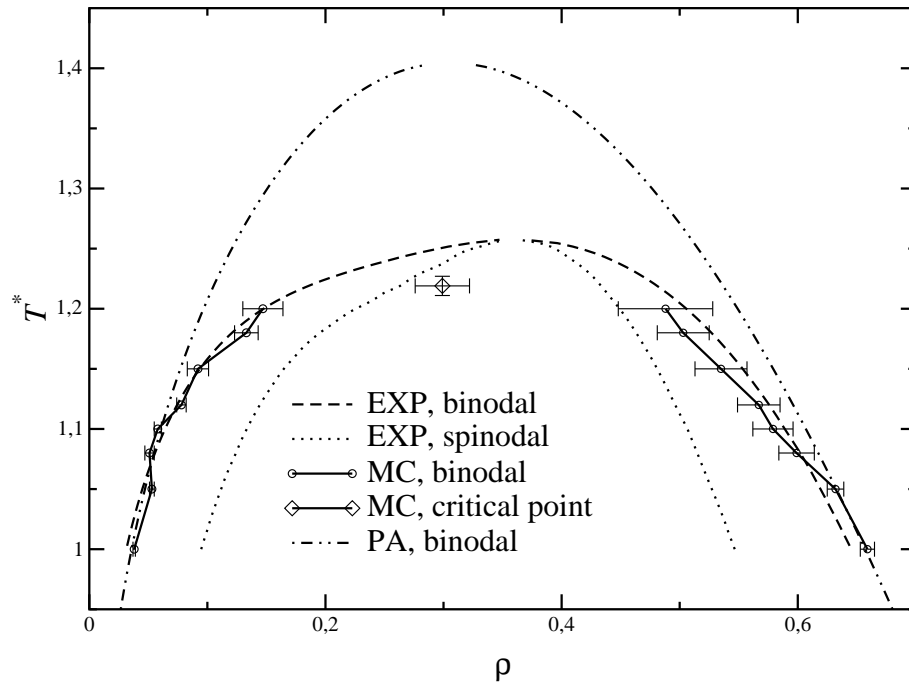


Figure 6.53: Vapor-liquid phase transition of the square-well fluid with $\lambda = 1.75$. Symbols see figure 6.51.

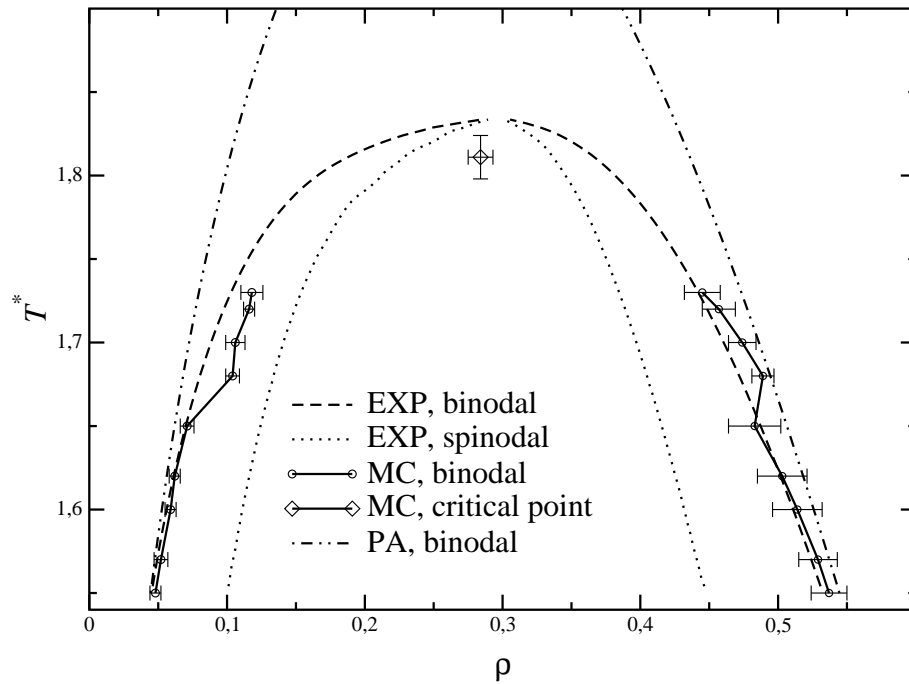
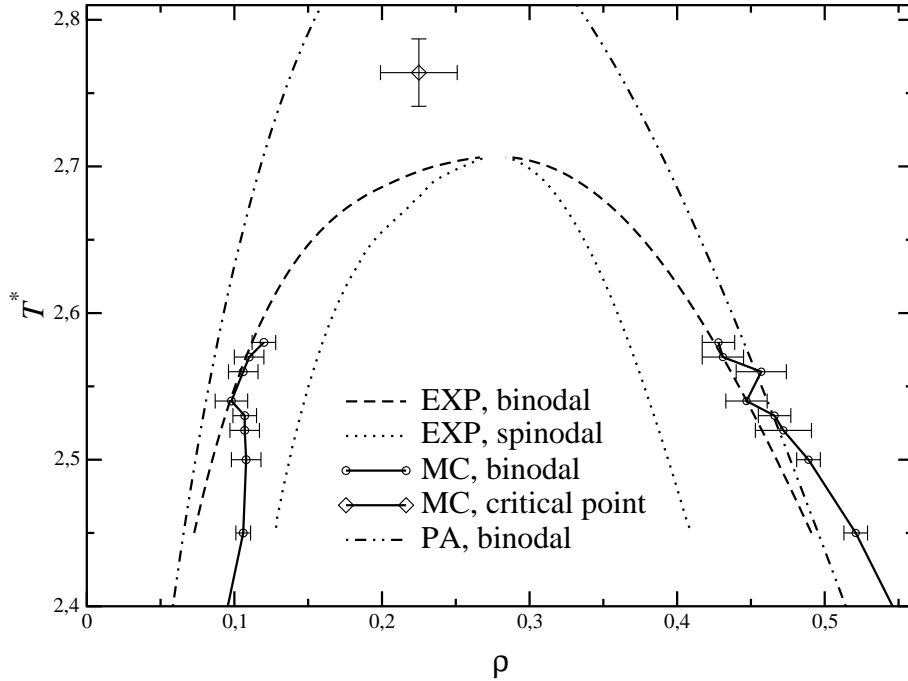


Figure 6.54: Vapor-liquid phase transition of the square-well fluid with $\lambda = 2.0$. Symbols see figure 6.51.



interaction potential was separated into a reference, hard-sphere part and a perturbation. The free energy of the inhomogeneous system was calculated by employing the MWDA for the reference part and a mean-field type approach (similar to the one discussed in subsection 4.4) for the perturbation.

In this thesis, for the solid we have used three approaches that again have a perturbative character:

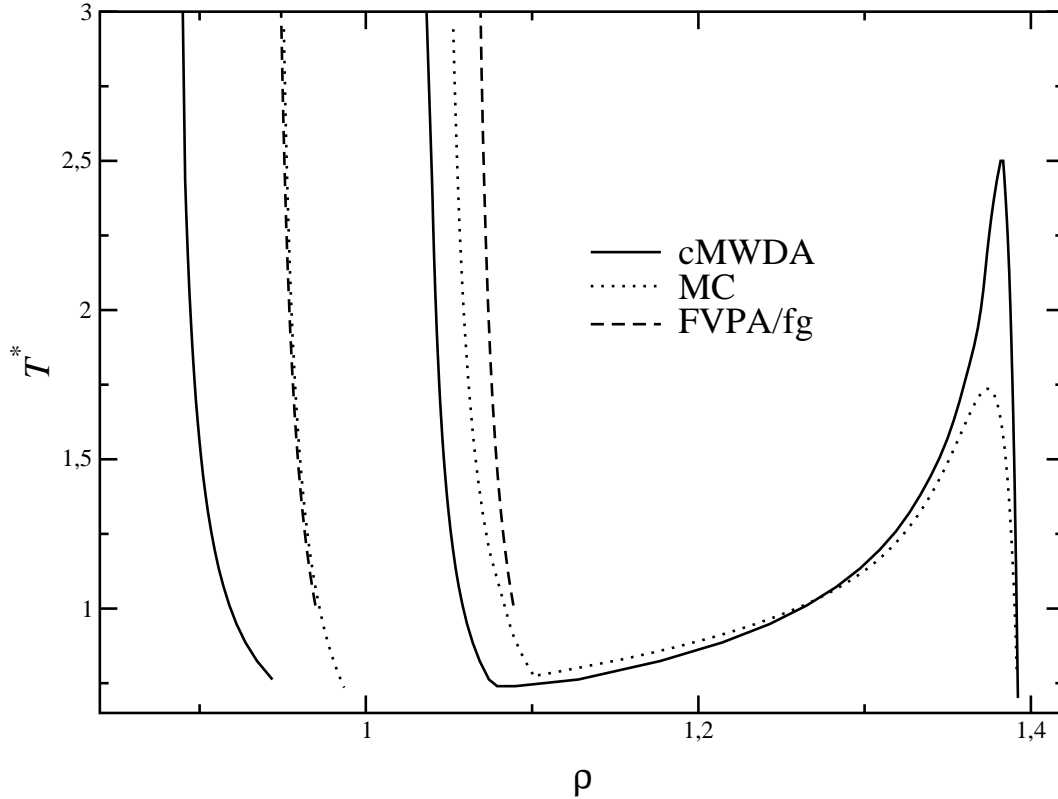
MPA The reference part is calculated in the framework of the MWDA; the minimization of the Helmholtz free energy A with respect to α [equation (4.77)] is done together with the perturbation potential; the perturbation part is evaluated using equation (4.117).

MPA/fg In a first (temperature independent) step the reference solid (i.e., without the perturbation part) is calculated using the MWDA; so the minimization of A in equation (4.77) with respect to the localization parameter α is now done without the perturbation potential. The perturbation part of the potential is then taken into account using equation (4.116).

FVPA/fg This approach is very similar to the MPA/fg; the difference is that the reference part is calculated using the free volume approximation for the free energy in the solid (see subsection 4.1.8).

In all cases, in the fluid phase the perturbation part of the potential is taken into account using an HTA-style approximation defined by equation (4.26). If not explicitly pointed

Figure 6.55: Liquid-solid and solid-solid phase transitions of the square-well fluid with $\lambda = 1.01$. The MC results were taken from [107].

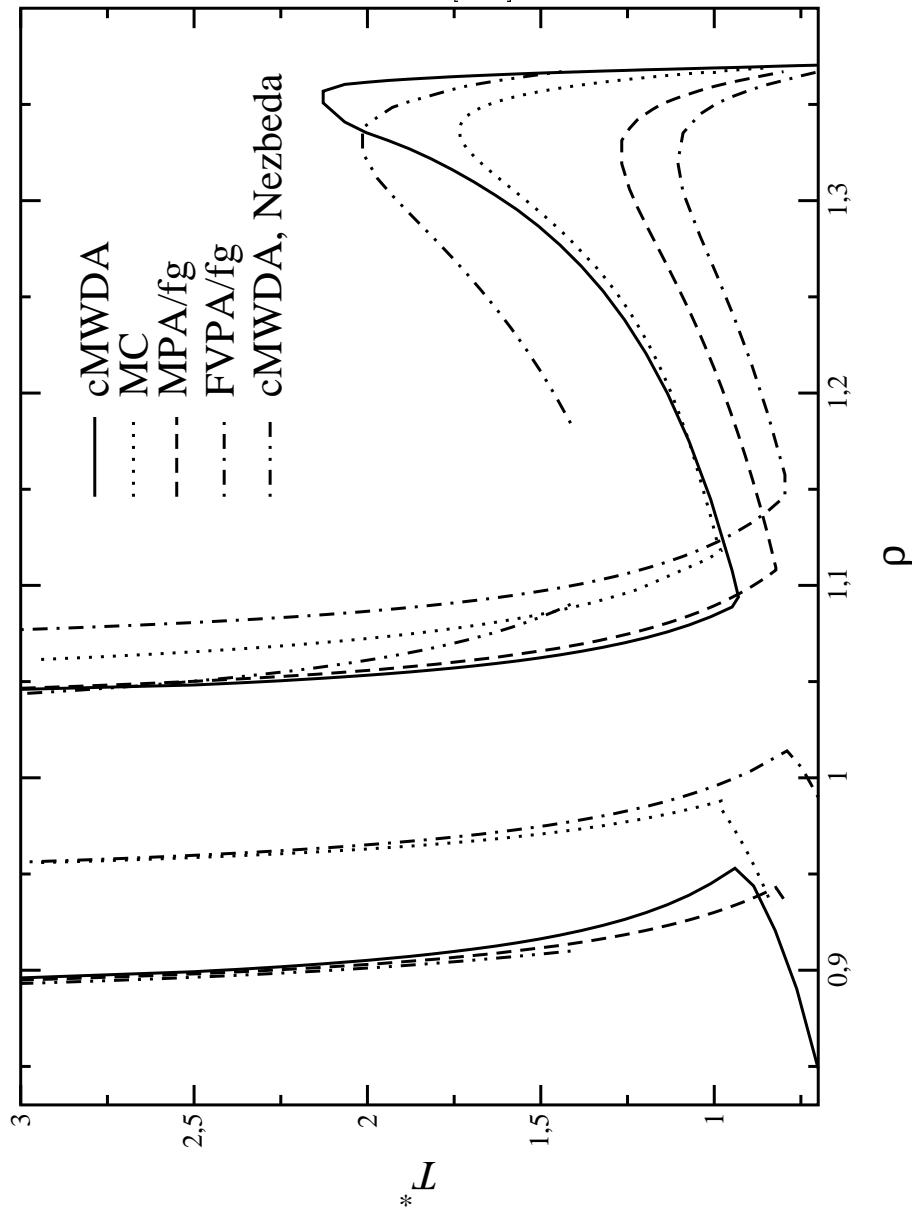


out, the reference part was always calculated using the VW parameterization. Beside these theories, we have also treated the excess free energy in the solid in a non-perturbative fashion using the MWDA (subsection 4.3.1) and the cMWDA (subsection 4.3.2). For these theories the fluid phase was calculated using the EXP; the HS reference system was treated using the VW parameterization.

At first we will present the results for the square-well system. In figure 6.55 the results for $\lambda = 1.01$ is shown. Although the cMWDA results are close to the MC data for the solid fcc-fcc transition up to $T^* = 1.5$, the critical point is overestimated ($\approx 150\%$ with respect to the temperature). For the FVPA/fg result we were, due to numerical restrictions, unable to evaluate the fcc-fcc phase transition with satisfactory precision; however, the liquid side of the liquid-solid transition is predicted with great accuracy when compared with the MC results.

In figure 6.56 we have also include the cMWDA results with Nezbeda's solution (both for the liquid phase and as input to the solid phase, see also [110]) and the MPA/fg result. It is obvious from this graph, that the simple perturbation theories (MPA/fg and FVPA/fg) are underestimating the critical temperature of the isostructural solid-solid transition. One can also see that, obviously, the theories where the reference system is calculated using the VW parameterization (cMWDA, MPA/fg) converge to the same results for the liquid-solid transition for high temperatures. The cMWDA with the Nezbeda input gives

Figure 6.56: Liquid-solid and solid-solid phase transitions of the square-well fluid with $\lambda = 1.02$. The MC results were taken from [107].

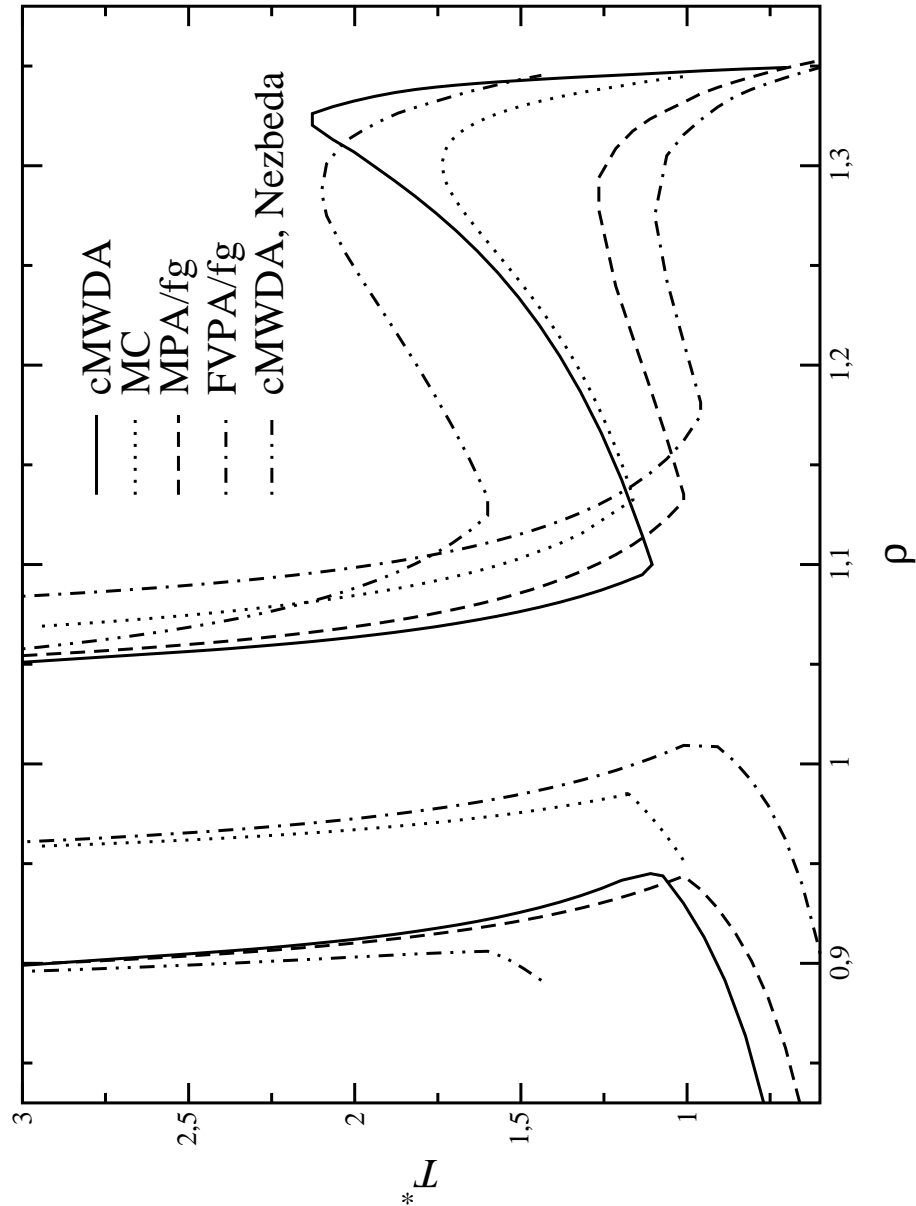


a critical temperature of the fcc-fcc transition which is closer to the MC results than the one predicted by the cMWDA, but the shape of the transition curve is significantly worse than the one one gets using the cMWDA with the EXP as input.

In figure 6.57 the quality of the different results from the different theories are comparable to the previous figure. The cMWDA with Nezbeda input now give results down to temperatures below the triple point at $T_t^* \approx 1.58$.

At $\lambda = 1.04$ (figure 6.58), the phase diagram calculated using the FVPA/fg contains no *stable* fcc-fcc transition anymore, the liquid-solid transition is energetically preferable.

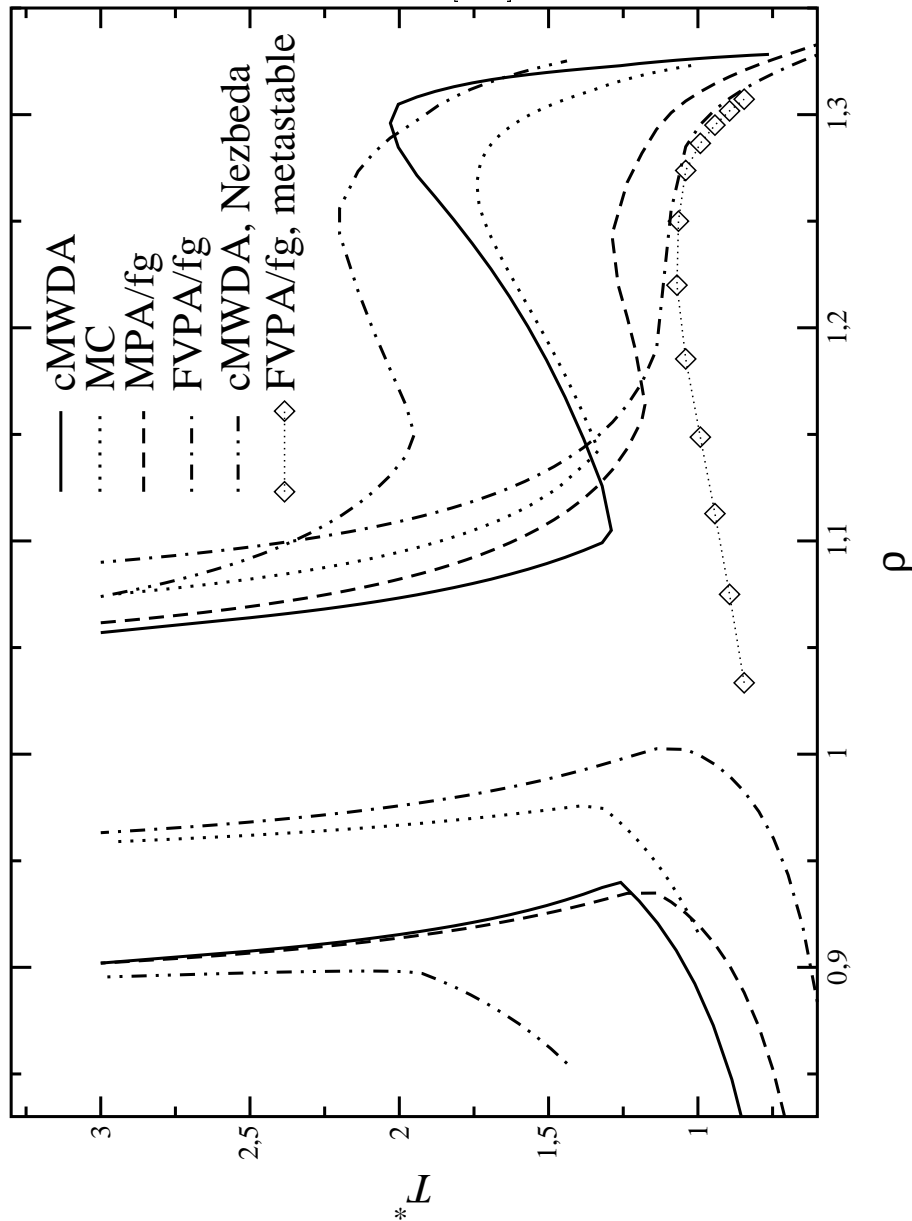
Figure 6.57: Liquid-solid and solid-solid phase transitions of the square-well fluid with $\lambda = 1.03$. The MC results were taken from [107].



However, for this perturbation potential width the computer simulation still predicts a distinct fcc-fcc transition. So for this kind of perturbation, the FVPA (together with the simple treatment of the perturbation as discussed in section 4.4) is unable to predict the phase behavior even in a qualitative way, hence we discard the solution of this theory for the perturbation potential widths with $\lambda > 1.04$.

For $\lambda = 1.05$ (see figure 6.59), both the MPA/fg solution and the cMWDA theory with Nezbeda input are predicting a metastable fcc-fcc transition, whereas this transition is still stable when calculated using the cMWDA/EXP. It should be noted, that these two

Figure 6.58: Liquid-solid and solid-solid phase transitions of the square-well fluid with $\lambda = 1.04$. The MC results were taken from [107].



theories (MPA/fg and cMWDA/Nezbeda) yield (qualitatively) similar results for the fcc-fcc transition at systems with $\lambda < 1.05$.

For square-well potentials with perturbation potential widths $\lambda \leq 1.05$, we can summarize that the cMWDA when used along with the EXP/VW parameterization gives the best results for the liquid-solid and solid-solid phase transitions. However, the numerical effort for this theory is significantly higher than the effort to solve one of the other theories used.

Finally, in figure 6.60 the phase diagrams for the square-well system with $\lambda = 1.06$ to

Figure 6.59: Liquid-solid and solid-solid phase transitions of the square-well fluid with $\lambda = 1.05$. The MC results were taken from [107].

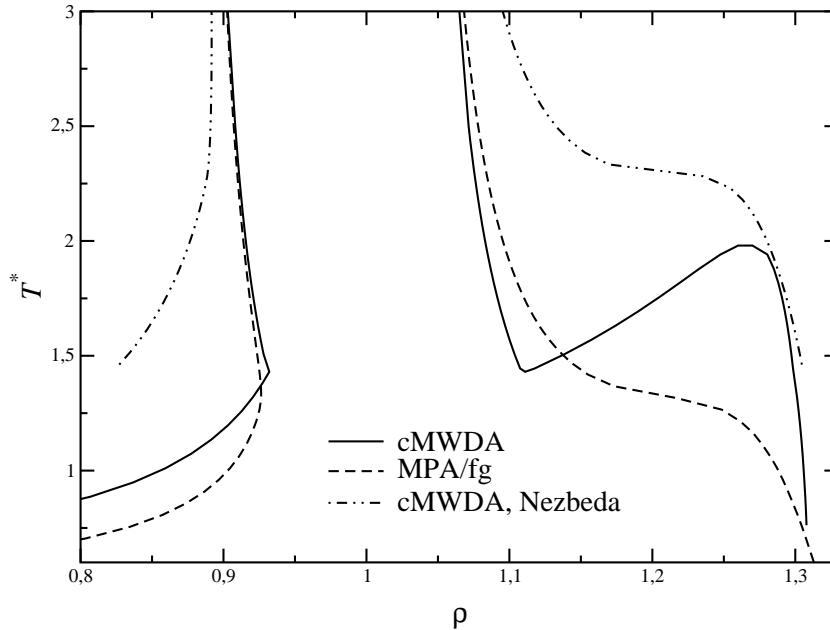
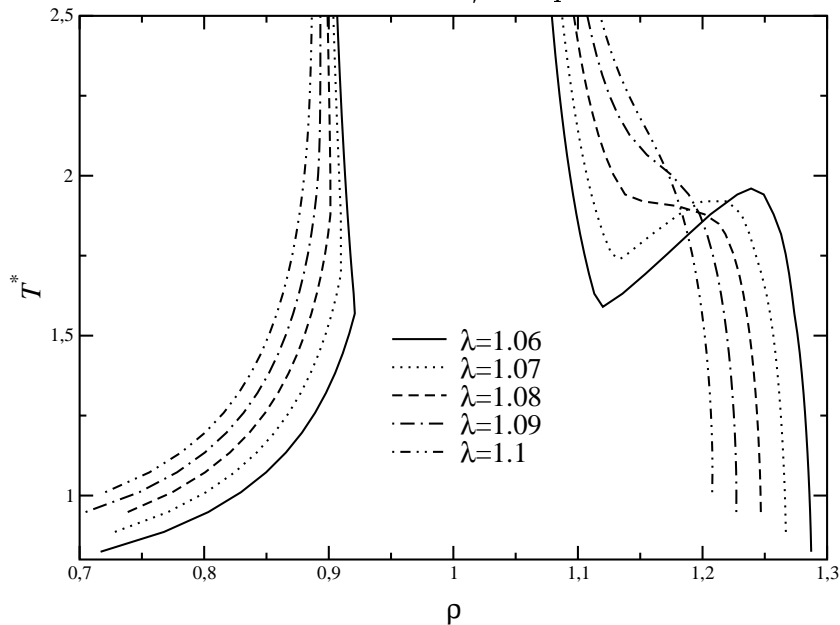
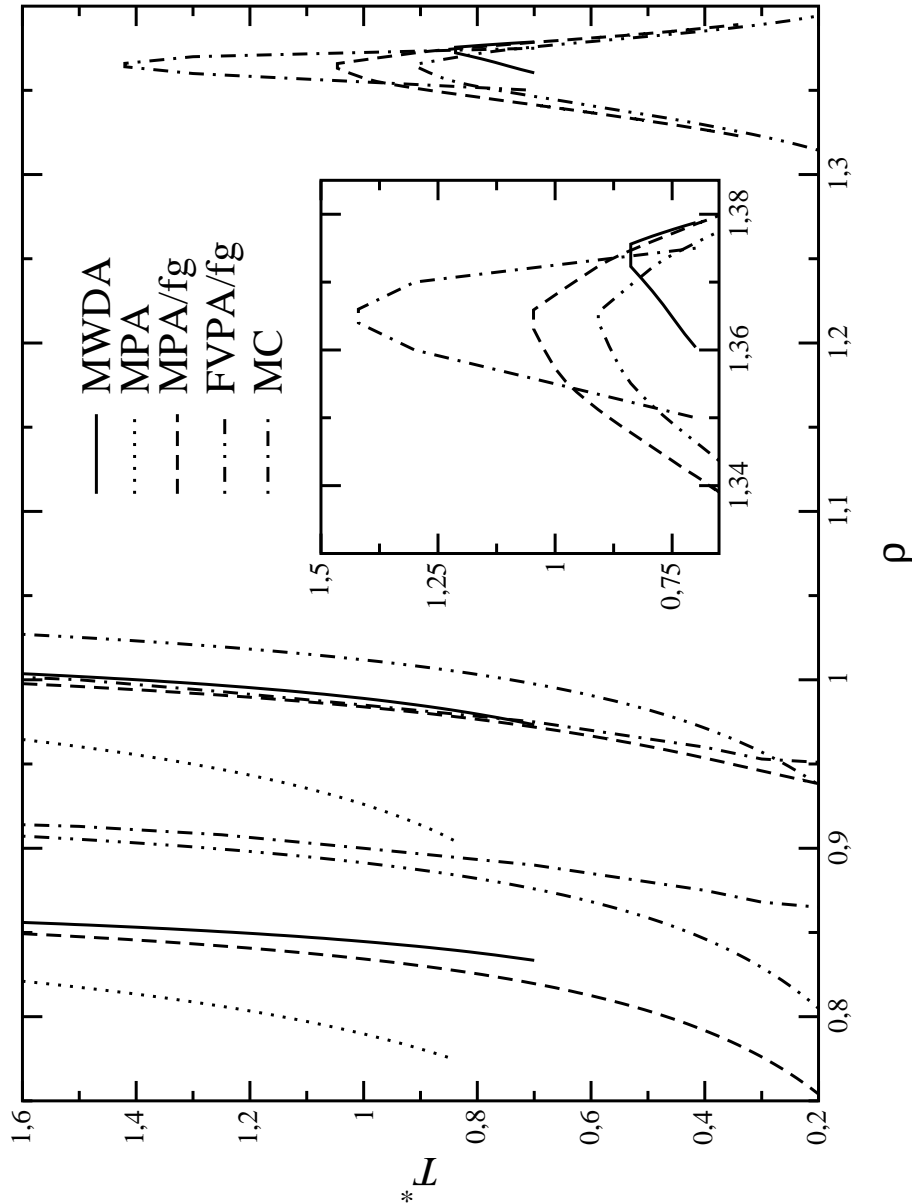


Figure 6.60: Liquid-solid and solid-solid phase transitions of the square-well fluid with λ from 1.06 to 1.1 for the cMWDA with the EXP/VW parameterization as liquid input.



$\lambda = 1.1$ for the cMWDA (with EXP/VW) are shown. For $\lambda = 1.06$ and $\lambda = 1.07$, the fcc-fcc transition remains stable and disappears for $\lambda \geq 1.08$. The simulation data from [108] are predicting a 'crossover'-width of $\lambda = 1.06$, i.e. the fcc-fcc transition is metastable

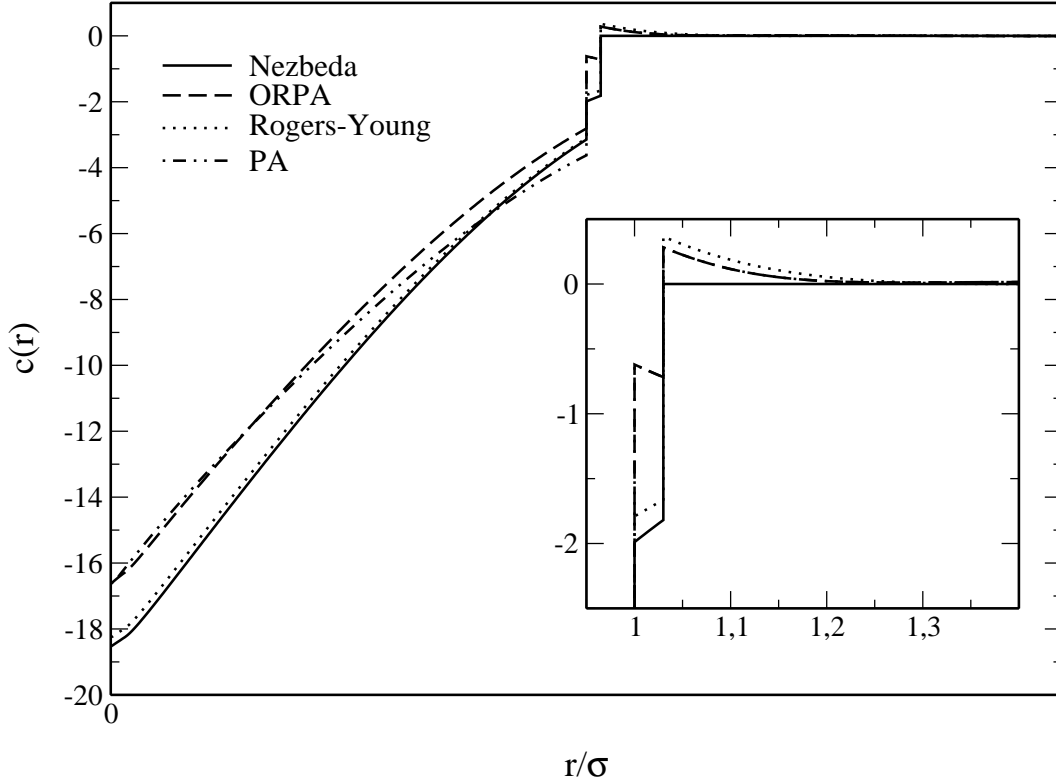
Figure 6.61: Liquid-solid and solid-solid phase transitions of the square-shoulder fluid with $\lambda = 1.03$. The MC results were taken from [108].



for $\lambda \geq 1.07$.

For square-shoulder systems we have applied the same theories as for square-well systems. Because the restrictions that lead to the introduction of the cMWDA do not exist for the square-shoulder system (see section 4.3.2), we used the MWDA instead of the cMWDA for the square-shoulder potential. However, applying the MWDA together with Nezbeda's solution as input to the square-shoulder system, the result seriously overestimates the critical temperature for the isostructural fcc-fcc transition. We obtain $T_c^* \approx 5 - 6$ for $1.04 \leq \lambda \leq 1.08$, in disagreement with the result from simulations [108],

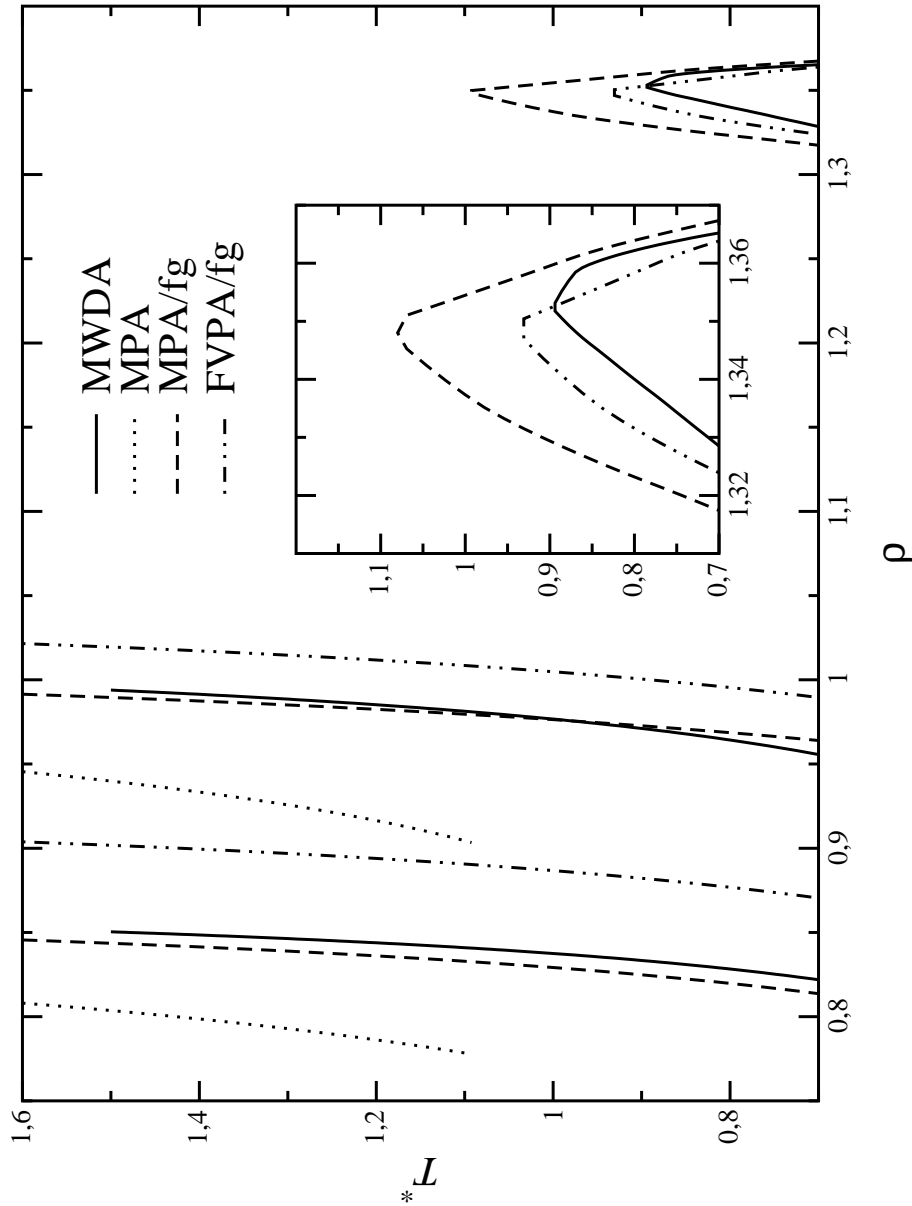
Figure 6.62: Comparison of the Nezbeda, ORPA, PA and RY direct correlation functions of a $\lambda = 1.03$ square-shoulder liquid at packing fraction $\eta = 0.35$ and temperature $T^* = 1.0$. The insets shows the region around $r = \sigma$.



where the result is $T_c^* \approx 1.5$. On the other hand, if we use the EXP result for $c(r; \eta)$ as input, the critical temperature turns out to be between 0.8 and 1.4, i.e. in much better agreement with the simulation. However, as can be seen in figure 6.61, the MPA/fg (and, but to a lesser extent, the FVPA/fg), gives a significantly better approximation to the MC results than the MWDA with EXP input. The MPA is even unable to predict the isostructural transition.

The extreme sensitivity of T_c^* to the liquid-state input of the MWDA requires some explanation. The basic idea behind the MWDA is that the effective liquid whose excess free energy equals that of the solid has a density ρ_{liquid} which is much lower than ρ_{solid} . Indeed, the solid, being highly inhomogeneous, pays a high price in ideal free energy, which disfavors spatial modulations, and a relatively low price in excess free energy. Referring to equation (4.76), we observe the following: the contribution of the second term on the right hand side consists of sums over shells in real space, the zeroth shell being included. The contributions from the higher order shells (i.e., first, second etc neighbors of a given site) are practically *vanishing* if the Nezbeda solution for $c(r; \rho)$ is used, as in this approximation the direct correlation function is identical zero for $r > \lambda\sigma$. In reality, however, the function $c(r; \rho)$ has a ‘tail’ in the region $r > \lambda\sigma$, where it attains positive values. This tail is reproduced in both the EXP and the RY solution; see figure 6.62. In this figure,

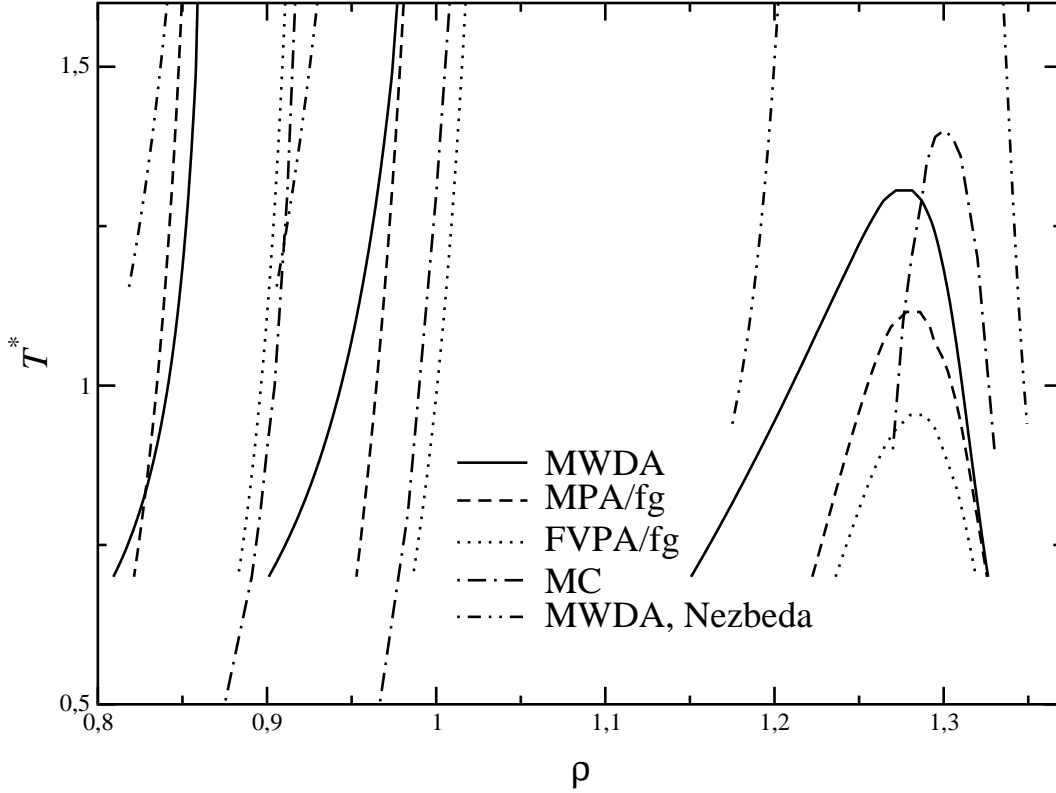
Figure 6.63: Liquid-solid and solid-solid phase transitions of the square-shoulder fluid with $\lambda = 1.04$. The MC results were taken from [108].



the PA solution is equal to the EXP outside the core ($r > \sigma$); inside the core, the PA solution is interpolating between the EXP and the Nezbeda/RY approximation.

As the tail of the EXP is positive, $\rho(r)$ is also positive and so is the double integral on the right hand side of equation (4.76); it turns out that if the Nezbeda solution is used, certain negative contributions to the determination of $\hat{\rho}$ are left out (because $c(r) = 0$ for $r > \lambda\sigma$). This yields an effective density $\hat{\rho}$ which is *too high*. Indeed, for $\lambda = 1.05$ and $T^* = 1.0$, we find, typically, $0.75 < \hat{\rho} < 1.05$ in the region of the fcc-fcc coexistence. For such high values of ρ , the validity of the PY approximation (inherent in the Nezbeda

Figure 6.64: Liquid-solid and solid-solid phase transitions of the square-shoulder fluid with $\lambda = 1.08$. The MC results were taken from [108].

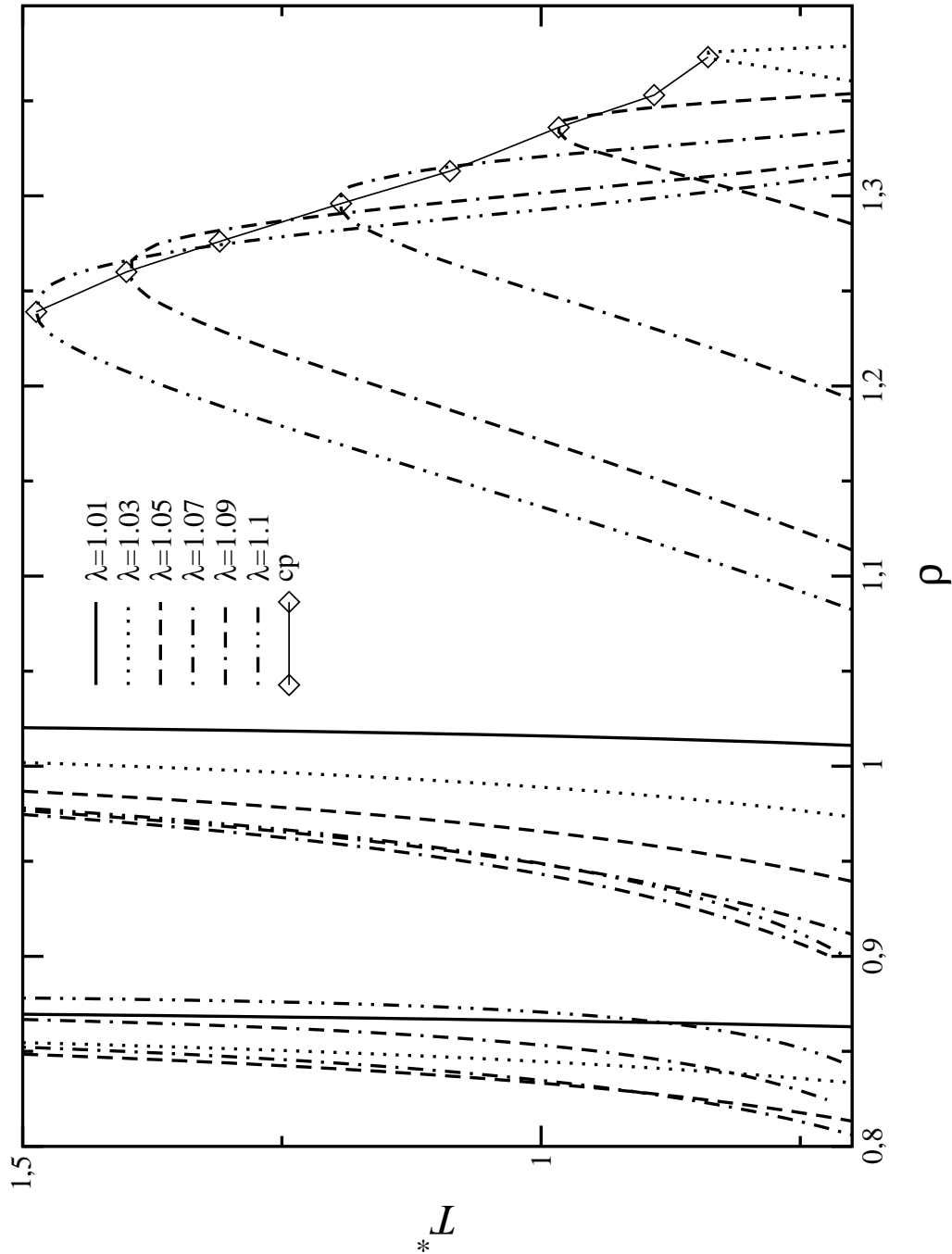


solution) is questionable. Moreover, the excess free energy of the solid turns out to be artificially high. And as the critical temperature is very sensitive to the details of the free energy, this causes a too high critical temperature for the fcc-fcc transition.

This problem was *not* observed in the case of the fcc-fcc coexistence of the square-well system because there the high *positive* value of $c(r; \rho)$ in the region $\sigma \leq r \leq \lambda\sigma$ brings about *very low* values of $\hat{\rho}$, irrespective of the tail of the direct correlation function outside $r = \lambda\sigma$. In the present case, where $c(r; \rho)$ is negative everywhere but for $r > \lambda\sigma$, taking into account the existence of the tail turns out to be very important. On a more quantitative basis, the non-perturbative approach yields critical temperatures which are even lower than the simulation results. Indeed, in the simulation the critical temperature has the value $T_c^* \approx 1.5$ and is practically independent of the width of the potential. My results, however, show a dependence on the width of the repulsive shoulder which is also absent in the previous perturbative approach [109]. This is the same effect as was observed in the non-perturbative approach to the isostructural fcc-fcc transition of the square-well potential [13].

In figure 6.64 the coordinate of the critical temperature of the Nezbeda solution is equal to $\rho_c = 1.28$, $T_c^* = 5.1$. For this potential width ($\lambda = 1.08$), the FVPA/fg is able to predict the liquid-solid transition with great accuracy when compared with the computer simulation results.

Figure 6.65: Phase diagram of the square-shoulder fluid, calculated using the MWDA with EXP/VW as input. Shown are the results for $\lambda = 1.01, 1.03, 1.05, 1.07, 1.09$ and 1.1 . cp denotes the critical points.



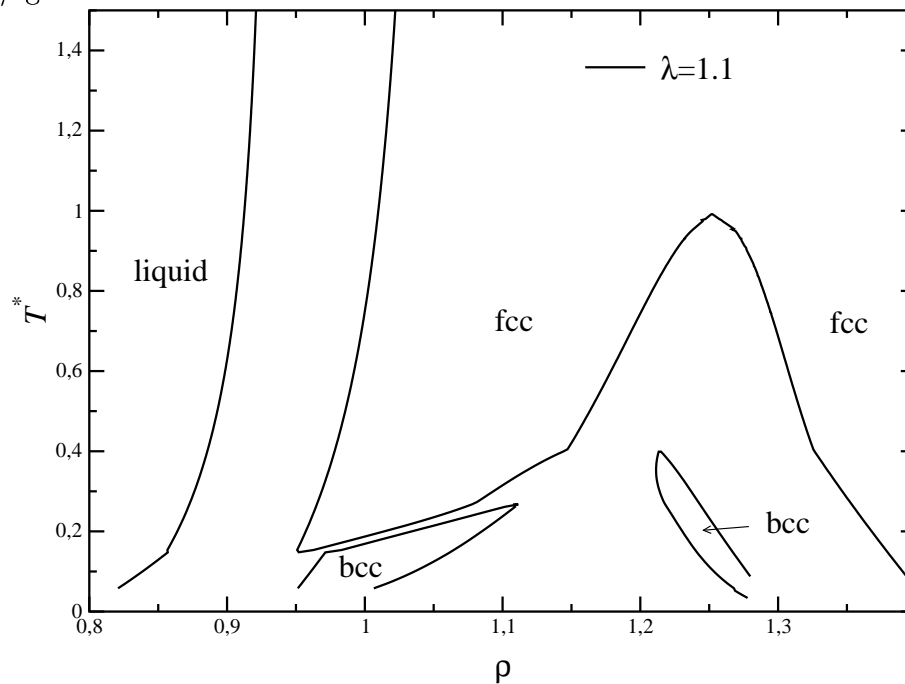
The temperature dependence of the critical point of the fcc-fcc transition is shown in figure 6.65, the results shown were obtained using the MWDA with the EXP/VW parameterization as input. The critical points of all results from $\lambda = 1.03$ up to $\lambda = 1.1$ are

denoted by small diamonds. Obviously, the critical point temperature is connected to the potential width through a function linear in λ with a positive slope. In contrast to this, if one makes the same approximation for the critical point temperatures obtained using computer simulations, the slope had to be *negative*.

If the phase diagram is calculated using the FVPA/fg, the temperature of the critical points also depends on the perturbation potential width, but to a much lesser extent (for $\lambda = 1.03$, T_c^* is equal to ≈ 0.9 ; for $\lambda = 1.1$ $T_c^* \approx 1.0$). The MPA/fg yields critical temperatures that are higher than those from the FVPA/fg, but still too low to yield a good approximation of the computer simulation results ($\lambda = 1.03 \rightarrow T_c^* = 1.05$, $\lambda = 1.1 \rightarrow T_c^* = 1.19$).

6.4.3.1 Evolution of the square-shoulder phase diagram

Figure 6.66: Phase diagram for the square-shoulder system with $\lambda = 1.1$, calculated using the FVPA/fg.



Up to this point, all results for the phase diagram of the square-well/square-shoulder potential have shown no stable bcc phase. However, if one goes down to lower temperatures or wider perturbation widths, the phase diagram for the square-shoulder system contains a stable bcc phase. Not all theories are able to explore these parts of the λ - T^* parameter space; in fact only the FVPA/fg yields solutions that are physically meaningful for those parameters where the bcc crystal was stable.

In figures 6.66 ($\lambda = 1.1$) to 6.71 ($\lambda = 1.2$), the evolution of the phase diagram of a square-shoulder system is shown. For $\lambda = 1.1$ (figure 6.66), the theory predicts two regions where the bcc crystal is stable. The upper part of this figure ($T^* > 0.4$) shows the typical

Figure 6.67: Phase diagram for the square-shoulder system with $\lambda = 1.12$, calculated using the FVPA/fg.

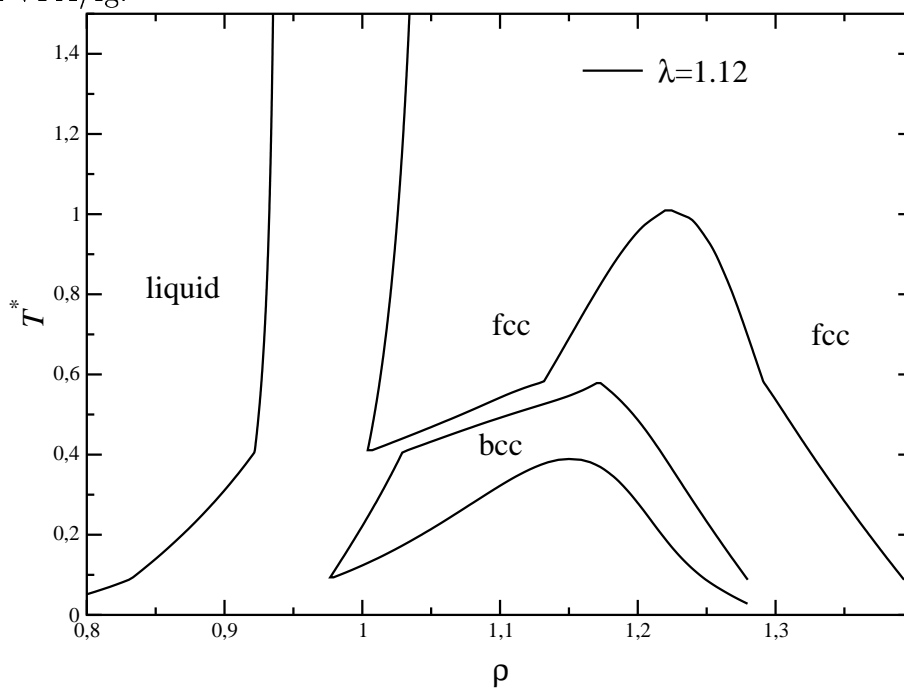


Figure 6.68: Phase diagram for the square-shoulder system with $\lambda = 1.14$, calculated using the FVPA/fg.

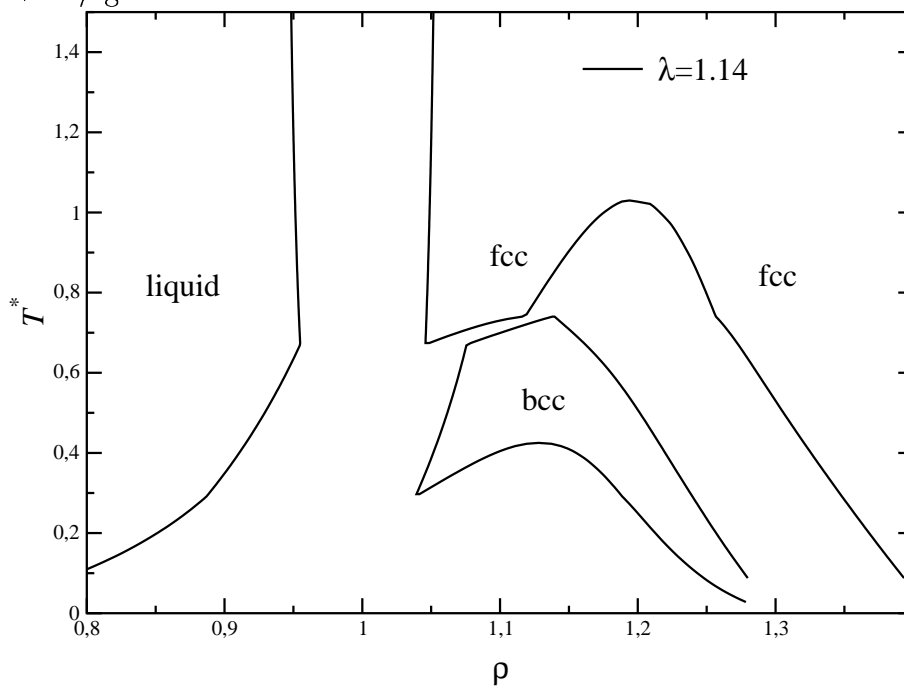


Figure 6.69: Phase diagram for the square-shoulder system with $\lambda = 1.16$, calculated using the FVPA/fg.

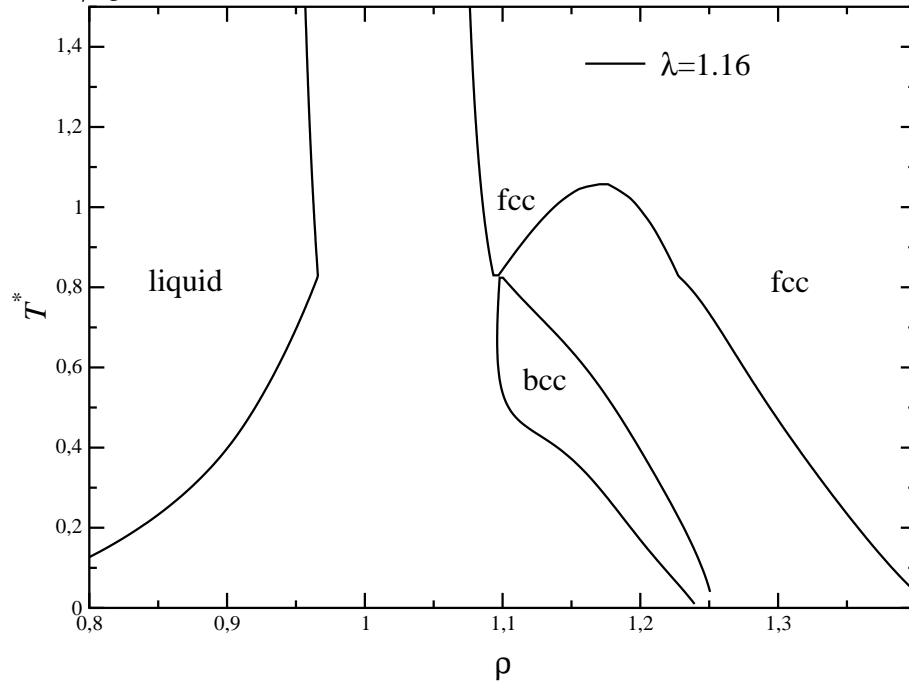


Figure 6.70: Phase diagram for the square-shoulder system with $\lambda = 1.18$, calculated using the FVPA/fg.

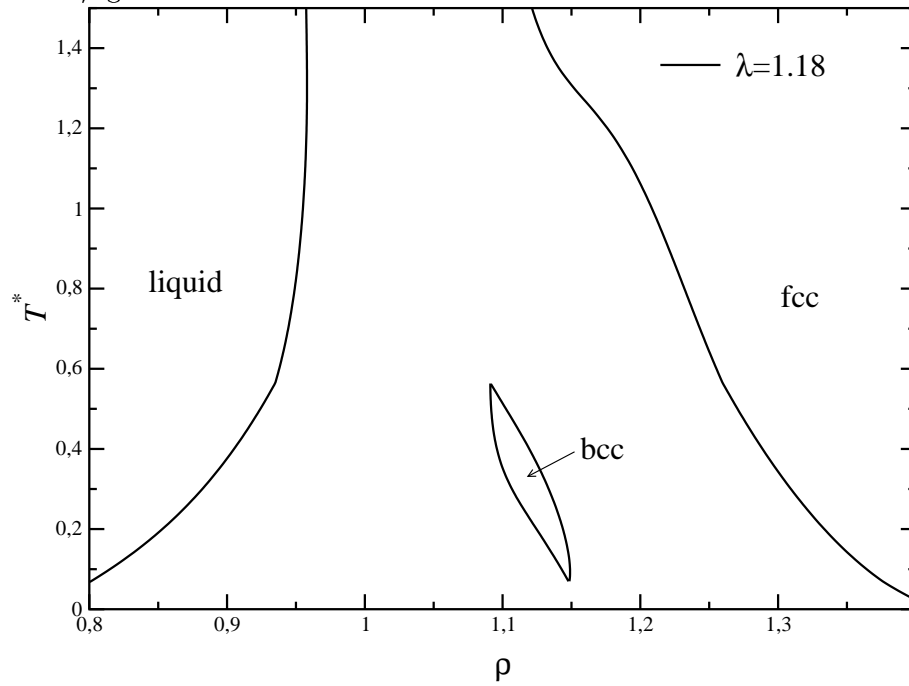
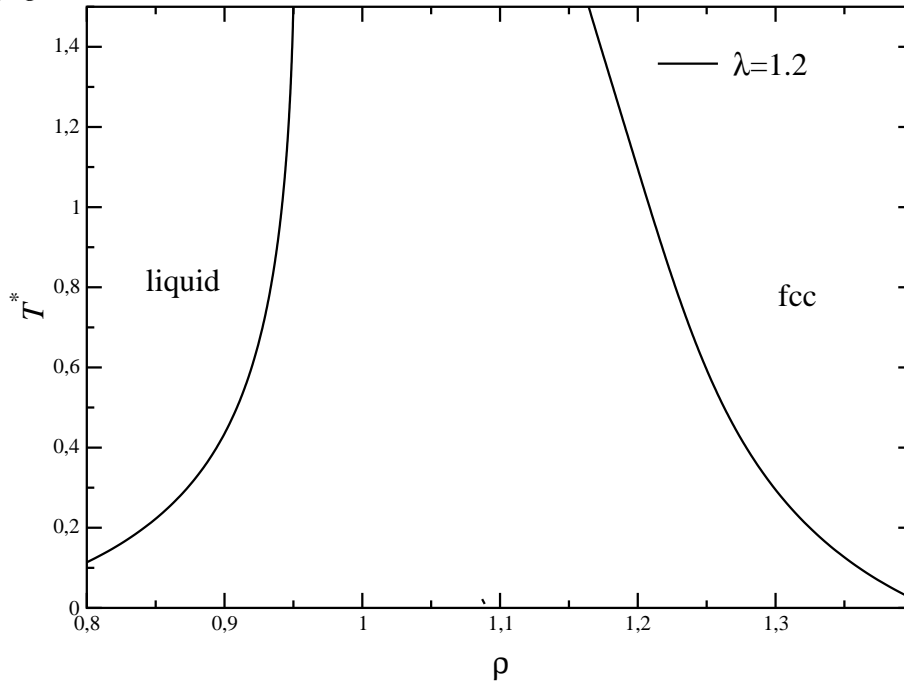


Figure 6.71: Phase diagram for the square-shoulder system with $\lambda = 1.2$, calculated using the FVPA/fg.



square-shoulder phase behavior as discussed in subsection 6.4.3. As the shoulder width increases to $\lambda = 1.12$ and $\lambda = 1.14$ (figure 6.67 and 6.68), the two separated regions of bcc stability are united, so the isostructural bcc-bcc transition located in the temperature range $T^* \approx 0.1 - 0.4$ is terminated by a critical point. For $\lambda = 1.16$ (figure 6.69), the phase diagram is losing its isostructural bcc-bcc transition. For $\lambda = 1.18$ (figure 6.70), the phase diagram has also lost its isostructural fcc-fcc transition. The stable bcc crystal is now constrained to a small area in the ρ - T^* plane. And finally, for $\lambda = 1.2$ the bcc crystal is metastable in the whole phase diagram.

Due to the simple treatment of the perturbation in this theory (FVPA/fg), the solution (especially for the wider perturbation widths) is questionable.

6.5 Asakura-Oosawa potential

In this section we will present the results we obtained for the Asakura-Oosawa potential as described in subsection 2.2.4. We examined the systems with $q = 0.1$, $q = 0.4$, $q = 0.6$ and $q = 0.8$. As reference data, we took the computer simulation results for the effective Hamiltonian (mapping from the binary system of colloid particles and polymer coils onto an effective one-component system with Asakura-Oosawa potential) from [30] (these results are in fairly good agreement with the ones from the direct simulation of the true binary mixture). It should be noted that this mapping is only exact for $q < 0.154$. In figures 6.72 to 6.76, the results we obtained for the phase diagram (using various theories) are shown together with the computer simulation data from [30]. The axes are denoted with η (packing fraction of the colloids with diameter σ , see subsection 2.2.4) and η_p^r (reservoir packing fraction, see subsection 2.2.4). At $\eta_p^r = 0$, the system is recovering the known freezing transition of the pure hard-sphere system (see table 6.2). For the abbreviations of the various theories used to obtain the results, we refer to subsection 6.4.3. The $\Delta s = 0$ line (calculated using the EXP) present in all graphs in this subsection acts as an indicator for the freezing transition (see section 5.3).

For $q = 0.1$ (figure 6.72), the EXP/cMWDA predicts a *stable* isostructural solid fcc-fcc transition, whereas in [30] this transition turned out to be *metastable*. However, the location of this transition is near to the one predicted by the simulation results. The results of the simple perturbation theories (MPA/fg and FVPA/fg) are showing the same widening of the fluid-solid transition when η_p^r is increased sufficiently. This implies that the coexisting fluid and solid phases become progressively more dilute and dense, respectively, upon increasing η_p^r . This effect is consistent with earlier findings by Gast [111] in perturbation theory studies of the same pair-potential model. From the shape of the fluid-solid phase transition in figure 6.72 (and, but to a lesser extend, figure 6.74) it is obvious that for such small q -values the fluid phase only persists at very low values of η if η_p^r is sufficiently high. The EXP is able to predict a metastable fluid-fluid transition for high reservoir packing fractions, similar to the one found in [30].

For $q = 0.2$ (figure 6.73, no computer simulation results are available) the isostructural solid-solid transitions predicted by the EXP/cMWDA for $q = 0.1$ has vanished.

For $q = 0.4$ (figure 6.74), the results from the FVPA/fg become unphysical for the fluid-solid transition (the width of this phase transition decreases as η_p^r increases), hence we discarded them for all figures with $q \geq 0.4$ (the fluid-fluid transition of the FVPA/fg is, of course, identical with the one from the MPA/fg). Although the MPA/fg provides us with a solution for the coexisting phases for the whole range of reservoir packing fraction, the fluid-solid transition shows an unphysical behavior (the width of the fluid-solid transition decreases as η_p^r increases, similar to the FVPA/fg for $q = 0.4$) for $\eta_p^r \approx 0.4$. Nevertheless, the fluid-fluid transition is still predicted to be metastable. The EXP provides us with a very good approximation of this transition, thus proving once more that the EXP is still an excellent theory for the liquid state.

For $q = 0.6$ and $q = 0.8$ (figures 6.75 and 6.76), the fluid-fluid coexistence becomes stable. The EXP/cMWDA is in fairly good agreement with the results from [30] for these q -values.

For small reservoir packing fractions η_p^r , the effective pairwise (depletion) potential of

Figure 6.72: Phase diagram of the Asakura-Oosawa potential with $q = 0.1$. Shown are the results for the EXP/cMWDA, the MPA/fg and the FVPA/fg. The computer simulation results (MC) were taken from [30] (non-additive, effective one-component system).

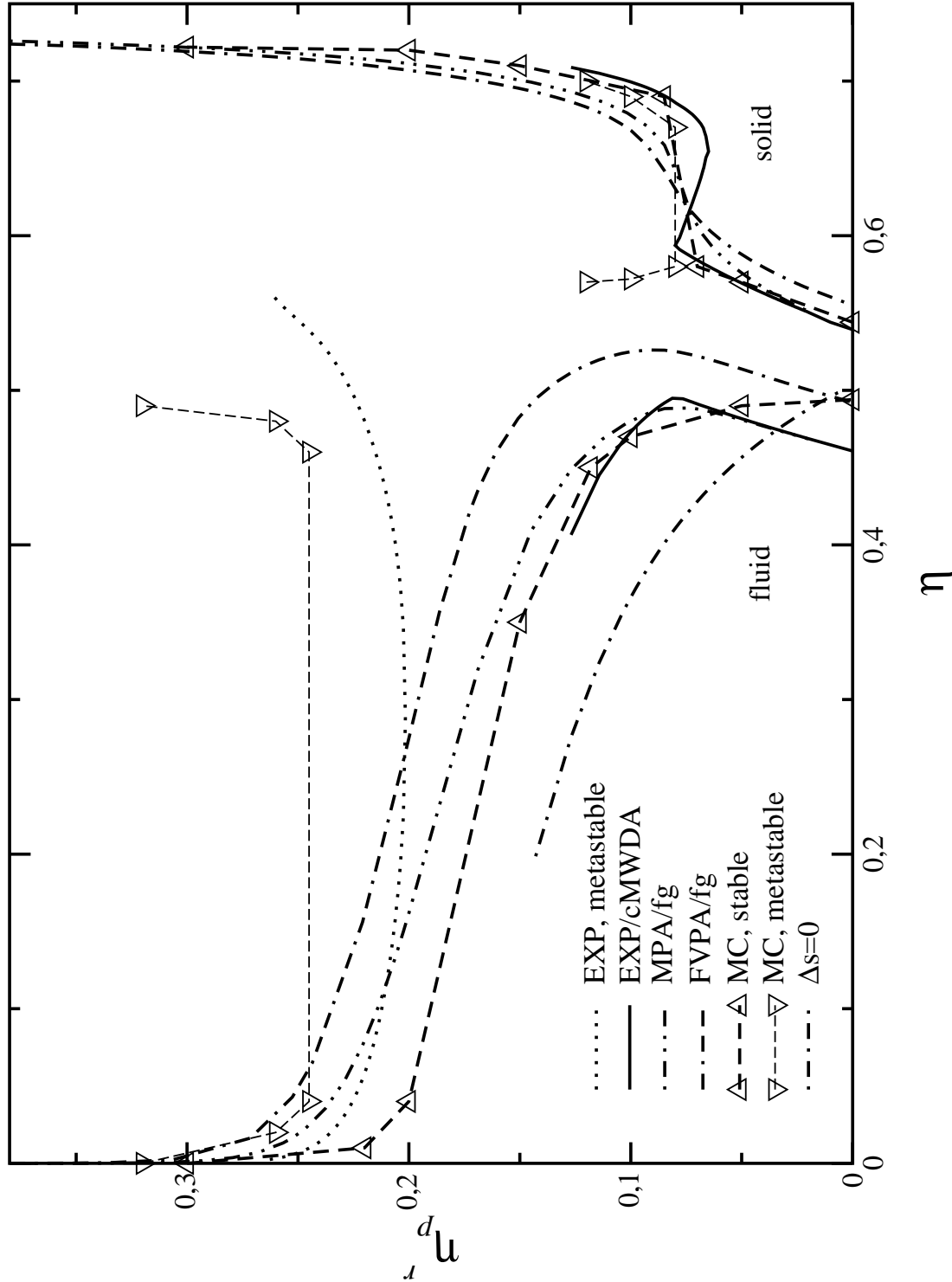


Figure 6.73: Phase diagram of the Asakura-Oosawa potential with $q = 0.2$. Shown are the results for the EXP/cMWDA, the MPA/fg and the FVPA/fg. No computer simulation results are available.

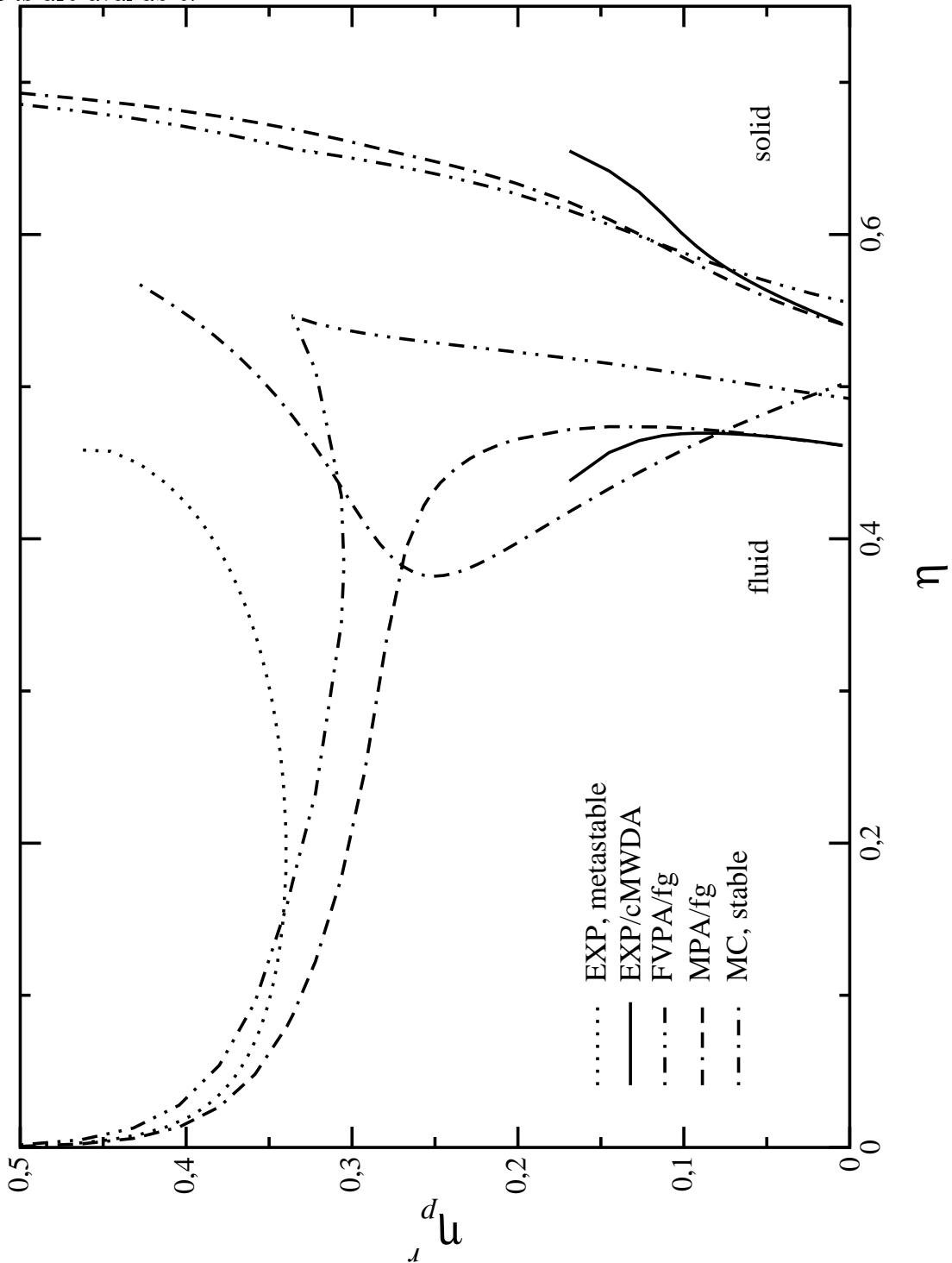


Figure 6.74: Phase diagram of the Asakura-Oosawa potential with $q = 0.4$. Shown are the results for the EXP/cMWDA, the MPA/fg and the FVPA/fg. The computer simulation results (MC) were taken from [30] (non-additive, effective one-component system).

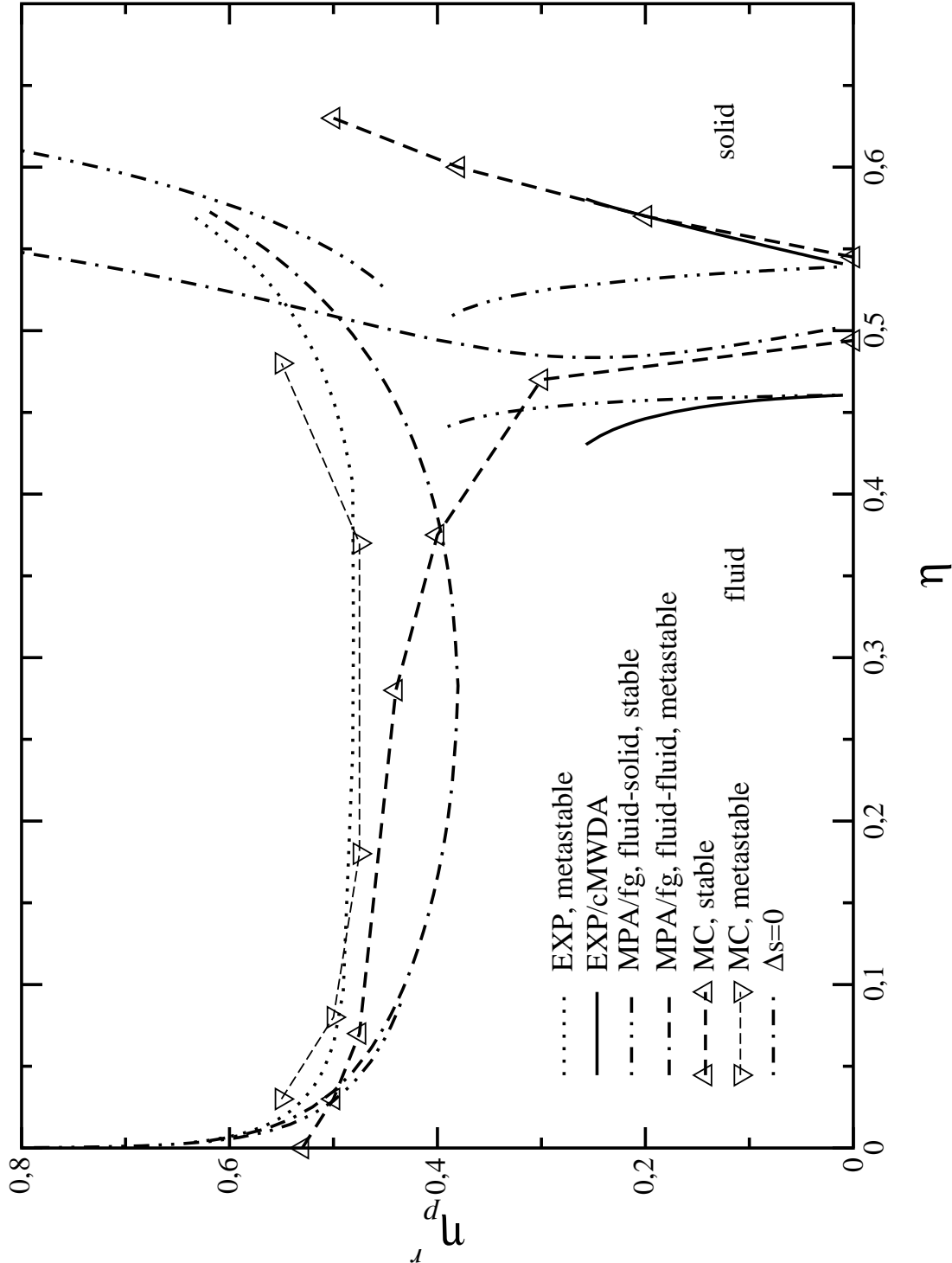


Figure 6.75: Phase diagram of the Asakura-Oosawa potential with $q = 0.6$. Shown are the results for the EXP/cMWDA, the MPA/fg and the FVPA/fg. The computer simulation results (MC) were taken from [30] (non-additive, effective one-component system).

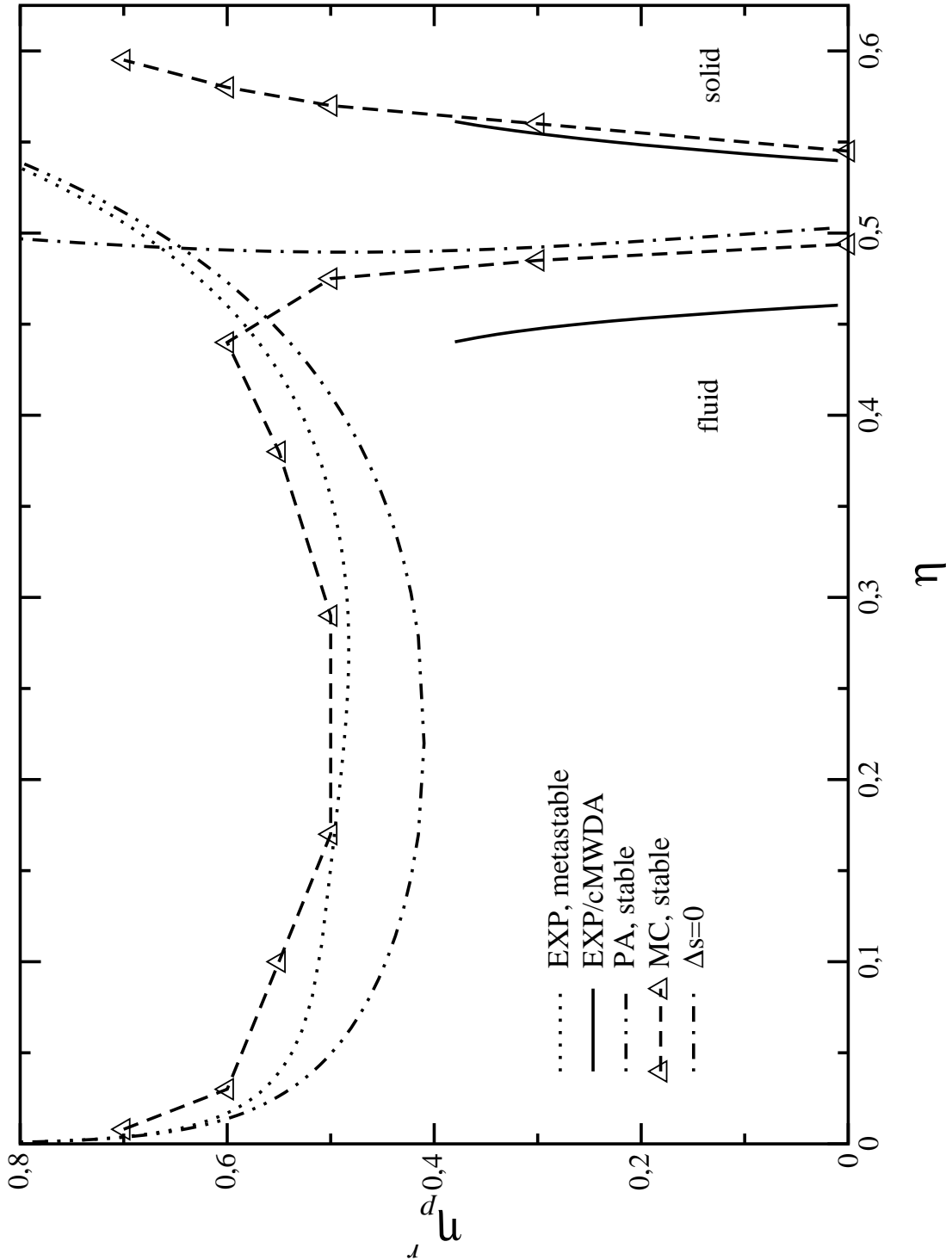


Figure 6.76: Phase diagram of the Asakura-Oosawa potential with $q = 0.8$. Shown are the results for the EXP/cMWDA, the MPA/fg and the FVPA/fg. The computer simulation results (MC) were taken from [30] (non-additive, effective one-component system).

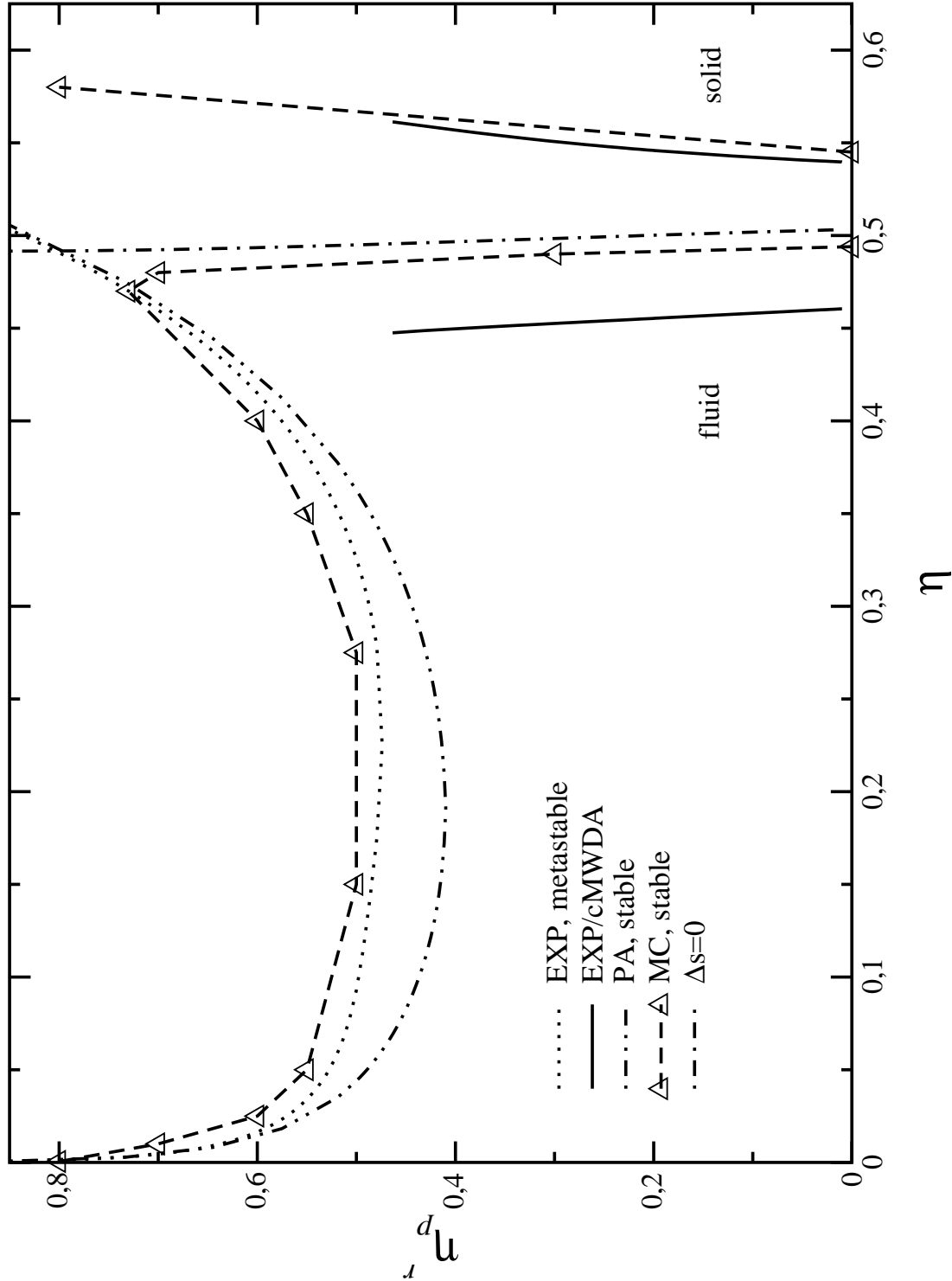


Figure 6.77: Phase diagram of the Asakura-Oosawa potential with $q = 0.1$. Shown are the results for the EXP/cMWDA, the MPA/fg and the FVPA/fg. The computer simulation results (MC) were taken from [31] (additive, effective one-component system), see also figure 6.72.

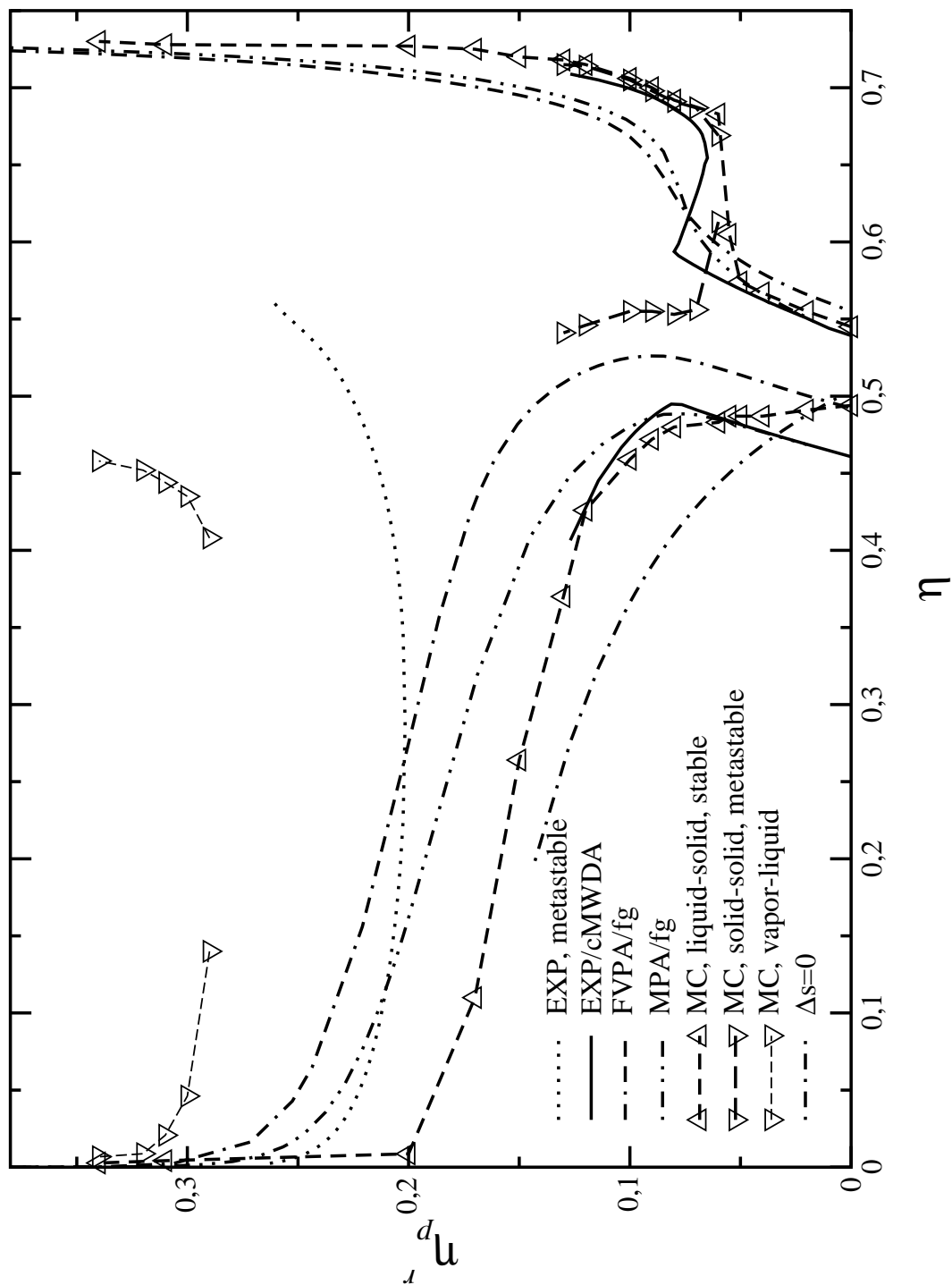
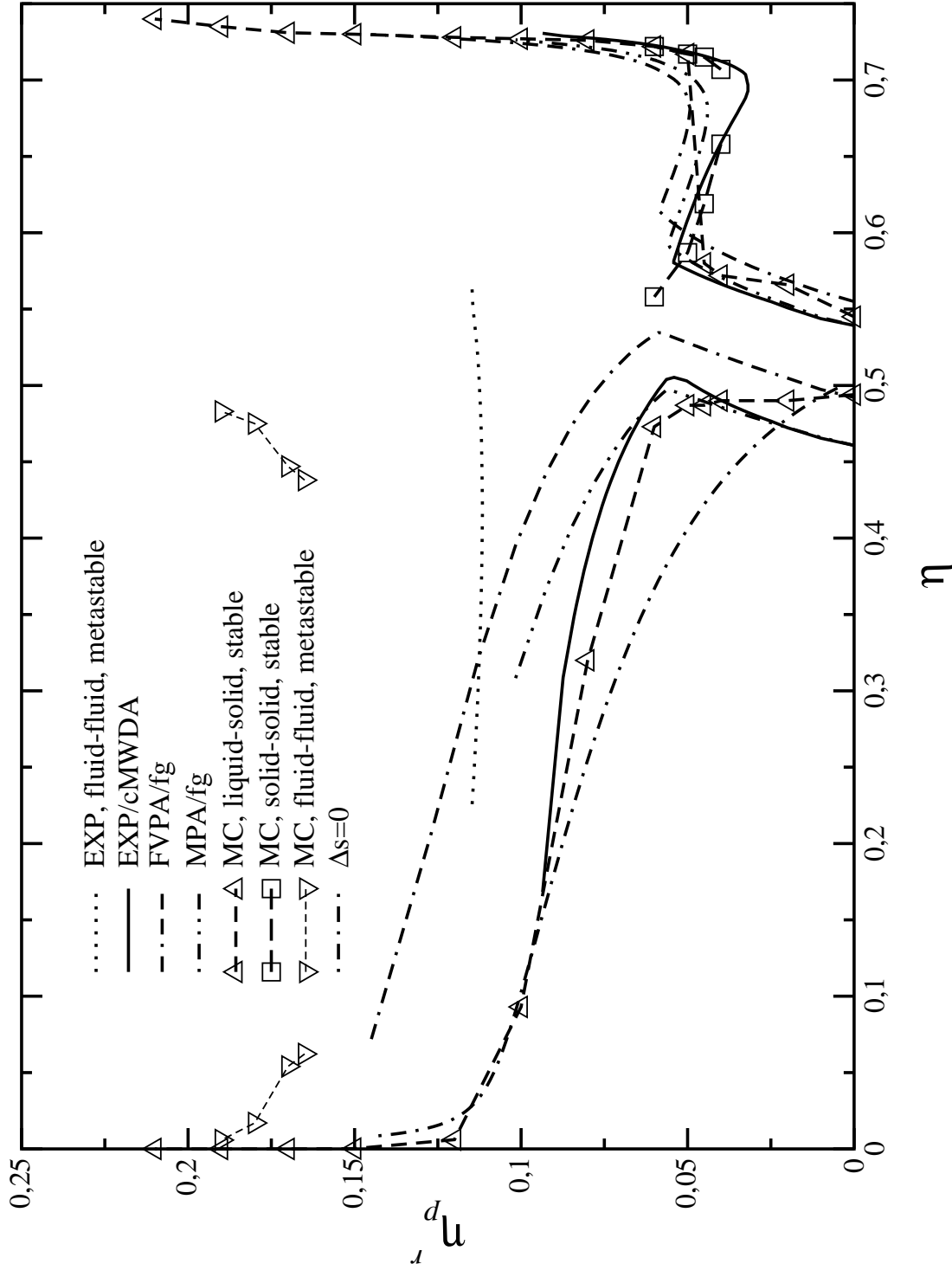


Figure 6.78: Phase diagram of the Asakura-Oosawa potential with $q = 0.05$. Shown are the results for the EXP/cMWDA, the MPA/fg and the FVPA/fg. The computer simulation results (MC) were taken from [31] (additive, effective one-component system).



additive binary hard-sphere mixtures reduces to the Asakura-Oosawa pair potential [30, 31]. Thus, one can expect very similar phase transitions for the two types of mixtures [binary hard-spheres mixtures and colloid-polymer mixtures (a non-additive binary hard-sphere mixture, see subsection 2.2.4)] at small values of the reservoir packing fraction η_p^r . Since the phase boundaries of the additive hard-sphere mixture shift to small reservoir packing fractions for small values of q [31], the phase boundaries for very asymmetric additive hard-sphere mixtures should resemble those of very asymmetric non-additive colloid-polymer mixtures. In figure 6.78, the results for $q = 0.05$ are shown; the computer simulation data were taken from [31]. The results of the EXP/cMWDA are in very good agreement with the computer simulation data (except the metastable fluid-fluid transition). For such small values of q , the system is very sensitive to small changes in the reservoir packing fraction η_p^r . The system is only behaving like a pure hard-sphere system, as long as η_p^r is very low. The isostructural transition can only occur in a very small range of $\eta_p^r \approx 0.03 - 0.05$, and for η_p^r above ≈ 0.12 the system is in fact permanently separated in a very dilute fluid and a very dense solid.

The $\Delta_s = 0$ freezing lines were calculated within the framework of the EXP. For small q -values ($q < 0.2$), the $\Delta_s = 0$ line indicates a freezing transition that occurs at too low colloid packing fractions. For $q = 0.2$, the $\Delta_s = 0$ line has an interesting shape, predicting the fluid-solid transition at high colloid packing fractions $\eta > 0.45$ for low ($\eta_p^r < 0.15$) and high ($\eta_p^r > 0.35$) reservoir packing fractions, whereas for intermediate values of $\eta_p^r \approx 0.25$ this transition is predicted to happen at lower colloid packing fractions $\eta < 0.4$. The quality of the fluid-solid transition predicted by $\Delta_s = 0$ gets better as q increases; the shape straightens and comes close to a perfect line with $\eta_{\Delta_s=0} \approx 0.5$ at $q = 0.8$. Obviously, for $q \geq 0.6$ the fluid side of the freezing transition one gets using computer simulations is in nearly perfect agreement with the $\Delta_s = 0$ line.

6.6 One-component Yukawa potential

The one-component hard-sphere Yukawa potential (see subsection 2.2.3) has been the object to rather extensive studies in the recent years (for an overview see [48]), both for the vapor-liquid coexistence [112] and the vapor-fluid-solid phase diagram [113, 114]. In this section, we will compare the results we have obtained for the one component Yukawa potential with κ ranging from 1.8 (long range) to 9.0 (short range) with the results of the methods used in these papers.

6.6.1 Vapor-liquid coexistence

In [112] a whole range of advanced liquid state theories have been used to calculate the vapor-liquid coexistence of the one component Yukawa fluid. Additionally, critical point parameters from [114] (obtained using computer simulations) and [113] (obtained using the perturbation weighted density approximation (PWDA), see also [115, 116]) were compared with our results (obtained using the ORPA/EXP and the PA).

The EXP results of the vapor-liquid coexistence curves as shown in figures 6.79

Figure 6.79: Vapor-liquid phase transition of the Yukawa potential with $\kappa = 1.8$.

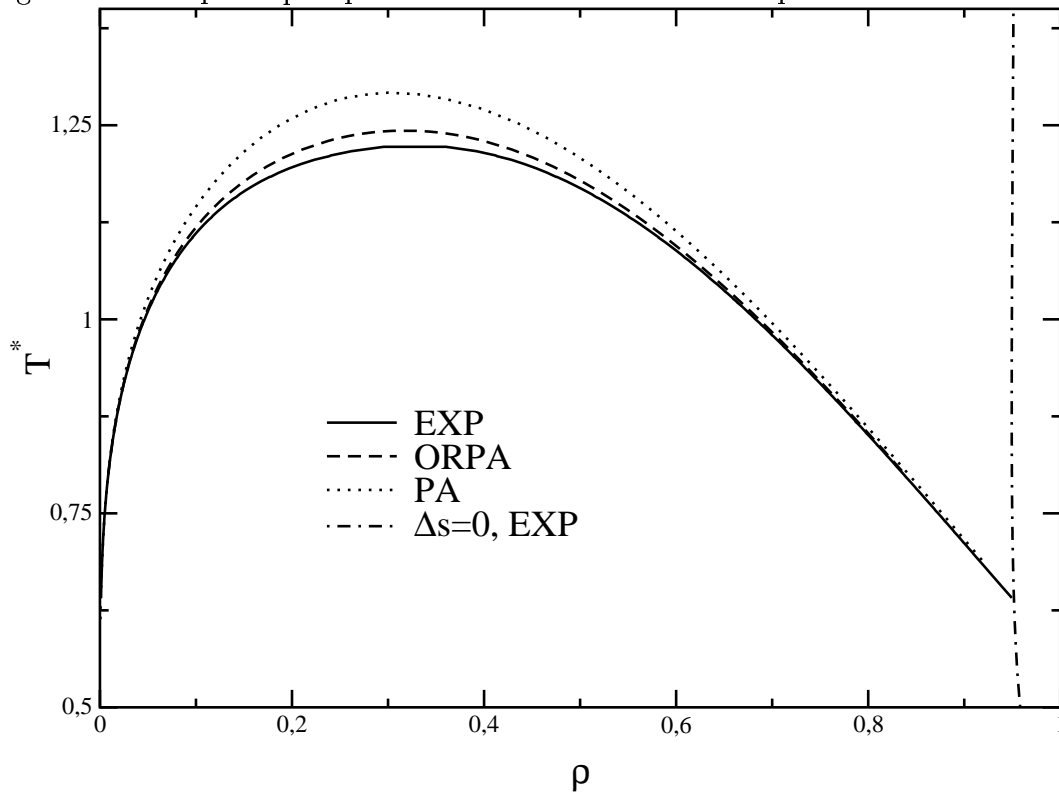


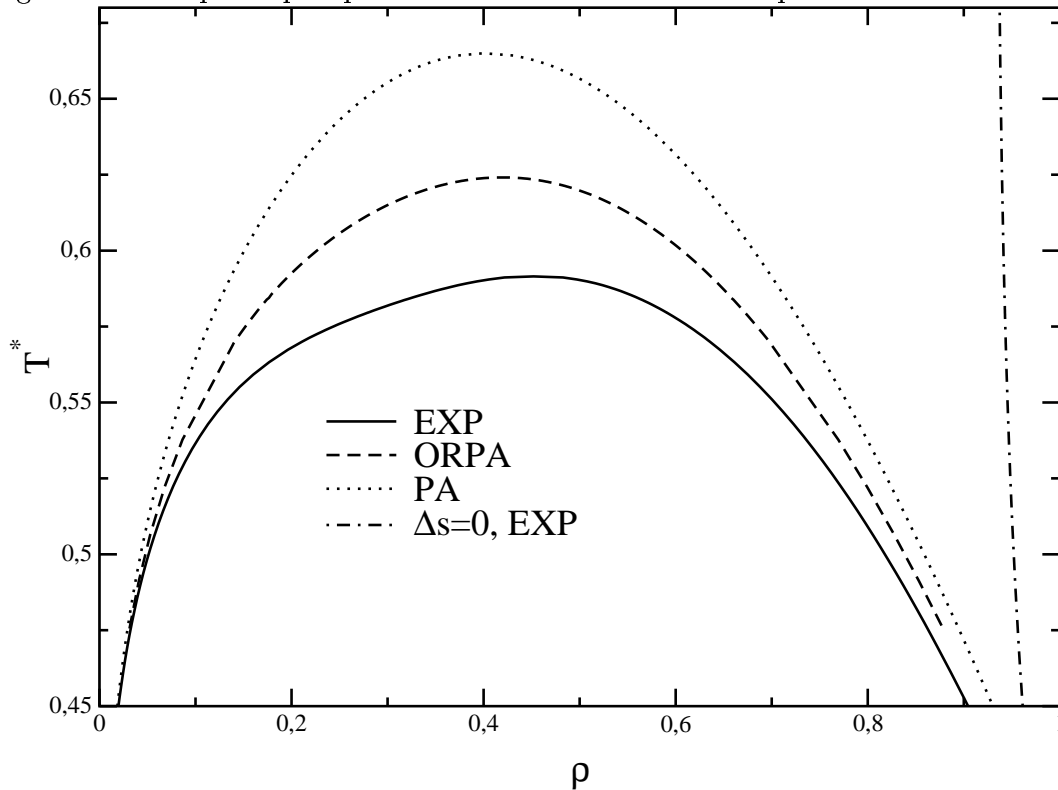
Figure 6.80: Vapor-liquid phase transition of the Yukawa potential with $\kappa = 4.0$.

Table 6.8: Theoretical and simulation critical point parameters for the one-component Yukawa system (see [112]). The abbreviations are discussed in the text.

	$\kappa = 1.8$		$\kappa = 4.0$		$\kappa = 7.0$	
	T_c^*	ρ_c	T_c^*	ρ_c	T_c^*	ρ_c
MC	1.212(2) ¹	0.312(2) ¹	0.576(6) ²	0.377(21) ²	0.411(2) ³	0.50(2) ³
GMSA	1.199	0.312	0.576	0.324		
MHNC	1.193	0.326	0.581	0.412		
MHNC ⁴	1.21	0.28				
HRT	1.214	0.312	0.599	0.394	0.435	0.424
SCOZA	1.219	0.314	0.591	0.3895	0.419	0.4575
ORPA	1.243	0.318	0.624	0.419	0.451	0.5375
EXP	1.224	0.327	0.5915	0.452	0.410	0.565
PA	1.292	0.302	0.665	0.405	0.4815	0.518

($\kappa = 1.8$, only vapor-liquid coexistence), 6.81 ($\kappa = 1.8$), 6.80 ($\kappa = 4.0$) and 6.83 ($\kappa = 7.0$)

¹Finite-size scaling MC simulation of [117].

²Gibbs-ensemble MC simulations of [118].

³Gibbs-ensemble MC simulations of [114].

⁴MHNC calculations with Verlet-Weis bridge functions of [119].

Table 6.9: Comparison of the critical point temperature T_c^* of the vapor-liquid transitions for the one-component Yukawa system (see [113]).

κ	3.9	7.0	7.6	7.8	8.0
ORPA	0.635	0.451	0.434	0.428	0.423
EXP	0.603	0.410	0.390	0.384	0.378
PA	0.677	0.482	0.462	0.456	0.451
PWDA	0.645	0.471	0.460	0.456	0.450

Table 6.10: Comparison of the critical point parameters of the vapor-liquid transitions for the one-component Yukawa system (see [114]). MC/fop denotes the first order perturbation theory, also from [114].

κ	T_c^*				ρ_c			
	3.9	5.0	7.0	9.0	3.9	5.0	7.0	9.0
ORPA	0.635	0.542	0.451	0.4	0.415	0.46	0.538	0.6
EXP	0.603	0.506	0.390	0.359	0.447	0.5	0.565	0.337
MC	0.555		0.411		0.35		0.497	
MC/fop	0.645	0.571	0.483	0.427	0.40	0.44	0.50	0.57

Table 6.11: Vapor-liquid coexistence densities for the one-component Yukawa system with $\kappa = 3.9$. The computer simulation results (MC) are taken from [114].

$1/T^*$	1.85	1.9	1.95	2.0	2.05
ρ_v (ORPA)	0.078	0.0625	0.0505	0.0411	0.0335
ρ_v (EXP)	0.09	0.0698	0.055	0.04375	0.03507
ρ_v (MC)	0.16 ± 0.04	0.14 ± 0.05	0.11 ± 0.02	0.07 ± 0.02	0.07 ± 0.02
ρ_l (ORPA)	0.776	0.8023	0.82575	0.8469	0.8663
ρ_l (EXP)	0.7465	0.7778	0.80475	0.8285	0.8501
ρ_l (MC)	0.59 ± 0.03	0.61 ± 0.04	0.72 ± 0.02	0.74 ± 0.02	0.74 ± 0.02

Table 6.12: Vapor-liquid coexistence densities for the one-component Yukawa system with $\kappa = 7.0$. The computer simulation results (MC) are taken from [114].

$1/T^*$	2.5	2.6	2.7
ρ_v (ORPA)	0.136	0.094	0.065
ρ_v (EXP)	0.222	0.1095	0.068
ρ_v (MC)	0.32 ± 0.04	0.16 ± 0.02	0.13 ± 0.02
ρ_l (ORPA)	0.885	0.929	0.9675
ρ_l (EXP)	0.747	0.841	0.9
ρ_l (MC)	0.69 ± 0.05	0.84 ± 0.02	0.88 ± 0.02

are in good agreement with the results of the theories discussed in [112]. Especially the critical temperature T_c obtained using the EXP are in very good agreement with the results of the self consistent Ornstein-Zernike approximation (SCOZA, see [120, 121, 117]), as can be seen from table 6.8. Beside the SCOZA results, in this table the generalized mean spherical approximation (GMSA, see [122, 123, 124, 125]), the modified hypernetted chain (MHNC, see [90]) and the hierarchical reference theory (HRT, see [126, 127, 128]) results are presented. The critical density of the EXP is shifted towards higher densities for increasing values of κ (towards shorter interaction ranges). The nearly vertical lines consisting of the $\Delta s = 0$ loci (freezing) is, for $\kappa = 1.8$ and $\kappa = 4.0$, in fact not distinguishable from the SCOZA and MHNC results. The ORPA and the PA are not giving results with the same quality (when compared with [112]), furthermore none of these theories gave a physically meaningful $\Delta s = 0$ line.

Another comparison of vapor-liquid critical point temperatures is shown in table 6.9. The most interesting result is that the PWDA yields results for high κ values that are in fact identical to the PA. Hence, if one keeps in mind that the results of the vapor-liquid transition presented in [113] are in no good agreement with the computer simulation results from [114]. A comparison of the critical point temperatures and densities with the results from [114] is made in table 6.10.

Summarizing, for $\kappa = 1.8$, all three theories (EXP, ORPA and PA) reproduce with considerable accuracy the critical point parameters of the vapor-liquid phase coexistence when compared with the results from [112]. The shape of the coexistence curve is a little too broad (for $\kappa = 3.9$ see table 6.11, for $\kappa = 7.0$ see table 6.12). For higher κ 's, the results for the critical point start to differ in a way that the ORPA and the PA are overestimating the attractive effect of the Yukawa tail, hence leading to an increased critical temperature.

6.6.2 Fluid-solid coexistence

In this subsection we will present the fluid-solid coexistence of the hard-sphere Yukawa system (with inverse screening lengths κ varying between $\kappa = 1.8$ and $\kappa = 9.0$). For this parameter range, the EXP and the MPA are the only theories where a physically meaningful solution for the liquid-solid transition was found.

For $\kappa = 1.8$ (figure 6.81), no computer simulation data were available. For the higher κ values, $\kappa = 3.9$ (figure 6.82), 7.0 (figure 6.83) and 9.0 (6.84) the computer simulation data are taken from [114]. For the latter two figures, the fluid-solid transition calculated using the EXP/cMWDA yields good agreement when compared to the MC data. In contrast to the MPA, which is not able to give satisfactory results for the phase diagram.

Figure 6.81: Fluid-solid phase transitions of the Yukawa potential with $\kappa = 1.8$. No computer simulation results available.

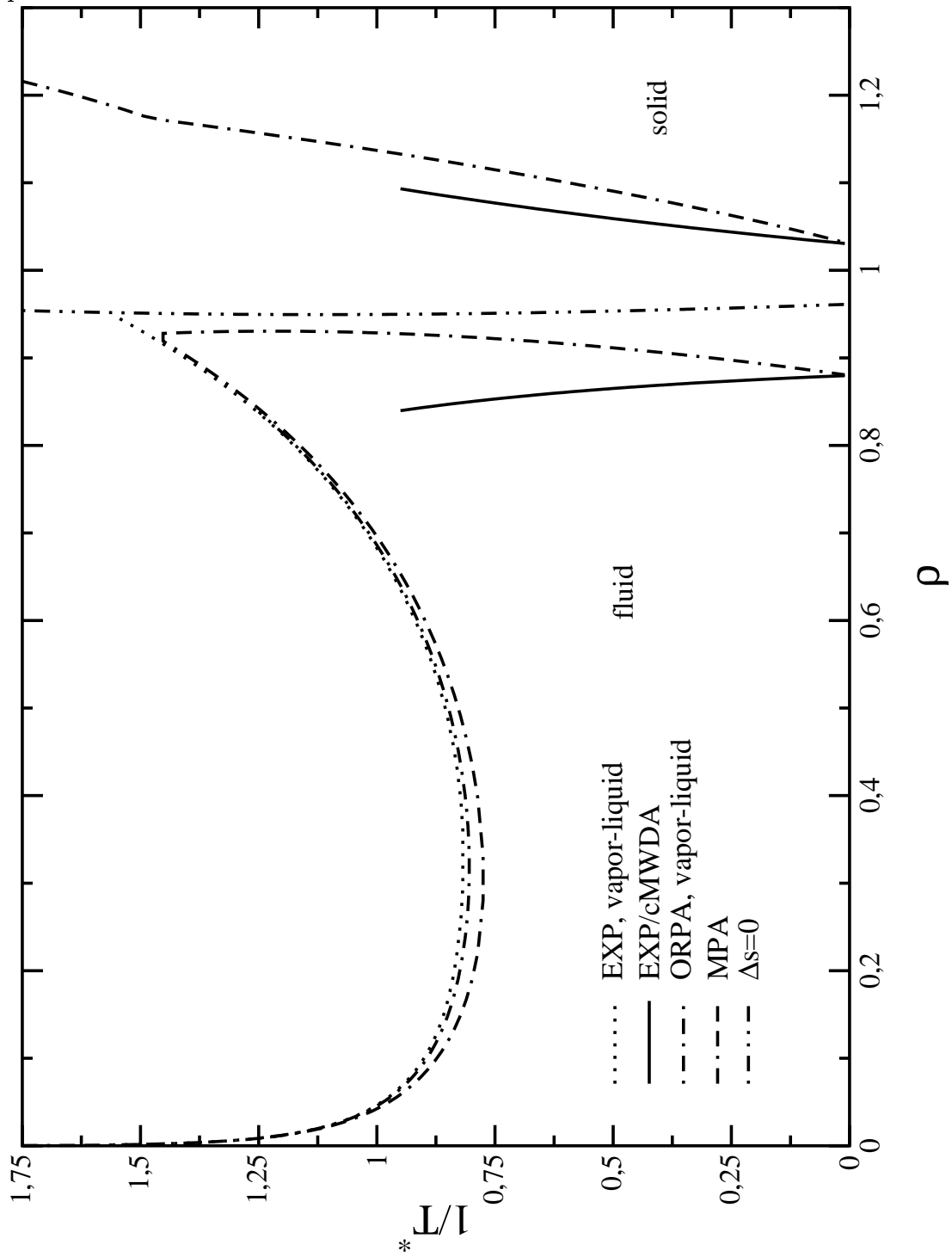


Figure 6.82: Fluid-solid phase transitions of the Yukawa potential with $\kappa = 3.9$. The Monte-Carlo results are taken from [114].

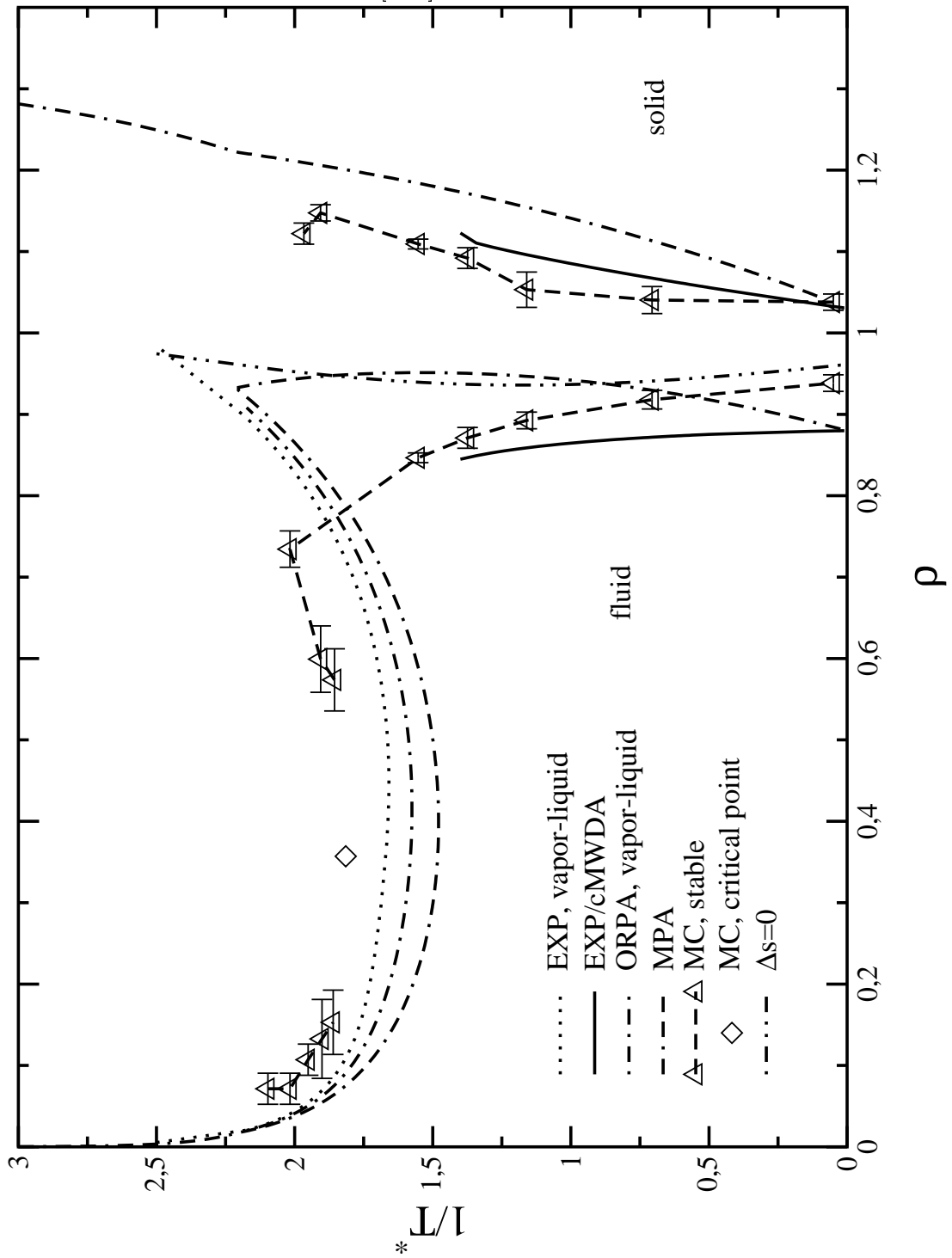


Figure 6.83: Fluid-solid phase transitions of the Yukawa potential with $\kappa = 7.0$. The Monte-Carlo results are taken from [114].

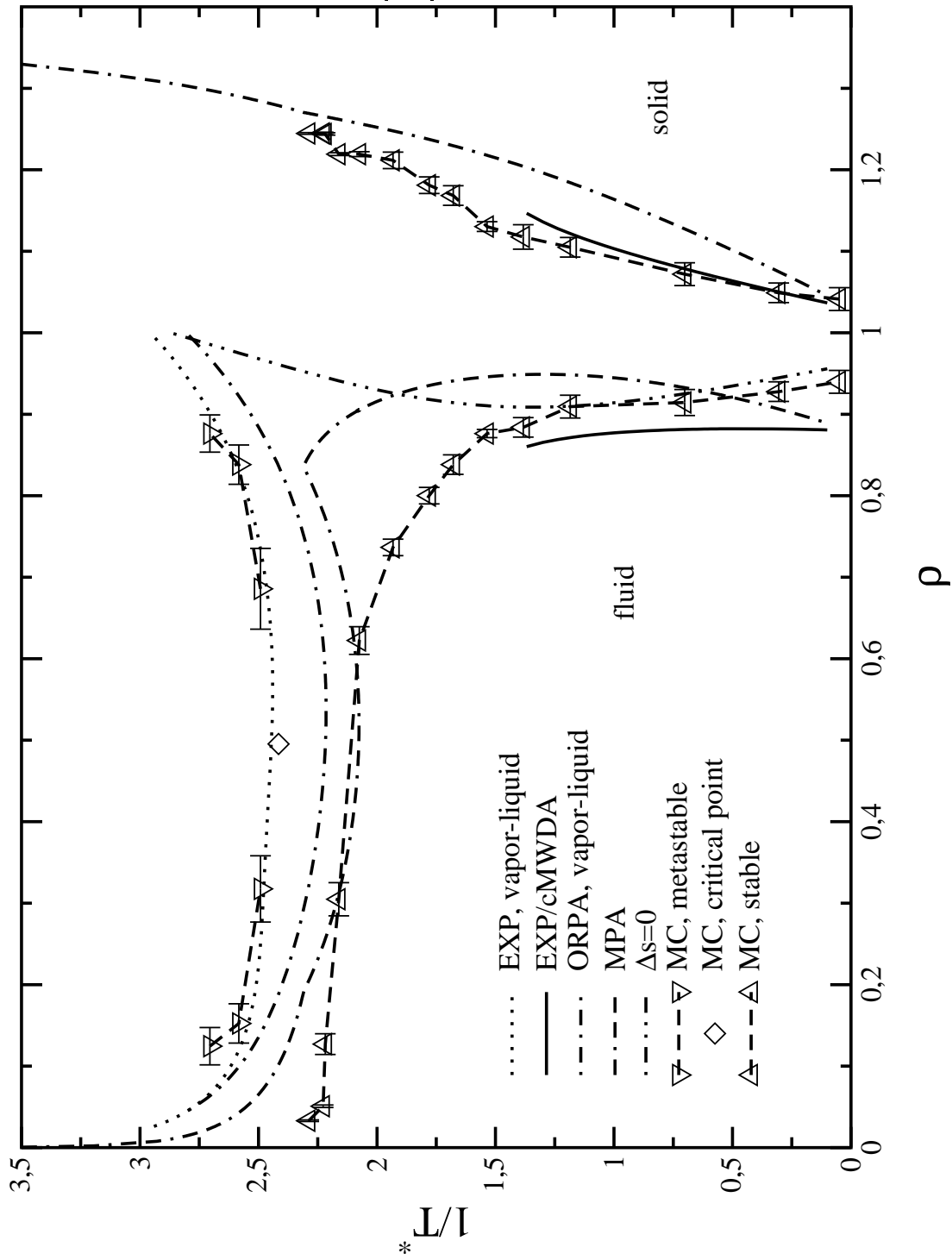
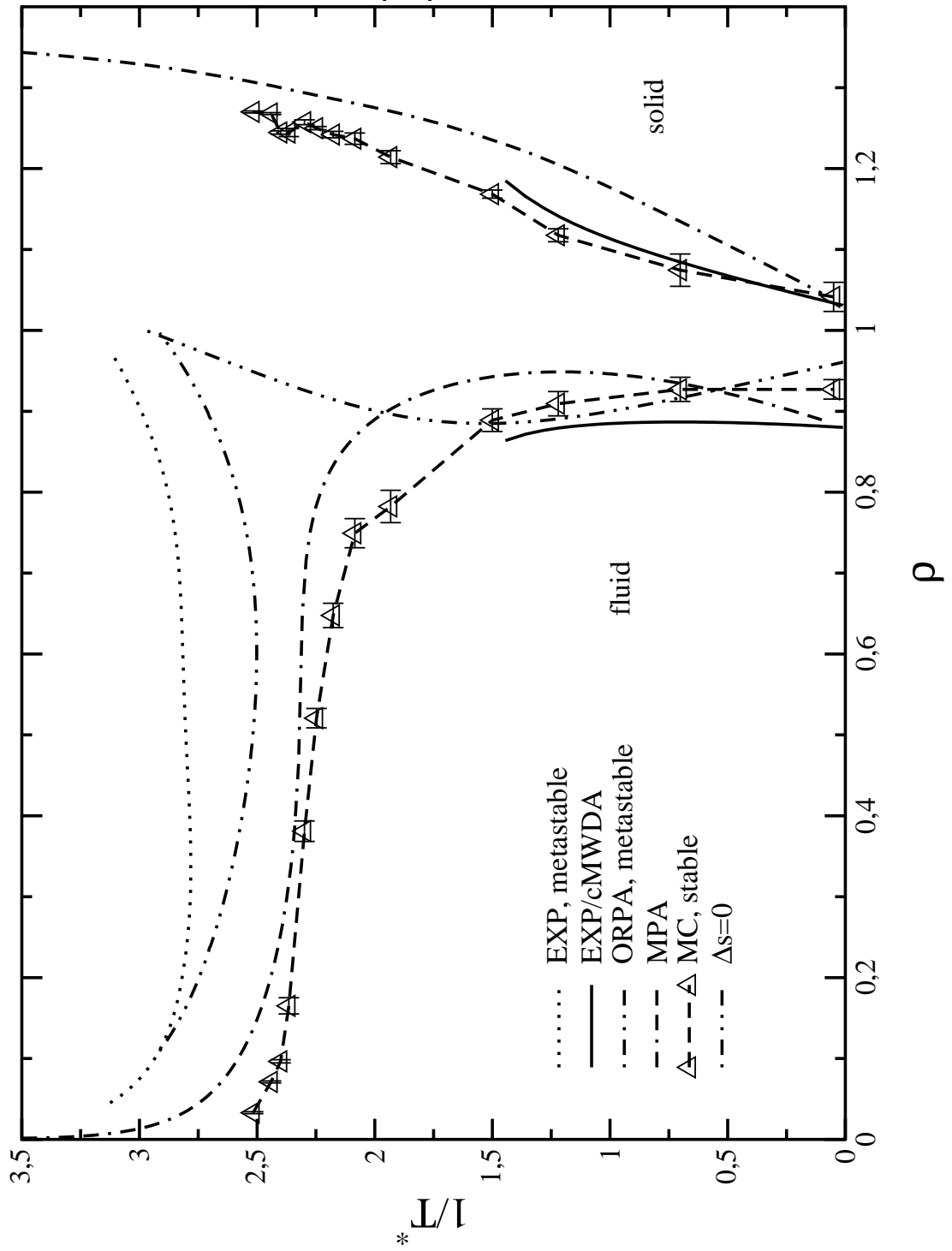
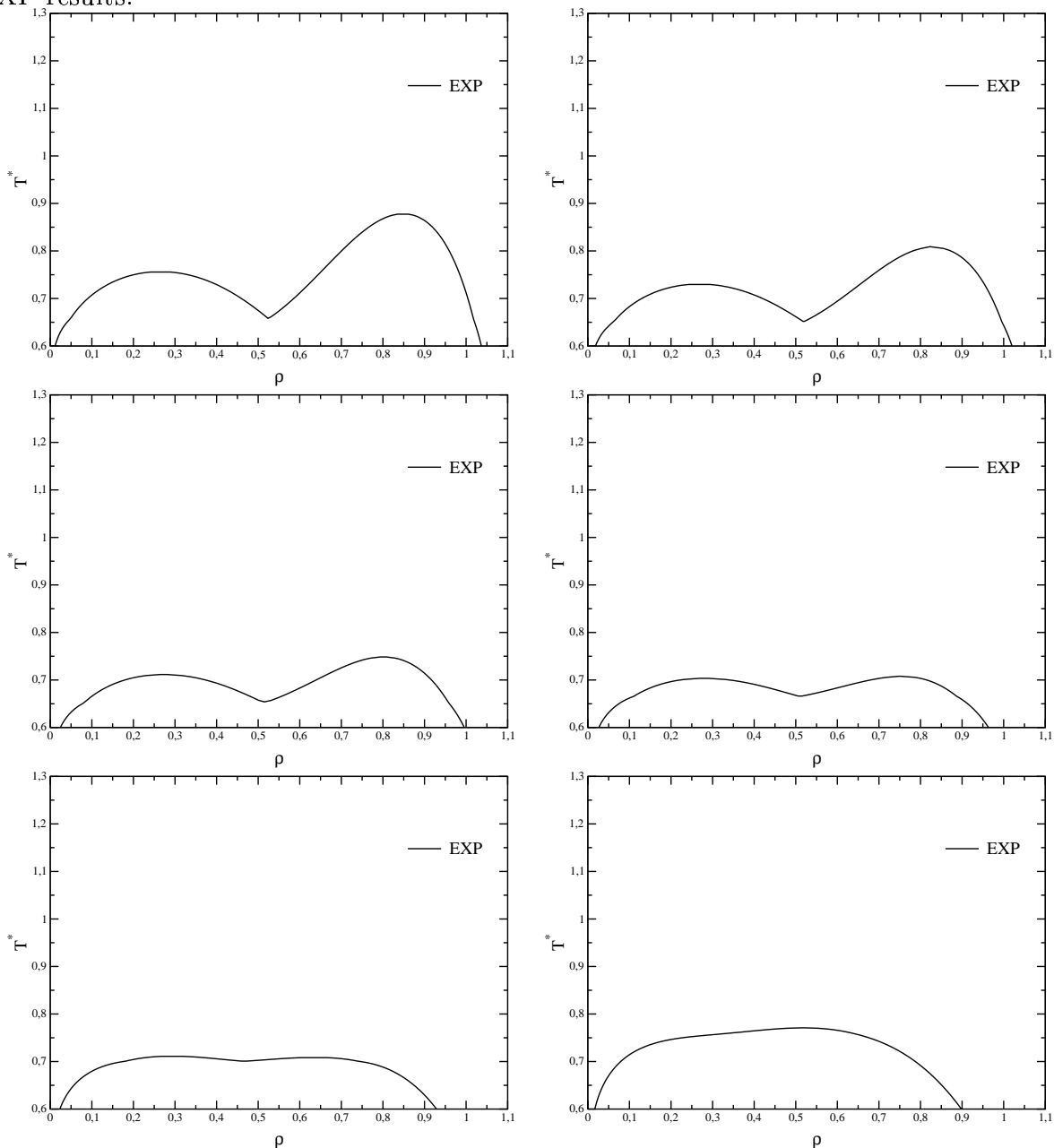


Figure 6.84: Fluid-solid phase transitions of the Yukawa potential with $\kappa = 9.0$. The Monte-Carlo results are taken from [114].



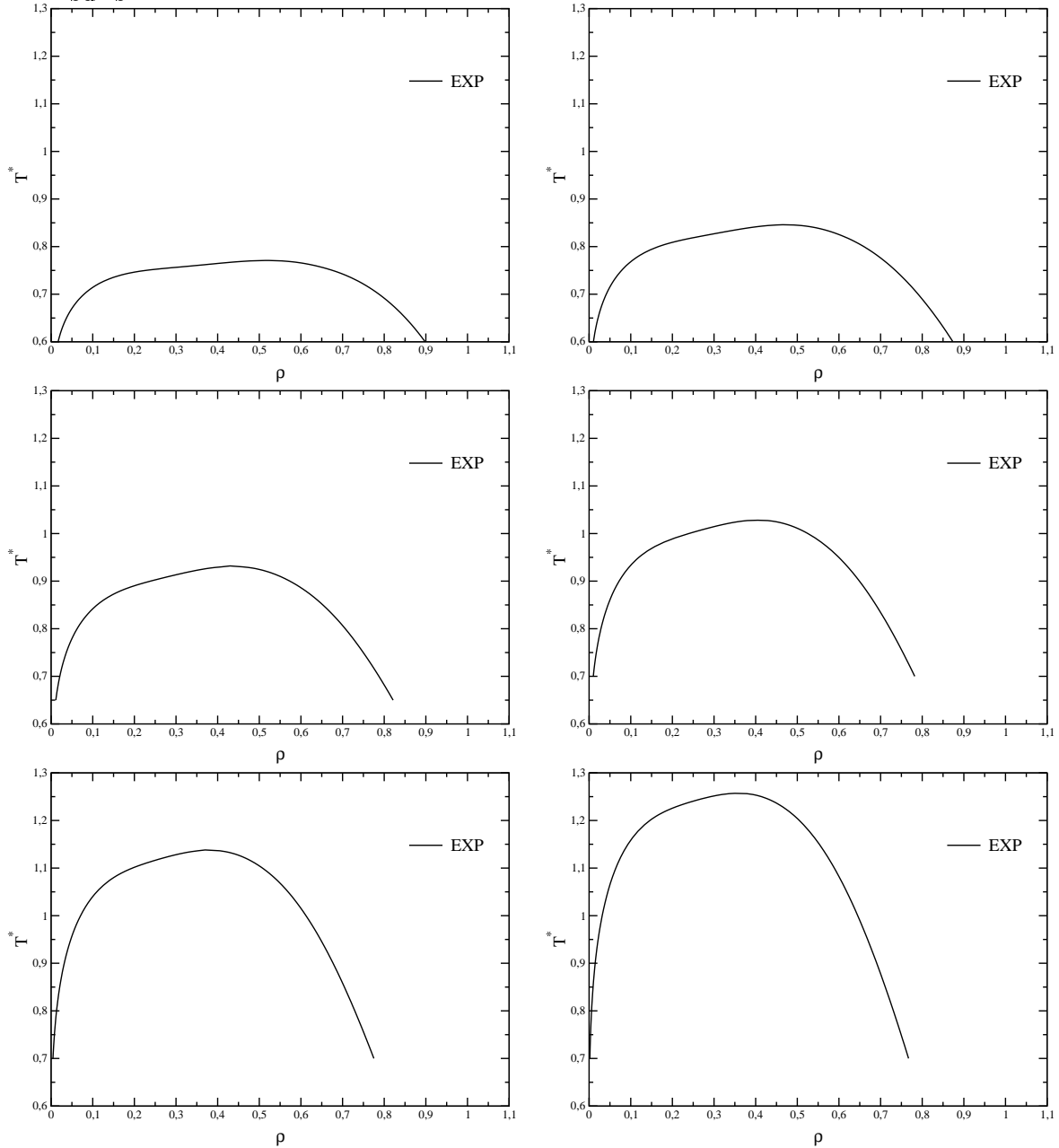
6.7 Double square-well/square-shoulder potential

Figure 6.85: Evolution of the phase diagram of a double square-well/square-shoulder fluid, $\varepsilon_r = -1.0$ (upper left graph) to $\varepsilon_r = 0.0$ (lower right graph), $\Delta\varepsilon_r = 0.2$. Shown are the EXP results.



Double square-well/square-shoulder systems (for the definition of the potential and its parameters see subsection 2.2.2.1) can, even for the vapor-liquid transition, show a wide variety of different phase behaviors. Because of an increased number of system parameters

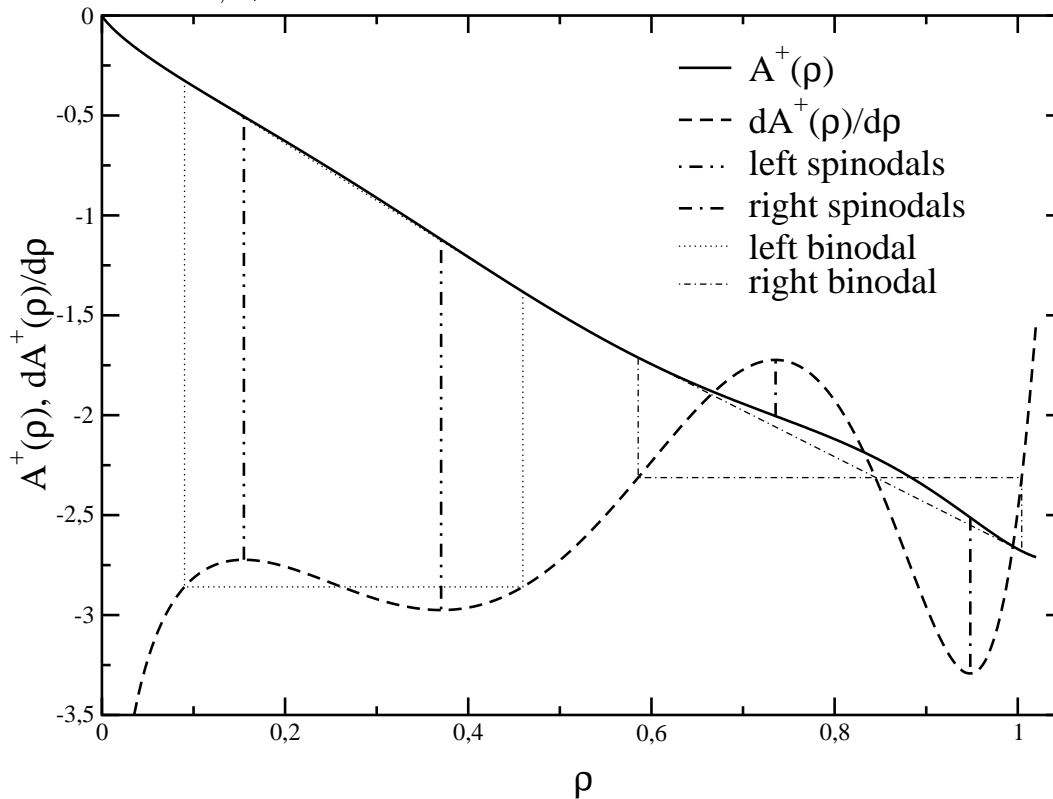
Figure 6.86: Evolution of the phase diagram of a double square-well/square-shoulder fluid, $\varepsilon_r = 0.0$ (upper left graph) to $\varepsilon_r = 1.0$ (lower right graph), $\Delta\varepsilon_r = 0.2$. Shown are the EXP results.



(the parameter space is three dimensional, two width parameters and one for the ratio of the potential heights), we will focus our investigations on the following potential: Hard-sphere core with an adjacent square-well with width $\lambda_1 = 1.25$, the second step has the width $\lambda_2 = 1.5$ and its height is connected to the height of the first step, ε_1 , via

$$\varepsilon_2 = \varepsilon_1 \varepsilon_r,$$

Figure 6.87: Double tangent construction for a double square-well/square-shoulder potential with $T^* = 0.7$, $\varepsilon_r = -1.0$.



the inverse reduced temperature $\frac{1}{T^*}$ is equal to the strength of the first step. The parameter ε_r has been varied from $\varepsilon_r = -1.0$ (square-well with a square-shoulder of equal strength) over $\varepsilon_r = 0.0$ (pure square-well potential with $\lambda = 1.25$) to $\varepsilon_r = 1.0$ (pure square-well potential with $\lambda = 1.5$), stepsize was $\Delta\varepsilon_r = 0.2$.

This potential shows two critical points for $\varepsilon_r \leq -0.2$ (see also figures 6.85 and 6.86), while for $\varepsilon_r > -0.2$ the systems shows only one critical point. It should also be noted that this kind of phase diagram only shows up if one uses the EXP for the calculation of the Helmholtz free energy; if one uses the ORPA (or the PA) for this potential, no double-transition will occur.

In order to show a phase behavior similar to the upper left graph of figure 6.85, there has to be a underlying mechanism that modifies the free energy curves in such a way that two double tangents can occur (for a given temperature). Figure 6.87 shows the free energy curve together with its first derivative for potential (a), $\varepsilon_r = -1.0$ at $T^* = 0.7$. The two binodals can easily be identified (see also figure 6.85), the spinodals are also shown.

To get a better understanding of the whole problem, we have calculated the pair distribution functions for this system parameters ($\varepsilon_r = -1.0$) at the densities $\rho = 0.00005$, 0.25, 0.5, 0.8 and 1.0 (see figure 6.88). For increasing density ρ , $g(r)$ shows an unusual behavior when compared to the pair distribution function of the potential with $\varepsilon_r = 0$ (same temperature T^* , see figure 6.89): the maximum of $g(r)$ inside the first potential

Figure 6.88: Pair distribution functions $g(r)$ obtained using the EXP for a double square-well/square-shoulder potential with $T^* = 0.7$, $\varepsilon_r = -1.0$, at various densities.

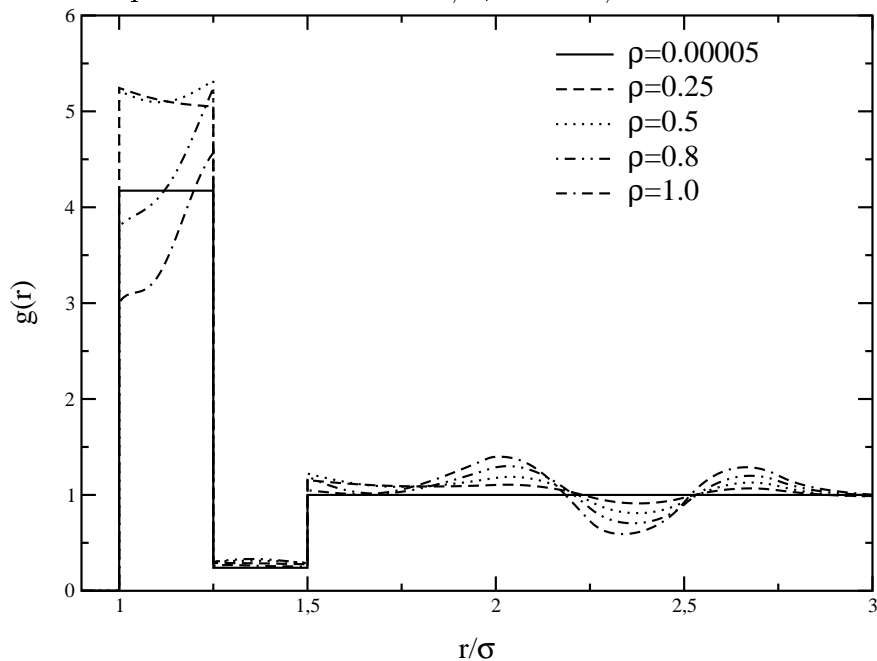
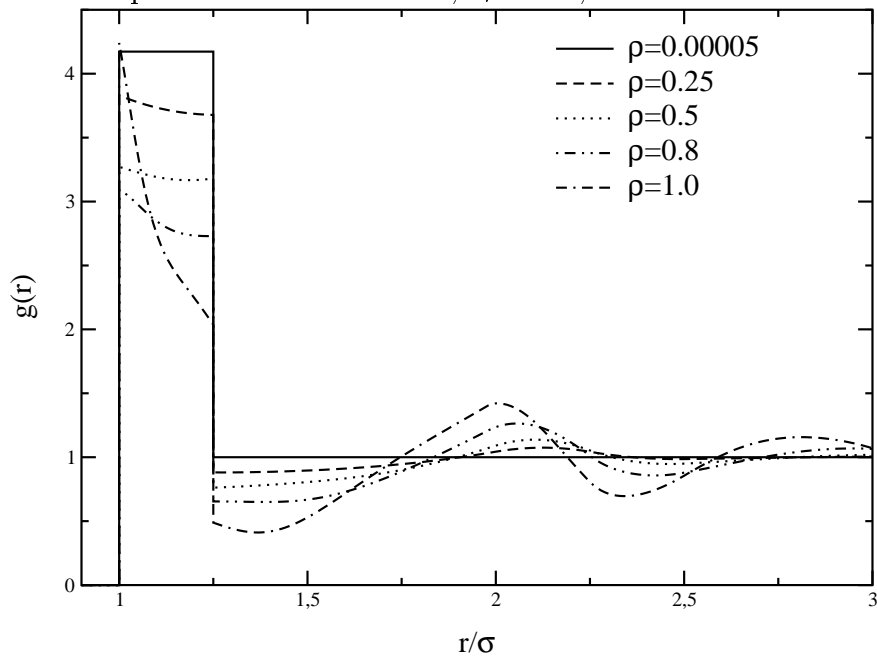


Figure 6.89: Pair distribution functions $g(r)$ obtained using the EXP for a double square-well/square-shoulder potential with $T^* = 0.7$, $\varepsilon_r = 0.0$, at various densities.



step ($\sigma < r < \lambda_1\sigma$) is located at $r \rightarrow \lambda_1\sigma$, whereas one would expect the maximum of the pair distribution function at $r \rightarrow \sigma$. To understand this behavior, one has to remember the special shape of the potential which is responsible for the pair distribution functions as shown in figure 6.88. However, no explanation was found within the timeframe of this thesis, but there are ongoing investigations with respect to this problem.

6.8 Binary phase diagrams

In this section we will present the phase diagrams we obtained for symmetric binary fluid mixtures.

6.8.1 Truncated hard sphere-Yukawa potentials

In this subsection we will discuss the phase diagrams for symmetric binary system (see subsection 2.1.2) where the particles are interacting via tHSY potentials with an attractive tail as defined in subsection 2.2.3.1. The interaction potentials between the different species are defined as

$$\phi_{12}(r) = \phi_{21}(r) = \varepsilon_r \phi_{11}(r) = \varepsilon_r \phi_{22}(r) \quad ; \quad \varepsilon_r \leq 1, \quad (6.12)$$

i.e. similar species interactions are energetically more favorable than dissimilar species interactions. For this type of interaction, Wilding *et al.* [85] pointed out three different topologies of phase diagrams for a symmetric binary fluid mixture (when projected to the density-temperature plane) using a simple mean-field theory. These three different topologies can be specified via the number and type of stable phase transitions:

- (a) Two stable phase transitions: mixed vapor/demixed liquid and mixed vapor/mixed liquid.
- (b) Three stable phase transitions: mixed vapor/demixed liquid, mixed vapor/mixed liquid and mixed liquid/demixed liquid.
- (c) One stable phase transition: mixed vapor/demixed liquid.

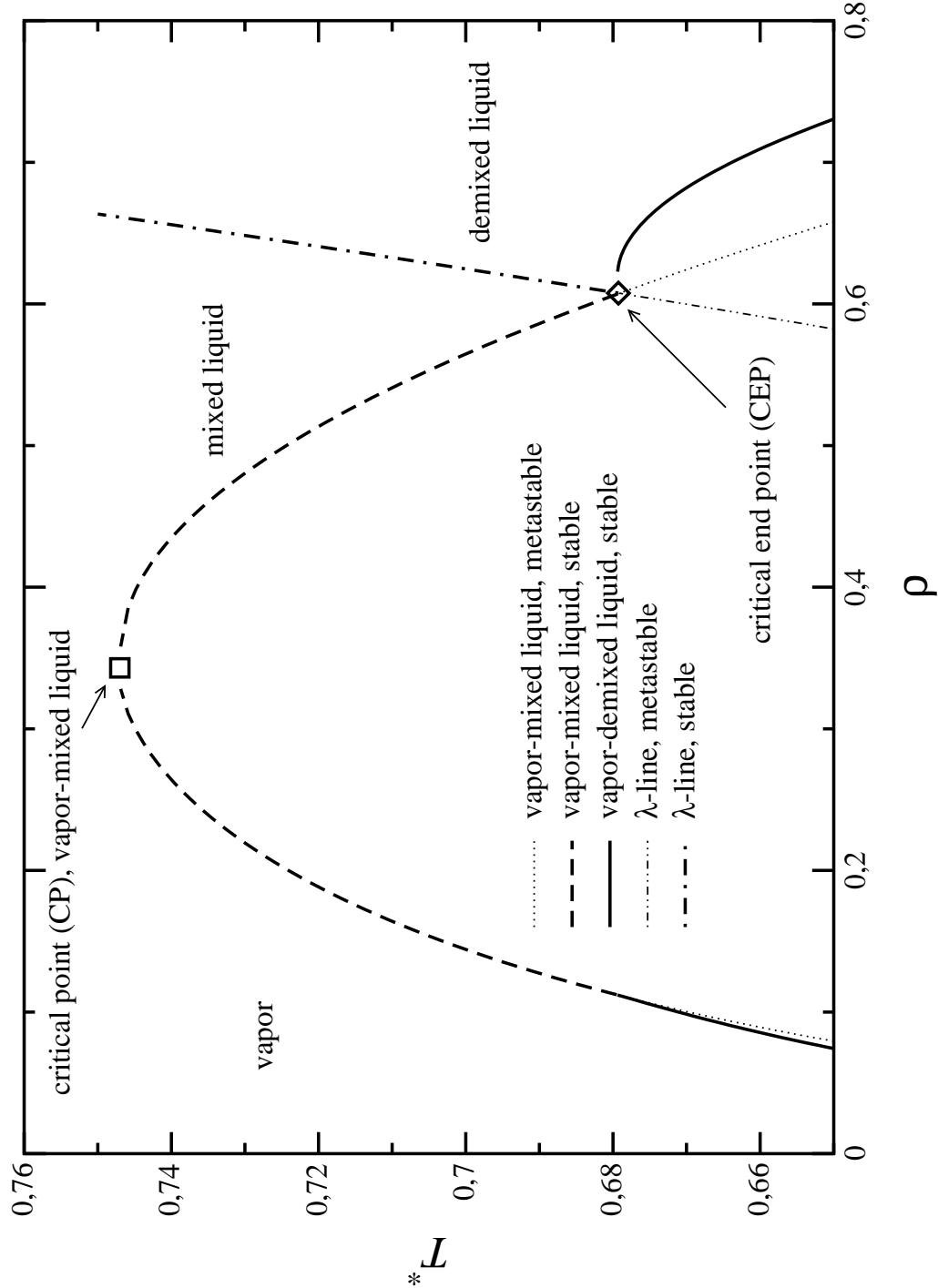
These topologies also showed up in our results, for which ε_r was decreased from $\varepsilon_r = 0.75$ (see figure 6.90) to $\varepsilon_r = 0.65$ (see figure 6.94); in contrast to [85] we have used the more sophisticated ORPA.

The interaction conditions as defined in (6.12) provide a consolute point (critical demixing behavior) at some finite temperature T_c . For temperatures $T < T_c$ there is coexistence

Table 6.13: Estimated vapor-mixed liquid critical point density ρ_c and temperature T_c^* for symmetric binary fluid mixtures.

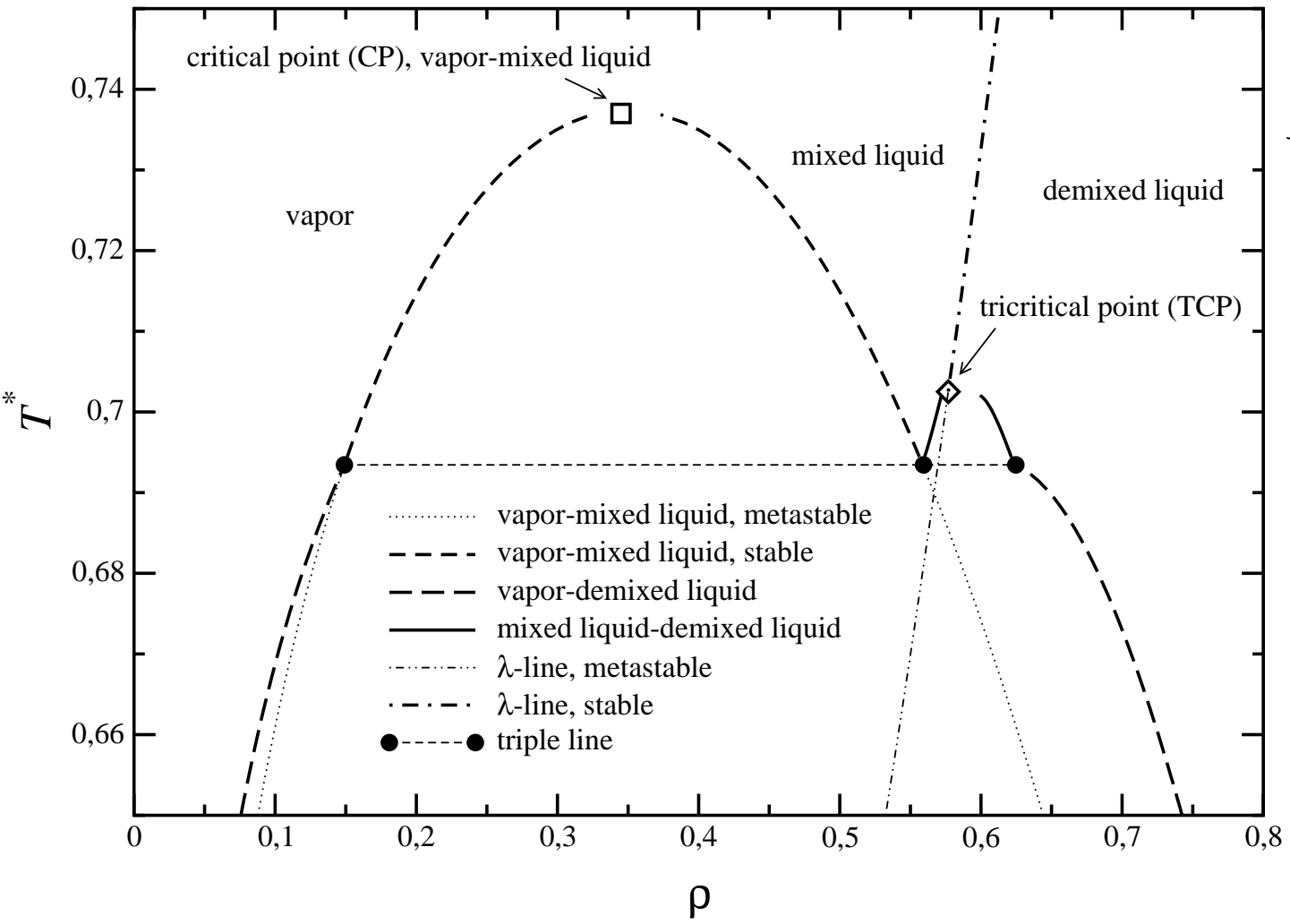
ε_r	ρ_c	T_c	type
1.0	0.346	0.851	stable, one-component
0.9	0.343	0.808	stable
0.8	0.342	0.767	stable
0.75	0.345	0.747	stable
0.725	0.347	0.7375	stable
0.7	0.35	0.728	stable
0.675	0.354	0.718	stable
0.65	0.354	0.709	metastable

Figure 6.90: Phase diagram of a symmetric binary mixture. System type is truncated HS-Yukawa (tHSY) with $\sigma_{ii} = 1$, $\kappa_{ii} = 2.5$, $\lambda_{ii} = 2.5$ and $\varepsilon_r = \varepsilon_{12}/\varepsilon_{11} = 0.75$. The structure and thermodynamics were calculated using the ORPA (PY reference system).



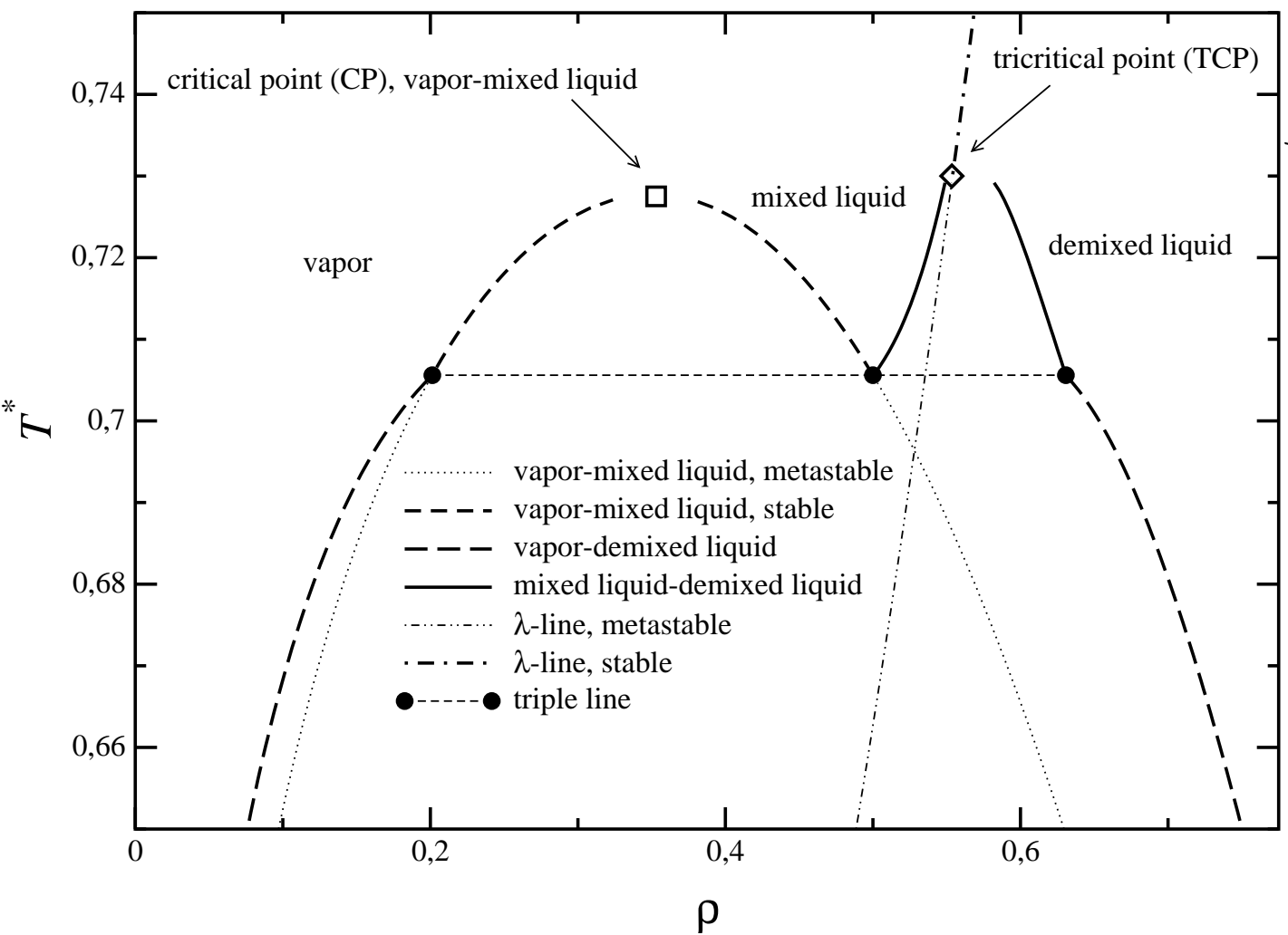
between an species 1-rich liquid and an species 2-rich liquid (demixed liquid), while for

Figure 6.91: Phase diagram of a symmetric binary mixture. System parameters as in figure 6.90 with $\epsilon_r = 0.725$.



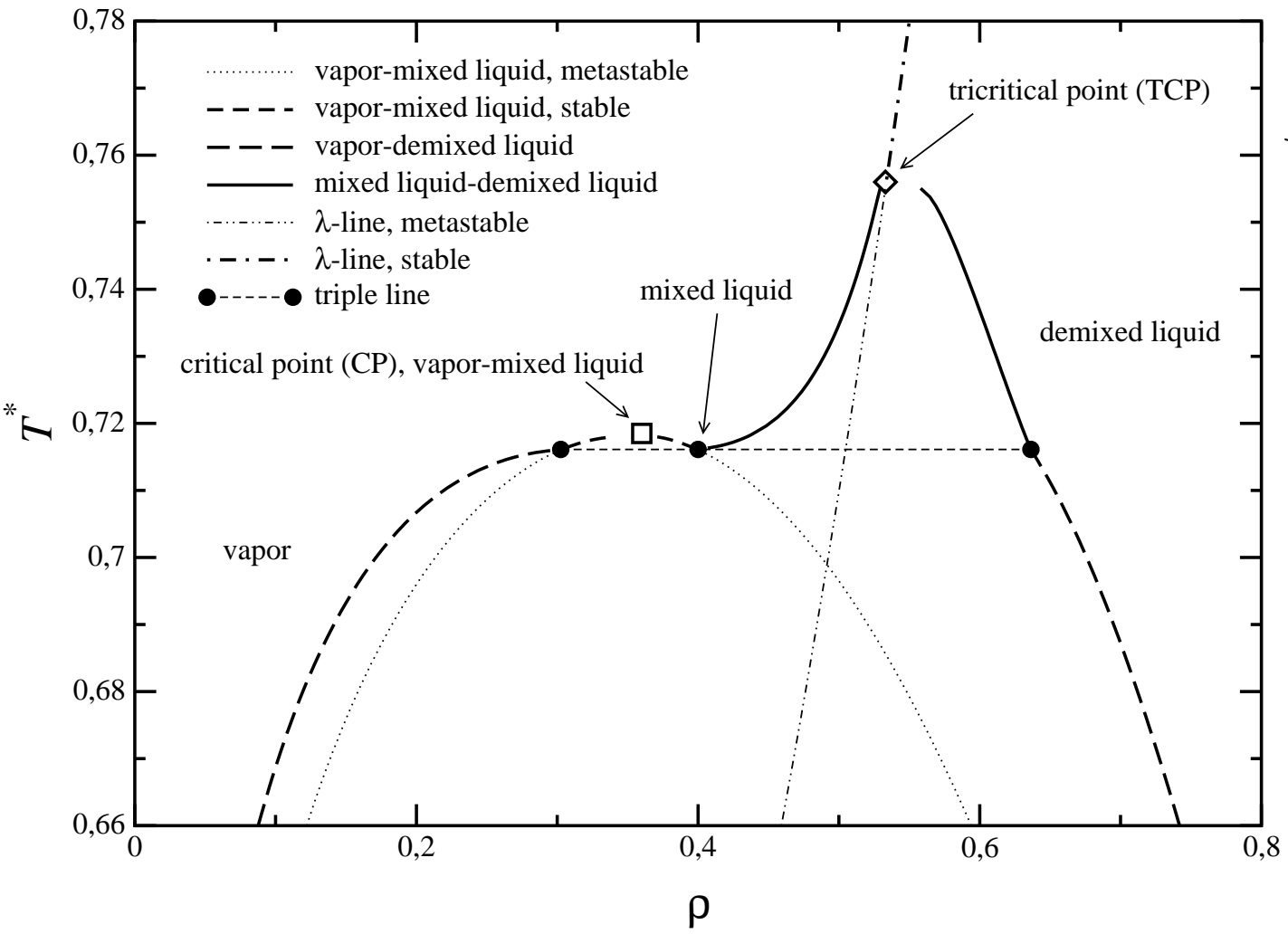
$T > T_c$ is a homogeneous mixture of species 1 and 2 (mixed vapor or mixed liquid). In addition to this behavior, binary fluids can also exhibit vapor-liquid (both mixed and

Figure 6.92: Phase diagram of a symmetric binary mixture. System parameters as in figure 6.90 with $\varepsilon_r = 0.7$.



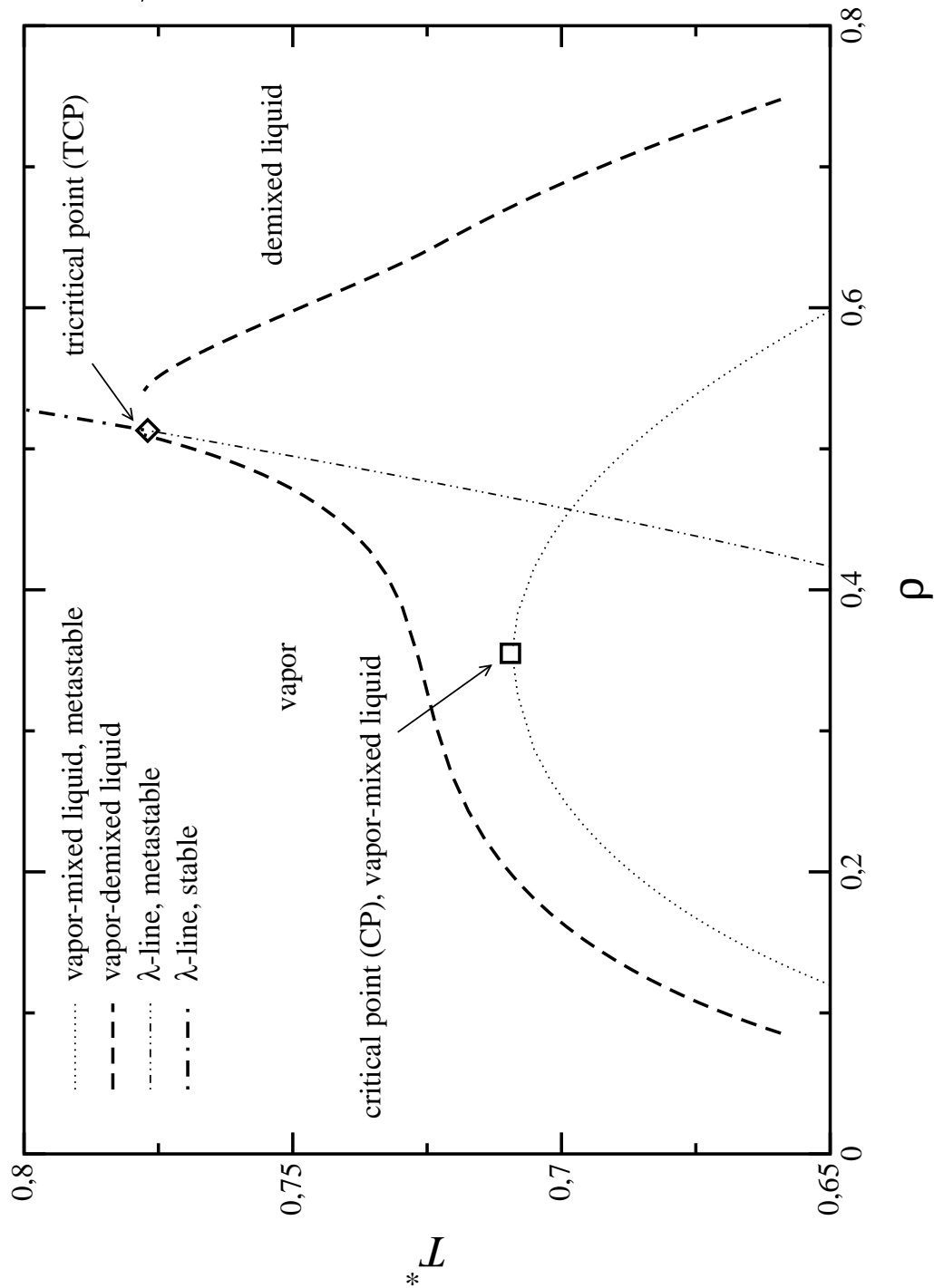
demixed) coexistence, similar to a one component fluid. It should be noted, that for symmetric binary systems there is no fundamental difference (apart from the density)

Figure 6.93: Phase diagram of a symmetric binary mixture. System parameters as in figure 6.90 with $\varepsilon_r = 0.675$.



between the vapor and the mixed-liquid state. For both of them the concentration of the two species is equal ($c_1 = c_2 = 0.5$). In fact, one can only distinguish between these two

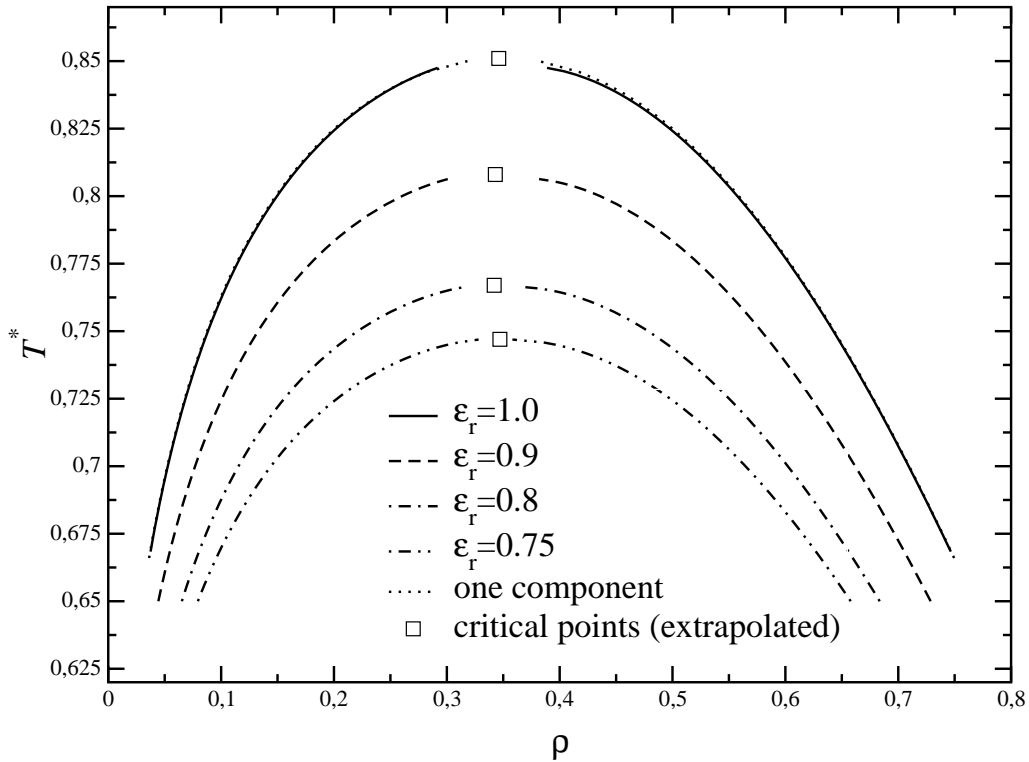
Figure 6.94: Phase diagram of a symmetric binary mixture. System parameters as in figure 6.90 with $\varepsilon_r = 0.65$.



phases in case of a phase transition between them.

Figure 6.90 shows the phase diagram for $\varepsilon_r = 0.75$ [type (a)]. We observe a (one-

Figure 6.95: One-component limit for the phase diagram of a symmetric binary mixture. Vapor-mixed liquid phase transition for $\varepsilon_r = 1.0, 0.9, 0.8$ and 0.75 and the one component case. The estimated critical points are denoted by squares. System parameters as in figure 6.90.



component like) vapor-mixed liquid phase transition, which can be explained by the attraction between particles of different species (for $\varepsilon_r = 1$ the phase diagram would be equal to the according one component phase diagram, as shown in figure 6.95), this transition terminates in a critical point (CP, denoted by the square in figure 6.90).

The λ -line intersects the vapor-mixed liquid coexistence at a so called critical end point (CEP). A CEP is a point where a line of critical points (of second order phase transitions) meets a line of a first order phase transition. Hence, at the CEP (temperature T_{CEP}) a critical liquid coexists with a noncritical vapor. Below the CEP, the vapor is in coexistence with a species 1-rich liquid and a (symmetric) species 2-rich liquid (demixed liquid). These two liquids have, owing to the symmetry, the same density. The vapor-mixed liquid coexistence is, as shown in figure 6.95, metastable below the temperature of the CEP.

In figure 6.91 [type (b)] we have decreased the factor ε_r (unlike particle species interaction) to $\varepsilon_r = 0.725$. The λ -line now ends in a tricritical point (TCP, [129]), in which three phases (a vapor, a species one rich liquid and a species two rich liquid) simultaneously become critical [130].

It should be noted that due to numerical problems the TCP can actually only be reached up to a certain gap with respect to the density ρ . We observe a triple-point, where the vapor coexists with a mixed liquid at intermediate densities and a demixed liquid of higher

density. In the temperature range between the triple point and the TCP the vapor coexists with a mixed liquid and, at higher densities, a mixed liquid coexists with a demixed liquid. Similar to figure 6.90, the vapor-mixed liquid transition is metastable below the triple point.

Figures 6.92 ($\varepsilon_r = 0.7$) and 6.93 ($\varepsilon_r = 0.675$) [both type (b)] are similar to figure 6.91 ($\varepsilon_r = 0.725$). For $\varepsilon_r = 0.7$ (figure 6.92), the temperature of the TCP, T_{TCP} , is greater than the temperature of the critical point (CP) of the vapor-mixed liquid phase transition T_{CP} . For $\varepsilon_r = 0.675$ (figure 6.93) the vapor-mixed liquid coexistence and also the mixed liquid-demixed liquid coexistence are metastable in nearly the whole temperature range. For $\varepsilon_r = 0.65$ (figure 6.94) [type (c)] the vapor-mixed liquid is metastable for all temperatures. Therefore the triple point has vanished, and the phase diagram consists of only two stable phase transition, the vapor-demixed liquid transition.

In table 6.13 we have summarized the densities and temperatures of the vapor-mixed liquid critical points. In figure 6.95 the transition of the vapor-mixed liquid phase transition from symmetric binary systems with $\varepsilon_r < 1.0$ to the one-component case $\varepsilon = 1.0$ is shown.

Conclusion

In this work we have applied a wide range of liquid- and solid-state methods to various interparticle potentials. The results we got (thermodynamic properties, structure functions and phase diagrams) were compared between the different theories and, whenever possible, with computer simulation data.

Before we summarize the results for the different potentials, we give an overview with respect to the theories used in this thesis:

- The EXP is, albeit its introduction decades ago, still able to give some remarkably good results throughout the whole range of discussed hard-core potentials. These results are even superior to the already very satisfactory results we got from the ORPA.
- Most of the ‘modern’ theories [Rogers-Young approximation (RY) and zero separation theory (ZSEP)] are very limited in terms of solvable potentials and reachable thermodynamic parameters (for example the inability of the RY approximation to yield results for the square-well potential near the vapor-liquid phase-transition).
- The FMT Ansatz of Rosenfeld gives, when applied to other systems than the hard-sphere system, no satisfactory (i.e. physically meaningful) results. This behavior might be attributed to the ansatz, which is difficult to extend (in a physically correct manner) beyond the hard-core potential.

During the work on this thesis, we often tried to improve unsatisfactory results by increasing the complexity of the used theory, but in nearly all cases the results hardly improved (in contrast to the computational effort, where both the complexity of the programs and the execution time increased). The best results were achieved by using numerically simple methods and theories.

In this thesis, we have examined the structure and phase diagrams of a broad range of one-component systems interacting via pair potentials, both bounded and unbounded ones. The phase diagram we got for the Gaussian core results shows qualitatively the same behavior that was predicted by Stillinger (for instance reentrant melting). We have also discussed the phase behavior of bounded potentials in general, which lead us to a simple criterion (based on a mean field approach) to determine if a given potential will show clustering or reentrant melting. We have applied the Rosenfeld functional (a fundamental measure theory) onto the hard-sphere potential to examine the freezing transition of this system. This new method gave us also the opportunity to take a look inside the

crystal. Furthermore, we have examined the thermodynamic properties and phase behavior of a various square-well/square-shoulder systems, for which the phase diagram shows (beside the liquid-solid phase transition) an isostructural solid-solid phase coexistence. The results we got for the Asakura-Oosawa potential showed a very rich phase diagram, including a vapor-liquid, a liquid-solid and a solid-solid phase transition. We have also calculated phase diagrams for the double square-well/square-shoulder system; we observed a rather strange behavior (two critical points in the fluid phase), that is subject to ongoing investigations.

The results we got for the phase diagrams of symmetric binary hard-sphere Yukawa systems for different interaction potentials [where the dissimilar species interaction $\phi_{12}(r)$ were always weaker than the similar species interaction $\phi_{11}(r) = \phi_{22}(r)$ by a factor $\varepsilon_r < 1.0$, $\phi_{12}(r) = \varepsilon_r \phi_{11}(r)$] showed an enormous richness of phase transitions. Beside first-order (phase coexistence) and second-order (λ -line and critical points) phase transitions, the binary system also showed critical end points (coexistence of a critical liquid with a noncritical vapor) and tricritical points (three phases become simultaneously critical).

Appendix A

Abbreviations

A.1 List of abbreviations

Table A.1: List of abbreviations, A-H

Abbreviation	Meaning	section
AO	Asakura-Oosawa (potential)	2.2.4
CEP	Critical end point	6.8
CP	Critical point	6.8
CS	Carnahan Starling	4.1.6
DFT	Density functional theory	4.3
DSS	Double square-well (potential)	2.2.2.1
DSW	Double square-shoulder (potential)	2.2.2.1
ERF	Error function (potential)	2.2.8
EXP	Exponential approximation	4.1
FDM	Fermi distribution model	2.2.6
FFT	Fast Fourier transform	B.1.4
FMT	Fundamental measure theory	4.3.3
FVPA	Free volume perturbation theory	4.1.8
GB	Gibbs-Bogoliubov	4.5
GCM	Gaussian core model	2.2.5
GMSA	Generalized mean spherical approximation	6.6.1
HNC	Hypernetted chain approximation	4.2.2
HRT	Hierarchical reference theory	6.6.1
HS	Hard sphere (potential)	2.2.1
HSY	Hard sphere yukawa (potential)	2.2.3
HTA	High temperature approximation	4.1

Table A.2: List of abbreviations, I-Z

Abbreviation	Meaning	section
IET	Integral equation theory	4.2
LEXP	Linearized version of the EXP	4.1.2
LMV	Labik-Malijevsky-Vonka	4.2.5.2
MC	Monte-Carlo	6.1.1
MCSL	Mansoori, Carnahan, Starling and Leland	4.1.7
MFA	Mean field approximation	6.2.1
MHNC	Modified hypernetted chain approximation	6.6.1
MPA	Modified perturbation approximation	6.4.3
MSA	Mean spherical approximation	4.1.5
MWDA	Modified weight density approximation	4.3.1
ORPA	Optimized random phase approximation	4.1
OZ	Ornstein-Zernike	3.1
PA	Perturbation approximation	4.1.4.4
PSM	Penetrable spheres model	2.2.7
PT	Perturbation theory	4.1
PWDA	Perturbation weighted density approximation	6.6.1
PY	Percus-Yevick	4.2.1
RPA	Random phase approximation	4.1
RY	Rogers-Young	4.2.3
Rsf	Rosenfeld	6.3.1
SCOZA	Self consistent Ornstein-Zernike approximation	6.6.1
SD	Steepest descent	D.1
SFMT	Soft fundamental measure theory	4.3.6
SS	Square-shoulder (potential)	2.2.2
SW	Square-well (potential)	2.2.2
TCP	Tricritical point	6.8
TPL	Test particle limit	4.3.7
VW	Verlet-Weis	4.1.6
WDA	Weighted density approximation	4.3.1
ZSEP	Zero separation closure	4.2.4
cMWDA	correlation MWDA	4.3.2
tHSY	truncated hard-sphere Yukawa potential	2.2.3.1

Appendix B

Mathematical definitions

This Appendix gives some technical and mathematical information about some methods used in this thesis.

B.1 Fourier transformation

In this section we will discuss the various aspects, definitions and (numerical) problems of the Fourier transformations that were used in this thesis.

B.1.1 Fourier transformation of a scalar function

For the Fourier transformations in three dimensional space we use the following notations which simplify for radially symmetric functions as indicated:

$$\tilde{f}(\vec{k}) = \int_{\mathbb{R}^3} d^3r e^{i\vec{k}\vec{r}} f(\vec{r}) \longrightarrow \tilde{f}(k) = \frac{4\pi}{k} \int_0^{\infty} dr r \sin(kr) f(r) \quad (\text{B.1})$$

$$f(\vec{r}) = \frac{1}{(2\pi)^3} \int_{\mathbb{R}^3} d^3k e^{-i\vec{k}\vec{r}} \tilde{f}(\vec{k}) \longrightarrow f(r) = \frac{1}{(2\pi)^3} \frac{4\pi}{r} \int_0^{\infty} dk k \sin(kr) \tilde{f}(k). \quad (\text{B.2})$$

In one dimension we use

$$\tilde{f}(k) = \int_{-\infty}^{\infty} dr f(r) e^{ikr} \longrightarrow \tilde{f}(k) = \int_{-\infty}^{\infty} dr f(r) \cos(kr) + i \int_{-\infty}^{\infty} dr f(r) \sin(kr) \quad (\text{B.3})$$

$$f(r) = \frac{1}{2\pi} \int_{-\infty}^{\infty} dk \tilde{f}(k) e^{-ikr} \longrightarrow f(r) = \frac{1}{2\pi} \int_{-\infty}^{\infty} dk \tilde{f}(k) \cos(kr) - \frac{i}{2\pi} \int_{-\infty}^{\infty} dk \tilde{f}(k) \sin(kr). \quad (\text{B.4})$$

We also introduce the so called one dimensional sine and cosine Fourier transforms, defined as

$$\tilde{f}(k) = \int_0^{\infty} dr \cos(kr) f(r) \longleftrightarrow f(r) = \frac{2}{\pi} \int_0^{\infty} dk \cos(kr) \tilde{f}(k) \quad (\text{B.5})$$

$$\tilde{f}(k) = \int_0^{\infty} dr \sin(kr) f(r) \longleftrightarrow f(r) = \frac{2}{\pi} \int_0^{\infty} dk \sin(kr) \tilde{f}(k). \quad (\text{B.6})$$

B.1.2 Fourier transformation of a vector function

In this subsection we will derive the equations needed for the Fourier transformation of a radially symmetric vector function of the following form:

$$\vec{f}(\vec{r}) = \frac{\vec{r}}{r} f(r).$$

The transform from r to k space with r written in spherical coordinates reads as

$$\tilde{\vec{f}}(\vec{k}) = \int_{\mathbb{R}^3} d^3r e^{i\vec{k}\vec{r}} f(r) \frac{\vec{r}}{r} = \int_0^{\infty} dr r^2 \int_0^{\pi} d\Theta \sin \Theta \int_0^{2\pi} d\varphi e^{i\vec{k}\vec{r}} f(r) \begin{pmatrix} \cos \varphi \sin \Theta \\ \sin \varphi \sin \Theta \\ \cos \Theta \end{pmatrix}.$$

Without loss of generality we can set the direction of \vec{k} parallel to the z -axis

$$\vec{k} = k\vec{e}_z,$$

thus eliminating the φ dependence from $e^{i\vec{k}\vec{r}}$:

$$e^{i\vec{k}\vec{r}} = e^{ikr \cos \Theta}.$$

The resulting function $\tilde{\vec{f}}(\vec{k})$ has only a nonzero component along the z axis, so we can write the transformation in the following form

$$\tilde{\vec{f}}(\vec{k}) = 2\pi\vec{k} \int_0^{\infty} dr r^2 f(r) \int_0^{\pi} d\Theta \sin \Theta e^{ikr \cos \Theta} \cos \Theta.$$

After doing some simple calculations we get the result

$$\tilde{\vec{f}}(\vec{k}) = \frac{\vec{k}}{k} \tilde{f}(k) = 4\pi i \frac{\vec{k}}{k} \int_0^{\infty} dr f(r) \left[\frac{\sin(kr)}{k} - r \cos(kr) \right]. \quad (\text{B.7})$$

The inverse transformation has the form

$$\vec{f}(\vec{r}) = \frac{\vec{r}}{r} f(r) = -4\pi i \frac{1}{(2\pi)^3} \frac{\vec{r}}{r} \int_0^{\infty} dk \tilde{f}(k) \left[\frac{\sin(kr)}{r} - k \cos(kr) \right]. \quad (\text{B.8})$$

These two equations can easily be evaluated using one dimensional sine and cosine Fourier transforms.

B.1.3 Fourier transformation of a tensor function

In this subsection we will derive the equations needed for the three dimensional Fourier transformation of a radially symmetric tensor function of the following form:

$$\mathcal{F}(\vec{r}) = \frac{\vec{r}\vec{r}}{r^2} f(r) \quad ; \quad \mathcal{F}(\vec{r}) \rightarrow \tilde{\mathcal{F}}(\vec{k}), \quad (\text{B.9})$$

where $\vec{r}\vec{r}$ denotes a dyadic product, leading to (using spherical coordinates)

$$\frac{\vec{r}\vec{r}}{r^2} = \begin{pmatrix} \cos^2 \varphi \sin^2 \Theta & \cos \varphi \sin \varphi \sin^2 \Theta & \cos \varphi \sin \Theta \cos \Theta \\ \cos \varphi \sin \varphi \sin^2 \Theta & \sin^2 \varphi \sin^2 \Theta & \sin \varphi \sin \Theta \cos \Theta \\ \cos \varphi \sin \Theta \cos \Theta & \sin \varphi \sin \Theta \cos \Theta & \cos^2 \Theta \end{pmatrix}.$$

The Fourier transform from r to k space is defined as

$$\tilde{\mathcal{F}}(\vec{k}) = \int_0^\infty dr r^2 \int_0^\pi d\Theta \sin \Theta \int_0^{2\pi} d\varphi e^{i\vec{k}\vec{r}} f(r) \frac{\vec{r}\vec{r}}{r^2}$$

Without loss of generality we set the direction of \vec{k} along the z -axis, thus

$$\tilde{\mathcal{F}}(k\vec{e}_z) = \pi \int_0^\infty dr r^2 f(r) \int_0^\pi d\Theta \sin \Theta e^{ikr \cos \Theta} \begin{pmatrix} \sin^2 \Theta & 0 & 0 \\ 0 & \sin^2 \Theta & 0 \\ 0 & 0 & 2 \cos^2 \Theta \end{pmatrix}.$$

After doing the Θ integration this equation reads as

$$\tilde{\mathcal{F}}(k\vec{e}_z) = \frac{4\pi}{k^3} \int_0^\infty dr \frac{f(r)}{r} \left[\sin(kr) \begin{pmatrix} 1 & 0 & 0 \\ 0 & 1 & 0 \\ 0 & 0 & k^2 r^2 - 2 \end{pmatrix} - kr \cos(kr) \begin{pmatrix} 1 & 0 & 0 \\ 0 & 1 & 0 \\ 0 & 0 & -2 \end{pmatrix} \right].$$

The resulting Fourier transformed tensor for $\vec{k} = k\vec{e}_z$ has only nonzero components for the xx/yy element

$$\tilde{F}_{xx}(k) = \left(\tilde{\mathcal{F}} \right)_{xx}(k\vec{e}_z) = \left(\tilde{\mathcal{F}} \right)_{yy}(k\vec{e}_z) = \frac{4\pi}{k^3} \int_0^\infty dr \frac{f(r)}{r} [\sin(kr) - kr \cos(kr)] \quad (\text{B.10})$$

and the zz element

$$\tilde{F}_{zz}(k) = \left(\tilde{\mathcal{F}} \right)_{zz}(k\vec{e}_z) = \frac{4\pi}{k^3} \int_0^\infty dr \frac{f(r)}{r} [\sin(kr) (k^2 r^2 - 2) + 2kr \cos(kr)].$$

This tensor has to be rotated using the Euler rotation matrices

$$\mathcal{R}(\alpha, \beta, \gamma) = \mathcal{R}_z(\alpha) \mathcal{R}_x(\beta) \mathcal{R}_z(\gamma),$$

where the index denotes the fixed axis for the rotation. The rotated tensor $\mathcal{F}(\vec{k})$ is calculated using

$$\tilde{\mathcal{F}}(\vec{k}) = \mathcal{R}^{-1}(\alpha, \beta, \gamma) \tilde{\mathcal{F}}(k\vec{e}_z) \mathcal{R}(\alpha, \beta, \gamma).$$

The desired destination vector for the tensor rotation has the coordinates

$$\vec{k} = k \begin{pmatrix} \cos \varphi \sin \Theta \\ \sin \varphi \sin \Theta \\ \cos \Theta \end{pmatrix},$$

hence the Euler angles have the following values:

$$\alpha = 0 \quad ; \quad \beta = \Theta \quad ; \quad \gamma = \varphi + \frac{\pi}{2}.$$

It should be noted that the value of α has no impact on the rotation of a tensor like $\tilde{\mathcal{F}}$ (because of the symmetry $(\tilde{\mathcal{F}})_{xx}(k\vec{e}_z) = (\tilde{\mathcal{F}})_{yy}(k\vec{e}_z)$ and the zeroness of all elements beside the main diagonal). The result of the tensor rotation is

$$\tilde{\mathcal{F}}(\vec{k}) = \left[\tilde{F}_{zz}(k) - \tilde{F}_{xx}(k) \right] \frac{\vec{k}\vec{k}}{k^2} + \tilde{F}_{xx}(k) \mathbb{1}.$$

Using the relation

$$2\tilde{F}_{xx}(k) + \tilde{F}_{zz}(k) = \frac{4\pi}{k} \int_0^\infty dr r \sin(kr) f(r) = \tilde{f}(k)$$

the result reads as

$$\tilde{\mathcal{F}}(\vec{k}) = \tilde{F}(k) \left[\frac{\vec{k}\vec{k}}{k^2} - \frac{1}{3} \mathbb{1} \right] + \tilde{f}(k) \frac{1}{3} \mathbb{1} = \tilde{F}(k) \frac{\vec{k}\vec{k}}{k^2} + \tilde{F}_{xx}(k) \mathbb{1} \quad (\text{B.11})$$

with

$$\tilde{F}(k) = \tilde{F}_{zz}(k) - \tilde{F}_{xx}(k) = \frac{4\pi}{k^3} \int_0^\infty dr \frac{f(r)}{r} [\sin(kr) (k^2 r^2 - 3) + 3kr \cos(kr)]. \quad (\text{B.12})$$

Equation (B.11) shows that the result can be split into two parts; a position dependent part $[\tilde{F}(k)]$ and a distance dependent part $[\tilde{F}_{xx}(k)]$.

The inverse Fourier transformation ($k \rightarrow r$) of a tensor

$$\tilde{\mathcal{F}}(\vec{k}) = \frac{\vec{k}\vec{k}}{k^2} \tilde{F}(k) \quad ; \quad \tilde{\mathcal{F}}(\vec{k}) \rightarrow \mathcal{F}(\vec{r}),$$

yields the result

$$\mathcal{F}(r\vec{e}_z) = \frac{1}{2\pi^2 r^3} \int_0^\infty dk \frac{\tilde{F}(k)}{k} \left[\sin(kr) \begin{pmatrix} 1 & 0 & 0 \\ 0 & 1 & 0 \\ 0 & 0 & k^2 r^2 - 2 \end{pmatrix} - kr \cos(kr) \begin{pmatrix} 1 & 0 & 0 \\ 0 & 1 & 0 \\ 0 & 0 & -2 \end{pmatrix} \right],$$

which is the same as for the $r \rightarrow k$ transformation. With the following definitions for the xx/yy [$(\mathcal{F})_{xx}(r\vec{e}_z) = (\mathcal{F})_{yy}(r\vec{e}_z)$] and zz element and the difference between the zz and xx element

$$\begin{aligned} F_{xx}(r) = (\mathcal{F})_{xx}(r\vec{e}_z) &= \frac{1}{2\pi^2 r^3} \int_0^\infty dk \frac{\tilde{F}(k)}{k} [\sin(kr) - kr \cos(kr)] \\ F_{zz}(r) = (\mathcal{F})_{zz}(r\vec{e}_z) &= \frac{1}{2\pi^2 r^3} \int_0^\infty dk \frac{\tilde{F}(k)}{k} [\sin(kr) (k^2 r^2 - 2) + 2kr \cos(kr)] \\ F(r) = F_{zz}(r) - F_{xx}(r) &= \frac{1}{2\pi^2 r^3} \int_0^\infty dk \frac{\tilde{F}(k)}{k} [\sin(kr) (k^2 r^2 - 3) + 3kr \cos(kr)] \end{aligned}$$

we get the result

$$\mathcal{F}(\vec{r}) = F(r) \frac{\vec{r}\vec{r}}{r^2} + F_{xx}(r) \mathbb{I}. \quad (\text{B.13})$$

B.1.4 Fast Fourier transformation

The Fourier transform described in the previous section are numerically realized using so called ‘fast Fourier transforms’ (FFTs)¹ based on the work of Cooley and Tukey [131]. In this thesis the only FFTs used were the ones for the one dimensional sine and cosine Fourier transform (for the three dimensional radially symmetric form one has to multiply all functions with their argument to get the one dimensional sine Fourier transform).

The fast Fourier transform algorithm is based on discrete Fourier transforms (DFTs). The DFTs replaces the (continuous) integral by a (discrete) sum: every function has to be discretized on a mesh [$f(r_i) \rightarrow f_i$, distance between two mesh points Δr , and $\tilde{f}(k_i) \rightarrow \tilde{f}_i$, distance between two mesh points Δk] with size N_p . In this thesis we have used FFTs based on the FFTPACK² version 4. The expression for the DFT for the one dimensional cosine Fourier transform is given by

$$\tilde{f}_i = \frac{\Delta x}{2} \left[f_0 + (-1)^i f_{N_p} + 2 \sum_{j=1}^{N_p-1} f_j \cos \frac{ij\pi}{N_p-1} \right] \quad ; \quad i = 0, \dots, N_p, \quad (\text{B.14})$$

whereas the expression for the DFT for the one dimensional sine Fourier transform reads as

$$\tilde{f}_i = \Delta x \sum_{j=0}^{N_p} f_j \sin \frac{ij\pi}{N_p-1} \quad ; \quad i = 0, \dots, N_p. \quad (\text{B.15})$$

Here f_j is the original function and \tilde{f}_i is the Fourier transformed function. Both equations are valid for the transformation from r to k space (where Δx is equal to Δr) and k to r

¹A good starting point for the search of modern, up-to-date FFTs is the page www.fftw.org, or just search for fast Fourier transform at www.google.com.

²<http://www.netlib.no/netlib/fftpack/>

space (where Δx is equal to Δk). The number of grid points N_p for the r - and k -mesh has to be the same and equal to

$$N_p = 1 + 2^m,$$

where m is an integer greater than or equal to zero. This restriction for N_p is based on the internal structure of the FFT. The implementation of the algorithm is very straightforward if N_p is restricted to these values³. The two parameters Δr and Δk from table B.1.4

Parameter	r mesh	k mesh
number of points	N_p	N_p
mesh point distance	Δr	Δk
largest vector	$r_{max} = (N_p - 1)\Delta r$	$k_{max} = (N_p - 1)\Delta k$

Table B.1: Mesh parameters for fast Fourier transforms.

can not be set independently from each other. The relation they have to fulfill can be derived using the following arguments. The largest vector in k space is equal to the highest frequency that can be detected in r space. This oscillation incorporates 3 mesh points, spanning a distance of $2\Delta r$:

$$k_{max} = \frac{2\pi}{2\Delta r} \rightarrow \Delta r \Delta k = \frac{\pi}{N_p - 1}.$$

The appropriate choice of the mesh parameters can be a tricky task. The number of grid points should not be too small, because then we lose too much information by discretization. On the other hand, if N_p is too large, the time a program spends inside the FFT code will increase significantly [see table B.2]. The hardware used was:

m	mesh size N_p	(I)	(II)	(III)	(IV)
10	1025	3	3	2	2
11	2049	7	9	6	5
12	4097	19	21	13	12
13	8193	61	63	53	48
14	16385	215	213	165	155

Table B.2: Approximate execution time in seconds for various mesh sizes. 10000 iterations were made for each run, every iteration consists of both transforms ($r \rightarrow k$ and $k \rightarrow r$) using a one dimensional cosine Fourier transform kernel.

(I) Athlon (512 kB external cache) with 750 MHz on an Asus K7V (VIA KX133), Fujitsu Fortran compiler V1.0.

³However, most modern FFT programs are capable of computing the Fourier transform of functions with an arbitrary length.

- (II) Alpha EV56 (2 MB external cache) with 600 MHz on an LX Board, Compaq Fortran V1.0-920.
- (III) Athlon Thunderbird (256 kB internal cache) with 900 MHz on an Abit KT7 (VIA KT133), Fujitsu Fortran compiler V1.0.
- (IV) Athlon Thunderbird (256 kB internal cache) with 1000 MHz on an Asus A7V (VIA KT133), Fujitsu Fortran compiler V1.0.

Besides the number of mesh points one can choose a second parameter (because all other parameters depend on these two), for instance r_{max} . In this thesis, r_{max} is in most cases set to 10.24, leading to a $\Delta r = 0.01\sigma$ for $m = 10$. This choice of r_{max} is sufficient unless the system is near the spinodal or near the critical region. Then the pair correlation function $g(r)$ can become long ranged [see also section 3.3] and a larger r_{max} is needed. If r_{max} has been set to an appropriate value, one has to make a compromise regarding N_p . A high N_p value is needed if the functions in r space (pair potential $\phi(r)$ and correlation functions) are fast varying functions of r (otherwise one will lose too much information by the discretization) or if we need the Fourier transformed functions up to a very high k vector. But, as shown above, a high value for N_p will lead to very long program runs. In table B.3 we have collected some common mesh parameters.

	(A)	(B)	(C)
$r_{max} =$	10.24	20.48	40.96
$\Delta k = \frac{\pi}{r_{max}} =$	0.306796158	0.153398079	0.076699039
(1) $m = 10$	$\Delta r = 0.01$	$\Delta r = 0.02$	$\Delta r = 0.04$
$N_p = 1025$	$k_{max} = 100\pi$	$k_{max} = 50\pi$	$k_{max} = 25\pi$
(2) $m = 11$	$\Delta r = 0.005$	$\Delta r = 0.01$	$\Delta r = 0.02$
$N_p = 2049$	$k_{max} = 200\pi$	$k_{max} = 100\pi$	$k_{max} = 50\pi$
(3) $m = 12$	$\Delta r = 0.0025$	$\Delta r = 0.005$	$\Delta r = 0.01$
$N_p = 4097$	$k_{max} = 400\pi$	$k_{max} = 200\pi$	$k_{max} = 100\pi$

Table B.3: Common mesh parameters

B.1.5 Numerical problems

The FFT is by no means a perfect equivalent to the analytical Fourier transform. Besides the numerical and theory imminent restrictions stated in the previous subsection, FFTs have some other drawbacks we will show in this subsection.

One problem every almost every FFT is suffering from is that the algorithm can not give you the correct value for $k = 0$ or $r = 0$. So this value has to be calculated using an additional integration (which can be tricky if the integration kernel has discontinuities). This was done using a simple Simpson algorithm. To test the one dimensional sine and cosine Fourier transform, we have chosen the following two test functions which are

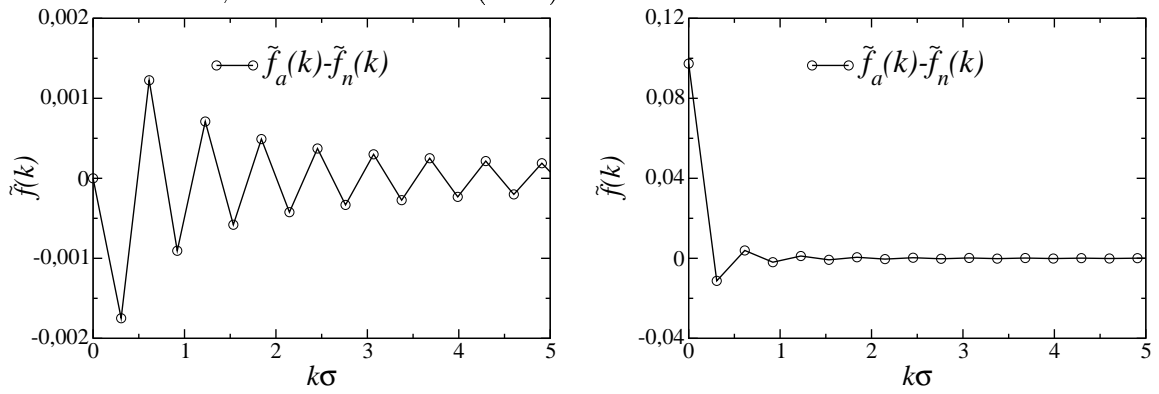
analytically Fourier transformable:

$$f_{\sin}(r) = \frac{r}{1+r^4} \longrightarrow \tilde{f}_{\sin}(k) = \frac{\pi}{2} e^{-\frac{k}{\sqrt{2}}} \sin \frac{k}{\sqrt{2}} \quad (\text{B.16})$$

$$f_{\cos}(r) = \frac{1}{1+r^2} \longrightarrow \tilde{f}_{\cos}(k) = \frac{\pi}{2} e^{-k}. \quad (\text{B.17})$$

For the numerical Fourier transforms in this chapter we choose set A2 from table B.3.

Figure B.1: Absolute errors $\tilde{f}_{\text{analytical}}(k) - \tilde{f}_{\text{numerical}}(k)$ for one dimensional fast Fourier transforms. Left side: sine Fourier transform, error of function (B.16), right side: cosine Fourier transform, error of function (B.17).



In figure B.1 one can see some absolute errors for the Fourier transform for r to k space. It should be noted that the transformation of the (numerical) Fourier transformed from k space back to r space leads to a result that is (for $r > 0$) equal to the input function $\pm 10\varepsilon$, where ε is the machine precision ($\approx 2.22 \times 10^{-16}$). For $r = 0$ the error is about 1000ε , due to the rather simple treatment of this value.

We have tested the one dimensional fast Fourier transform with another analytical transformable test function:

$$f(r) = \Theta(0.1 - r) \quad ; \quad \begin{cases} \tilde{f}_{\cos}(k) = \frac{\sin(0.1k)}{k} & ; \tilde{f}_{\cos}(0) = 0.1 \\ \tilde{f}_{\sin}(k) = \frac{1 - \cos(0.1k)}{k} & ; \tilde{f}_{\sin}(0) = 0 \end{cases} .$$

In figure B.2 and B.3 the comparison between the analytic and numeric solution for the one dimensional sine and cosine Fourier transform is shown. From equation (B.15) it is clear that $\tilde{f}(0)$ and $\tilde{f}(k_{\text{max}})$ is always equal to zero. The analytical (sine and cosine) Fourier transform of our test function is a smooth function of k , and the numerical Fourier transform shows the same behavior. However, because the two boundary points are fixed, the (sine) FFT shifts the result down for higher k values to meet the boundary point. The cosine Fourier transform shows a similar behavior. Here $\tilde{f}(k_{\text{max}})$ is equal to $f_0 \Delta r / 2 = 0.0025$ (f_0 being the function value at $r = 0$), so the FFT has to increase the amplitude of the oscillation to meet the end point. However, the result of the retransformation ($k \rightarrow r$)

Figure B.2: Sine Fourier transform of $\Theta(0.1 - r)$. Shown are the analytic solution, the numeric result and the difference $\tilde{f}_{analytic}(k) - \tilde{f}_{numeric}(k)$.

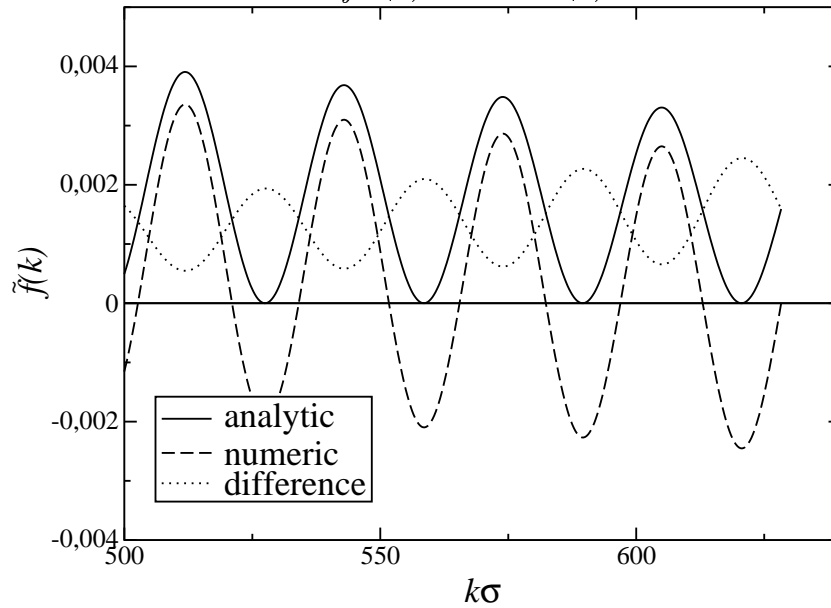
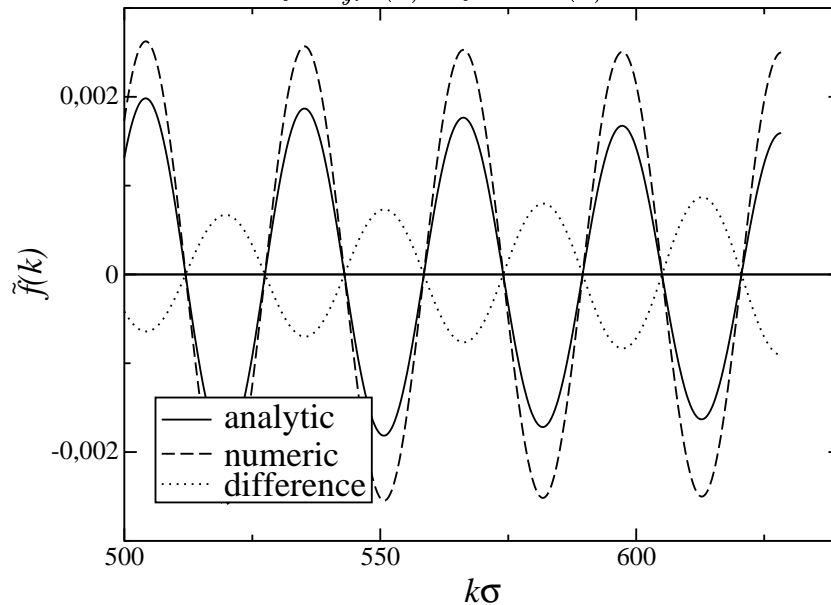


Figure B.3: Cosine Fourier transform of $\Theta(0.1 - r)$. Shown are the analytic solution, the numeric result and the difference $\tilde{f}_{analytic}(k) - \tilde{f}_{numeric}(k)$.



is in excellent agreement to the starting test function, with absolute errors in the order of magnitude of $\pm 10\varepsilon$ (the only exception is the result of $f(r = 0)$ for the sine transform, which is equal to zero and hence the absolute error is equal to one).

Summarizing we can say that the overall stability ($r \rightarrow k \rightarrow r'$ and vice versa) of the

FFTs used in this thesis is very good with errors that are, in general, in the order of magnitude of $(10 - 100)\varepsilon$ (depending on the chosen mesh size N_p).

B.2 Convolutions

In this section we will derive the equations for the convolution of a scalar radially symmetric function $f(r)$ with a radially symmetric scalar, vector or tensor function [$g(r)$, $\vec{g}(r)$ or $\mathcal{G}(r)$] in r space.

B.2.1 Scalar-Scalar

The convolution $c(r)$ is defined as

$$c(r) = \int_{\mathbb{R}^3} d^3 r' f(r') g(|\vec{r} - \vec{r}'|).$$

By expressing these three functions as their Fourier transforms we get

$$\tilde{c}(k) = \tilde{f}(k)\tilde{g}(k).$$

B.2.2 Scalar-Vector

The convolution of a scalar function $f(r)$ with a vector function $\vec{g}(r)$ defined as

$$\vec{g}(\vec{r}) = g(r)\frac{\vec{r}}{r}$$

can be written as

$$\vec{c}(\vec{r}) = \int_{\mathbb{R}^3} d^3 r' f(r') \vec{g}(|\vec{r} - \vec{r}'|) = \int_{\mathbb{R}^3} d^3 r' f(r') g(r') \frac{\vec{r}'}{r'}.$$

Now we express the scalar function $f(r)$ and the vector function $\vec{g}(r)$ via their Fourier transforms and we get

$$\vec{c}(\vec{k}) = \tilde{f}(k)\tilde{g}(k) = \tilde{f}(k)\tilde{g}(k)\frac{\vec{k}}{k}.$$

To get the final result we have to Fourier transform this product back to r space using equation (B.8).

B.2.3 Scalar-Tensor

The convolution $\mathcal{C}(\vec{r})$ of a scalar function $f(r)$ with a tensor function $\mathcal{G}(r)$ [see equation (B.9)] can be written as

$$\mathcal{C}(\vec{r}) = \int_{\mathbb{R}^3} d^3 r' f(|\vec{r} - \vec{r}'|) g(r) \frac{\vec{r}' \vec{r}'}{r'^2}.$$

The evaluation of this equation is straightforward, yielding the result

$$\tilde{\mathcal{C}}(\vec{k}) = \tilde{f}(k) \tilde{\mathcal{G}}(\vec{k}) = \tilde{f}(k) \left[\tilde{G}_p(k) \frac{\vec{k} \vec{k}}{k^2} + \tilde{G}_d(k) \mathbb{I} \right],$$

where the subscripts $_p$ and $_d$ are denoting the position and distance dependence of the tensor parts. One gets the final result after Fourier transforming the right hand side of this equation back to r space [see equation (B.13)].

B.3 Parseval theorem

The Parseval theorem states that, if for a function $f(t)$ and $|f(t)|^2$ the integral with respect to t over the interval $(-\infty, \infty)$ exists then

$$\int_{-\infty}^{\infty} dr |f(r)|^2 = \frac{1}{2\pi} \int_{-\infty}^{\infty} dk |\tilde{f}(k)|^2.$$

In \mathbb{R}^3 this equation reads

$$\begin{aligned} \int_{\mathbb{R}^3} d^3 r_1 f(\vec{r}_1) g(\vec{r}_1) &= \frac{1}{(2\pi)^3} \int_{\mathbb{R}^3} d^3 k_1 \tilde{f}(\vec{k}_1) \tilde{g}(\vec{k}_1) \\ &= \frac{1}{(2\pi)^3} \int_{\mathbb{R}^3} d^3 k_1 \left[\int_{\mathbb{R}^3} d^3 r_2 e^{i\vec{k}_1 \vec{r}_2} f(\vec{r}_2) \right] \left[\int_{\mathbb{R}^3} d^3 r_1 e^{i\vec{k}_1 \vec{r}_1} g(\vec{r}_1) \right] \\ &= \int_{\mathbb{R}^3} d^3 r_2 f(\vec{r}_2) \int_{\mathbb{R}^3} d^3 r_1 g(\vec{r}_1) \frac{1}{(2\pi)^3} \int_{\mathbb{R}^3} d^3 k_1 e^{i\vec{k}_1 (\vec{r}_1 + \vec{r}_2)} \\ &= \int_{\mathbb{R}^3} d^3 r_1 f(\vec{r}_1) g(-\vec{r}_1). \end{aligned}$$

So we see that

$$(f * g)(r = 0) = \frac{1}{(2\pi)^3} (\tilde{f} * \tilde{g})(k = 0).$$

if $g(\vec{r}_1) = g(-\vec{r}_1)$ (which is valid for all radially symmetric functions).

Appendix C

Ordered solid state

C.1 Lattice parameters

In table C.1 we compare various lattice parameters for the three lattice types sc, fcc and bcc. The cubic cell has a side length of a . The definition of the simplex and its graphical representation is described in section 4.3.4.2.

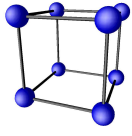
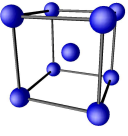
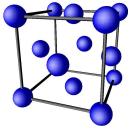
	sc	bcc	fcc
			
N_c^1	1	2	4
V_c/V_s^2	48	96	192
Simplex	$0 \leq x \leq a/2$ $0 \leq y \leq x$ $0 \leq z \leq y$	$0 \leq x \leq a/2$ $0 \leq y \leq x$ $0 \leq z \leq \min(y, a/2 - x)$	$0 \leq x \leq a/2$ $0 \leq y \leq \min(x, a/2 - x)$ $0 \leq z \leq y$

Table C.1: Lattice parameters for the sc, fcc and bcc lattice.

C.2 One-particle density for the ordered solid state

In this thesis we have used the following parameterization of a crystal:

$$\rho(\vec{r}) = \left(\frac{\alpha}{\pi}\right)^{\frac{3}{2}} \sum_{\{\vec{R}\}} e^{-\alpha(\vec{r}-\vec{R})^2}, \quad (\text{C.1})$$

¹Number of atoms in the cubic cell.

²Ratio of volume of the cubic cell to volume of the simplex.

i.e., normalized Gaussian peaks (with width α) centered at the lattice points $\{\vec{R}\}$ of a given lattice (bcc, fcc, sc, etc.). The Fourier transform of $\rho(\vec{r})$ is given by

$$\begin{aligned}\tilde{\rho}(\vec{k}) &= \left(\frac{\alpha}{\pi}\right)^{\frac{3}{2}} \sum_{\{\vec{R}\}} \int_{\mathbb{R}^3} d^3r e^{-\alpha(\vec{r}-\vec{R})^2} e^{i\vec{k}\vec{r}} \\ &= \left(\frac{\alpha}{\pi}\right)^{\frac{3}{2}} \sum_{\{\vec{R}\}} \frac{4\pi}{k} e^{i\vec{k}\vec{R}} \int_{r=0}^{\infty} dr r \sin(kr) e^{-\alpha r^2} \\ &= e^{-\left(\frac{k}{2\alpha}\right)^2} \sum_{\{\vec{R}\}} e^{i\vec{k}\vec{R}}\end{aligned}$$

A frequently required expression is the double-convolution of a radially symmetric function, $f(r)$, with the solid density, $\rho(\vec{r})$ as parameterized in (C.1):

$$\begin{aligned}\frac{1}{2} \int_{\mathbb{R}^3} d^3r \int_{\mathbb{R}^3} d^3r' \rho(\vec{r}) \rho(\vec{r}') f(|\vec{r}-\vec{r}'|) &= \\ &= \frac{1}{2} \left(\frac{\alpha}{\pi}\right)^3 \sum_{\{\vec{R}\}} \int_{\mathbb{R}^3} d^3x f(x) \sum_{\{\vec{R}'\}} \int_{\mathbb{R}^3} d^3y e^{-\alpha y^2} e^{-\alpha(\vec{y}-\vec{x}+\vec{R}-\vec{R}')^2},\end{aligned}$$

now we can change the second integration variable y for every contribution to the sum over $\{\vec{R}'\}$ so that the second integral always yields the same result (i.e., the second integral gets invariant from $\{\vec{R}'\}$):

$$\begin{aligned}\frac{1}{2} \int_{\mathbb{R}^3} d^3r \int_{\mathbb{R}^3} d^3r' \rho(\vec{r}) \rho(\vec{r}') f(|\vec{r}-\vec{r}'|) &= \\ &= \frac{N}{2} \left(\frac{\alpha}{2\pi}\right)^{\frac{3}{2}} \sum_{\{\vec{R}\}} \int_{\mathbb{R}^3} d^3x f(x) e^{-\frac{\alpha}{2}(\vec{x}-\vec{R})^2} \\ &= \frac{N}{2} \left(\frac{\alpha}{2\pi}\right)^{\frac{3}{2}} \sum_{\{\vec{R}\}} e^{-\frac{\alpha}{2}R^2} \int_{\mathbb{R}^3} d^3x f(x) e^{-\frac{\alpha}{2}x^2} e^{\alpha\vec{x}\vec{R}} \\ &= \frac{N}{2} \sqrt{\frac{\alpha}{2\pi}} \sum_{\{\vec{R}\}} \frac{1}{R} \int_0^{\infty} dx x f(x) \left(e^{-\frac{\alpha}{2}(x-R)^2} - e^{-\frac{\alpha}{2}(x+R)^2} \right).\end{aligned}\tag{C.2}$$

In the case of a regular lattice (fcc, bcc, etc) the set of lattice vectors $\{\vec{R}\}$ can be arranged in shells (labeled i) centered around the origin. Each shell contains n_i lattice points at a distance R_i from the origin. The first (degenerated) shell with index 0 has a radius of 0 and contains only one point. Equation (C.2) can be written as

$$\frac{1}{2} \int_{\mathbb{R}^3} d^3r \int_{\mathbb{R}^3} d^3r' \rho(\vec{r}) \rho(\vec{r}') f(|\vec{r}-\vec{r}'|) = \tag{C.3}$$

$$= \frac{N}{2} \sqrt{\frac{\alpha}{2\pi}} \left[2\alpha \int_0^{\infty} dx x^2 e^{-\frac{\alpha}{2}x^2} f(x) + \sum_{i=1}^{\infty} \frac{n_i}{R_i} \int_0^{\infty} dx x f(x) \left(e^{-\frac{\alpha}{2}(x-R_i)^2} - e^{-\frac{\alpha}{2}(x+R_i)^2} \right) \right]$$

C.3 Pair distribution function in the solid

The angle-averaged pair distribution function in the solid is needed for the perturbation and mean-field approximations for the Helmholtz free energy of the solid (as described in section 4.4).

For the solid pair distribution function $g(r)$ of a hard sphere system we make the ansatz [82, 83]

$$g(r) = \frac{A}{r} e^{-\frac{\alpha_1}{2}(r-r_1)^2} + \frac{1}{4\pi\rho} \sqrt{\frac{\alpha}{2\pi}} \sum_{i=2}^{\infty} \frac{n_i}{R_i r} \left[e^{-\frac{\alpha}{2}(r-R_i)^2} - e^{-\frac{\alpha}{2}(r+R_i)^2} \right] \quad \text{for } r \geq \sigma \quad (\text{C.4})$$

and $g(r) = 0$ inside the core. n_i and R_i have the same meaning as above.

This Ansatz for $g(r)$ consists of two parts (the superscript 2 indicates that for this part the ‘shell-summation’ starts at the second shell):

$$g(r) = g_f(r) + g_0^2(r). \quad (\text{C.5})$$

The first part models the contribution of the nearest neighbors, whereas the second part is the long range correlation part. This long range correlation part models the behavior the particles would have if they could move around a lattice site independently of each other. This contribution (including the nearest neighbor contribution (first shell), hence the superscript is now 1) is equal to

$$g_0^1(r) = \frac{1}{4\pi V \rho^2} \int d\Omega \int_{\mathbb{R}^3} d^3 r' \rho(\vec{r}') \rho(\vec{r}' + \vec{r}),$$

where $d\Omega$ is the differential solid angle aperture around \vec{r} . Using this equation with equation (C.3) one gets

$$g_0^1(r) = \frac{1}{4\pi\rho} \sqrt{\frac{\alpha}{2\pi}} \sum_{i=1}^{\infty} \frac{n_i}{R_i r} \left[e^{-\frac{\alpha}{2}(r-R_i)^2} - e^{-\frac{\alpha}{2}(r+R_i)^2} \right], \quad (\text{C.6})$$

where the first ‘shell’ (index $i = 0$) has been discarded (self-contribution).

The nearest neighbor contribution is modeled as

$$g_f(r) = \frac{A}{r} e^{-\frac{\alpha_1}{2}(r-r_1)^2} \quad \text{for } r \geq \sigma$$

and $g_f(r) = 0$ inside the core. The three parameters A , α_1 and r_1 are calculated to fulfill three restrictions:

- The first restriction sets the mean displacement for the nearest neighbors of the long range correlation (C.6) equal to the modified ansatz (C.5):

$$\frac{n_1}{\rho} \langle r \rangle = \int_0^{\infty} dr r g_0^1(r) = \int_0^{\infty} dr r g(r),$$

where n_1 is the number of nearest neighbors.

- The second restriction sets the normalization for $g_f(r)$ equal to n_1 :

$$n_1 = 4\pi\rho \int_0^{\infty} dr r^2 g_f(r).$$

- The last restriction is the virial equation, which for the solid reads as [6]

$$\frac{\beta P}{\rho} = p^* = 1 + 4\eta g(\sigma).$$

Appendix D

Numerical methods

D.1 Steepest descent algorithm

For the minimization of the ORPA functional (4.10) and (4.16) we use the so called steepest descent (SD) method. This method is based on the Taylor expansion of a function (or, without loss of generality, functional) F around an extremum:

$$F(\vec{x}_0 + \Delta\vec{x}) \approx F(\vec{x}_0) + \Delta\vec{x} \vec{\nabla} F(\vec{x}) \Big|_{\vec{x}=\vec{x}_0} + \frac{1}{2} \sum_{i,j} \frac{\partial^2 F(\vec{x})}{\partial x_i \partial x_j} \Big|_{\vec{x}=\vec{x}_0} \Delta x_i \Delta x_j. \quad (\text{D.1})$$

The gradient $\vec{\nabla} F(\vec{x})$ is always pointing in the opposite direction of the steepest descent. So if one follows the negative gradient, one should reach a (possibly local) minimum. The absolute value of the gradient decreases as the minimum approaches and vanishes at the minimum.

In the SD method the size of the step $\Delta\vec{x}$ is a priori not fixed. In practical applications the size of the step has to be determined rather empirically (proceed along the direction of the negative gradient until the function values start to rise again). In our case we set the step size equal to a parameter λ times the negative gradient:

$$\Delta\vec{x} = -\lambda \vec{\nabla} F(\vec{x}) \Big|_{\vec{x}=\vec{x}_0}, \quad (\text{D.2})$$

where λ is restricted to $\lambda \in (0, 1]$. Inserting this equation (D.2) into equation (D.1) and neglecting the quadratic terms leads to

$$F(\vec{x}_0 + \Delta\vec{x}) = F(\vec{x}_0) - \lambda \left(\vec{\nabla} F(\vec{x}) \Big|_{\vec{x}=\vec{x}_0} \right)^2.$$

λ can be adopted to the ‘local’ situation: where the function is varying fast, the step size becomes bigger because in such a region the function will hardly have a minimum.

D.2 Newton-Raphson method

The Newton-Raphson method is used in this thesis to find the root \vec{x}_0 of the equation

$$\vec{F}(\vec{x}_0) = \vec{F}_0.$$

In this method one calculates, starting from an initial guess \vec{x}_1 , a sequence of values, \vec{x}_2, \dots , which should converge to the solution \vec{x}_0 . The first step is to linearize $\vec{F}(\vec{x})$:

$$\vec{F}(\vec{x}_0) = \vec{F}_0 = \vec{F}(\vec{x}_1) + \vec{\nabla} \vec{F}(\vec{x}) \Big|_{\vec{x}=\vec{x}_1} (\vec{x}_0 - \vec{x}_1) + O((\vec{x}_0 - \vec{x}_1)^2), \quad (\text{D.3})$$

where the gradient $\vec{\nabla} \vec{F}(\vec{x}) \Big|_{\vec{x}=\vec{x}_1}$ is the Jacobian matrix \mathcal{J}_1 defined as

$$(\mathcal{J})_{1,ij} = \left(\frac{\partial F_i}{\partial x_j} \right) \Big|_{\vec{x}=\vec{x}_1}.$$

Neglecting the last term in equation (D.3) leads to

$$\vec{F}_0 = \vec{F}(\vec{x}_1) + \mathcal{J}_1 \Delta \vec{x}_{01},$$

With the inverted Jacobian \mathcal{J}_1^{-1} this equation can be written as

$$\Delta \vec{x}_{01} = \mathcal{J}_1^{-1} \left[\vec{F}_0 - \vec{F}(\vec{x}_1) \right].$$

We thus obtain \vec{x}_2 via

$$\vec{x}_2 = \vec{x}_1 + \Delta \vec{x}_{01},$$

which now replaces \vec{x}_1 in equation (D.3) in order to obtain successive approximations of \vec{x}_i to \vec{x}_0 . It should be noted that the choice of the first guess can be crucial for the overall convergence of the algorithm.

List of Tables

6.1	Numerical comparison between CS and RY results for the HS fluid	126
6.2	Fluid-solid phase transition for the HS system	127
6.3	Thermodynamic parameters for the solution of the square-well potential . .	139
6.4	Thermodynamic parameters for the solution of the square-shoulder potential	142
6.5	Thermodynamic properties for the square-well fluid, ORPA and EXP results	147
6.6	Thermodynamic properties for the square-shoulder fluid, ORPA and EXP results	147
6.7	Coordinates of the critical point for the vapor-liquid phase transition of the square-well fluid	149
6.8	Theoretical and simulation critical point parameters for the one-component Yukawa system	176
6.9	Critical point temperatures for the one-component Yukawa system	177
6.10	Critical point parameters for the one-component Yukawa system	177
6.11	Vapor-liquid coexistence densities for the one-component Yukawa system with $\kappa = 3.9$	177
6.12	Vapor-liquid coexistence densities for the one-component Yukawa system with $\kappa = 7.0$	177
6.13	Vapor-mixed liquid critical point (ρ_c, T_c^*) for symmetric binary fluid mixtures	188
A.1	List of abbreviations, A-H	199
A.2	List of abbreviations, I-Z	200
B.1	Mesh parameters for fast Fourier transforms.	206
B.2	Approximate execution time in seconds for various mesh sizes	206
B.3	Common mesh parameters	207
C.1	Lattice parameters	213

Bibliography

- [1] *Liquids, Freezing and Glass Transition (Les Houches Lectures, Session LI)* (North-Holland, Amsterdam, 1991), edited by J.P. Hansen, D. Levesque, and J. Zinn-Justin.
- [2] H. Löwen, *Phys. Rep.* **237**, 249 (1994).
- [3] *Fundamentals of Inhomogeneous Fluids* (Dekker, New York, 1992), edited by D. Henderson.
- [4] D.W. Oxtoby, in: *Liquids, Freezing and Glass Transition (Les Houches, Session LI)* (North-Holland, Amsterdam, 1991), edited by J.P. Hansen, D. Levesque, and J. Zinn-Justin.
- [5] R. Evans, and M. Chan, *Physics World* **9**, 48 (1996).
- [6] J.P. Hansen, and I.R. McDonald, *Theory of simple liquids* (Academic Press, London, 1986), 2nd edition.
- [7] H.C. Andersen, and D. Chandler, *J. Chem. Phys.* **57**, 1918 (1972).
- [8] F. Lado, *Phys. Rev.* **135**, A1013 (1964).
- [9] J.M.J Van Leeuwen, J. Groenveld, and J. De Boer, *Physica* **25**, 792 (1959).
- [10] J.K. Percus, and G.L. Yevick, *Phys. Rev.* **110**, 1 (1958).
- [11] F.A. Rogers, and D.A. Young, *Phys. Rev. A* **30**, 999 (1984).
- [12] A.R. Denton, N.W. Ashcroft, and W.A. Curtin, *Phys. Rev. E* **51**, 65 (1995).
- [13] C.N. Likos, and G. Senatore, *J. Phys.: Condens. Matter* **7**, 6797 (1995).
- [14] Y. Rosenfeld, *Phys. Rev. Lett.* **63**, 980 (1989).
- [15] M. Schmidt, *Phys. Rev. E.* **62**, 4976 (2000).
- [16] Y. Rosenfeld, *J. Chem. Phys.* **98**, 8126 (1993).
- [17] J.R. Henderson, *Mol. Phys.* **48**, 389 (1983).
- [18] C.N. Likos, *Effective interactions in soft condensed matter physics*, *Phys. Rep.* (in press).

-
- [19] V. Degiorgio, R. Piazza, M. Corti, and J. Stavans, *J. Chem. Soc. Faraday Trans.* **87**, 431 (1991).
- [20] J.C. Crocker and D.G. Grier, *Phys. Rev. Lett.* **73**, 352 (1994).
- [21] J.C. Crocker and D.G. Grier, *Phys. Rev. Lett.* **77**, 352 (1996).
- [22] N.F. Carnahan, and K.E. Starling, *J. Chem. Phys.* **51**, 635 (1969).
- [23] L. Verlet, and J.J. Weis, *Phys. Rev.* **A5**, 939 (1972).
- [24] D. Henderson, and E.W. Grundke, *J. Chem. Phys.* **63**, 601 (1975).
- [25] I. Nezbeda, *Czech. J. Phys. B* **27**, 247 (1977).
- [26] B.V. Derjaguin, and L. Landau, *Acta Physicochimica (URSS)* **14**, 633 (1941).
- [27] E.J. Verwey, and J.T.G. Overbeek, *Theory of the Stability of Lyophobic Colloids* (Elsevier, Amsterdam, 1948).
- [28] S. Asakura, and F. Oosawa, *J. Chem. Phys.* **22**, 1255 (1954);
S. Asakura, and F. Oosawa, *J. Polym. Sci.* **33**, 183 (1958).
- [29] A. Vrij, *Pure Appl. Chem.* **48**, 471 (1976).
- [30] M. Dijkstra, J.M. Brader, and R. Evans, *J. Phys.: Condens. Matter* **11**, 10079 (1999).
- [31] M. Dijkstra, R. van Roij, and R. Evans, *Phys. Rev. E* **59**, 5744 (1999);
M. Dijkstra, R. van Roij, and R. Evans, *Phys. Rev. Lett.* **81**, 2268 (1998);
M. Dijkstra, R. van Roij, and R. Evans, *Phys. Rev. Lett.* **82**, 117 (1998).
- [32] P.J. Flory, and W.R. Krigbaum, *J. Chem. Phys.* **18**, 1086 (1950).
- [33] F.H. Stillinger, *J. Chem. Phys.* **65**, 3968 (1976).
- [34] F.H. Stillinger, and T.A. Weber, *J. Chem. Phys.* **68**, 3837 (1978).
- [35] F.H. Stillinger, and T.A. Weber, *Phys. Rev. B* **22**, 3790 (1978).
- [36] F.H. Stillinger, *J. Chem. Phys.* **70**, 4067 (1979).
- [37] F.H. Stillinger, *Phys. Rev. B* **20**, 299 (1979).
- [38] O.F. Olaj, *Makromol. Chem.* **177**, 3427 (1976).
- [39] O.F. Olaj, W. Lantschbauer, and K.H. Pelinka, *Macromolecules* **13**, 299 (1980).
- [40] O.F. Olaj, and W. Lantschbauer, *Ber. Bunsenges. Phys. Chem.* **81**, 985 (1977).
- [41] A.Y. Grosberg, P.G. Khalatur, and A.R. Khokhlov, *Makromol. Chem. Rapid Commun.* **3**, 709 (1982).
-

-
- [42] L. Schäfer, and A. Baumgärtner, *J. Physique* **47**, 1431 (1986).
- [43] B. Krüger, L. Schäfer, and A. Baumgärtner, *J. Physique* **50**, 3191 (1989).
- [44] J. Dautenhahn, and C.K. Hall, *Macromolecules* **27**, 5933 (1994).
- [45] A.A. Louis, P.G. Bolhuis, J.P. Hansen, and E.J. Meier, *Phys. Rev. Lett.* **85**, 2522 (2000).
- [46] A. Lang, C.N. Likos, M. Watzlawek, and H. Löwen, *J. Phys.: Condens. Matter* **24**, 5087 (2000).
- [47] L.S. Ornstein, and F. Zernike, *Proc. Akad. Sci. (Amsterdam)* **17**, 793 (1914).
- [48] C. Caccamo, *Phys. Rep.* **274**, 1 (1996).
- [49] H.C. Andersen, D. Chandler, and J.D. Weeks, *Adv. Chem. Phys.* **34**, 105 (1976).
- [50] B. Widom, *J. Chem. Phys.* **39**, 2808 (1963).
- [51] G. Pastore, F. Matthews, O. Akinlade, and Z. Badirkhan, *Mol. Phys.* **84**, 653 (1995).
- [52] L. Verlet, and J.J. Weis, *Mol. Phys.* **28**, 665 (1974).
- [53] A. Lang, *Diplomarbeit, TU-Wien*, 1998 (unpublished).
- [54] J.L. Lebowitz, and J.K. Percus, *Phys. Rev.* **144**, 251 (1966).
- [55] E. Thiele, *J. Chem. Phys.* **39**, 474 (1963).
- [56] M.S. Wertheim, *Phys. Rev. Lett.* **10**, 321 (1963);
M.S. Wertheim, *J. Math. Phys.* **5**, 643 (1964).
- [57] W.R. Smith, and D. Henderson, *Mol. Phys.* **19**, 411 (1970).
- [58] J.L. Lebowitz, and J.S. Rowlinson, *J. Chem. Phys.* **41**, 133 (1964).
- [59] R.J. Baxter, *J. Chem. Phys.* **52**, 4559 (1970).
- [60] E.W. Grundke, and D. Henderson, *Mol. Phys.* **24**, 269 (1972).
- [61] J.J. Salacuse, and G. Stell, *J. Chem. Phys.* **77**, 3714 (1982).
- [62] S. Leroch, *Diplomarbeit, TU-Wien*, 1998 (unpublished).
- [63] E. Velasco, L. Mederos, and G. Navascues, *Langmuir* **14**, 5652 (1998).
- [64] L. Verlet, *Phys. Rev.* **165**, 202 (1968).
- [65] L.L. Lee, *J. Chem. Phys.* **97**, 8606 (1992).
- [66] L.L. Lee, D. Ghonasgi, and E. Lomba, *J. Chem. Phys.* **104**, 8058 (1996).
-

-
- [67] M.J. Fernaund, E. Lomba, and L.L. Lee, *J. Chem. Phys.* **112**, 810 (2000).
- [68] A.A. Broyles, *J. Chem. Phys.* **35**, 493 (1963).
- [69] S. Labik, A. Malijevsky, and P. Vonka, *Molec. Phys.* **56**, 709 (1985).
- [70] Y. Singh, *Phys. Rep.* **207**, 351 (1991).
- [71] *Fundamentals of Inhomogeneous Fluids* (Dekker, New York, 1992), edited by D. Henderson.
- [72] M. Jaric, and U. Mohanty, *Phys. Rev. Lett.* **58**, 230 (1987);
M. Jaric, and U. Mohanty, *Phys. Rev. Lett.* **59**, 1170 (1987);
M. Jaric, and U. Mohanty, *Phys. Rev. B* **37**, 4441 (1988).
- [73] P. Tarazona, *Phys. Rev. A* **31**, 2672 (1985).
- [74] W.A. Curtin, and N.W. Ashcroft, *Phys. Rev. A* **32**, 2909 (1985);
W.A. Curtin, and N.W. Ashcroft, *Phys. Rev. Lett.* **56**, 2775 (1986).
- [75] A.R. Denton, and N.W. Ashcroft, *Phys. Rev. A* **39**, 4701 (1988).
- [76] Y. Rosenfeld, *Phys. Rev. A* **32**, 1834 (1985).
- [77] P. Tarazona, and Y. Rosenfeld, *Phys. Rev. E* **55**, 4873 (1997).
- [78] P. Tarazona, *Phys. Rev. Lett.* **84**, 694 (2000).
- [79] Y. Rosenfeld, M. Schmidt, H. Löwen, and P. Tarazona, *Phys. Rev. E* **55**, 4245 (1997).
- [80] Y. Rosenfeld, *Phys. Rev. E* **54**, 2827 (1996).
- [81] *International tables for crystallography, Volume A: Space group symmetry* (Kluwer Academic Publishers, Dordrecht/Boston/London, 1992), edited by T. Hahn.
- [82] C. Rascon, L. Mederos, and G. Navascues, *J. Chem. Phys.* **23**, 10527 (1996).
- [83] C. Rascon, L. Mederos, and G. Navascues, *Phys. Rev. E* **54**, 1261 (1996).
- [84] C.F. Tejero, A. Daanoun, H.N.W. Lekkerkerker, and M. Baus, *Phys. Rev. E* **51**, 558 (1995).
- [85] N.B. Wilding, F. Schmid, and P. Nielaba, *Phys. Rev. E* **58**, 2201 (1998).
- [86] P.V. Giaquinta, and G. Giunta, *Physica A* **187**, 145 (1992);
P.V. Giaquinta, G. Giunta, and S. Prestipino Giarritta, *Phys. Rev. A* **45** R6966 (1992).
- [87] F. Saija, P.V. Giaquinta, G. Giunta, and S. Prestipino Giarritta, *J. Phys.: Condens. Matter* **6**, 9853 (1994);
C. Caccamo, *Phys. Rev. B* **51**, 3387 (1995).
-

-
- [88] M. Watzlawek: Dissertation, *Phase Behavior of Star Polymers* (Shaker Verlag, Aachen, 2000).
- [89] F.H. Stillinger, and D.K. Stillinger, *Physica A* **244**, 358 (1997).
- [90] Y. Rosenfeld, and N.W. Ashcroft, *Phys. Rev. A* **20**, 1208 (1979).
- [91] M. Watzlawek, C.N. Likos, and H. Löwen, *Phys. Rev. Lett.* **82**, 5289 (1999).
- [92] J.P. Hansen, and L. Verlet, *Phys. Rev.* **184**, 151 (1969).
- [93] J.P. Hansen, and D. Schiff, *Mol. Phys.* **25**, 1281 (1973).
- [94] R. Evans, *Adv. Phys.* **28**, 143 (1979).
- [95] A.A. Louis, P.G. Bolhuis, and J.P. Hansen, *Phys. Rev. E* **62**, 7961 (2000).
- [96] C.N. Likos, M. Watzlawek, and H. Löwen, *Phys. Rev. E* **58**, 3135 (1998).
- [97] B.J. Alder, and T.E. Wainwright, *J. Chem. Phys.* **27**, 1208 (1957).
- [98] W.W. Wood, and J.D. Jacobson, *J. Chem. Phys.* **27**, 1207 (1957).
- [99] B.J. Alder, W.G. Hoover, and D.A. Young, *J. Chem. Phys.* **49**, 3688 (1968).
- [100] W.G. Hoover, and F.H. Ree, *J. Chem. Phys.* **49**, 3609 (1968).
- [101] A.D.J. Haymet, and D. Oxtoby, *J. Chem. Phys.* **84**, 1769 (1986).
- [102] J.M. Kincaid, and J.J. Weis, *Mol. Phys.* **34**, 931 (1977).
- [103] A. Lang, G. Kahl, C.N. Likos, H. Löwen, and M. Watzlawek, *J. Phys.: Condens. Matter* **11**, 10143 (1999).
- [104] J. Bergenholtz, P. Wu, J. Wagner, and B. D'Aguzzo, *Mol. Phys.* **87**, 331 (1996).
- [105] G. Zerah, and J.P. Hansen, *J. Chem. Phys.* **84**, 2336 (1986).
- [106] P. Bolhuis, M. Hagen, and D. Frenkel, *Phys. Rev. E* **50**, 4880 (1994).
- [107] P. Bolhuis, and D. Frenkel, *Phys. Rev. Lett.* **72**, 2211 (1994).
- [108] P. Bolhuis, and D. Frenkel, *J. Phys.: Condens. Matter* **9**, 381 (1997).
- [109] A.R. Denton, and H. Löwen, *J. Phys.: Condens. Matter* **9**, L1 (1997).
- [110] C.N. Likos, Zs.T. Nemeth, and H. Löwen, *J. Phys.: Condens. Matter* **6**, 10965 (1994).
- [111] A.P. Gast, C.K. Hall, and W.B. Russel, *J. Colloid Interface Sci.* **96**, 251 (1983).
- [112] C. Caccamo, G. Pellicane, D. Costa, D. Pini, and G. Stell, *Phys. Rev. E* **60**, 5533 (1999).
-

-
- [113] L. Mederos, and G. Navascues, *J. Chem. Phys.* **101**, 9841 (1994).
- [114] M.H.J. Hagen, and D. Frenkel, *J. Chem. Phys.* **101**, 4093 (1994).
- [115] L. Mederos, G. Navascues, P. Tarazona, and E. Chacon, *Phys. Rev. E* **47**, 4284 (1993).
- [116] L. Mederos, G. Navascues, and P. Tarazona, *Phys. Rev. E* **49**, 2161 (1994).
- [117] D. Pini, G. Stell, and N.B. Wilding, *Mol. Phys.* **95**, 483 (1998).
- [118] E. Lomba, and N.E. Almarza, *J. Chem. Phys.* **100**, 8367 (1994).
- [119] C. Caccamo, G. Giunta, and G. Malescio, *Mol. Phys.* **84**, 125 (1995).
- [120] J.S. Hoye, and G. Stell, *J. Chem. Phys.* **67**, 439 (1977).
- [121] J.S. Hoye, and G. Stell, *Mol. Phys.* **52**, 1071 (1984).
- [122] E. Waisman, *Mol. Phys.* **25**, 45 (1973).
- [123] J.S. Hoye, J.L. Lebowitz, and G. Stell, *J. Chem. Phys.* **61**, 3253 (1974).
- [124] J.S. Hoye, and L. Blum, *J. Stat. Phys.* **19**, 317 (1978).
- [125] L. Blum, *J. Stat. Phys.* **22**, 661 (1980).
- [126] A. Parola, and L. Reatto, *Phys. Rev. Lett.* **53**, 2417 (1984);
A. Parola, and L. Reatto, *Phys. Rev. A* **31**, 3309 (1985);
A. Meroni, A. Parola, and L. Reatto, *ibid.* **42**, 6104 (1990);
M. Tau, A. Parola, D. Pini, and L. Reatto, *Phys. Rev. E* **52**, 2644 (1995).
- [127] A. Parola, and L. Reatto, *Adv. Phys.* **44**, 211 (1995).
- [128] L. Reatto, in *New Approaches to Old and New Problems in Liquid State Theory*, edited by C. Caccamo, J.P. Hansen, and G. Stell, Vol. 529 of *NATO advanced Studies Institute Series B: Physics* (Kluwer, Dordrecht, 1999).
- [129] R.B. Griffiths, *Phys. Rev. Lett.* **24**, 715 (1970).
- [130] K. Huang, *Statistical Mechanics* (John Wiley & Sons, 1987), 2nd edition.
- [131] J.W. Cooley, and J.W. Tukey, *Mathematics of Computation* **19**, 297 (1965).
-

Acknowledgment

This work was supported by the Österreichische Forschungsfond under Project Nos P11194-PHY and P13062-TPH and the Österreichische Nationalbank under Project No 6241. I also acknowledge financial support by the Deutsche Forschungsgemeinschaft within the SFB 237.

During the last three years, I was supported by a great number of people. For the opportunity to spend over half of a year in Düsseldorf I would like to thank Hartmut Löwen. During this period of time, Matthias Schmidt introduced me into the fundamental measure theory.

In Vienna, I would like to thank Dieter Gottwald, Hans Renezeder and Elisabeth Maria Schöll-Paschinger for many fruitful physical discussions.

Beside the people mentioned above, this work was made possible by the following people: Gerhard Kahl because of his support and for giving me the opportunity to work in his group, and Christos N. Likos for introducing me into the wonderful world of physics.

However, this work was only made possible because of the strong support from my family and friends (including Gerhard and Christos). My biggest thanks goes to my parents, my sister (with little Hannes), my closest friend Martin and, of course, my girlfriend Sabine for her love, support and strength to drive me through the last three years.

In memory of Karl Rieder, 20. 8. 1973 - 20. 8. 2000.

Curriculum Vitae

- Personal:

- Name: Andreas Lang
- Date of Birth: March 18th 1972
- Place of Birth: Bruck a. d. Mur, Styria
- Address: Bendlgasse 24/3, 1120 Vienna, Austria

- Education:

- 4 years primary school (September 1978 - June 1982)
- 4 years secondary school (September 1982 - June 1986)
- 5 years technical highschool (HTL) (September 1986 - June 1991)
- 11 terms Technical Physics at the Technical University of Vienna (October 1992 - January 1998)
- 3 years PhD at the Technical University of Vienna (March 1998 - April 2001)
(6 months at the Heinrich Heine University Düsseldorf and Jülich)